Universidad Rey Juan Carlos

DOCTORAL THESIS

Structural integrity of composite solid propellant based on carboxyl-terminated polybutadiene binder

Author:

Mario Martínez Sánchez

Supervisors:

Alicia Salazar López

Raúl López Sánchez

Doctoral Program in Industrial Technologies: Chemical, Environmental, Energetic, Electronic, Mechanics and Materials

International Doctoral School

2024

"Learning without thought is labour lost;

thought without learning is perilous."

Confucius

Acknowledgements

Aunque la redacción de este documento sea principalmente en inglés, los agradecimientos los escribiré en la lengua que más cómodo me siento.

Como no puede ser de otra manera, quiero comenzar los agradecimientos por los que han sido mis directores de tesis, Alicia y Raúl. En vosotros he podido ver durante todos estos años, que no son pocos, la pasión y dedicación a la ciencia. Muchas gracias a ambos por estar siempre no sólo guiándome, si no arrimando el hombro. Alicia, simplemente decir que es un placer trabajar y aprender contigo. Una vez te oí decir que, de los lugares en los que habías estado trabajando, lo más importante no eran sus capacidades de investigación, si no las personas que formaban los grupos. Podrá resultar manido, pero me uno a esa opinión. Raúl, muchas gracias por todos los ánimos durante el camino y por toda la generosidad con la que me has tratado siempre. Creo que, en el mejor sentido de las palabras, nunca conoceré a nadie como tú.

Casi como a un tercer director he de agradecer a Jesús su apoyo durante la tesis. Gracias por ayudarme a pensar siempre un poco más allá de lo evidente y gracias por tener siempre la puerta abierta. Este último agradecimiento me gustaría extenderlo a los miembros del grupo de Durabilidad e Integridad de Mecánica de Materiales Estructurales (DIMME), profesores e investigadores

de las áreas de Ingeniería Mecánica y Mecánica de Medios Continuos y Teoría de Estructuras de la Universidad Rey Juan Carlos. Todos y todas siempre tenéis 5 minutitos, que nunca lo son, para lo que haga falta.

Parte especial del DIMME han sido para mí Alberto, David, Rocío y Sole. Gracias por hacerme sentir más seguro porque siempre habéis estado para todo. Espero que siga habiendo barbacoas, teatros, viajes y cafés para poder seguir escribiendo las memorias de Zipi y Zape. Sin vosotros, estos años no habrían sido lo mismo...

Formalmente, quiero agradecer al Instituto Nacional de Técnica Aeroespacial por contribuir al desarrollo de la tesis, permitiéndome hacer uso de sus instalaciones, así como proporcionando material. Aprovecho para agradecer a aquellos de La Marañosa con los que he compartido tiempo y DESEIDes. Especialmente, debo dar las gracias a David Chimeno por ponérmelo tan fácil siempre. Mucho ánimo, ahora es tu turno.

During this thesis I was welcomed to stay in *Göteborg* for 3 months. I am sincerely grateful to prof. Ragnar Larsson to accept me in the Material and Computational Mechanics division from Chalmers University of Technology. People at MCM were all welcoming and inclusive from the very beginning, I still miss fika time. It was such a nice time there.

I would also like to thank prof. Richard Schapery for attending our concerns. Your guidance will shape our coming work.

Para el final dejo el mejor bocado. Acabo dando las gracias a mi familia, tan importante para mí. Es gracias a ell@s que hoy estoy aquí, terminando esta tesis. Somos una familia peculiar, pero, sobre todo, bonita. Tengo que agradeceros que es gracias a vosotros que soy quien soy. Gracias por transmitirme los valores que espero también tener. Para mí, los más importantes, ser buena persona y cuidar a los tuyos. María, no te dedico otro párrafo para ti porque, cómo no, también eres parte de esta familia, que espero también consideres tuya. Gracias por tu paciencia infinita y por tu apoyo. Gracias por venir conmigo a la jungla. Gracias por formar un hogar junto a mí.

Resumen

Los motores de cohetes de propulsante sólido de material compuesto se almacenan habitualmente durante largos períodos de tiempo. A lo largo de este periodo de almacenamiento en el polvorín, los motores sufren diversos procesos de degradación o daño, comúnmente denominados como envejecimiento, los cuales suponen el origen de defectos, tales como grietas, en el propulsante. Estos envejecimientos que se dan a lo largo de la vida del motor tienen su causa en procesos químicos, promovidos por la exposición a altas temperaturas, a humedad o a oxidantes atmosférico; y procesos mecánicos, tales como las vibraciones en los transportes, las deformaciones inducidas debidas al propio peso del grano o a tensiones de origen térmico provocadas por los ciclos día-noche o las estaciones del año, por ejemplo.

Los motores de este tipo de propulsantes utilizados en aplicaciones de defensa tienen un tiempo de vida útil recomendado por el fabricante. Sin embargo, debido a su alto coste las naciones se ven incentivadas a optimizar su vida útil, de manera que su vida en servicio real se suele alargar al máximo posible. Esta optimización requiere un equilibrio delicado entre la rentabilidad y la fiabilidad operativa. Para evaluar la idoneidad operativa de un motor, es habitual la implementación de un conjunto de pruebas, conocidas, en su conjunto, como programa de vigilancia.

Estos programas de vigilancia definen las pruebas a realizar, las metodologías de análisis de datos y establecen los criterios de decisión. En España, la Subdirección de Sistemas Terrestres del Instituto Nacional de Técnica Aeroespacial (INTA) es la responsable de los ensayos de laboratorio para la vigilancia de motores de propulsante de material compuesto.

Un aspecto crítico que afecta la vida útil de los motores de propulsante sólido es la aparición de grietas en el seno del grano. La geometría del grano se diseña para lograr un perfil de empuje predeterminado durante la combustión. La presencia de grietas altera la superficie de quemado durante el vuelo del cohete, poniendo en peligro su operatividad. Es por ello, por lo que se reconoce que la evaluación de la integridad estructural del propulsante del motor es de suma importancia.

Sin embargo, debido al complejo comportamiento mecánico y a fractura de este tipo de materiales, actualmente faltan procedimientos estandarizados para evaluar su comportamiento en fractura. La razón principal es que aún no existe un consenso sobre cuál es el parámetro de control o el enfoque de la mecánica de la fractura para evaluar la respuesta mecánica de estos materiales. Los propulsantes sólidos de material compuesto están formados por múltiples constituyentes con respuestas mecánicas muy diferentes: partículas cerámicas oxidantes con comportamiento elástico lineal, combustible metálico con comportamiento mecánico elasto-plástico y la matriz elastomérica que actúa como aglutinante y con respuesta mecánica hiperviscoelástica. A pesar de esta variedad, generalmente se acepta que el comportamiento mecánico de estos materiales se rige principalmente por la matriz elastomérica, que suele ser el constituyente minoritario.

La evaluación del comportamiento a fractura de los propulsantes sólidos de material compuesto en España es un área de investigación reciente y aún no está plenamente integrada en los programas de vigilancia actuales. Este hecho, sumado a la propia complejidad del problema, genera un área de interés para la investigación, de manera que se establece el objetivo de esta tesis en la evaluación del comportamiento mecánico y a fractura bajo tres tipos de

envejecimientos acelerados (mecánico, térmico y por ozono) de un propulsante sólido procedente del motor de aceleración de cohetes de dos etapas. Los envejecimientos acelerados realizados cubren todos los procesos de degradación que sufre el grano de un motor durante su vida útil y que son posibles fuentes de generación de defectos y grietas. El material objeto de estudio fue un propulsante de alta energía con matriz de polibutadieno carboxiterminal, partículas oxidantes de perclorato amónico y aluminio micronizado como combustible. Previo al análisis del efecto del envejecimiento, se determinó la respuesta mecánica y a fractura del propulsante a distintas velocidades de deformación para establecer el comportamiento del material virgen. Desde el punto de vista metodológico se empleó la mecánica de la fractura viscoelástica desarrollada por Schapery, usando como parámetro de control tanto la integral J, como la apertura de la punta de la grieta (CTOD, por sus siglas en inglés).

Del análisis inicial sobre el efecto de la velocidad de deformación en el comportamiento mecánico y a fractura se determinó el marcado comportamiento viscoelástico del propulsante analizado, es decir, su importante dependencia del tiempo. Esto se tradujo en un material más rígido y que soportaba mayores cargas y deformaciones a mayores velocidades de deformación. Además, se identificó que la principal causa por la que crecen las grietas es el desgarro de la matriz. No obstante, para velocidades de deformación suficientemente elevadas, la energía aportada en el proceso de carga es capaz de romper la intercara que une las partículas oxidantes de perclorato amónico con la matriz elastomérica. Respecto al comportamiento a fractura, los valores de iniciación y propagación tanto de la integral J, como de la apertura de la punta de la grieta han sido mayores cuanto mayor era la velocidad de deformación, evidenciando la dependencia de los fenómenos viscosos en el comportamiento a fractura del propulsante.

A continuación, se evaluaron los efectos de tres tipos de envejecimiento acelerado sobre el comportamiento mecánico y a fractura del propulsante analizado. Los envejecimientos propuestos fueron: mecánico, imponiendo una precarga en la dirección del ensayo hasta alcanzar una deformación del 15% y

del 30%; térmico, introduciendo las probetas de propulsante en un horno a una temperatura constante de 80 ºC durante 24 y 36 días; y con ozono, exponiendo al propulsante a una concentración constante de aproximadamente 160 ppm durante 14, 21, 32 y 42 días. En este caso, también se realizó la caracterización a fractura a través de la aproximación de la mecánica de la fractura viscoelástica propuesta por R. Schapery. Los ensayos llevados a cabo fueron, igualmente, ensayos de relajación, tracción uniaxial y fractura. En esta campaña experimental, todos los ensayos se realizaron a la misma velocidad de desplazamiento de 5 mm/min. Asimismo, se realizó un análisis fractográfico de las superficies de fractura para observar los mecanismos de propagación de las grietas. Además, se llevó a cabo una caracterización química para determinar la densidad de entrecruzamiento de la matriz del propulsante para todos los envejecimientos estudiados.

De los resultados obtenidos se determinó que:

- El envejecimiento mecánico se relaciona con la decohesión entre las partículas oxidantes de perclorato amónico y la matriz elastomérica, además de apreciarse un ligero endurecimiento de ésta, sin dar lugar a cambios en la densidad de entrecruzamiento. El comportamiento a relajación no se vio alterado por este envejecimiento y el comportamiento a tracción mostró un marcado efecto Mullins. El comportamiento a la fractura tampoco se vio significativamente afectado, de manera que el proceso de propagación de la grieta requirió ligeramente menos de energía en el propulsante más envejecido. Esta variación de la energía de fractura se asoció a la energía para producir la decohesión de parte de las partículas oxidantes de la matriz, ya que ésta no experimenta cambios significativos de la densidad de entrecruzamiento.
- El envejecimiento térmico se ha asociado con un aumento en la densidad de entrecruzamiento y correlacionado con un drástico aumento en la rigidez y resistencia del propulsante, reduciendo significativamente su capacidad de deformación. En este caso, el comportamiento a fractura del material envejecido resultó en un proceso de propagación de grieta más estable, directamente relacionado con los cambios en las

capacidades mecánicas de la matriz elastomérica y el hecho de que el proceso de fractura se produce principalmente a través del desgarro de la misma.

- El envejecimiento por ozono se ha empleado con éxito para simular el envejecimiento producido por la exposición al ambiente atmosférico y a la humedad. Las reacciones de ozonólisis afectaron la matriz elastomérica reduciendo su densidad de entrecruzamiento. Esto resultó en una disminución de la rigidez, la capacidad de carga y el desempeño en fractura. Las grietas en el propulsante envejecido comenzaron a crecer con menores energías de fractura, implicando una propagación menos resistente y estable en comparación con el material no envejecido, lo que se relaciona directamente con la ruptura de las cadenas poliméricas, ya que el progreso de la fractura ocurre fundamentalmente a través del desgarro de la matriz.

Asimismo, teniendo como referencia para la aplicación de la aproximación de la mecánica de la fractura viscoelástica el material en el instante inicial antes de iniciar la relajación, las energías de fracturas y el CTOD determinados reducen su valor alrededor del 70% respecto a los determinados sin tener en cuenta el efecto de los procesos viscosos. Se observó que, para las altas velocidades de deformación, cuando el propulsante no tiene tiempo para relajar dar lugar a los fenómenos disipativos, los valores de energía de fractura y el CTOD apenas se veían modificados, resaltando la necesidad de la aplicación de la mecánica de la fractura viscoelástica.

Con relación a la aplicación de esta aproximación de la mecánica de la fractura viscoelástica en la caracterización a fractura de los propulsantes sólidos de material compuesto, se ha de tener en cuenta que los parámetros de fractura obtenidos a través de dicha metodología resultan depender de una constante arbitraria. No obstante, se ha podido determinar que la tensión cohesiva en la punta de la grieta es independiente de dicha arbitrariedad y, por tanto, supone un parámetro de fractura con una mayor aplicabilidad.

Los envejecimientos han producido diversos cambios en el propulsante de partida, lo cual se ha visto reflejado en las diferentes propiedades determinadas durante la caracterización, observándose diferentes tendencias para cada una en función del tipo de envejecimiento. Para salvar la problemática de identificar el daño soportado por el propulsante según el tipo y grado de envejecimiento que predomina sobre el material, se ha empleado de manera satisfactoria el análisis por componentes principales, permitiendo identificar de manera clara aquellos materiales envejecidos en unas condiciones concretas respecto de las demás.

Abstract

The work summarised in this thesis comprises an extensive experimental campaign focused on the evaluation of the structural integrity of an ageing composite solid propellant (CSP) coming from booster stage of a two-stage rocket motor. This propellant was a high energy carboxyl-terminated polybutadiene (CTPB) based binder matrix with ammonium perchlorate (AP) oxidiser and aluminium (Al) powder fuel. The experimental campaign was divided into two parts: a preliminary characterisation centred on the starting material and a second characterisation focused on the evaluation of the behaviour of the propellant under several ageing conditions. In both characterisation stages, the time-dependent behaviour of the CSP has been assessed through relaxation, uniaxial tensile and fracture tests. Fracture characterisation was performed using the viscoelastic fracture mechanics approach developed by R. Schapery (Schapery, 1984), due to the remarkable viscous nature of the studied CSP.

During the preliminary characterisation, the strain rate effect on mechanical and fracture behaviours. It was observed that increasing the strain rate translated to a stiffer, more resistant material with unusual higher straining capability at the same time. The primary mechanism responsible for the growth of defects was the matrix tearing. Nevertheless, it was found that strain rate

may influence this primary fracture mechanism by increasing the strain rate, producing not only the matrix tearing, but also the decohesion between the greater oxidiser particles and the matrix, phenomenon called dewetting. This well-known damage in CSP was also detected by dilatation phenomenon and Poisson's ratio reduction. Determined fracture energies presented a dependency on the strain rate, being required more energy to initiate crack growth and propagate the crack when higher strain rates are applied, even when the viscoelastic fracture mechanics was applied.

In the following characterisation, the CSP was subjected to three types of accelerated ageing: mechanical, thermal and ozone. These accelerated ageing sources were chosen to represent the main ageing phenomena that a CSP rocket motor might experience during its lifetime. Measurements of crosslinking density of the CSP were done to relate it to the variations of the mechanical and fracture responses.

The accelerated mechanical ageing, as an applied preload, was manifested as a dewetting promotion inducing a mechanical behaviour affected by Mullin's effect. The fracture behaviour was not significantly modified by this type of ageing where fracture energy was slightly less demanding. Crosslinking density measurements did not show a change with the ageing. Therefore, the conclusion was that the small changes in the fracture energy are related to the generated dewetted surface during the preload, while the matrix tearing process, which is more significant, was unaltered.

Thermal accelerated ageing, which consisted in isothermal ageing, significantly changed the mechanical response of the CSP, severely increasing its stiffness and strength, while drastically reducing the straining capability. The fracture behaviour was determined to be more energetically demanding after the ageing. These changes were connected to the increase of the crosslinking density, resulting in higher energies required to tear the stiffer and more crosslinked matrix.

The ozone accelerated ageing, which is a novel procedure proposed in this thesis, also produced significant alterations of the mechanical and fracture

behaviours. It was observed a relevant decrease of the stiffness and load bearing capacity of the CSP, as well as less demanding crack growth initiation and propagation. The induced ozonolysis reactions produced the rupture of the polymeric chains, decreasing the crosslinking density. Thus, the matrix tearing process required lower energy.

Following the strip yield models, the fracture process zone (FPZ) models assume a region around the crack tip where the material is not fully damaged and there exist stresses holding the sides of the crack. This closure or cohesive stress was determined as the one of the best fracture parameters to characterise the fracture of the CSP using the viscoelastic fracture mechanics approach. It was found that this closure or cohesive stress at the failure zone at the crack tip is related to the dewetting stress determined through the uniaxial tensile behaviour.

Reported parameters during the characterisation are numerous and each of them follows a different trend for the different ageing source. To handle all this information, the principal component analysis (PCA) statistical multivariate method was successfully employed to reduce the number of variables involved and identify the material that has been subjected to a specific type and grade of ageing.

Contents

Acronyms and symbols

Acronym	
Symbol	**Description**
$\vec{T}_0$	Surface tractions vector
$\hat{f}_C(p)$	Laplace-Carson transformed function
$\dot{m}_b$	Mass flow rate of combustion gases
$\dot{m}_e$	Exit mass flow rate
$\vec{u}_0$	Applied displacements on the boundary
$\bar{x}_j$	Mean value of the j^{th} variable
Γ^*	Contour surrounding a crack tip section
Π_F	Body forces energy
Π_T	Work done by tractions
Π_{To}	Total energy
Π_s	Stored deformation energy
A^*	Area surrounding a crack tip section
A_b	Burning surface area
A_t	Area of the nozzle's throat
C_1	Power law constant for J-resistance curves
C_1'	Power law constant for CTOD-resistance curves
C_2	Power law exponent for J-resistance curves

Acronym

Symbol	Description
C_2'	Power law exponent for CTOD-resistance curves
C^R	Flexibility of the elastic reference material
D_R	Reference compliance or compliance of the reference elastic material
$\bar{E}(t)$	Normalised relaxation function
E_0	Instantaneous or glassy modulus
E_∞	Equilibrium modulus
E_R	Reference modulus or elastic modulus of the reference elastic material
E^R	Apparent elastic modulus from stress, σ, versus pseudo strain, ε^R, curve
E_a	Apparent activation energy
E_i	Modulus of the spring of a i^{th} Maxwell element
G^R	Shear modulus of the elastic reference material
I_{sp}	Specific impulse
J_{Ic}	Critical J integral for mode I
J^R	Pseudo J integral or viscoelastic J integral
J_c	Critical J integral
J_{pl}	Plastic J integral
K^R	Bulk modulus of the elastic reference material
R^2	Coefficient of determination
S^*	Surface contour surrounding a crack tip
S_0	Initial cross-section
S_{ij}	Separation parameter
$\vec{T}$	Tractions vector
T_a	Accelerated ageing temperature
T_g	Glass transition temperature
T_i	Tractions vector
T_i^R	Pseudo tractions vector
T_s	Storage temperature
U^R	Energy under the load versus pseudo displacement curve
U_{el}	Elastic energy under load versus displacement curve

Acronym

Symbol	Description
U_{pl}	Plastic energy under load versus displacement curve
U_{pl}	Energy under the load versus plastic displacement
V_0	Initial volume
W_F	Work of fracture
W_S	Work needed to produce new surface
W_f	Final propellant mass
W_i	Initial propellant mass
$\vec{b}$	Body forces
c_F	Thrust coefficient
e_{max}	Engineering strain at maximum of uniaxial stress vs strain curve
f_t	Maximum stress in a cohesive linear softening function
p_c	Combustion chamber's pressure
$\dot{r}$	Burning rate
s_j	Standard deviation of the j^{th} variable
s_{max}	Engineering stress at maximum of uniaxial stress vs strain curve
t_1	Time to reach the applied strain in a relaxation test
t_{25}	Equivalent storage time at 25 °C
t_a	Accelerated ageing time
t_s	Storage time
$\vec{u}$	Displacement vector
$\dot{u}$	Displacement rate
u^R	Applied pseudo displacement in fracture test
u_c	Crack tip displacement to complete failure of a cohesive linear softening function
u_i	Displacements vector
u_i^R	Pseudo displacements vector
u_{nl}^R	Non-linear displacement of the reference elastic body
u_{pl}	Plastic displacement
x_{ij}	Value of the j^{th} variable corresponding to the i^{th} observation
z_{ij}	Standardised value of the j^{th} variable corresponding to the i^{th} observation
δ^R	Pseudo crack tip opening displacement

Acronym	
Symbol	Description
ε_0	Applied strain in uniaxial extension configuration
ε_{11}	Longitudinal strain in direction 1
ε^R	Strain in the reference elastic body or pseudo strain
ε_{dew}	Dewetting strain
ε_{dew}^R	Dewetting strain of the reference elastic material
ε_{ij}	Second-rank strain tensor
ε_l	Longitudinal strain
ε_{max}	True strain at maximum of uniaxial stress vs strain curve
ε_t	Transverse strain
η_{el}	Elastic constraint or calibration factor
η_{pl}	Plastic constraint or calibration factor
ν_0	Initial Poisson's ratio
ν_0^R	Initial Poisson's ratio of the reference elastic material
ν^R	Poisson's ratio of the reference elastic material
ρ_p	Density of the propellant
σ_0	Applied stress in uniaxial stress configuration
σ_{11}	Normal stress in direction 1
σ_Y	Yield stress
σ_{dew}	Dewetting stress
σ_{ij}	Second-rank stress tensor
σ_m	Closure or cohesive stress
σ_{max}	True stress at maximum of uniaxial stress vs strain curve
τ_i	Relaxation time of the dashpot of a i^{th} Maxwell element
ω_F^R	Pseudo body forces energy density
ω_S^R	Pseudo strain energy density
$\dot{\boldsymbol{\varepsilon}}$	Second-rank strain rate tensor
$\boldsymbol{\varepsilon_0}$	Second-rank initial strain tensor
Δa	Crack extension
ADN	Ammonium dinitramide
AK	Potassium nitrate
AN	Ammonium nitrate
AP	Ammonium perchlorate

Acronym Symbol	Description
BTTN	Butane-1,2,4-triol trinitrate
CLD	Crosslinking density
CMOD	Crack mouth opening displacement
CSP	Composite solid propellant
CT	Compact tension configuration
CTOD	Crack tip opening displacement
CTPB	Carboxyl-terminated polybutadiene
DIC	Digital image correlation
DMA	Dynamic mechanical análisis
DMP	Dimethyl phthalate
DOA	Dioctyl adipate
DOP	Dioctyl phthalate
DSC	Differential scanning calorimetry
FA	Factor analysis
FDM	Fused deposition modelling
GAP	Glycidyl azide polymer
GC	Gas chromatography
HMDI	Hexamethylene diisocyanide
HPLC	High-performance liquid chromatography
HTPB	Hydroxyl-terminated polybutadiene
IDP	Isodecyl pelargonate
INTA	Instituto Nacional de Técnica Aeroespacial
IPDI	Isophorone diisocyanate
KP	Potassium perchlorate
MAPO	Methyl aziridinyl phosphine oxide
MD	Molecular dynamics
MTN	Metriol trinitrate
NC	Nitrocellylose
NG	Nitroglicerine
PBAA	Polybutadiene acrylic acid
PBAN	Polybutadieneacrylic acid acrylonitrile
PC	Principal component

Acronym Symbol	Description
PCA	Principal component analysis
PLA	Polylactic acid
PSAN	Phase-stabilised ammonium nitrate
ROI	Region of interest
SEM	Scanning electron microscopy
SENB	Single-edge-notched-bending configuration
SENT	Single-edge-notched-tension configuration
SVD	Singular value decomposition
TDI	Toluene-2,4-diisocyanate
TEGDN	Triethylene glycol dinitrate
TGA	Termogravimetric análisis
TMETN	Trimethylol ethane trinitrate
TMP	Trimethylol propane
Π	Potential energy
A	Crack surface
B	Thickness
$D(t)$	Uniaxial creep compliance function
E	Apparent elastic modulus
$E(t)$	Uniaxial tensile relaxation function or relaxation modulus
F	Thrust
G	Energy release rate
$G(t)$	Shear modulus or deviatoric relaxation function
H	Deformation function
$H(t-t_0)$	Heaviside step function
J	J integral
K	Factor loading matrix
$K(t)$	Bulk modulus or volumetric relaxation function
P	Load
P	Factor scores matrix
Q	Proportionality constant between separation parameter, S_{ij}, and the geometric function, g
R	Ideal gas constant

Acronym

Symbol	Description
R	Correlation matrix
S	Soluble fraction
S	Sol fraction
S	Cross-section
S	Scaling diagonal matrix whose values correspond to the square root of RR^T
T	Temperature of the combustion chamber
U	Energy under load versus displacement curve
U	Rotation matrix whose columns are the eigenvectors of RR^T
V	Volume
V	Crack mouth opening displacement
V	Rotation matrix who rows are the eigenvectors of R^TR
W	Width
Z	Standardised variables matrix
a	Crack length
b	Ligament
e	Engineering strain
$f(t)$	Function in the time domain
g	Gravitational constant
g	Geometric function
k	Function for the determination of the burning rate
m	Power law exponent of the geometric function g
m	Crack tip triaxiality dimensionless constant
n	Exponent for the determination of the burning rate
n	Number of observations
p	Complex variable of the Laplace-Carson domain
r	Rotation factor
s	Engineering stress
u	Applied displacement in fracture test
$\mathbb{L}$	Fourth-rank linear operator
α	Empirical constant used to determine the accelerated thermal ageing times

Acronym	
Symbol	Description
γ	Specific heats ratio
δ	Crack tip opening displacement
ε	True strain
η	Constraint or calibration factor
ν	Poisson's ratio
ρ	Density
σ	True stress
τ	Time
ω	Elastic energy density
$\boldsymbol{\varepsilon}$	Second-rank strain tensor
$\boldsymbol{\sigma}$	Second-rank stress tensor

Chapter 1. Problem statement

Composite solid rocket propellant (CSP) motors can be designed to its direct use after manufacture, which could be the case of some specific applications, but motors are usually stored for large periods of time. Over the storage time, these motors undergo several degradation processes, usually termed as ageing or damaging processes, that are one of the sources of defects/crack generation and can be caused mainly by:

- The exposition to high temperatures or humid atmospheres, promoting oxidation reactions during shelf life.
- Vibrations during transport, handling of the motors, gravity and periodic rotations (used to lessen weight induced strains) and thermal variations during storage and transport.

The more direct strategy to evaluate the degradation phenomena during a lifecycle of CSP is through accelerated ageing procedures. Accelerate ageing permits the evaluation of aged CSP properties in a reasonable time span. CSP motors utilised in defence applications typically possess a service life expectancy, as designated by the manufacturer. However, disposal decisions are not solely based on this timeframe and may consider degradation in various motor components (Reeling Brouwer et al., 2005). To assess a motor's continued operational suitability, a comprehensive suite of tests, collectively known as a surveillance program, is implemented (Torry et al., 2001). High lifecycle costs of rocket motors incentivise nations to optimise their service life. This optimisation necessitates a delicate balance between cost-effectiveness and operational reliability (Bennet, 1997). Surveillance programs serve as a cornerstone in this endeavour, ensuring the safety of munitions while maximising their usable lifespan. Consequently, the selection of tests employed within the surveillance program, the data analysis methodologies utilised and the established decision criteria all hold paramount importance.

International surveillance programs for CSP motors vary due to the designation of responsible institutions by individual nations. The selected institutions rule their individual test selections, data analysis methodologies and

decision criteria. In Spain, the National Institute of Aerospace Technology (*Instituto Nacional de Técnica Aeroespacial*, INTA) manages CSP motor surveillance through its Subdirectorate of Terrestrial Systems.

A critical aspect impacting CSP motor lifespan is propellant grain aging. Established surveillance programs typically employ the following chemical and mechanical tests (STANAG 4581, 2022):

- High-performance liquid chromatography (HPLC) to determine remaining antioxidant.
- Sol-gel measurements to determine the soluble fraction or crosslinking density.
- Gas chromatography (GC) to calculate the content of plasticiser.
- Uniaxial tensile tests to evaluate the mechanical performance.
- Dynamic mechanical analysis (DMA) used to evaluate the viscoelastic capability of the propellant.
- Shore A Hardness.

Despite exhibiting excellent chemical stability during extended storage and transportation, CSP reliability is primarily challenged by crack development within the propellant grain. Grain geometry is specifically designed to achieve a predetermined thrust profile during combustion. The presence of cracks alters the combustion surface area throughout rocket flight, jeopardising motor performance. Therefore, structural integrity assessment of the propellant grain holds paramount importance (Tussiwand et al., 2009).

However, due to the complex mechanical and fracture behaviour of CSP materials, standardised procedures for evaluating their fracture performance are currently lacking (NATO-AOP-46, 2022). The reason is that there is not even yet a consensus on which is the control parameter or the fracture mechanics approach to evaluate the mechanical response of these materials. CSP are formed by multiple constituents with very different mechanical responses: ceramic oxidiser particles with linear elastic behaviour, metallic fuel with elastoplastic mechanical performance and the elastomeric matrix acting as binder

and with hyper-viscoelastic mechanical response. Despite this miscellany, it is generally accepted that the mechanical performance of these CSP is mainly governed by the elastomeric binder, which is usually the minor principal constituent. Consequently, for a proper fracture characterisation, the use of the viscoelastic fracture mechanics is mandatory to account for the time-dependent behaviour of the elastomeric matrix. In this work, approach developed by Schapery (Schapery, 1984) has been employed. The underlying problem is that the methodology under this fracture approach still presents some open questions which prevents its widespread application.

Fracture assessment for these materials in Spain is a recent area of investigation and is not yet integrated into established surveillance programs. This thesis contributes to INTA's efforts towards enhancing its surveillance capabilities by focusing on the fracture behaviour of a CSP based on carboxyl-terminated polybutadiene (CTPB) binder system, coming from the booster stage of a two-stage rocket, under three distinct (accelerated) ageing conditions. The degradation conditions selected were mechanical ageing, thermal ageing and ozone ageing, thus covering all natural degradations a CSP can experience during its lifetime.

Finally, the potential of principal component analysis (PCA) as a decision-making tool for surveillance programs is explored. Implementation of PCA could potentially optimise the number of tests and data analysis procedures, leading to reduced surveillance costs for CSP motors.

Chapter 2. Introduction

2.1. Solid propellants. Description and performance characteristics

From horses to rockets, propulsion systems have been one of the cornerstones of the development of the human society. These systems have helped us to evolve technologies such as vehicles, railways, ships or aircrafts. Their development has shaped our present and will define our future. The context of this thesis is framed under the rocket propulsion technologies. A graphic representation of the state-of-the-art propulsion technologies is given in **Fig. 1**, where it can be appreciated the wideness of the rocket propulsion field. Although new propulsion systems are being explored, only chemical, electrostatic and electrothermal technologies are commercially available. Indeed, chemical propulsion systems represent the unique solution to access to space due to the power density and achieved vehicle acceleration, despite the modest specific impulse. Solid rocket propulsion is one of the chemical rocket technologies.

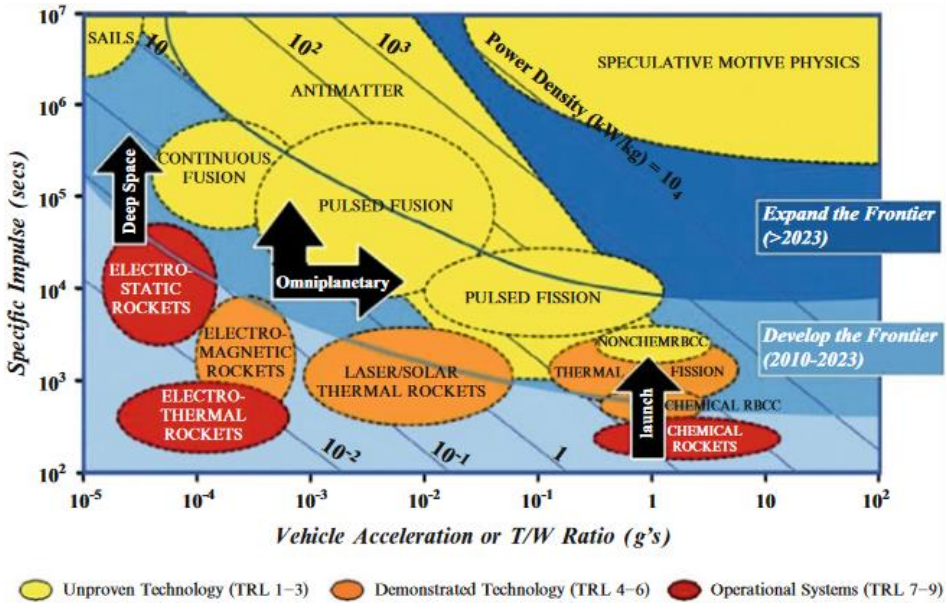

***Fig. 1**. Propulsion technologies' state of the art by NASA. From (DeLuca et al., 2017c).*

The solid propulsion systems are based on solid fuels to power the motor of aircrafts or missiles in civil or military applications, such as air-to-air missiles

(Sutton et al., 2017). Amongst the nonmilitary applications, it stands out the space launches and safety devices in the automotive and aviation industries such as inflators and airbags. Other applications are gas generators suited for fire suppression, emergency surfacing of submarines, ships or sinking objects (Bozic et al., 2017).

Solid propellants are known for their high energy density, long storage times, high reliability, manufacturability and low cost, amongst others (DeLuca et al., 2013; Singh, 2017). Due to these characteristics, solid propellant motors have been and still are one of the most popular technologies employed on rocket propulsion (Humble, 1995). Solid propellant technology has come a long way since its inception and continues to evolve to improve performance, safety and environmental impact (DeLuca, 2016; Trache et al., 2017).

The development of solid propellants is somehow hidden or difficult to track (Hunley, 1999), perhaps due to the fact that this development is closely related to defence and military matters. The early days of these propellants are believed to begin centuries ago, around 1000-220 B.C. (DeLuca et al., 2017b; Krishnamurthy et al., 2017; Sutton et al., 2017), in the ancient China where they used a kind of "black powder" for leisure (pyrotechnics) and defence (firing and flying arrows) (Geisler et al., 2010; DeLuca et al., 2017b). The first steps towards todays rocket launchers were made by the Chinese Wan Hoo around 1500 A.D., sadly unsuccessfully (Krishnamurthy et al., 2017). That technology advanced to the first castable composite solid propellant which was developed by John W. Parsons around 1942 (Hunley, 1999). This was the earliest application to jet-assisted take-off (JATO) units, whose principal composition was potassium perchlorate within a pourable asphalt binder (Sforza, 2016). It was the II World War the principal driving force for the development of composite solid propellants in the missiles field, which until then had been only used in gas generators and guns (Krishnamurthy et al., 2017; Sforza, 2016).

A summary of the developments of different solid propellants is displayed in **Fig. 2**. As cited before, motivated by the II World War during the 1950s-1970s, there was high interest in the production of improved materials. A remarkable manufacturer was Thiokol company, responsible for the invention of PBAN (used for large motors) and, later, they introduced CTPB (Hunley, 1999). Those were the most popular until the 1970s (Klager, 1984), when HTPB gained its place, although it was first developed in the earlies 1960s (Quagliano Amado et al., 2022).

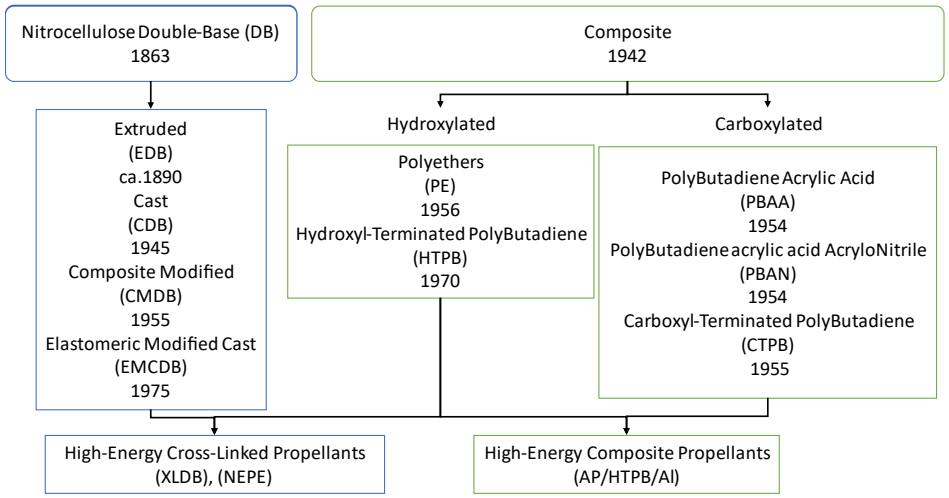

***Fig. 2**. Historical development of some significant solid rocket propellants technologies. Adapted from (DeLuca et al., 2017b).*

Although the military use has been the great motivation of these materials, the aerospace industry gain weight in the development and use of solid rocket motors. The propellant mass employed in missile motors can range in the order of magnitude of tens or hundreds of kilograms (Jain, 2002). Nevertheless, solid stages in space launches can reach the impressive figures of approximately half a million kilograms as shown in **Fig. 3**. Such importance could be devised through the fact that several nations have developed their own solid propellant motors (as first-stage) for launch vehicles, e. g., Scout, Delta, Titan, Atlas, Pegasus and Space Shuttle (U.S.), Ariane (France), H-2 (Japan) or Long March CZ-2E (China) (Humble, 1995).

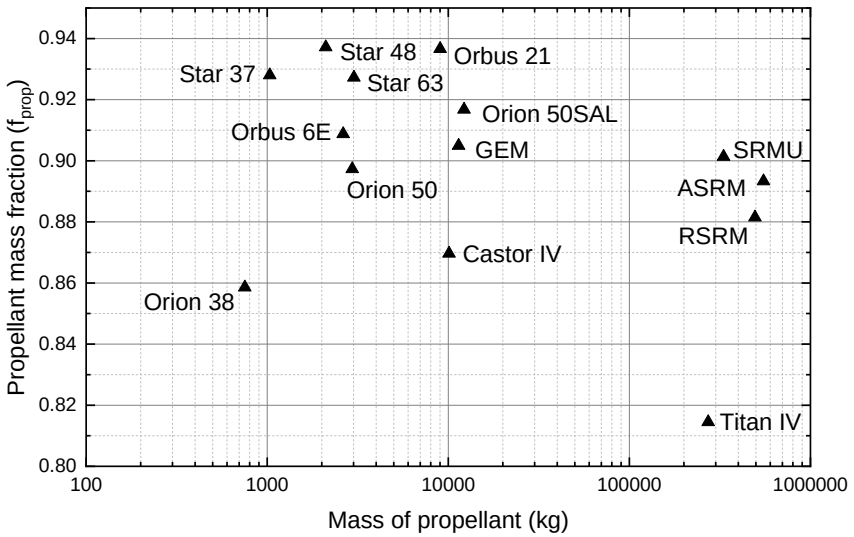

***Fig. 3**. Propellant mass fraction versus total mass of propellant for various solid stage motors. Adapted from (Humble, 1995).*

Although composite solid propellant materials must gather a large list of characteristics to be used in missile and rocket motors, the thrust profile provided to the motor is always the final aim. The specific impulse, I_{sp}, is a measure of the efficiency of the motor to convert the propellant's energy into thrust, F, (Sforza, 2016).

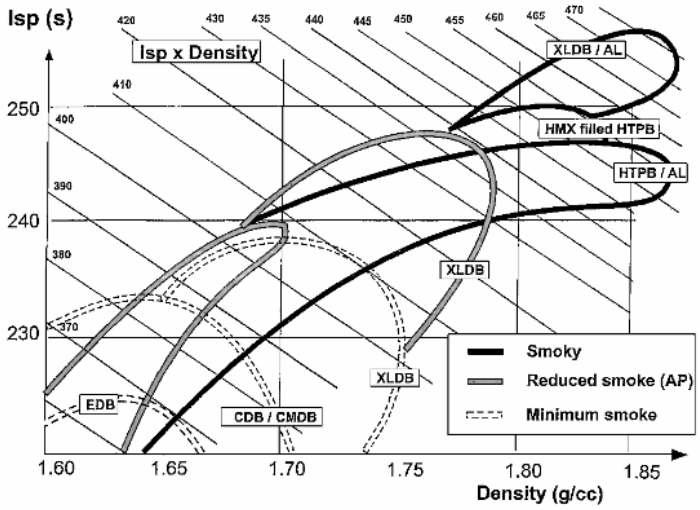

***Fig. 4**. Specific impulse versus mass density chart for different composite solid propellant technologies. From (Davenas, 2003).*

Specific impulse is proportional to the thrust as described in (1), whose relation depends on the exit mass flow rate $\dot{m}_e$ and gravitational constant g. As it can be seen in **Fig. 4**, the specific impulse, that is, the thrust of a composite solid propellant rocket motor supplied by the propellant is strongly dependent on the propellant's composition. For this reason, the pursuit of more energetic compositions is constant (Singh, 2017).

$$I_{sp} = \frac{F}{\dot{m}_e g} \tag{1}$$

Nevertheless, this is not the only important characteristic to consider in order to provide the required thrust. The geometrical design of the propellant grain in the motor is also a vital to deliver the amount of power at the right time. **Fig. 5** shows a collection of several grain geometries, whose designs are intended to develop the burning or combustion surface to produce a specific thrust during flight.

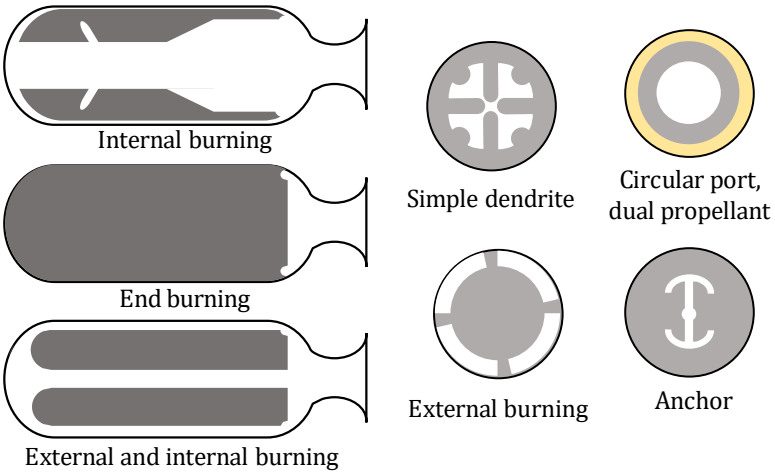

***Fig. 5**. Schematic of various examples of propellant grain geometries. Adapted from (James S. et al., 1973).*

Several cross-sections together to their typical thrust profile are shown in **Fig. 6**. These thrust profiles can be described depending on the thrust, pressure and burning surface area evolution during the flight (El-Sayed, 2016):

- Neutral burning: thrust, pressure and burning surface are maintained constant.
- Progressive burning: an increase in thrust, pressure and burning surface are shown during this stage.
- Regressive burning: at this stage the thrust, pressure and burning surface area decrease.

In any case, the design of the cross-sections of the composite solid propellant rocket motors must also consider the structural integrity of the propellant's grain, since stress concentrations can be induced by the geometry, which would eventually induce the generation and propagation of cracks that modify the initially designed burning surface and in so, altering the profile thrust during the flight of the motor.

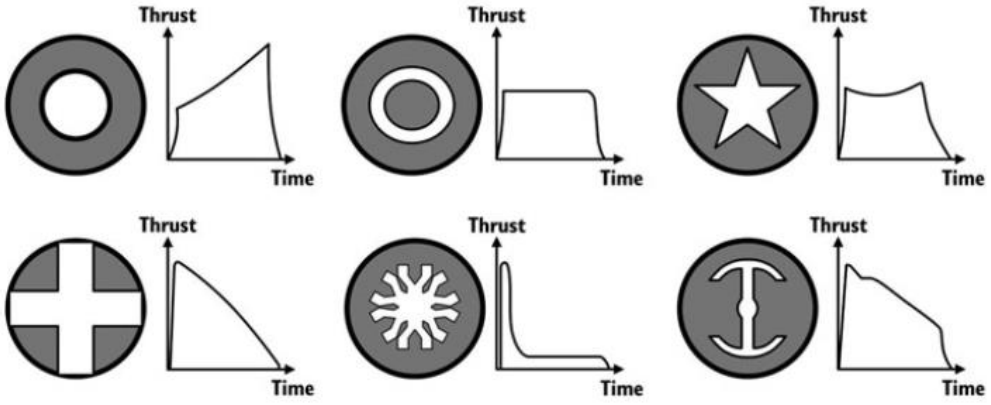

***Fig. 6**. Schematic of some examples of different grain sections and the thrust they provide during the burning time. From (El-Sayed, 2016).*

2.1.1. Solid propellant types

Solid propellant motors are classified in diverse ways attending to its application, size, composition or thrust action, amongst others (Sutton et al., 2017). One commonly employed is the classification by their composition. This classification divides solid propellants into two great families: homogeneous and heterogeneous propellants.

2.1.1.1. Homogeneous solid propellants

Homogeneous solid propellants (double-base) are the earliest kind of modern solid propellants and are still in use (Whitehouse et al., 1997), as shown in **Fig. 2**. Usually, they are named with regard to a subclassification: single, double and triple-base propellants. Double-based solid propellants are the most utilised of their type.

Double-base solid propellants consist of a colloidal mixture of nitroglycerine (NG) and nitrocellulose (NC), plus additives. The NC is the solid binder of the grain and appears in a 30-50 wt%, usually plasticised with NG in 20-50 wt% (Sutton et al., 2017). Some classifications refer to propellants containing NC as nitrocellulose ones, as the one in **Fig. 2**. The NG is probably the most popular reactive plasticiser (liquid and explosive), but it is not the only used. Here, the NC serves as a stabiliser for the NG and the NG serves as gelification agent for the NC (Sforza, 2016). Amid all the varied additives, one might expect burning rate modifiers, coolant, opacifiers, stabiliser, antioxidants, visible flame suppressants or lubricants (Sutton et al., 2017).

Stabiliser could be considered vital, since they are responsible for preventing ageing of the nitrocellulose binder, slowing down its natural intrinsic and autocatalytic decomposition (AOP-48, 2008; Bohn, 2017). Regarding this aspect, surveillance systems for nitrocellulose munitions make emphasis on these reactions and their consequences on impulse and structural integrity of the grain. Also, accelerated ageing procedures are developed taking into account this fact (AOP-48, 2008).

2.1.1.2. Heterogeneous solid propellants

The heterogeneous solid propellants are more often referred to as composite solid propellants, being during the last decades the most utilized technology in the industry (Krishnamurthy et al., 2017; Sutton et al., 2017). In these energetic materials, the components possess a completely different nature and properties. The basic concept of a composite solid propellant is formed by a

polymeric binder matrix plus oxidiser solid particles in high wt%, such as ammonium perchlorate (NH_4ClO_4), ammonium nitrate (NH_4NO_3), or potassium perchlorate ($KClO_4$) (Sforza, 2016). In the following subsections, the employed ingredients in composite technology are described.

Oxidisers

Oxidisers are typically manifested as ceramic solid particles (crystals). The selection of materials for this purpose will require a high oxygen content and a high heat of formation (Humble, 1995; Krishnamurthy et al., 2017), since they are the greatest contributors to the oxygen supply in the combustion reaction. These oxidisers are typically the most abundant ingredient in the composite propellant grains, representing a weight percentage of up to 70%, approximately (Sutton et al., 2017).

***Table 1**. Common inorganic oxidisers in composite solid propellant compositions. Adapted from (Klager et al., 1967; Humble, 1995; DeLuca, 2016; Sutton et al., 2017).*

Compound	Chemical formula	Oxygen content total/available (wt%)	Remarks
Ammonium perchlorate (AP)	NH_4ClO_4	54.5/34.0	Low cost, high performance
Ammonium nitrate (AN)	NH_4NO_3	60.0/20.0	Low cost, medium performance
Ammonium dinitramide (ADN)	$NH_4N(NO_2)_3$	51.6/25.8	Moderate cost
Potassium perchlorate (KP)	$KClO_4$	46.2/40.4	Medium performance
Potassium nitrate (KN)	KNO_3	47.5/39.5	Low cost

Some of the typical oxidisers used in composite solid propellants are gathered in **Table 1**. Potassium perchlorate (KP) was one of the first crystalline oxidisers to be used in castable composite solid propellant rockets (Pang et al.,

2023), but it is more frequently found in pyrotechnic mixtures or gas generators (DeLuca et al., 2017a). During the last five decades, the most frequent oxidiser found in current propellant motors is ammonium perchlorate (AP) due to a good performance, compatibility with many other ingredients employed in propellants and its availability on the market (Chaturvedi et al., 2019). Its properties suit so well that it is considered as a "miracle" for the industry (Davenas, 2003; DeLuca, 2016). They are white crystals that are used in different sizes: ultrafine 5 μm, fine 5-15 μm, medium 50-200 μm and coarse 200-600 μm (Sutton et al., 2017). Depending on the hazard, AP is classified in explosive levels where the finer configurations are more explosive.

Nitrates compounds, ammonium nitrate (AN) and potassium nitrate (KN), are also compatible with other solid propellant ingredients (Humble, 1995). On the downside, they do not present as good performance as AP. However, they are used in some other different applications due to its lower cost, clean and non-toxic exhaust (Chaturvedi et al., 2019).

For the past three decades, there has been an increase in interest in the development of new formulations to reduce costs, improve performance and minimize the environmental impact. The latter represents a concern for the society, involving many industries, as it is solid propellants'. Some of the environmental issues are related to ground water contamination, depletion of the ozone layer, acid rain or toxic impact on humans, amongst others (Trache et al., 2017). These effects are bound to the presence of AP in the ingredients, so new formulations are focused on replacing AP by other oxidisers such as phase-stabilised ammonium nitrate (PSAN) or ammonium dinitramide (ADN), although there is no substitute yet (Gohardani et al., 2014; Trache et al., 2017; Lysien et al., 2021).

Fuels

Most of the high energy composite propellants includes metal fuels in their ingredient list. They are mainly used to increase the specific impulse and density of the solid propellant through the enhancement of the heat of

combustion (Krishnamurthy et al., 2017), being present in up to 30 wt%, mostly around 16-20 wt%. Elements such as aluminium (Al), boron (B), beryllium (Be), iron (Fe), lithium (Li), magnesium (Mg), nickel (Ni) or zirconium (Zr), amongst others, have been under study to its use as fuels in propellants (Gorman et al., 1970; Lempert et al., 2011; Whittaker et al., 2012; Reid et al., 2014; Pang et al., 2021). Nevertheless, Al, B, Be, Mg and Zr have been of major interest (DeLuca et al., 2017a). Some of these metals, their common oxides and the heat of combustion, Δh_c, are collected in **Table 2**.

***Table 2**. Fuels for composite propellants, common oxides and heat of combustion, Δh_c. Adapted from (Bondarchuk et al., 2018).*

Metals	Common oxides	Δh_c (kJ/g)
Al	Al_2O_3	31.4
B	B_2O_3	57.2
Mg	MgO	25.1
Ti	TiO_2	15.7
Zr	ZrO_2	12.0

Amid the aforementioned metals, beryllium has proved to be great in improving the specific impulse (Krishnamurthy et al., 2017), but its combustion products are heavily toxic for humans and animals (Gorman et al., 1970; IARC monographs on the evaluation of carcinogenic risks to humans, 1993). Magnesium represents also one of the most employed metallic fuels. Although it has a lower performance compared to the aluminium, it is used in clean exhaust motors and as igniter for other metals (Doll et al., 1992; J. Mills et al., 1965; Krishnamurthy et al., 2017). Boron presents a similar performance in both gravimetric and volumetric terms as beryllium (Hashim et al., 2019), therefore boron and borides are one of the most popular fuels giving place to high energy technologies for diverse applications (Pang et al., 2019). Despite their good performance, the inefficiency of combustion constrains their use, so large research campaigns are developed to overcome this issue (Pang et al., 2011; Whittaker et al., 2012; Pang et al., 2019).

The addition of aluminium in the composition to improve the performance of composite motors is known and used for decades (Davis, 1963). Although the use of aluminium presents some problems such as agglomerations during combustion or a smoky exhaust (Geisler, 2002; Sutton et al., 2017), it is the most used metal fuel in composite propellants by far. It is considered as a standard in the industry given that aluminized propellants exhibit enough specific impulse, combustion stability and long storage periods at a fair cost (Geisler, 2002; DeLuca et al., 2017c). Its presence in the propellant's composition is usually about 14 wt% - 20 wt% in the form of small particles ranging from nano to micro sizes. As a matter of fact, today's research is focused on the development of nano-sized metallic powders (Pang et al., 2021) due to an enhancement of the combustion through changes in the combustion process.

Binders

The primary constituents of the composite solid propellant are particulate oxidisers and fuels. A binder is essential to consolidate the material and impart a specific geometry to the grain, which should be maintained during storage and flying conditions. They are intended to keep the structural integrity of the propellant grain while using the minimum quantity, which is up to 15 wt% approximately (Sutton et al., 2017).

Since the beginning of the first castable composite solid propellant in 1942 by J. W. Parsons, who used asphalt pitch as binder (Pang et al., 2023), the development of new binder systems has never stopped in the pursue of a better performance, improved ageing behaviour, reductions in costs of materials and manufacturing and more sustainable and safe technologies. Binders are also called fuels since they are also oxidised during the combustion process and, attending to the combustion energy that they can supply, binders can be classified as inert (lower energy) or energetic (higher energy) binders. The principal components of binder systems are polymers, curing agents or cross linkers and plasticiser. Some of the most common binder polymers are summarised in **Table 3**.

***Table 3**. Common binder polymers in composite solid propellant technologies. Adapted from (Badgujar et al., 2017; Sforza, 2016).*

Binder energetics	Type	Pre-polymer
Inert	Polybutadiene	CTPB: carboxyl-terminated polybutadiene
		HTPB: hydroxyl-terminated polybutadiene
		PBAA: polybutadiene acrylic acid
		PBAN: polybutadiene acrylonitrile acrylic acid
	Polyether/ Polyester	HTPE: hydroxyl-terminated polyether
		PCP: polycaprolactone polyol
		PEG: polyethylene glycol
		PGA: polyglycol adipate
		PPG: polypropylene glycol
		PU: polyurethane
Energetic		AMMO (monomer): 3-Azidomethyl-3-methyl oxetane
		BAMO (monomer): 3, 3-Bis-azidomethyl oxetane
		GAP: glycidyl azide polymer
		GLYN (monomer): glycidyl nitrate
		NIMMO (monomer): 3-Nitratomethyl-3-methyl oxetane

Polymers employed in composite solid rocket propellants are also classified as thermoplastic or thermosetting polymers. The latter are the ones that have been more explored to today. They are produced through the cross linking of a pre-polymer, which gives its name to the polymer binder system. As illustrated in **Fig. 2**, the chronological order of development and success of polybutadiene binders (most common) are PBAA, PBAN, CTPB and HTPB, being nowadays HTPB the workhorse of composite solid propellant motors (Jain, 2002). From a microstructural point of view, the main difference between CTPB and HTPB pre-polymers are the chain ends that are carboxyl or hydroxyl terminations, respectively, as shown in **Fig. 7**. Both have been used as an ideal solution for large scale rockets (Jain, 2002). Nevertheless, the aerospace industry pushes to find even better solutions, mainly with the objective of gaining specific impulse for the most demanding aerospace missions

(Cheng, 2019). Energetic binders are the propellants explored for that purpose. The usual energetic polymers are gathered in **Table 3**, being GAP the most common energetic polymer in use and under research (Pang et al., 2023).

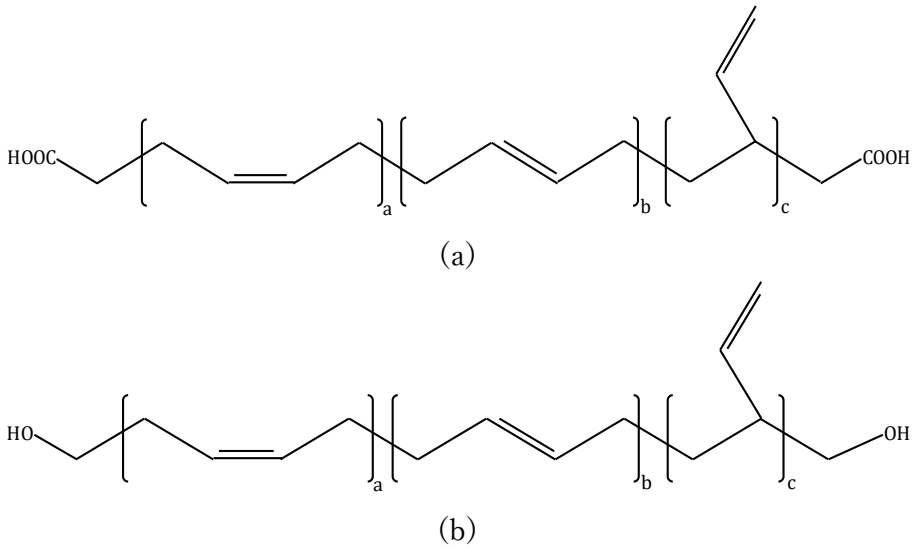

Fig. 7*. Basic structures of (a) CTPB and (b) HTPB.*

Plasticisers

Plasticisers are ingredients whose main purpose is to lower the viscosity of the binder, reducing its stiffness and strength, while increasing the elongation. This is useful for the manufacturing of the propellant grains, allowing a better response to mechanical loads than a more rigid material and a higher filling ratio (Sutton et al., 2017; Pang et al., 2023). Plasticisers act also as fuel and, depending on the energy supply, are frequently classified as inert or energetic (Badgujar et al., 2017). Some of the common non-energetic plasticisers are dioctyl phthalate (DOP), dioctyl adipate (DOA), dimethyl phthalate (DMP) or isodecyl pelargonate (IDP) (Sutton et al., 2017). Regarding the energetic plasticisers, those are commonly nitro compounds or nitrate esters and some examples are nitroglycerine (NG), metriol trinitrate/ trimethylol ethane trinitrate (MTN/ TMETN), triethylene glycol dinitrate (TEGDN) or butane-1,2,4-triol trinitrate (BTTN) (Badgujar et al., 2017).

Special attention is placed over plasticisers due to its capability to migrate during ageing and deterioration of the propellant grain (Tormey et al., 1963; Gottlieb et al., 2003). This problem results in changes on the mechanical properties, affects the interface bonding such as binder-filler or propellant-insulator and modifies the burning rate properties of the propellant (Venkatesan et al., 1993; Gottlieb et al., 2003).

Curing agents or crosslinkers

Curing agents or crosslinkers are catalysts of the curing reaction (creation of crosslinks) of the polymer binder. They are likewise fundamental in the physical and mechanical properties of the propellant, having an impact on the processability and ageing of the material. Some common curing agents are methyl aziridinyl phosphine oxide (MAPO), isophorone diisocyanate (IPDI), toluene-2,4-diisocyanate (TDI), hexamethylene diisocyanide (HMDI) or trimethylol propane (TMP) (Sutton et al., 2017).

Burning rate modifiers

Burning rate modifiers are used to control the burning reaction, i.e., they are catalysts for the combustion reaction. The specific use of these catalysts is to design the grain geometries to give a specific thrust during the flight of the motor (Chaturvedi et al., 2019).

Other additives

Minor components are not only plasticisers, curing agents and burning rate modifiers, but also other ingredients with specific objectives such as facilitation of the manufacture, viscosity modification, opacity or colour modification, bonding between filler and matrix, reduction of migration of components or improvement of the ageing behaviour of the propellant (Sutton et al., 2017).

2.2. Degradation of composite solid propellants

Composite solid rocket propellant motors can be designed for direct use after manufacturing, which could be the case of some specific applications, but motors are usually stored for large periods of time. Although storage times are usually around 5 to 25 years (Sutton et al., 2017), these storage times are not fully prescribed and munition systems are controlled through the so-called surveillance systems, tests or programs. The high costs of manufacturing new motors and the handling of their disposal, which is getting increasingly strict when it comes to environmental issues, push towards storage periods that are as long as possible, even longer than the previously mentioned. Over the storage time, these motors undergo several degradation processes, usually termed as ageing or damaging processes. Although solid propellants are diverse and depend strongly on their unique composition, which affects to the degradation processes that are more or less severe with the specific propellant, a general classification of the degradation processes is as follows (Cerri et al., 2009):

- Physical: depletion and migration of components such as plasticisers, phase transition and debonding of the matrix-particle interface, commonly denoted as dewetting in the composite propellants' field.
- Chemical: formation and rupture of bonds in the polymeric matrix, i.e., chain-scission or cross-linking that may occur due to the exposition to high temperatures or humid atmospheres and oxidation reactions.
- Mechanical: dewetting, Mullins and/or Payne effect (Payne, 1962; Mullins, 1969; Diani et al., 2009). These are mainly caused by vibrations during transport, handling of the motors, gravity and periodic rotations (used to lessen weight induced strains) and thermal variations during storage and transport, which lead to static or cyclic loading of the propellant's grain.

Binder and binder-particle interface degradation are considered the main concerns in the structural integrity of the composite solid propellants (Celina et al., 2002). Therefore, it is relevant to deepen on properties that characterise the degradation of both binder and binder-particle interface, which are mostly related to the modifications of polymer chains as it is illustrated in **Fig. 8**.

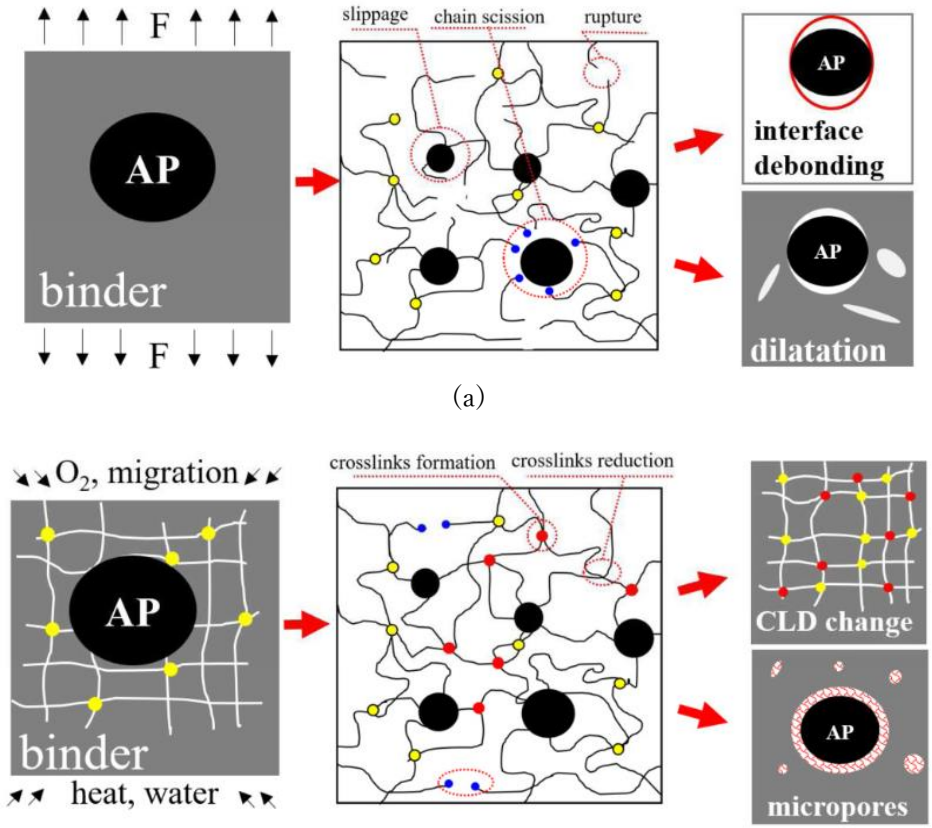

***Fig. 8**. Degradation of composite solid propellant matrix. Assumptions for (a) mechanical damage and (b) environmental damage. CLD stands for crosslinking density. From (Wubuliaisan et al., 2023a).*

Surveillance systems are intended to evaluate the physical, chemical and mechanical properties of the propellant's grain to check usability and provide remaining life time of the motors (Bennet, 1997). Natural damage takes place in long periods so artificial ageing procedures are, in general, called accelerated ageing procedures. To determine the remaining shelf time, it is necessary to

artificially accelerate the deterioration or ageing of the solid propellant that is to be evaluated. In the following sections, accelerated ageing for different damage processes are described.

2.2.1. Accelerated mechanical ageing

Handling, transportation and storage of rocket motors subject the propellant grain to mechanical strains, i.e., the motor is subjected to a mechanical loading history (Tormey et al., 1963). Some examples of in-service cyclic loadings are gathered in **Table 4**. The loading history of a motor is more a random accumulation of those situations and others not included in **Table 4**. This is a complex issue to address since it requires the monitorization of environmental and other conditions throughout the long storage periods (Chelner et al., 2005; Miller et al., 2007).

***Table 4**. Cyclic loading of solid propellant motors (Tormey et al., 1963).*

Service condition	Frequency
Vibration in flight	100-500 Hz
Vibration during ground transport	10-500 Hz
Temperature daily cycle	1 cycle/day
Rotation in storage	1 cycle/month

It is well known that certain filled elastomers undergo changes from previous applied strains. No matter if strains are small, where Payne's effect (Payne, 1962) consisting in a decrease in the storage modulus in dynamic loading appears, or large, where Mullin's effect (Mullins, 1969) occurs as a softening in the stress-strain curve up to the previous applied strain. Constitutive models have been derived to account for these types of damage and some explanations have been explored, although no agreement is reached yet (Diani et al., 2009). The hypothesis used for explaining the phenomena observed are varied, comprising rupture of the particle-matrix bond (Blanchard et al., 1952; Bueche, 1960), slip of the particles in the matrix with regenerating bonds (Houwink, 1956), rupture of the filler particles (Kraus et al., 1966) or changes in the chain entanglements between fillers in the straining direction (Hanson

et al., 2005), amongst others. It is necessary to consider that binder systems are a mixture of different components with different characteristics and functionalities. Thus, the mechanisms involved in the strain induced damage are extremely complex to be determined (Dannenberg, 1986) and remain as mystery.

Amid the research for composite solid propellant constitutive models, one can find phenomenological models that describe cyclic loading (Schapery, 1982; Özüpek et al., 1997; Wubuliaisan et al., 2023a), although still most of them are more hardening models (single monotonous loading) (Wang et al., 2015; Lei et al., 2020; de Francqueville et al., 2021; Li et al., 2023). Focus on some specific pre-strain conditions have been studied, such as constant pre-strain applied during the accelerated ageing (Zhou et al., 2016; Wang et al., 2020; Wubuliaisan et al., 2023a), dynamic mechanical behaviour with applied pre-strain in the same loading direction (Azoug et al., 2013a; Thorin et al., 2012) or in orthogonal directions (Azoug et al., 2013b; Jalocha et al., 2015a, 2015b) or crack growth on pre-strained propellant (Liu, 1995).

It is in general considered that macro strains lead to higher local strains that produce dewetting of the particles and consequent dilatation (variation in the Poisson's ratio), that can derive in the migration of some components of the binder system (Tormey et al., 1963). Severe affection to the shelf-life has been reported for composite solid propellants with cumulative damage, leading to a premature failure (Gligorijević et al., 2015). Widening of the knowledge is essential to completely understand and model a complete mechanical history of composite solid propellant.

2.2.2. Accelerated thermal ageing

The accelerated thermal ageing for composite solid propellants consists mainly in the degradation of the polymeric binder by accelerating the kinetics of the oxidative cross-linking process when submitting the propellant to relatively high temperatures (Coquillat et al., 2007). Also, chain-scission is

produced delivering oxidation products such as alcohols, carboxylic acids, esters and CO_2 for polybutadiene based propellants (Harris et al., 2001).

As mentioned, some properties are tracked through the ageing process. The correlation between actual and accelerated conditions are usually modelled by an Arrhenius type relationship, also named after Layton's ageing law, not only, but specifically for butadiene binders (Layton, 1974, 1975; Christiansen et al., 1981), which can be written in the form

$$\ln\frac{t_s}{t_a} = \frac{E_a}{R}\left(\frac{1}{T_s} - \frac{1}{T_a}\right) \tag{2}$$

where t and T represent time and temperature, respectively, and their subindexes s and a reflect the storage and accelerated ageing conditions, respectively; E_a is the apparent activation energy and R is the ideal gas constant. Hence, a property that is measured after the exposition of the sample to a temperature T_a during an accelerated time t_a will be equivalent to the measure of that property if the propellant was stored at temperature T_s during time t_s. It is equivalent to the Van't Hoff's equation and other derived empirical relations (Cerri et al., 2009).

Accelerated ageing procedures are widely used and there are several standards that assess the process specifically for composite solid propellants, such as AOP-48 (AOP-48, 2008) and STANAG 4581 (STANAG 4581, 2022). The ageing procedure is not trivial. The consequent deterioration will depend on the followed methodology. Procedures can be classified in, at least, three types: isothermal, non-isothermal and cyclic (Naseem et al., 2021).

The isothermal type consists in the exposition of a block of propellant to a constant temperature in a furnace. It is the most widespread method as the equipment requirements are low and it is easy to carry out. Employed temperatures are usually around 60 ºC to 70 ºC, since natural ageing processes seem to be the dominant ones up to that range (Naseem et al., 2021), although commonly employed temperatures vary in the range from 60 ºC to 90 ºC (Husband,

1992; Bunyan et al., 1993; Celina et al., 2002; Harris et al., 2001; Seyidoglu et al., 2017; Wang et al., 2020). Non-isothermal procedures are fast methods to obtain kinetic parameters of the degradation processes. They consist in thermogravimetric (TGA) and differential scanning calorimetry (DSC). These methods have found to be non-adequate for its use with composite solid propellants since temperatures needed in both techniques are too high to represent natural ageing (Naseem et al., 2021). Cyclic thermal accelerated ageing methods try to represent the temperature variations during day-night shifts and/or seasons, imposing heating and cooling stages during the accelerated ageing process. Several authors have employed these methods, but still no clear advantage with respect to isothermal methods are found (Naseem et al., 2020; Wang et al., 2022e).

Characterisation of the thermal degradation of the composite solid propellants are commonly addressed by tensile tests, dynamic mechanical analysis (DMA), DSC and cross-linking density (CLD) measurements through the sol-gel method. Monitoring variables from those tests are to be explained below.

Uniaxial tensile tests are part of most of the surveillance programs of composite solid propellants. Various properties can be monitored during ageing, such as the (apparent) elastic modulus E, the engineering and true stress at maximum, s_{max} and σ_{max}, respectively, and the engineering and true strain at maximum, e_{max} and ε_{max}, respectively (cf. **Fig. 9**). This standardised test is found in STANAG 4506 (STANAG 4506, 2000).

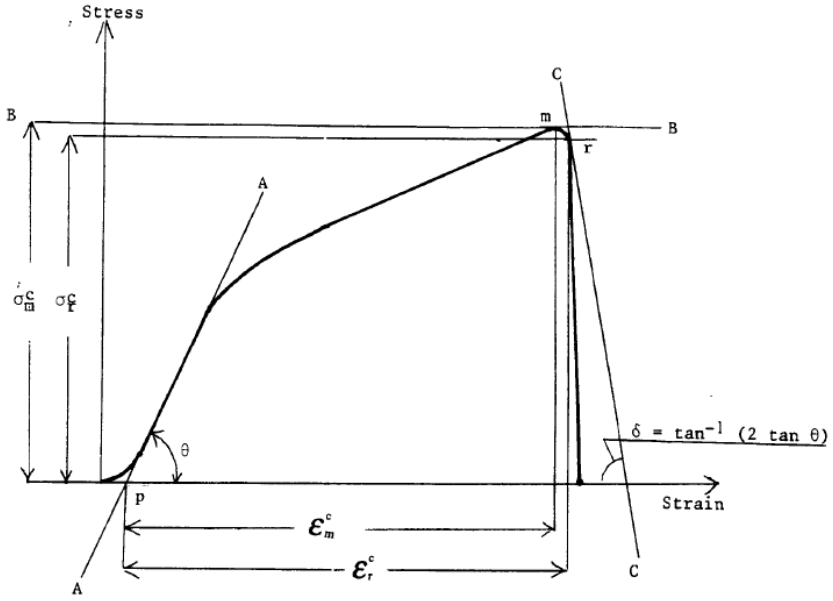

Fig. 9. Representative true stress versus true strain curve of a composite solid propellant (STANAG 4506, 2000).

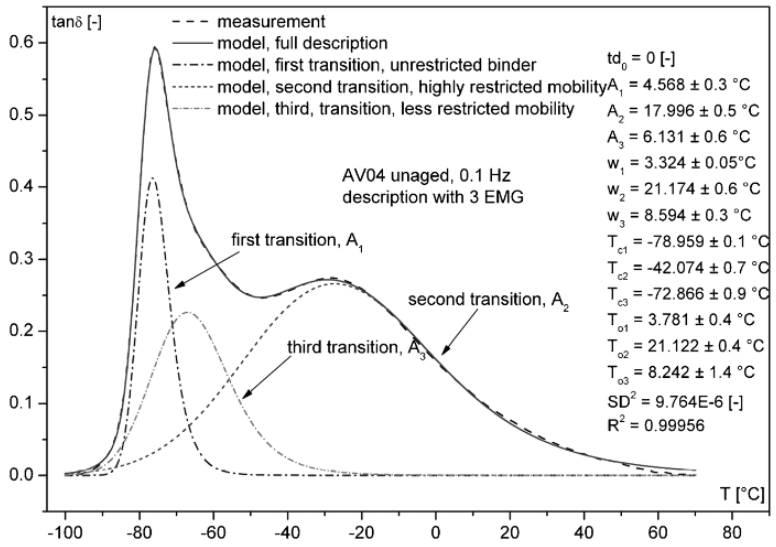

Fig. 10. Loss factor (tan δ) in a dynamic mechanical analysis (DMA) of temperature sweep type test for a composite solid propellant and its fitting to an exponentially modified Gaussian model. From (Cerri et al., 2013).

Different modes of testing can be made in DMA methodology. Frequency sweeps can be used to get the relaxation behaviour of the composite propellant

(Ji et al., 2022). Nevertheless, the most common are temperature sweeps, where more information is obtained, e.g., changes in the glass transition temperature T_g (first transition) due to the ageing (Fuente et al., 2003), the reduction of the second transition area related to the cross-linking or the increase of the third transition area related to chain scission, c.f. **Fig. 10**, (Cerri et al., 2013). Temperature sweep procedure and the determination of T_g using DMA is standardized in STANAG 4540 (STANAG 4540, 2002). From DSC tests the glass transition temperature T_g can be monitored as well (de la Fuente, 2009). Through the sol-gel method, the soluble fraction S and crosslink density CLD can be determined during the ageing period following STANAG 4581 (STANAG 4581, 2022).

2.2.3. Accelerated humid ageing

Exposition to humid ambient, which leads to hydrolysis in the polymeric binder and binder-filler bonding, is considered as one of the most relevant deterioration processes, particularly for CTPB based propellants (Chevalier et al., 2003).

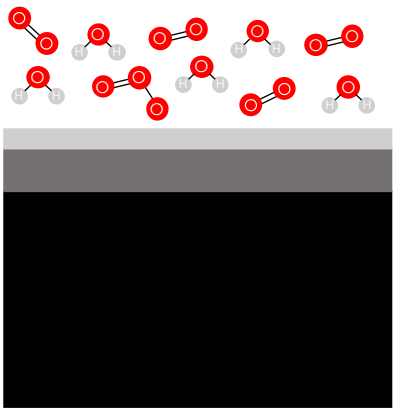

***Fig. 11**. Schematic of a solid propellant grain exposed to atmospheric environment. Adapted from (Davis, 2001).*

During the storage of the motor, diffusion of the humidity through the structure of the motor is considered. Nevertheless, seals of the motors lose their hermeticity capabilities with time, so humidity enters into the combustion

chamber and, then, diffuses through the propellant grain. Therefore, the propellant is exposed to an ambient containing oxygen, ozone and water vapour, amongst others, as depicted in **Fig. 11**.

The presence of oxygen is necessary to produce the oxidative cross-linking (Torry et al., 2001) and water vapour might lead to other processes, e.g., hydrolysis. It is recognised that during an initial stage, the propellant stiffens due to post-curing and oxidative cross-linking. After that, hydrolysis becomes more relevant and the propellant's grain loosens, being more flexible and reducing the load bearing capability (Davis, 2001; Adel et al., 2019). It has been found that moisture is relevant not only during storage, but also during the manufacturing process and affects the polybutadiene backbone and the particle-matrix interface making the propellant softer (Iqbal et al., 2006). This softening, linked to chain scission and binder-filler degraded interaction, is reflected in the mechanical performance as shown in **Fig. 12**.

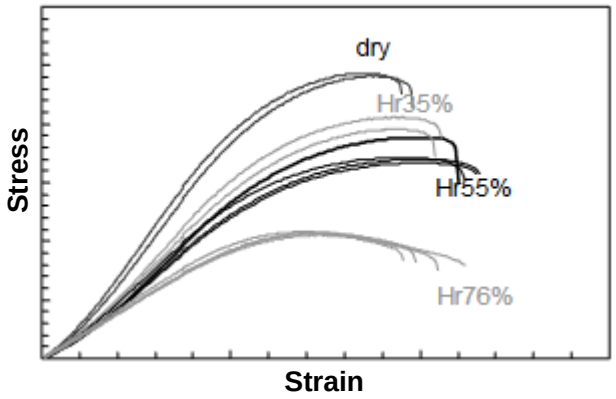

***Fig. 12**. Stress versus strain curves for HTPB propellant subjected to humid ageing. Adapted from (Chevalier et al., 2003).*

Several authors have conducted research works regarding the ageing of composite solid propellant under humid conditions (Chang et al., 2000; Chevalier et al., 2003; Torry et al., 2001; Iqbal et al., 2006; Adel et al., 2019; Zhang et al., 2023b). Despite the importance of this issue, the humid degradation of composite solid propellants is still an unresolved problem (Davis, 2001;

Naseem et al., 2021), and there is actual need to widen the research activities on the topic (Naseem et al., 2021).

2.2.4. Accelerated ozone ageing

As seen in **Fig. 11**, propellant's grain is exposed to oxygen, ozone and water vapour during the motor's shelf life, conditions under which hydrolysis occurs and plays a principal role in the grain's integrity. As an alternative to simulate the atmospheric exposition of the propellant, the use of ozone to produce ozonolysis reactions in the binder system leads to a similar degradation compared to hydrolysis effects. The presence of the ambient ozone has been a concern in the rubber industry for decades, as for example, the vehicle tire manufacturers interest in the degradation of tires caused by ozone attack (Cataldo, 2019). This issue acquired the sufficient relevancy to promote the elaboration of standards to characterise the effects of the exposition to ozone on rubbers (ASTM D1149, 2018; ISO 1431-1, 2022), but it has been rarely addressed for composite solid propellants (Merrit, 1981; López Sánchez, 2018).

Ozonisation of rubbers is believed to attack the double bonds on the backbone of the polymer (Anachkov et al., 1985), specifically for diene rubbers (Cataldo, 2019), similarly to the hydrolysis process. Although ozone attack is mainly superficial when static exposition is considered (Cataldo, 2019), the presence of a large amount of particles, as it is for composite solid propellants, might help the penetration of ozone into the bulk. Ozonolysis causes the formation of ozonides, that are carboxylic acids, alcohols and other reaction products (Lewis, 1986) in agreement with Criegee's mechanism (Criegee, 1975), without producing cross-linking or chain scission in diene rubbers (Zaikov et al., 2012). These mentioned products are similar to those described in previous subsections. Thus, if the evolution of the physical, chemical and mechanical properties with ozone ageing is affected in a comparable way to the humid ageing, ozone ageing would represent a feasible alternative to characterise the service life of composite solid propellant motors.

2.3. Difficulties in the mechanical characterisation of composite solid propellants

As alluded to, composite solid propellants are typically a heterogeneous mixture of oxidizer particles, fuel powder and binder. A representation of this microstructure is shown in **Fig. 13** where a CTPB/AP/Al could be identified, being black particles the ammonium perchlorate oxidiser, grey particles the aluminium fuel powder and yellow filling the carboxyl-terminated polybutadiene based binder. The mechanical behaviour is complex in as much as materials from very different natures are to take into consideration, also accounting for the interaction between them (Xu et al., 2008).

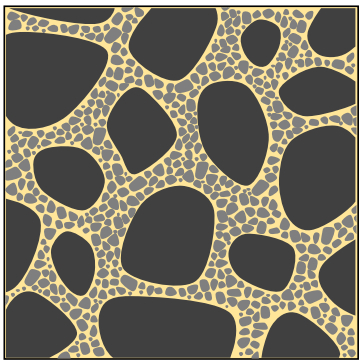

Fig. 13*. Schematic representation of the microstructure of a composite solid propellant. Oxidiser particles in black, fuel particles in grey and matrix in yellow.*

Oxidiser particles are ceramic with linear elastic and fragile expected behaviour. Fuel particles are metals, which present an elastic-plastic behaviour, being stiffer than the oxidiser particles. Binder systems are soft polymers and more complex since the employed ingredients could be widely varied for modifying the mechanical response. All of it makes the composite propellant dependent on a sum of factors. Most of today's binders allow large strains (Özüpek et al., 1992) and their mechanical behaviour is usually assumed to be hyper-viscoelastic (Xu et al., 2014; Tunç et al., 2017; Wang et al., 2018b). Elastomeric binder is also relevant for the strain rate dependence (Wang et al.,

2015; Hur et al., 2016; Wang et al., 2022c) or temperature dependence, where composite solid propellants are modelled as a thermorheologically simple material (Xu et al., 2014), although they are not (Özüpek et al., 1992). As alluded to, this matrix is affected by ageing or exposition to the environment (Wang et al., 2022b; Wubuliaisan et al., 2023a). Perfect filling is assumed and with no voids, cf. **Fig. 13**. However, voids may appear during the manufacturing process or during the natural deterioration of the material and defects might grow from them voids (Özüpek et al., 1992; Lei et al., 2020). Considering the bonding between particle and matrix, several consequences arise. A softening in the macro stress-strain behaviour is observed (Tunç et al., 2017; Wubuliaisan et al., 2023b) induced by the rupture of the interfaces, what is called dewetting. This phenomenon is approached either by modelling the decohesion of the surface using cohesive elements (Matous et al., 2007; de Francqueville et al., 2021; Wubuliaisan et al., 2022; Xiao et al., 2023; Zhang et al., 2023b) or using internal damage variables (Schapery, 1984; Xu et al., 2008, 2014; Wubuliaisan et al., 2023a). As a result of this decohesion, change in the volume and in the Poisson's ratio is experimented (Stedry et al., 1961; Shekhar et al., 2011; Cui et al., 2018; Wang et al., 2022a). In addition, hydrostatic pressure modifies the mechanical response of the composite propellant (Liu et al., 2006; Tunç et al., 2017) and cyclic loading or loading history is needed to determine the mechanical behaviour (Hur et al., 2016; Tunç et al., 2017). Due to the amount of ingredients and complexity of the production of the propellant motors, deviations in the mechanical properties are found intra- and inter-batch as well (James S. et al., 1973).

2.4. Structural integrity of composite solid propellants

A schematic of a composite solid propellant motor is shown in **Fig. 14**. The propellant's grain is located inside the metallic case and the cylinder perforation and slots represent the combustion chamber.

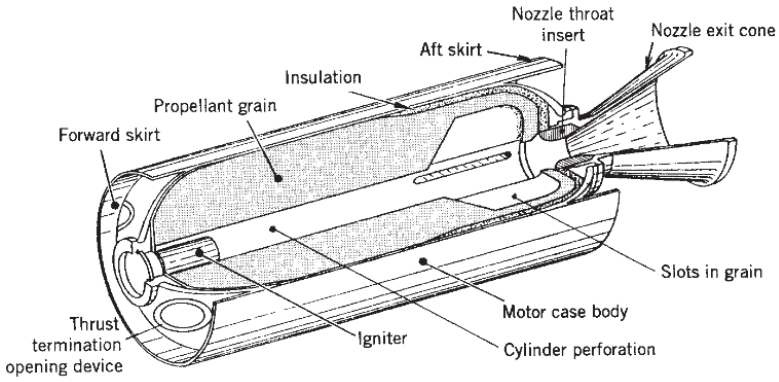

Fig. 14. Schematic of a typical solid propellant rocket motor. From (Sutton et al., 2017).

The thrust, F, that a composite solid propellant motor produces may be defined by

$$F = c_F p_c A_t \tag{3}$$

where c_F is the thrust coefficient, p_c is the combustion chamber's pressure and A_t is the area of the nozzle's throat. The thrust coefficient c_F and the area of the nozzle's throat are mainly a function of the nozzle, so they are considered as constant through the combustion process (Sutton et al., 2017). Therefore, the pressure in the combustion chamber is the main driver of the thrust during the motor's flight, i.e., $F(t) \propto p_c(t)$, being t the time variable. When steady-state or equilibrium conditions have been reached, the pressure in the combustion chamber can be defined as

$$p_c = \sqrt{\frac{RT}{\gamma\left(\frac{2}{\gamma+1}\right)^{\frac{\gamma+1}{\gamma-1}}}}\frac{\dot{m}_e}{A_t} \tag{4}$$

where R is the ideal gas constant, T is the temperature of the combustion chamber, γ is the specific heats ratio and $\dot{m}_e = \mathrm{d}m_e/\mathrm{d}t$ is the exit mass flow rate. An ideal design is given by the equilibrium between mass flow rate of combustion gases, $\dot{m}_b$, and exit gases, so that steady-state operation is achieved when

$$\dot{m}_b = \dot{m}_e \tag{5}$$

On the other hand, the mass flow rate of combustion gases is determined as

$$\dot{m}_b = \rho_p \dot{r} A_b \tag{6}$$

defining ρ_p as the density of the propellant, $\dot{r}$ as the burning rate and A_b the burning surface area. The burning rate $\dot{r}$ can be defined as the rate of regression of the burning surface, which is described by an empirical relationship, known as Vielle's law (El-Sayed, 2016):

$$\dot{r} = k p_c^n \tag{7}$$

where k is a function and n a constant, both characteristic of the propellant and dependent on the propellant's temperature. By introducing (7) in (6),

$$\dot{m}_b = \rho_p k p_c^n A_b \tag{8}$$

Then, using (8) and (4) in the equality (5), the pressure in the combustion chamber can be written as

$$p_c = \left[\rho_p k \sqrt{\frac{RT}{\gamma \left(\frac{2}{\gamma+1}\right)^{\frac{\gamma+1}{\gamma-1}}}} \frac{A_b}{A_t} \right]^{\frac{1}{1-n}} \tag{9}$$

Therefore, it can be seen that the pressure in the combustion chamber is dependent on the burning surface, which varies during the flight. Then, $p_c(t) \propto A_b(t)^{1/(1-n)}$, consequently the thrust is also dependent on the burning surface area $F(t) \propto A_b(t)^{1/(1-n)}$. As pointed out in **Fig. 5** and **Fig. 6**, composite solid propellant grain geometries are designed to provide thrust for a given operational condition, which has been motivated from (3) to (9). Hence, structural integrity of the composite solid propellant arises as a vital issue since changes in the grain's geometry give rise to an undesigned combustion process (Wang et al., 2023a) and results in peaks of pressure (Knauss, 2015; Sforza, 2016; Tussiwand et al., 2009), as depicted in the schematic of **Fig. 15**, showing

the change in the designed thrust profile of a solid propellant grain section in the presence of cracks.

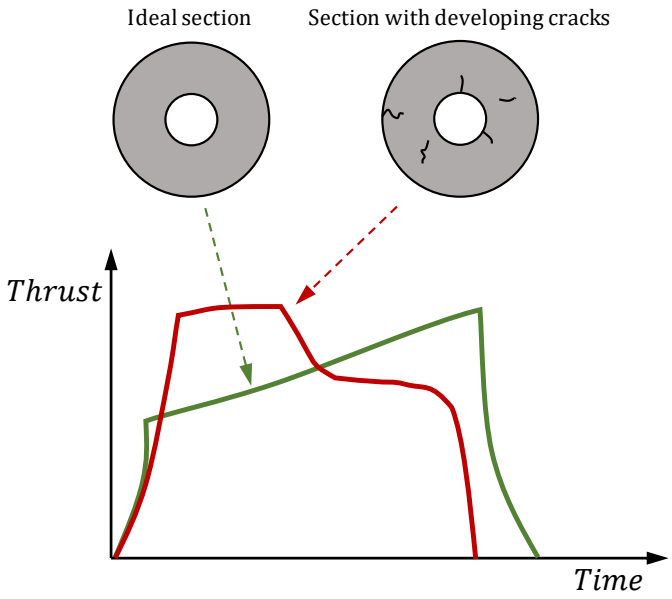

***Fig. 15**. Schematic of the thrust profile of a grain section modification due to the presence of developing cracks.*

Structural integrity of a component is a general term concerning its mechanical behaviour and loading bearing capacity. As alluded to, characterisation and modelling of the mechanical behaviour of composite solid propellants is a complex matter. Composite solid propellant surveillance programs concerning effects of the ageing (degradation) on the mechanical properties consist commonly of relaxation, creep, dynamic mechanical analysis and uniaxial tensile tests. Propellant grains exhibit defects where the most relevant are voids and cracks. These defects might have their origin in the manufacturing process. During their service life, the present voids and cracks get enlarged and new defects are generated due to thermal cycles experienced during the storage life, vibrations produced by the mishandling or inadequate transportation, inertial and gravity induced strains, shock during the ignition process and ageing of the propellant (Cerri et al., 2009; López et al., 2018; Rao, 1992; Sutton et al., 2017). The presence of cracks and voids exposes a greater area to the

combustion process which is even more important while the crack propagates. Although fracture analysis of the propellant grains is considered to be fundamental (Tussiwand et al., 2009), still nowadays failure criterions are mainly strain- or stress-based, or stress-strain failure envelops, which are not suitable for evaluating propellant grains under all different conditions that motors may suffer experience (James S. et al., 1973; Knauss, 2015; Wang et al., 2022d). As mentioned, international reports consider the significance of the fracture evaluation of the composite solid propellant grains, but they do not give specific instructions on how to addresses this issue (James S. et al., 1973; Whitehouse et al., 1997). It is relevant that there is no standard for fracture characterisation, unlike there are for the other mechanical characterisation techniques already pointed out.

In the following sections, the fracture characterization of composite solid propellants through the viscoelastic J-integral introduced by Schapery (Schapery, 1984) will be motivated, starting with the definition of linear viscoelasticity, followed by a description of the correspondence principle and the viscoelastic fracture mechanics based on the J integral convention. It is necessary to recall the highly viscous nature of the composite solid propellants, which is needed to be accounted for in the fracture characterisation.

2.4.1. Linear viscoelasticity

The basic Hooke's material model, that is suitable for materials under small displacements with linear, elastic and isotropic mechanical behaviour, may result inappropriate for polymers or biological tissues that present a time dependent behaviour. Hooke's material model can be extended to materials that exhibit a time-dependent response, considering small displacements, linearity, elasticity and isotropy. The Boltzmann material is then defined (Boltzmann, 1874), whose constitutive relation can be written in a general form as

$$\boldsymbol{\sigma} = \mathbb{L} \circ \dot{\boldsymbol{\varepsilon}} \tag{10}$$

where $\mathbb{L}$ represents a functional fourth-rank tensor which is a time-dependent linear operator, $\mathbb{L}(t)$, that transforms any given strain history in a stress history. The stress and strain rate tensors are represented by $\boldsymbol{\sigma}$ and $\dot{\boldsymbol{\varepsilon}}$, respectively. Note that both tensors are time dependent, so that $\boldsymbol{\sigma} \equiv \boldsymbol{\sigma}(t)$ and $\dot{\boldsymbol{\varepsilon}} \equiv \dot{\boldsymbol{\varepsilon}}(t)$. Besides, $\mathbb{L}(t) \circ \dot{\boldsymbol{\varepsilon}}(t)$ denotes the convolution product of $\mathbb{L}(t)$ and $\dot{\boldsymbol{\varepsilon}}(t)$.

These linear viscoelastic materials are also named after linear hereditary materials since the stress and strain states of the solid depend on the loading history, being part of the Hereditary Mechanics field as classified by Volterra (Volterra, 1909). The relation in (10) can be written in terms of the Riemann-Stieltjes convolution integral proposed by Gurtin and Sternberg (Gurtin et al., 1962), commonly known as hereditary integral, as

$$\boldsymbol{\sigma}(t) = \int_{-\infty}^{t} \mathbb{L}(t-\tau) \frac{\partial \boldsymbol{\varepsilon}(\tau)}{\partial \tau} \mathrm{d}\tau \tag{11}$$

given that at a specific time τ during a differential of time $\mathrm{d}\tau$, the strain increment is $[\partial \boldsymbol{\varepsilon}(\tau)/\,\partial \tau]\mathrm{d}\tau$. This strain $\boldsymbol{\varepsilon}$ has effect at any time t subsequent to τ, so that the operational $\mathbb{L}$ acts in the interval $t-\tau$ and it is known as the tensorial relaxation function. The lower limit of integration ranges even before a load is applied. Here it must be recalled the nonretroactivity axiom, where the linear operator $\mathbb{L}(t<0)=0$ assuming that the load is applied at time $t=0$ (see **Fig. 16**). Making use of the Boltzmann superposition principle, the integral in (11) is then reformulated as

$$\boldsymbol{\sigma}(t) = \mathbb{L}(t)\boldsymbol{\varepsilon}(t=0) + \int_{0}^{t} \mathbb{L}(t-\tau) \frac{\partial \boldsymbol{\varepsilon}(\tau)}{\partial \tau} \mathrm{d}\tau \tag{12}$$

or

$$\boldsymbol{\sigma}(t) = \mathbb{L}(t)\boldsymbol{\varepsilon}_0 + \mathbb{L}(t) \circ \dot{\boldsymbol{\varepsilon}}(t) \tag{13}$$

where $\boldsymbol{\varepsilon_0}$ represents the initial strain tensor.

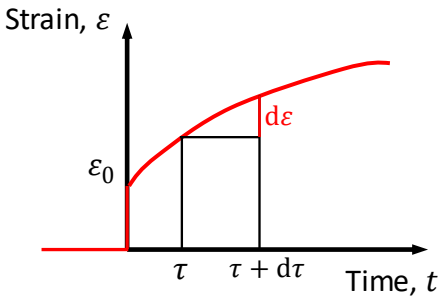

Fig. 16. *Arbitrary strain history for a linear viscoelastic solid with the initial applied strain* ε_0 *at time* $t = 0$.

The linear operator $\mathbb{L}(t)$ is defined for a linear isotropic and viscoelastic solid as

$$\mathbb{L}(t) = 2G(t)\left(\mathbb{I} - \frac{1}{3}\mathbf{1} \otimes \mathbf{1}\right) + K(t)\mathbf{1} \otimes \mathbf{1} \tag{14}$$

in terms of the deviatoric and volumetric parts, where $\mathbb{I}$ is the fourth-rank identity tensor, $\mathbf{1}$ the second-rank identity tensor and $G(t)$ and $K(t)$ are the deviatoric and volumetric relaxation functions, respectively.

2.4.2. Correspondence principle

Consider the viscoelastic problem for each material element of a body through the field stress ($\boldsymbol{\sigma}$), strain ($\boldsymbol{\varepsilon}$) and displacement ($\vec{u}$), with the tractions $\vec{T}_0$ applied on the surface S_t, displacements $\vec{u}_0$ applied on the surface S_u and body forces $\vec{b}$ applied to the volume V of the solid, defined in **Fig. 17**.

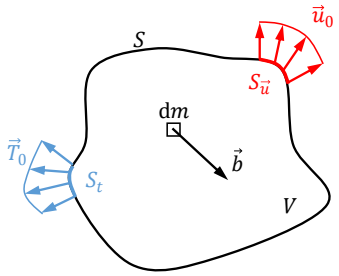

Fig. 17. *Schematic of a viscoelastic body subjected to applied tractions* $\vec{T}_0$ *and displacements* $\vec{u}_0$ *on surfaces,* S_t *and* $S_{\vec{u}}$*, respectively, and body forces* $\vec{b}$ *on its volume* V.

The correspondence principle is typically stated in terms of the s-multiplied Laplace or Laplace-Carson transformation (Tschoegl, 1989). The Laplace-Carson transform, $\hat{f}_C(p)$, of a real function $f(t)$ in the time domain, t, may be written as

$$\hat{f}_C(p) = p\int_0^\infty e^{-pt} f(t)\mathrm{d}t \tag{15}$$

which is the definition of the Laplace transform, $\hat{f}(p)$, multiplied by the complex variable p. Note the convenience of the Laplace transform, since this transform of the Heavyside function is 1 for all values of p. From this point forward, variables related to the transformed space will be denoted with the ˆ symbol and will depend on parameter p, instead of time t. As stated by the correspondence principle or elastic-viscoelastic analogy by Alfrey (Alfrey, 1944), the viscoelastic problem can be solved through an equivalent elastic problem. The corresponding variables defined for the equivalent elastic problem will be henceforth noted with the superscript R, since it represents the reference problem.

The boundary conditions, equilibrium, kinematics and constitutive equations for the viscoelastic, transformed viscoelastic and equivalent elastic problems are defined in **Table 5**, where material density is noted as ρ. It can be readily seen that the viscoelastic problem in the Laplace-Carson transformed space is formally equal to the elastic reference problem. This means that the viscoelastic problem can be solved through the inverse transform of the solution of the reference elastic problem, as previously mentioned. Having applied viscoelastic boundary conditions, such as $\vec{u}_0$ and $\vec{T}_0$, they are transformed and imposed in the reference elastic governing equations and then solved. Once the elastic solution is achieved, variables are inversely transformed to obtain the viscoelastic solution to the problem. The reference elastic problem is not a real or physical problem. For this reason, the variables concerning this reference problem will be named using the prefix "pseudo". Mechanical viscoelastic models are then stablished following the elastic formulation with the only need

to use the hereditary integrals to get the actual values of the viscous behaviour (Schapery, 1981, 1982, 1984).

***Table 5**. Correspondence between viscoelastic and elastic problem. Boundary conditions, equilibrium, kinematics and constitutive equations. Adapted from (Valiente Cancho, 2018).*

Action boundary	Viscoelastic problem	Transformed viscoelastic problem	Equivalent elastic problem
S_u	$\vec{u} = \vec{u}_0(t)$	$\hat{\vec{u}} = \hat{\vec{u}}_0(p)$	$\vec{u}^R = \hat{\vec{u}}_0$
S_t	$\vec{T}_0(t) = \boldsymbol{\sigma}\vec{n}$	$\hat{\vec{T}}_0(p) = \hat{\boldsymbol{\sigma}}(p)\vec{n}$	$\vec{T}_0^R = \boldsymbol{\sigma}^{\boldsymbol{R}}\vec{n}$
V	$\operatorname{div}\boldsymbol{\sigma}(t) + \rho\vec{b}(t) = \vec{0}$	$\operatorname{div}\hat{\boldsymbol{\sigma}}(p) + \rho\hat{\vec{b}}(p) = \vec{0}$	$\operatorname{div}\boldsymbol{\sigma}^{\boldsymbol{R}} + \rho\vec{b}^R = \vec{0}$
V	$\boldsymbol{\varepsilon}(t) = \operatorname{grad}^{\mathrm{s}}\vec{u}(t)$	$\hat{\boldsymbol{\varepsilon}}(p) = \operatorname{grad}^{\mathrm{s}}\hat{\vec{u}}(p)$	$\boldsymbol{\varepsilon}^{\boldsymbol{R}} = \operatorname{grad}^{\mathrm{s}}\vec{u}^R$
V	$\boldsymbol{\sigma}(t) = \mathbb{L}(t) \circ \dot{\boldsymbol{\varepsilon}}(t)$	$\hat{\boldsymbol{\sigma}}(p) = \hat{\mathbb{L}}(p)\hat{\boldsymbol{\varepsilon}}(p)$	$\boldsymbol{\sigma}^{\boldsymbol{R}} = \mathbb{L}^{\mathbf{R}}\boldsymbol{\varepsilon}^{\boldsymbol{R}}$

Analogously, Schapery stated three correspondence principles (Schapery, 1984), which are not exactly formulated as the previously mentioned. The second correspondence principle is of concern for this work. Regarding a viscoelastic body as depicted in **Fig. 17**, which is subjected to surface tractions, body forces and imposed displacements on its surface, this second correspondence principle assumes that stresses, tractions and forces are the same for the equivalent (or reference) elastic problem as they are for the viscoelastic body, cf. **Fig. 18**. This can be denoted as

$$\begin{aligned} \boldsymbol{\sigma} &= \boldsymbol{\sigma}^{\boldsymbol{R}} \\ \vec{T} &= \vec{T}^R \\ \vec{b} &= \vec{b}^R \end{aligned} \tag{16}$$

Deviatoric and volumetric stress terms in a linear, isotropic and viscoelastic solid with constant Poisson's ratio can be rewritten using (14) and (10), so that

$$\begin{aligned} &\text{Deviatoric:} && \boldsymbol{\sigma}' = 2G(t) * \dot{\boldsymbol{\varepsilon}}'(t) \\ &\text{Volumetric:} && \operatorname{tr}\boldsymbol{\sigma} = 3K(t) * [\operatorname{tr}\dot{\boldsymbol{\varepsilon}}(t)] \end{aligned} \tag{17}$$

where $'$ denotes the deviatoric part of a tensor. For a linear elastic reference solid, expressions in (17) are

$$\begin{aligned} &\text{Deviatoric:} && \boldsymbol{\sigma}'^{\mathbf{R}} = 2G_R\boldsymbol{\varepsilon}'^{\boldsymbol{R}} \\ &\text{Volumetric:} && \operatorname{tr}\boldsymbol{\sigma}^{\boldsymbol{R}} = 3K_R(\operatorname{tr}\boldsymbol{\varepsilon}^{\boldsymbol{R}}) \end{aligned} \tag{18}$$

where G_R and K_R are the shear and bulk modulus, respectively, of the reference elastic material. Taking into consideration the balance in (16) with expressions in (17) and (18), the relationship between strains in the viscoelastic and the reference elastic bodies in terms of the convolution integral are

$$\begin{aligned} &\text{Deviatoric:} && \boldsymbol{\varepsilon}'^{\boldsymbol{R}} = \frac{1}{G_R}\int_0^t G(t-\tau)\frac{\partial\boldsymbol{\varepsilon}'(t)}{\partial\tau}\mathrm{d}\tau \\ &\text{Volumetric:} && \operatorname{tr}\boldsymbol{\varepsilon}^{\boldsymbol{R}} = \frac{1}{K_R}\int_0^t K(t-\tau)\frac{\partial[\operatorname{tr}\dot{\boldsymbol{\varepsilon}}(t)]}{\partial\tau}\mathrm{d}\tau \end{aligned} \tag{19}$$

Since Poisson's ratio is considered as a constant, shear relaxation modulus, bulk relaxation modulus and shear and bulk reference modulus can be used interchangeably. It is common to express the hereditary relationship in terms of the uniaxial relaxation modulus, $E(t)$, and reference elastic modulus, E^R. Expressions for displacements can also be derived, leading to

$$\vec{u}^R(t) = \frac{1}{E_R}\int_0^t E(t-\tau)\frac{\partial\vec{u}(t)}{\partial\tau}\mathrm{d}\tau \tag{20}$$

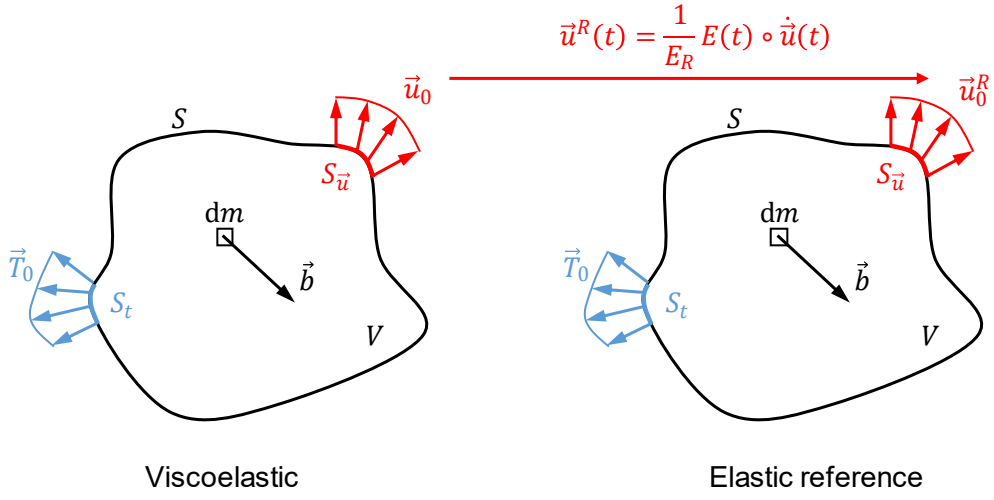

Fig. 18*. Schematic of viscoelastic and elastic reference bodies subjected to applied tractions $\vec{T}_0$ and displacements $\vec{u}_0$ on surfaces, S_t and $S_{\vec{u}}$, respectively, and body forces $\vec{b}$ on its volume V.*

Note that the followed sequel is the solution to the viscoelastic problem. The solution can be read as: body forces, surface tractions and stresses are equal in the viscoelastic and reference elastic problems, while displacements and strains in the viscoelastic problem are related through the hereditary integrals to its elastic reference counterpart, as represented in **Fig. 18**.

Expressions in (19) and (20) might be reversed if viscoelastic displacements or strains are to be determined from their pseudo counterparts. As an example, viscoelastic displacements are resolved through

$$\vec{u}(t) = \frac{1}{D_R}\int_0^t D(t-\tau)\frac{\partial \vec{u}^R(t)}{\partial \tau}\mathrm{d}\tau \tag{21}$$

where $D(t)$ is the uniaxial creep compliance function and D_R is the compliance of the reference elastic body, which is the inverse of E_R. The relationship between relaxation modulus and creep compliance can be motivated as follows.

Given a constant uniaxial stress applied as

$$\sigma_{11} = \sigma_0 H(t-t_0) \tag{22}$$

where σ_0 is the constant applied stress, t_0 the time when the loading is applied and H is the Heaviside step function defined as

$$H(t-t_0) = \begin{cases} 0 & t < t_0 \\ 1 & t > t_0 \end{cases} \tag{23}$$

the constitutive relation in (12) for such a creep loading case is defined as

$$\varepsilon_{11} = \int_0^t D(t-\tau)\frac{\partial \sigma_{11}}{\partial \tau}\mathrm{d}\tau \tag{24}$$

Alternatively, a stress relaxation case is defined for a given uniaxial extension as

$$\varepsilon_{11} = \varepsilon_0 H(t-t_0) \tag{25}$$

and the constitutive relation is

$$\sigma_{11} = \int_0^t E(t-\tau)\frac{\partial \varepsilon_{11}}{\partial \tau}\mathrm{d}\tau \tag{26}$$

By introducing (26) in (24), it is understood in (27) that both relaxation and creep functions satisfy

$$H(t-t_0) = \int_{t_0}^t D(t-\tau)\frac{\partial E(t-t_0)}{\partial \tau}\mathrm{d}\tau \tag{27}$$

Therefore, relaxation modulus and creep compliance are related through the convolution integral, which means that they are inverse in the transformed space, just as elastic modulus and compliance are inverse for the elastic reference material.

***Table 6**. Hereditary relations between variables in the viscoelastic and reference elastic domains, assuming constant Poisson's ratio.*

Variable	Viscoelastic to elastic	Elastic to viscoelastic
Displacements	$\vec{u}^R = E_R^{-1}\int_0^t E(t-\tau)\frac{\partial \vec{u}}{\partial \tau}\mathrm{d}\tau$	$\vec{u} = D_R^{-1}\int_0^t D(t-\tau)\frac{\partial \vec{u}^R}{\partial \tau}\mathrm{d}\tau$
Tractions	$\vec{T}^R = D_R^{*-1}\int_0^t D^*(t-\tau)\frac{\partial \vec{T}}{\partial \tau}\mathrm{d}\tau$	$\vec{T} = E_R^{*-1}\int_0^t E^*(t-\tau)\frac{\partial \vec{T}^R}{\partial \tau}\mathrm{d}\tau$
Body forces	$\vec{b}^R = D_R^{*-1}\int_0^t D^*(t-\tau)\frac{\partial \vec{b}}{\partial \tau}\mathrm{d}\tau$	$\vec{b} = E_R^{*-1}\int_0^t E^*(t-\tau)\frac{\partial \vec{b}^R}{\partial \tau}\mathrm{d}\tau$
Strains	$\boldsymbol{\varepsilon}^{\boldsymbol{R}} = E_R^{-1}\int_0^t E(t-\tau)\frac{\partial \boldsymbol{\varepsilon}}{\partial \tau}\mathrm{d}\tau$	$\boldsymbol{\varepsilon} = D_R^{-1}\int_0^t D(t-\tau)\frac{\partial \boldsymbol{\varepsilon}^{\boldsymbol{R}}}{\partial \tau}\mathrm{d}\tau$
Stresses	$\boldsymbol{\sigma}^{\boldsymbol{R}} = D_R^{*-1}\int_0^t D^*(t-\tau)\frac{\partial \boldsymbol{\sigma}}{\partial \tau}\mathrm{d}\tau$	$\boldsymbol{\sigma} = E_R^{*-1}\int_0^t E^*(t-\tau)\frac{\partial \boldsymbol{\sigma}^{\boldsymbol{R}}}{\partial \tau}\mathrm{d}\tau$

[oo] Note that $*$ superscript has been used to denote relaxation and creep functions and reference stiffness and compliance for tractions, forces and stresses other than those used for displacements and strains.

The relations between variables in the viscoelastic and reference elastic domains are presented in **Table 6**. Note that all these equations are written in terms of the hereditary integrals and can be motivated analogously to the sequel (16) to (20).

Note that E_R works as a normalising parameter and it is chosen as a free constant. For instance, $E^*(t)$, $D^*(t)$, E_R^* and D_R^* for tractions, forces and stresses used in **Table 6** are denoted with $*$ superscript to differentiate them from the used for displacements and strains. As an example, non-linear elasticity formulation is achieved when $E = E^* = D^{-1} = D^{*-1} = E_R = E_R^*$. As it is of interest here, linear or non-linear viscoelasticity is based on $E^* = D^{*-1} = E_R^*$, leading to the solution where tractions, forces and stresses in the viscoelastic and reference elastic problems are equal and displacements and strains in both problems are related through the hereditary integrals, corresponding to the second correspondence principle defined by Schapery (Schapery, 1984).

2.4.3. Viscoelastic Fracture Mechanics

As introduced previously in section 2.1, the interest on composite solid rocket propellant technology grew significantly around the 1950s (Hunley, 1999; Klager, 1984). By that time, concerns involving the structural integrity assessment of propellant grains containing defects such as cracks was the motivation to the US institutions to fund extensive research on the fracture behaviour of these materials (Knauss, 2015). As a result, the foundations of the Viscoelastic Fracture Mechanics emerged, beginning with the works of M. L. Williams (Williams, 1965). Notwithstanding, exhaustive knowledge has not been reached and further developments are needed. As a matter of fact, R. A. Schapery, who is one of the most important contributors to the field, began his work with solid propellants and viscoelastic fracture in the 1970s and still continues publishing updated models and their verification in the very current years (Schapery, 2022a, 2022b, 2023).

In this work, Schapery's approach to viscoelastic fracture assessment (Schapery, 1984) is followed. The choice of the Schapery's constitutive theory is based on the good approximation to describe the deformation behaviour of composite solid propellants, at the same time that relatively simple equations for viscoelastic and fracture analysis are derived (Schapery, 1984). Recalling the second correspondence principle, the viscoelastic problem will be solved

through the elastic reference problem. For a given solid (the sample containing a crack), the geometry and loads are the same in both problems, and displacements are related through the hereditary integrals, c.f. **Fig. 18**. This approach employs the viscoelastic J integral, which is derived as an extension of the J integral proposed by Rice (Rice, 1968). Before the definition of the Schapery's viscoelastic J integral, Rice's J integral will be outlined.

2.4.3.1. Path-independent contour J integral

All energetic fracture criteria are based on the energy release produced when a crack is generated, as stated by Griffith (Griffith, 1921) applying the first law of thermodynamics. The Griffith energy balance, under equilibrium conditions, for an incremental increase in the crack area $\mathrm{d}A$ in a body containing a crack surface, A, subjected to a constant stress σ can be expressed as

$$\frac{\mathrm{d}\Pi_{To}}{\mathrm{d}A} = \frac{\mathrm{d}\Pi}{\mathrm{d}A} + \frac{\mathrm{d}W_S}{\mathrm{d}A} \tag{28}$$

Where Π_{To} is the total energy, Π, is the potential energy in a solid defined as the difference between the elastic stored energy and the work done by the external loads, and W_S is the work needed to produce new surface (crack growth). Since the energy balance must remain constant, $\mathrm{d}\Pi_{To}/\mathrm{d}A = 0$, then

$$\frac{\mathrm{d}W_S}{\mathrm{d}A} = -\frac{\mathrm{d}\Pi}{\mathrm{d}A} \tag{29}$$

The term $\mathrm{d}W_S/\mathrm{d}A$ acquires different names and is defined under different contexts and assumptions, such as the energy release rate, G, early defined by Irwin in 1956 (Irwin, 1956) or the so-called J integral, J, proposed by Rice (Rice, 1968).

$$J = -\frac{\mathrm{d}\Pi}{\mathrm{d}A} \tag{30}$$

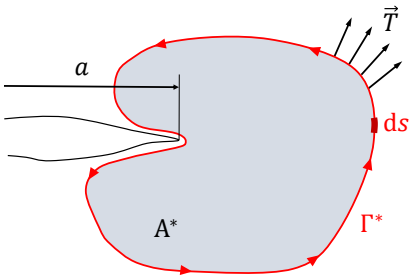

Fig. 19. Arbitrary anticlockwise contour, Γ^*, surrounding a crack, a, circumscribing an area A^* and subjected to tractions $\vec{T}$.

As stated above, the potential energy Π is the difference between the stored deformation energy and the work done by external loads, which can be written for a quasistatic case in the form

$$\Pi = \int_{A^*} \omega \mathrm{d}A - \int_{\Gamma^*} T_i u_i \mathrm{d}s \tag{31}$$

where no body forces are accounted, and ω is the elastic energy density (per unit thickness), T_i are the tractions specified in the Γ^* contour and u_i are the displacements. Γ^* is an arbitrary contour surrounding the crack tip that contains an area A^* and $\mathrm{d}s$ is a differential element of the contour as represented in **Fig. 19**. If considering a crack of length a, c.f. **Fig. 19**, its growth will result in a variation of this potential energy, which can be formulated as

$$\frac{\mathrm{d}\Pi}{\mathrm{d}a} = \int_{A^*} \frac{\mathrm{d}\omega}{\mathrm{d}a} \mathrm{d}A - \int_{\Gamma^*} T_i \frac{u_i}{\mathrm{d}a} \mathrm{d}s \tag{32}$$

since $\mathrm{d}T_i/\mathrm{d}a = 0$ where tractions are defined. The reference coordinate system shall move in the direction defined by x when the crack grows (assuming that the crack will grow in that direction), so (32) is modified as

$$\frac{\mathrm{d}\Pi}{\mathrm{d}a} = \int_{A^*} \left(\frac{\mathrm{d}\omega}{\mathrm{d}a} - \frac{\mathrm{d}\omega}{\mathrm{d}x}\right) \mathrm{d}A - \int_{\Gamma^*} T_i \left(\frac{u_i}{\mathrm{d}a} - \frac{u_i}{\mathrm{d}x}\right) \mathrm{d}s \tag{33}$$

Independently, $\mathrm{d}\omega/\mathrm{d}a$ is derived as

$$\frac{\mathrm{d}\omega}{\mathrm{d}a} = \frac{\mathrm{d}\omega}{\mathrm{d}\varepsilon_{ij}} \frac{\mathrm{d}\varepsilon_{ij}}{\mathrm{d}a} = \sigma_{ij} \frac{\partial}{\partial x_j} \left(\frac{\partial u_i}{\partial a}\right) \tag{34}$$

and employing the principle of virtual work, it leads to

$$\int_{A^*} \sigma_{ij} \frac{\partial}{\partial x_j}\left(\frac{\partial u_i}{\partial a}\right) \mathrm{d}A = \int_{\Gamma^*} T_i \frac{u_i}{\mathrm{d}a} \mathrm{d}s \tag{35}$$

which is introduced in (33) giving

$$\frac{\mathrm{d}\Pi}{\mathrm{d}a} = \int_{\Gamma^*} T_i \frac{u_i}{\mathrm{d}x} \mathrm{d}s - \int_{A^*} \frac{\mathrm{d}\omega}{\mathrm{d}x} \mathrm{d}A \tag{36}$$

Now, Green's Theorem is invoked, so

$$J = -\frac{\mathrm{d}\Pi}{\mathrm{d}a} = \int_{\Gamma^*} \omega \mathrm{d}y - T_i \frac{u_i}{\mathrm{d}x} \mathrm{d}s \tag{37}$$

which is the definition of the J integral proposed by Rice (Rice, 1968). Under a 2D configuration, it comprises a fracture parameter suitable for linear or non-linear time-independent materials. Note that constant unit thickness has been assumed from (30) to (37), so that (37) is equal to (30). Evaluation of the J integral through (37) is feasible for finite element analysis. Nevertheless, when evaluating J through (37) experimentally, it can be quite tedious to perform, as Read demonstrated with a contour path defined with strain gauges (Read, 1982). Experimental procedures are rather derived from (30) since the early works of Landes and Begley (Begley et al., 1972; Landes et al., 1972), where they applied a multi-specimen method, which was further developed by J. R. Rice and co-workers for single-specimen analysis (Bucci et al., 1972; Rice et al., 1973). The J integral definition through (30) implies several advantages, mainly efficiency when it comes to material need, simplicity of implementation and, therefore, less testing work required. More advances were made in the development of expressions to derive calculations of J integral from the fracture tests load-displacement curves (Landes et al., 1974; Ernst et al., 1979), leading to the definition of fracture testing standards (ASTM D6068, 2018; ASTM E1830, 2018; ISO 13586, 2018). Two main formulations are employed: one as (Ernst et al., 1981)

$$J = \frac{\eta U}{B(W-a)} \tag{38}$$

where B is the thickness of the specimen and W its width, η is a constraint factor dependent on geometry and mode of loading and U is the energy computed as the area under the load-displacement curve of the fracture test, defined by:

$$U = \int_0^u P \mathrm{d}u \tag{39}$$

where P is the applied load and u represents the displacement; the other formulation splits the expression in (38) into elastic and plastic contributions as

$$J = \frac{\eta_{el} U_{el}}{B(W-a)} + \frac{\eta_{pl} U_{pl}}{B(W-a)} \tag{40}$$

where subindexes el and pl denote elastic and plastic contributions, respectively. Expression in (38) is preferred for the evaluation of J integral of polymers, considering the tight difference of the results employing its split equivalent in (40) (Moore et al., 2001).

2.4.3.2. Viscoelastic J integral

The viscoelastic J integral or defined by Schapery (Schapery, 1984) is in essence an extension of the concept path-independent line integral developed by Rice (Rice, 1968). It is the far-field fracture parameter that suitably defines the conditions at the crack tip (Anderson, 2017). Schapery states all terms in the elastic reference problem defined in subsection 2.4.1, so superscript R will be employed whenever is needed.

Firstly, the potential energy Π will account for body forces as

$$\Pi = \Pi_s + \Pi_F - \Pi_T \tag{41}$$

being Π_s the stored deformation energy, Π_F the energy computed from the body forces and Π_T the work done by the tractions, analogous to (31). These

energy terms are defined for a 3D solid only assuming homogeneity with respect to the crack advancing direction and dependent on time, although time variable is used to account for effects such as damage or ageing. Viscoelastic J integral is developed for materials like composite solid propellants, whose crack might not be clearly defined, but rather they present a failure zone as represented in **Fig. 20**. To achieve a path-independent integral, the path must lay distant from the failure zone, so that the crack tip is located at the edge where path-independency is not achieved, cf. P in **Fig. 20**, and the path along the crack sides will extend further than the opposite end of the failure zone.

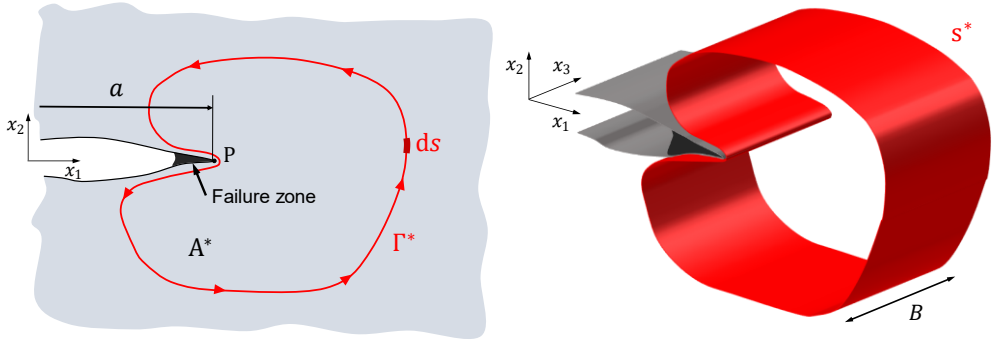

Fig. 20. Crack tip representation. (a) 2D representation of a crack presenting a failure zone at the tip and the arbitrary anticlockwise contour Γ^* surrounding the crack a, (b) 3D representation of the Γ^* contour extruded in the x_3 direction giving the surface contour S^* around a crack tip.

The viscoelastic J integral is the J integral determined in the elastic reference body. Therefore, in this thesis the term pseudo J integral will be preferred for the shake of clarity. Then, the pseudo J integral, J^R, is defined as

$$J^R = \frac{1}{B}\int_{S^*}\left[(\omega_S^R + \omega_F^R)n_x - T_i^R\frac{\partial u_i^R}{\partial x}\right]\mathrm{d}S \tag{42}$$

Where ω_S^R and ω_F^R are the strain and body forces energy densities, respectively, and S^* is not the line path defined by Rice, but it is rather the surface drawn by the contour (cross-section) indicated in **Fig. 20** along the thickness B, so pseudo J integral is a surface-independent integral. The relation in (30) still holds, therefore (38) can be used with a slight modification.

$$J^R = \frac{\eta U^R}{B(W-a)} \tag{43}$$

In (43) the term U^R replaces U in (38). That is the energy in the reference elastic problem which corresponds to the area under the load-pseudo displacement curve defined by

$$U^R = \int_0^{u^R} P du^R \tag{44}$$

where u^R are the displacements in the reference problem or pseudo displacements, which are obtained through the hereditary relations from the actual viscoelastic displacements u, as stated in (20), given by (45).

$$u^{\mathrm{R}} = E_R^{-1} \int_0^t E(t-\tau) \frac{\partial u}{\partial \tau} \mathrm{d}\tau \tag{45}$$

If tests are performed at a constant displacement rate (45) becomes

$$u^{\mathrm{R}} = E_R^{-1} \dot{u} \int_0^t E(t) \mathrm{d}t \tag{46}$$

where $\dot{u}$ is the displacement rate and $E(t)$ still means the uniaxial relaxation modulus. The reference modulus E_R is chosen in this work as the instantaneous modulus E_0 which corresponds to the relaxation modulus at time $t = 0$ (Bencher et al., 1995; Schapery, 2022a). Any other values are possible, such as $E_R = 1$ (Warby et al., 1992), but this choice has been made to give E_R the physical meaning of an unrelaxed body (Bencher et al., 1995). The instantaneous modulus represents the beginning of the relaxation function and the equilibrium modulus, E_∞, represents the asymptotic value of the relaxation function when t is sufficiently high to allow a complete relaxation of the viscoelastic solid. Both values, E_0 and E_∞, could be used based on the strain rate at which the tests are performed, although if $E_R = E_0$ no relaxation is omitted, unlike when $E_R = E_\infty$. If a normalised relaxation modulus $\bar{E}(t)$ is defined as

$$\bar{E}(t) = \frac{E(t)}{E_R} \tag{47}$$

the normalised function will begin at a value of 1 if $E_R = E_0$ and at a value greater than 1 if $E_R = E_\infty$. Therefore, J^R is affected by the definition in (44). When $E_R = E_\infty$ pseudo displacement will be larger than the actual viscoelastic displacements, leading to larger energy values. If $E_R = E_0$ pseudo displacements are smaller to the actual viscoelastic displacements, leading to smaller energy values. Then, using $E_R = E_0$ will better represent the fracture energy not accounting for the viscous energy dissipated during the fracture process that is not related to the actual surface creation process.

2.4.4. Calibration η factor. Load separation method

Expressions in (38) and (43) depend on the so-called dimensionless constraint or calibration factor η. The determination of this factor is possible by means of experimental (Salazar et al., 2008; Zhu, 2017) or numerical (Carvalho et al., 2010; Jia et al., 2020) means. One of the methodologies developed to use mainly in experimental procedures is the load separation method. It was proposed during the early 1980s by several authors (Ernst et al., 1979; Paris et al., 1980; Turner, 1980; Ernst et al., 1981) continuing the RPM (Rice Paris Merkle) solution (Rice et al., 1973). Load separation method was firstly employed to determine η_{pl} factors (Ernst et al., 1981; Sharobeam et al., 1991)., and later to explore a single specimen methodology to provide J-R resistance curves without the need to use tracking crack growth accessories during the tests (Sharobeam et al., 1993), or directly determining the critical value of J integral J_{Ic}, defined as the value of the integral J at crack growth initiation (Frontini et al., 2012). Although the method was developed and widely used for structural integrity evaluation of metals, it has been successfully applied to polymers (Wainstein et al., 2004; Rodríguez et al., 2009) and composites (Antich et al., 2006; Frontini et al., 2012).

Load separation property is one of the bases of the formulation in (38) and (43) and the existence of η factor (Ernst et al., 1981). This property states that the applied load, P, during a test can be represented by the product of two functions as

$$P(a, u_{pl}) = g(a)H(u_{pl}) \tag{48}$$

where $g(a)$ is a geometric function depending on crack size a and $H(u_{pl})$ is a deformation function that depends on the plastic displacement u_{pl}. Indeed, (48) is commonly expressed in terms related to the characteristic lengths of the solid, i.e., not only crack size a, but also the width W of the sample as

$$P(a/W, u_{pl}/W) = g(a/W)H(u_{pl}/W) \tag{49}$$

or in terms of the ligament of the sample $b = W - a$

$$P(b/W, u_{pl}/W) = g(b/W)H(u_{pl}/W) \tag{50}$$

The η_{pl} factor can be inferred from two formulations of the plastic fraction J integral, J_{pl}, being the first of them

$$J_{pl} = -\frac{\partial U_{pl}}{\partial a}\bigg|_{u_{\mathrm{pl}}} \tag{51}$$

where U_{pl} is the energy under the load versus plastic displacement curve. On the other hand, J_{pl} can be described as

$$J_{pl} = \eta_{\mathrm{pl}} \frac{U_{pl}}{b} \tag{52}$$

By equating (51) and (52), the η_{pl} factor can be derived as in (53).

$$\eta_{pl} = -\frac{g'\left(\frac{a}{W}\right)}{g\left(\frac{a}{W}\right)}\frac{b}{W} = \frac{g'\left(\frac{b}{W}\right)}{g\left(\frac{b}{W}\right)}\frac{b}{W} \tag{53}$$

To determine η_{pl} through experimental means, a separation parameter, S_{ij}, is defined. Given two samples with stationary cracks of different lengths, a_i and a_j, the ratio between loads at a specific plastic displacement of both samples can be written as

$$S_{ij} = \left.\frac{P_i\left(\frac{a_i}{W}, \frac{u_{pl}}{W}\right)}{P_j\left(\frac{a_j}{W}, \frac{u_{pl}}{W}\right)}\right|_{u_{pl}} = \left.\frac{P_i\left(\frac{b_i}{W}, \frac{u_{pl}}{W}\right)}{P_j\left(\frac{b_j}{W}, \frac{u_{pl}}{W}\right)}\right|_{u_{pl}} \tag{54}$$

where S_{ij} is the separation parameter. Substituting by the geometric and deformation functions

$$S_{ij} = \left.\frac{g\left(\frac{a_i}{W}\right) H\left(\frac{u_{pl}}{W}\right)}{g\left(\frac{a_j}{W}\right) H\left(\frac{u_{pl}}{W}\right)}\right|_{u_{pl}} = \left.\frac{g\left(\frac{b_i}{W}\right) H\left(\frac{u_{pl}}{W}\right)}{g\left(\frac{b_j}{W}\right) H\left(\frac{u_{pl}}{W}\right)}\right|_{u_{pl}} \tag{55}$$

so that deformation functions must be equal for that specific plastic displacement. Then

$$S_{ij} = \left.\frac{g\left(\frac{a_i}{W}\right)}{g\left(\frac{a_j}{W}\right)}\right|_{u_{pl}} = \left.\frac{g\left(\frac{b_i}{W}\right)}{g\left(\frac{b_j}{W}\right)}\right|_{u_{pl}} \tag{56}$$

The separation parameter S_{ij} represents the separation between load-plastic displacement curves from both samples. Separation property will hold for the u_{pl} range where S_{ij} is constant and, therefore, η_{pl} will exist for that range and crack lengths in between those of the tested samples $[a_i < a < a_j]$ (Ernst et al., 1981).

It is possible to derive the geometric function g from various S_{ij} parameters using a reference sample with crack length a_j, so that

$$S_{ij} = Qg\left(\frac{b_i}{W}\right), \text{for constant } b_j/W \tag{57}$$

Sharobeam and Landes (Sharobeam et al., 1991, 1993) proved that the geometric function g can acquire the power law form

$$g\left(\frac{b_i}{W}\right) = \left(\frac{b_i}{W}\right)^m \tag{58}$$

where $m = \eta_{pl}$ when used in (53) and the constant Q in (57) is

$$Q = \left(\frac{b_j}{W}\right)^{-m} \tag{59}$$

Then, the η_{pl} factor can be obtained through (53), (57) and (58)

$$S_{ij} = Q\left(\frac{b_i}{W}\right)^{\eta_{pl}}, \text{for constant } b_j/W \tag{60}$$

where η_{pl} is obtained from the power law fitting using (60) of the S_{ij} values for various a_i and a reference a_j.

Chapter 3. Objectives

The principal aim of this thesis is the effect of several ageing conditions of different nature on the mechanical and fracture behaviour of a high energy composite solid propellant based on carboxyl-terminated polybutadiene. The approach for the fracture characterisation was the viscoelastic fracture mechanics. To do so, the research has been divided into two parts. In a preliminary characterisation focused on the study of the starting material, with the following objectives:

- To evaluate the strain rate effect on the mechanical and fracture behaviour of the composite propellant.
- To determine the micromechanisms controlling the fracture process for the different studied strain rates.

After successfully fulfilling the preliminary characterisation, a new experimental campaign was completed for the composite solid material subjected to mechanical, thermal and ozone ageing. The following objectives were pursued:

- To study the mechanical response and fracture behaviour of the composite propellant with the evolution of time and type of ageing.
- To examine the changes in the microstructure of the propellant due to the ageing, through the measurement of the soluble fraction in the elastomeric matrix, and its influence on the mechanical and fracture behaviours and its controlling micromechanisms.
- To explore new methodologies to assess the ageing of composite solid rocket propellant motors in the surveillance programs.

Chapter 4. Experimental procedure

4.1. Grain extraction from the rocket

The material under study comes from a couple of two-stage composite solid rocket propellant motors, which are formed by two types of propellants named as sustainer and booster, cf. **Fig. 21** and **Fig. 22**a. The propellant analysed in this research belongs to the booster.

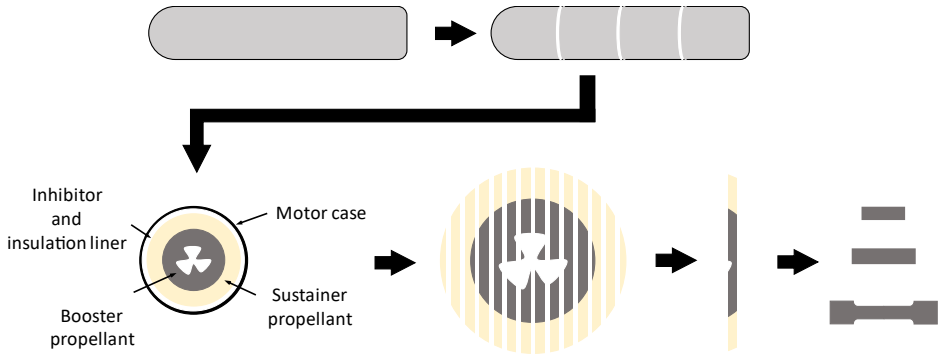

Fig. 21. Schematic of the propellant's grain extraction from the motor for the obtention of the testing samples.

To extract the propellant grain, the whole motor was first split (cut) into slices. Then the propellant grain was separated from the motor case using a hydraulic press and sliced to ease the handling and machining of the samples. All the samples were machined from each of the produced slices. A schematic of the process is shown in **Fig. 21**. Further details of the extraction of the propellant grain can be found in (López Sánchez, 2018). As an example, one of the slices of the motor, the machining process and some of the machined samples from the sustainer and booster propellants are presented in **Fig. 22**.

A chemical characterisation to determine the components of the composite propellant was extensively carried out previously by R. López in (López Sánchez, 2018). The composition of the booster composite solid propellant was determined as:

- Carboxyl-Terminated Polybutadiene (CTPB) elastomer as binder.

- Ammonium Perchlorate (AP) ceramic particles as oxidiser in 54 wt%. The diameter of these particles presented a normal distribution centred at 120 μm.
- Aluminium (Al) micronized powder as fuel in 16 wt%.
- Isodecyl pelargonate in 3.6 wt% as plasticiser.

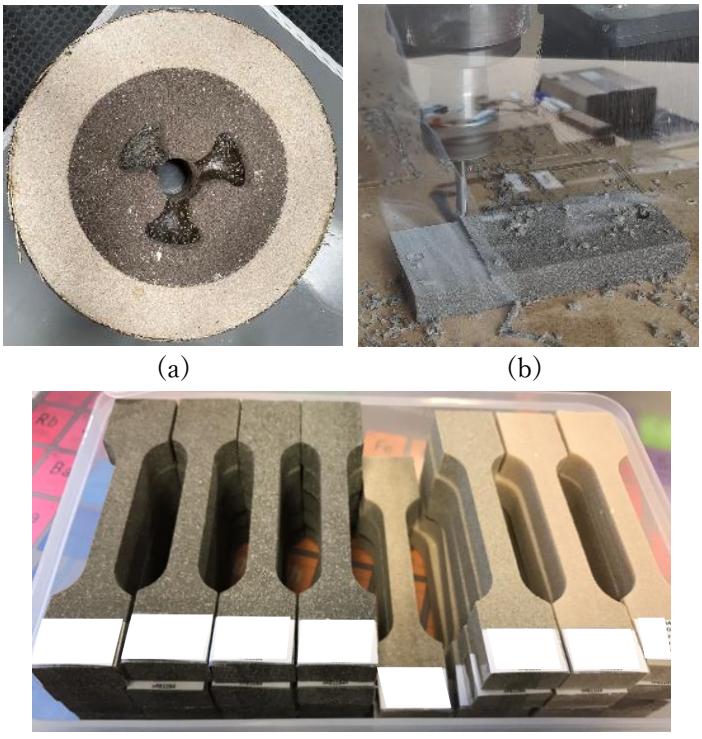

(a) (b)

(c)

Fig. 22*. Propellant grain at different stages of the extraction. (a) Slice of the motor (booster is the grey propellant and sustainer is the white propellant), (b) machining of the slices of propellant, and (c) resulting JANNAF samples for tensile tests.*

Two characterisations were performed in the present work. A primary characterisation, which was carried out with propellant extracted from the motor that has been described, to establish the mechanical and fracture behaviour under different strain rates. A secondary characterisation to study the degradation of the propellant under different conditions was developed with a similar composite propellant that came from a twin rocket motor. Since both are twin motors, in this work the compositions of both propellants are assumed to

be the same. Both characterisation stages will be denoted as "preliminary characterisation" and "ageing characterisation". The term "pristine" will be used to name the propellant extracted from the motor that is only naturally aged and has not been subjected to any kind of accelerated ageing.

4.2. Ageing processes

4.2.1. Accelerated mechanical ageing

Mechanical ageing of composite solid propellant grains is conceived as the cumulative effect of solicitations over the shelf life of the motor. These solicitations are mostly due to vibrations, gravity and temperature variations. Dewetting of the particles is the major concern produced by mechanical solicitations (Belitsky et al., 2023). To explore the results of severe mechanical ageing, the proposed ageing procedure consisted in the application of a strain during a loading-unloading cycle at a crosshead displacement rate of 500 mm/min. This value was chosen after the preliminary characterisation, where it was observed that dewetting damage was more intense with increasing strain rate. The applied loading-unloading cycle is shown in **Fig. 23** in terms of stress-strain curves in engineering magnitudes, where the viscous nature of the propellant is explicitly manifested.

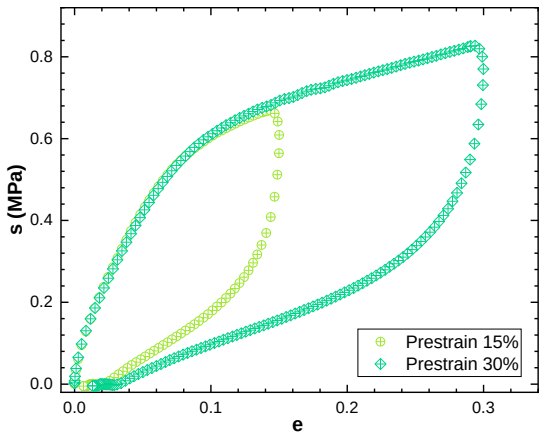

***Fig. 23**. Engineering stress, s, versus engineering strain, e, curves of the loading-unloading cycle applied to the mechanically aged samples, with applied strains of 15% and 30%, for the ageing characterisation.*

Relaxation, tensile and fracture tests were performed on mechanically aged samples, that were subjected to the described loading-unloading cycle up to 15% and 30% applied longitudinal engineering strain. The ageing procedure was carried out one hour before the corresponding relaxation, tensile or fracture test. This time was considered adequate to avoid influence of the prestraining process on the tests (Mullins, 1949).

4.2.2. Accelerated temperature ageing

As previously mentioned, isothermal accelerated temperature ageing process is a common procedure for its use in composite solid propellants. It is usually aged at temperatures in the range of 60 °C to 80 °C (Cerri et al., 2013; Zhang et al., 2023a). Following AOP-48 for isothermal accelerated ageing (AOP-48, 2008), the necessary accelerated ageing time, t_a, to produce an equivalent storage time can be determined as

$$t_a = t_{25} \exp\left(\frac{E_a}{RT_a} - \alpha\right) \tag{61}$$

where t_{25} is the equivalent storage time at 25 °C, E_a is the activation energy determined as 120 kJ/mol for ageing temperatures higher than 60 °C or 80 kJ/mol for ageing temperatures lower than 60 °C, R is the ideal gas constant ($R = 0.00831447\ kJ/K \cdot mol$) and α is a constant which is 46.713 for ageing temperatures higher than 60 °C or 32.272 for ageing temperatures lower than 60 °C. Note that (61) is an alternative form of Layton's law in (2).

For this work, relaxation, tensile and fracture samples were wrapped in aluminium foil and isothermally aged in an oven at a temperature of 80 °C with exposition times of 24 and 36 days. Making use of (61), the corresponding equivalent storage times at 25 °C are approximately 22.3 and 33.5 years. Note that (61) assumes an Arrhenius form, which is not suitable for all cases and time ranges (Celina et al., 2005), and activation energies are generic for composite solid propellant, but not for the specific composition. Therefore,

equivalent storage times must be understood solely as long storage times rather than precise dates.

4.2.3. Accelerated ozone ageing

The accelerated ozone ageing process of the composite solid propellant was carried out in an *ad hoc* ozone chamber. The description of the ozone chamber is made in Appendix I. Several technologies are available nowadays to produce ozone. High voltage corona discharge system has been chosen in this work for the ozone generation. The corona discharge ozone generation is suitable to avoid other kind of interactions with the propellant, as the case of ultraviolet (UV) light, which promotes other oxidative ageing processes, for example. The corona discharge technology is efficient and capable of producing ozone constantly during large periods, being economic and simple to use and replace.

Relaxation, tensile and fracture samples were aged in the ozone chamber for 14, 21, 32 and 42 days at room temperature. Samples were introduced in the chamber once the maximum allowable ozone concentration of approximately 160 ppm was reached, holding the ageing process at that concentration for the ageing period.

4.3. Chemical characterisation

Composite solid propellants are very complex materials characterised by the heterogeneity of their components. From the mechanical point of view, the mechanical response of the propellant is controlled by the binder, which is usually an elastomer, with the crosslinking density, CLD, being one of the key chemical properties that can indicate the state of the propellant and, in particular, the degree of ageing. The procedure to determine the crosslinking density consisted in measuring the soluble fraction through the method 1A indicated in the STANAG 4581 standard (STANAG 4581, 2022).

Initially, a sample of composite solid propellant with an initial mass, W_i, of 1-2 g was immersed in toluene to extract the free chains (sol fraction) from the binder. The propellant was maintained submerged in the solvent for four days changing the solvent every 24 h. After four days, the soluble fraction (sol) and the propellant mass (gel) are separated and the gel fraction was dried in an oven at 50 ºC until the final mass of the propellant, W_f, was constant. The sol fraction S was then determined as

$$S = \frac{W_i - W_f}{W_i} \tag{62}$$

and the crosslinking density expressed in term of the sol fraction is

$$CLD = \frac{(1-S)\left[2-\left(S+\sqrt{S}\right)\right]}{\left(S+\sqrt{S}\right)} \tag{63}$$

4.4. Mechanical characterisation

4.4.1. Time dependent characterisation

One of the common procedures to characterise the viscoelastic behaviour of polymers is the stress relaxation test. These tests were carried out to observe the changes in the viscoelastic capability of the propellant after damage has been produced. It is also relevant that the relaxation functions are required to obtain the pseudo displacements and pseudo strains according to the hereditary relations, cf. **Table 6**.

For the preliminary characterisation of the composite solid propellant extracted from the first motor, the relaxation tests were carried out in a TA Instruments DMA Q800 using parallelepipedal specimens in three-point bending configuration, cf. **Fig. 24**. The dimensions of the specimens were of 64x12x6.5 mm tested with a span of 50 mm at 20 ºC. A strain of 1.5% was applied in around 5 seconds and held for 30 min. These conditions were chosen to assure linear viscoelastic behaviour (Tussiwand et al., 2009; Xu et al., 2013).

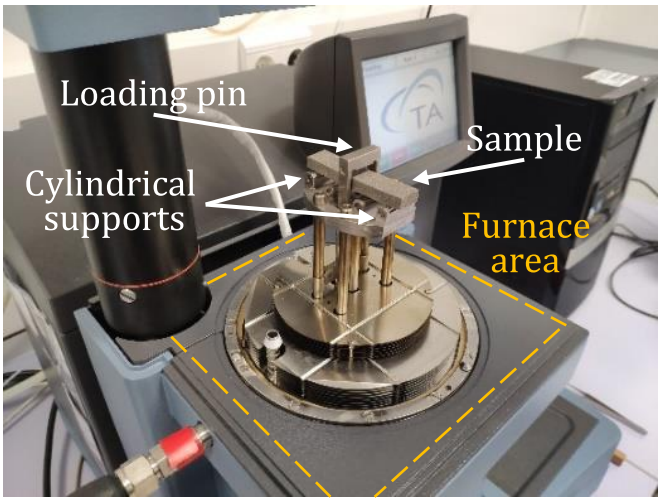

***Fig. 24**. Experimental set-up for the stress relaxation test in three-point bending configuration on the DMA Q800 machine for the preliminary characterisation.*

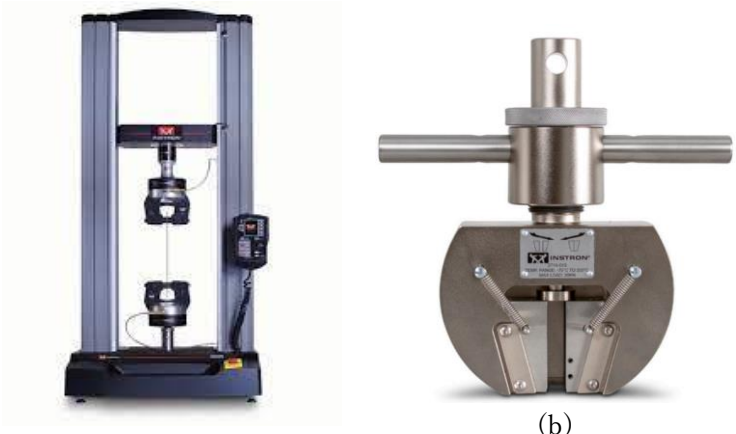

(a) (b)

***Fig. 25**. Relaxation testing equipment. (a) universal electromechanical Instron 5967 testing machine, and (b) manual wedge grips from Instron®.*

The propellant obtained from the second motor was tested in a different and more suitable configuration. The stress relaxation tests were carried out with parallelepipedal specimens with nominal dimensions of 50x10x10 mm in tensile configuration using a universal electromechanical testing machine Instron 5967 with a loadcell of ±500 N and manual wedge grips, c.f. **Fig. 25**. The imposed strain was chosen to be of 3% (Schapery, 1982; Tussiwand et al., 2009) for all specimens, except for the ones that were subjected to temperature

accelerated ageing, which were strained at 0.15%. The chosen strain was assumed not to influence the relaxation behaviour since it was proven as strain independent for low strains, i.e., $\varepsilon \leq 3\%$ (Bencher et al., 1995). Specimen size and imposed strain were chosen as a balance between material availability and load scale. Tests were done at room temperature with a ramp load of 50 mm/min and a holding time of 30 min. For the specimens subjected to accelerated thermal ageing, the ramp load was of 2 mm/min to reach the target strain in approximately 2 s, as it was for all the specimens.

To perform the tests, the samples were sticked to *ad hoc* designed tabs, cf. **Fig. 26**, that will be inserted into de wedges of the manual grips to avoid grip-induced failures in the propellant, cf. **Fig. 25**b. These tabs were manufactured by a fused deposition modelling (FDM) printer in polylactic acid (PLA) material and designed as shown in **Fig. 26**a. To solve complications associated to the printing process, the assembly of the samples and tabs is shown in **Fig. 26**b. To bond the propellant samples to the tabs, a quick set structural epoxy bicomponent adhesive from RS PRO was used. The adhesive was applied for at least 48 h prior to testing to ensure complete curing. Due to the different nature and limitations of each applied degradation, the procedure has been:

- Mechanically induced damage: the samples were sticked to the tab and once the epoxy resin was completely cured, the mechanical damage was introduced, followed by the waiting period of 1 h before the stress relaxation tests were carried out.
- Accelerated temperature ageing: the samples were first aged in the oven. After ageing, they were sticked to the tabs and left to cure. Finally, the stress relaxation tests were performed.
- Accelerated ozone ageing: the samples were first sticked to the tab and introduced in the ozone chamber. The curing of the resin was produced during the ageing process and no affection to the bonding between the propellant sample and the PLA tabs was found. After the ageing process, the stress relaxation tests were conducted.

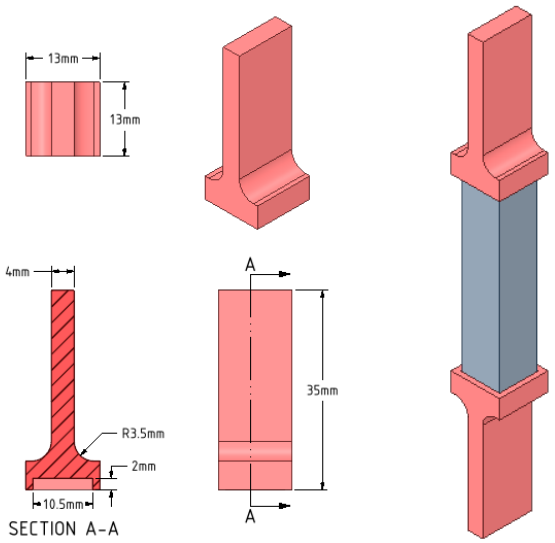

Fig. 26. Tensile stress relaxation samples performed on the propellant coming from the second motor for the ageing characterisation. (a) PLA printed tabs for relaxation tests, and (b) propellant sample configuration for tensile testing.

4.4.1.1. Relaxation functions

As alluded to, relaxation functions are necessary for the determination of the pseudo variables. These functions were derived from the experimental data obtained from the stress vs time curve from the stress relaxation tests. The procedure proposed by Xu et al. (Xu et al., 2013) was used, which is purely an extension of the viscoelastic equations for the entire test, including the loading region. The development of the equation is shown in the forthcoming paragraphs.

Commonly the loading step or loading ramp is ignored in the analysis of stress relaxation tests. It is an affordable approach as the requirements for data acquisition and processing are modest. Nevertheless this can have significant effect if the material relaxes in a sudden way, as is the case of solid rocket propellants or some biomaterials (Shetye et al., 2014), and interest is placed in the rapid response of the material. The stress relaxation test is briefly described in

Fig. 27, where a strain is imposed over a period of time while the evolution of the load (stress) is recorded.

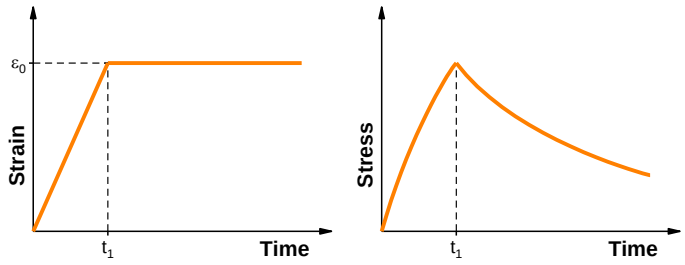

Fig. 27. Schematic of a stress relaxation test with ideal constant strain rate loading ramp.

If an ideal step loading is considered the stress-strain relation for a uniaxial loading case in (13) reduces to

$$\sigma(t) = E(t)\varepsilon_0 \tag{64}$$

where ε_0 is the target strain for the stress relaxation test. This relation holds whenever the loading ramp is ignored and, although it is convenient due to its simplicity, information from the test is missed. An alternative approach comes when considering the step loading as a constant strain rate ramp, as in **Fig. 27**.

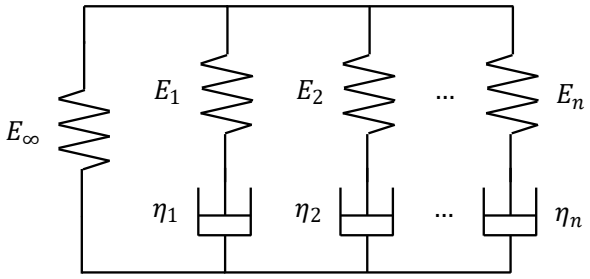

Fig. 28. Schematic of a generalized Maxwell-Wiechert model.

The relaxation function is taken here as a Prony series. Prony series are one of the most common representations for viscoelastic solids, whose mechanical analogy is the so-called generalized Maxwell-Wiechert model, c.f. **Fig. 28**. A Maxwell element is defined by a spring connected in series to a dashpot. The Maxwell-Wiechert model consist in the connection in parallel of as many

Maxwell elements as needed to represent the stiffness relaxation. It is also considered a spring connected in parallel to the other Maxwell elements to account for the possible remaining stiffness after the complete relaxation is reached.

Other functions, such as modified-power-law functions, have been employed for solid propellants(Darwell et al., 1966; Schapery, 1969), but they are hardly found in bibliography today. The relaxation function as Prony series can be written as

$$E(t) = E_\infty + \sum_{i=1}^{N} E_i e^{-t/\tau_i} \tag{65}$$

where E_∞ is the equilibrium modulus and E_i and τ_i are the modulus and relaxation times for the Maxwell i-th element, respectively. As one might observe in (65), this representation has a direct Laplace transformation, to use equations in the elastic reference problem, and Fourier transformation, to use for frequency domain data. That reason might have helped the Prony series to become the standard model used for composite solid propellants (James S. et al., 1973) and its implementation in finite element commercial codes.

To develop the stress-strain equation, the stress relaxation function $\sigma(t)$ during the relaxation test can be derived from the decomposition of the applied strain history (I) as shown in **Fig. 29**. A constant strain rate loading ramp defines the loading history (II), while a constant strain rate loading ramp beginning at t_1 defines the loading history (III), being 0 for $t \leq t_1$. Note that the difference between loading histories (II) and (III) gives (I).

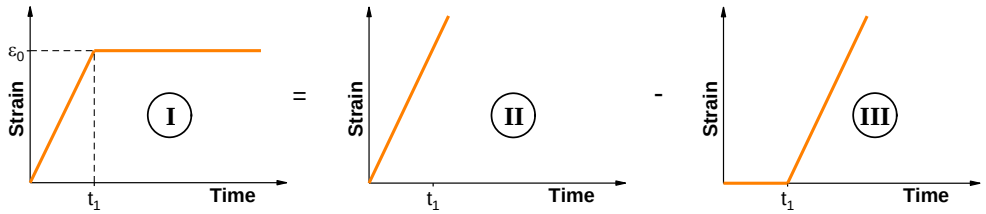

Fig. 29. Applied strain in stress relaxation tests and its decomposition.

The stress-strain relation for the loading history (II) can be written in the same form for all times t. Hence, it will be first developed from (13), which can be rewritten for a constant strain rate ramp as

$$\sigma^{\mathrm{II}}(t) = \frac{\varepsilon_0}{t_1}\int_0^t E(t-\tau)\mathrm{d}\tau \tag{66}$$

where t_1 is the time employed to reach the target strain ε_0. As an example, for a Prony series of 1st order the expression in (66) is redefined as

$$\sigma^{\mathrm{II}}(t) = \frac{\varepsilon_0}{t_1}\int_0^t \left(E_\infty + E_1 e^{-\frac{\tau}{\tau_1}}\right)\mathrm{d}\tau \tag{67}$$

The solution to the integral (67) is

$$\sigma^{\mathrm{II}}(t) = \frac{\varepsilon_0}{t_1}\left[E_\infty t + E_1\tau_1\left(1 - e^{-\frac{t}{\tau_1}}\right)\right] \tag{68}$$

Then, the expression in (68) can be generalized for a N-th order of the Prony series so that the stress-strain relation for a generalized Prony series during a constant strain rate loading ramp is

$$\sigma^{\mathrm{II}}(t) = \frac{\varepsilon_0}{t_1}\left[E_\infty t + \sum_{i=1}^{N} E_i\tau_i\left(1 - e^{-\frac{t}{\tau_i}}\right)\right] \tag{69}$$

Regarding the loading history (III), for times $t \le t_1$, $\sigma^{III}(t) = 0$. Consequently, $\sigma^{I}(t) = \sigma^{II}(t)$ for $t \le t_1$. Analogously, the stress-strain relation for loading history (III) at $(t \ge t_1)$ is obtained from (66) with lower and upper integration limits t_1 and t, respectively, giving the general form

$$\sigma^{\mathrm{III}}(t) = \frac{\varepsilon_0}{t_1}\left[E_\infty(t-t_1) + \sum_{i=1}^{N} E_i\tau_i\left(1 - e^{-\frac{t-t_1}{\tau_i}}\right)\right] \tag{70}$$

so that the difference $\sigma^{II}(t) - \sigma^{III}(t)$ for $t \ge t_1$ gives

$$\sigma^{\mathrm{I}}(t) = \frac{\varepsilon_0}{t_1}\left[E_\infty t_1 + \sum_{i=1}^{N} E_i\tau_i\left(e^{-\frac{t-t_1}{\tau_i}} - e^{-\frac{t}{\tau_i}}\right)\right] \tag{71}$$

To summarise, the stress-strain relation in tensile relaxation tests considering a constant strain rate loading ramp are described by (72)

$$\begin{aligned}\sigma(t) &= \frac{\varepsilon_0}{t_1}\left[E_\infty t + \sum_{i=1}^{N} E_i\tau_i\left(1 - e^{-\frac{t}{\tau_i}}\right)\right]; \qquad t \le t_1 \\ \sigma(t) &= \frac{\varepsilon_0}{t_1}\left[E_\infty t_1 + \sum_{i=1}^{N} E_i\tau_i\left(e^{-\frac{t-t_1}{\tau_i}} - e^{-\frac{t}{\tau_i}}\right)\right]; \quad t \ge t_1\end{aligned} \tag{72}$$

From stress relaxation tests, an average of the stress vs time curve from three samples is obtained for each condition. To obtain the relaxation function parameters in (65), a least-square fit is performed for a 4th order Prony series. For the fitting process, the only constraints applied were that all parameters must be positive to be in accordance with the rheology of the model.

4.4.2. Tensile tests

Tensile test are one of the most common procedures in the composite solid propellant motor surveillance programs, with the recognised international standard STANAG 4506 (STANAG 4506, 2000). From stress versus strain data of the uniaxial tensile tests, the following parameters are reported with regard to the standard: apparent modulus E, stress at maximum σ_{max}, stress at rupture σ_r, strain at maximum ε_{max} and strain at rupture ε_r. The described parameters are illustrated in **Fig. 30**.

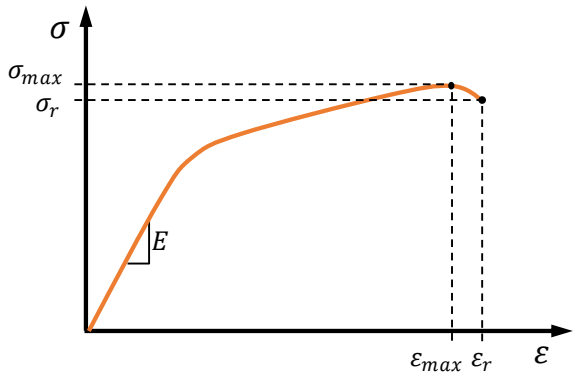

Fig. 30*. Schematic of a typical stress, σ, versus strain, ε, curve from a uniaxial tensile test of a composite solid propellant.*

Tensile tests were carried out using JANNAF specimens, described in STANAG 4506, with dimensions shown in **Fig. 31**a. Due to the nature of the composite solid propellant, *ad hoc* designed grips – as recommended by the standard – are employed, cf. **Fig. 31**b, on the same electromechanical universal testing machine shown in **Fig. 25**a.

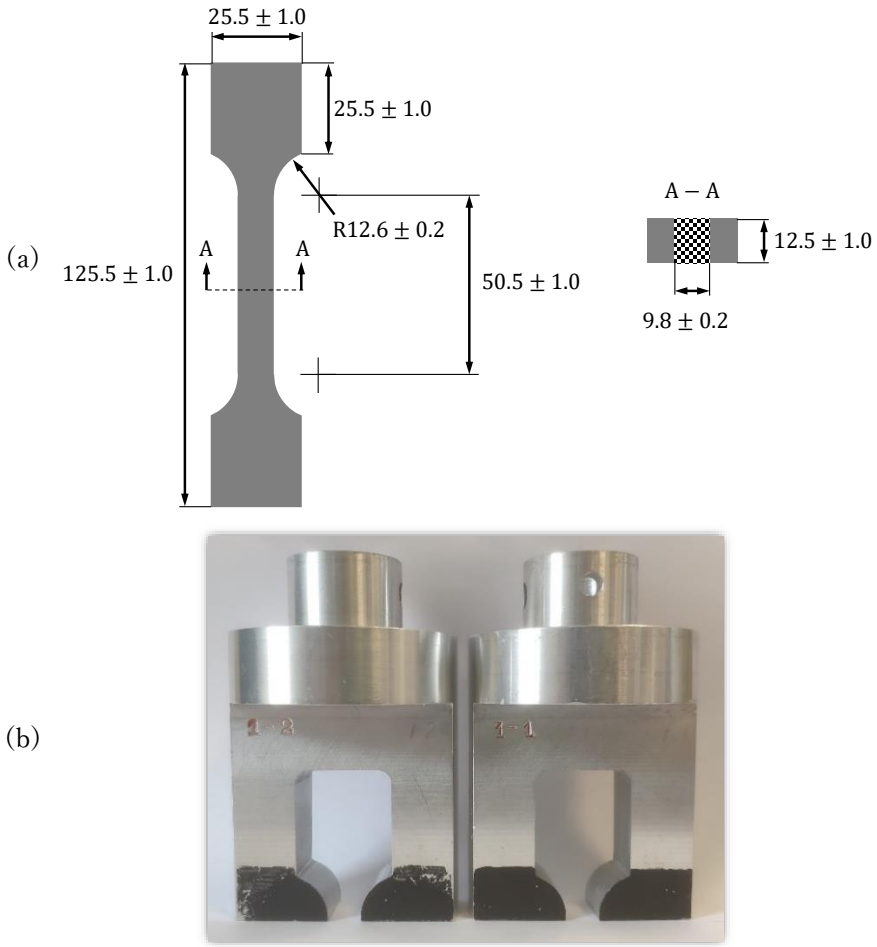

Fig. 31*. Tensile test set-up. (a) schematic of the JANNAF tensile specimen with dimensions in mm, and (b) ad hoc designed JANNAF tensile test grips.*

The determination of the strain from the machine crosshead displacement leads to inaccurate measurements (STANAG 4506, 2000). Using a contact extensometer is not appropriate for soft materials, as many composite solid propellants are. In this work, the determination of the strains has been done

through digital image correlation (DIC). It is a suitable method since no contact with the specimen is required and strains in all directions – in the plane in this case – can be computed.

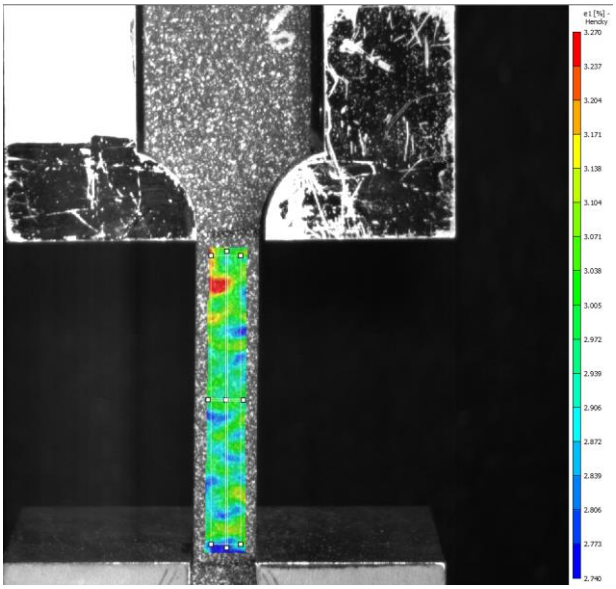

Fig. 32*. Digital image correlation set-up for the determination of the displacements and strains fields during the tensile tests.*

VIC 2D equipment from Correlated Solutions was employed to record the tests and determine the displacements and strains fields through DIC on a visible side of the sample, cf. **Fig. 32**. To carry out the DIC analysis, a speckle on the visible surface was made using a quick-dry acrylic enamel in white colour, directly spraying from the bottle of paint. Strains were measured in a region of interest (ROI) comprised in the gauge length as shown in **Fig. 32**. True strains were determined as the average of the strain field in the selected area with rectangular shape. The strains analysed were the longitudinal strain, ε_l, and the transverse strain, ε_t, corresponding to the direction of the gauge length and its perpendicular direction, respectively. To determine the engineering strain in one direction, virtual extensometers are placed along the desired direction.

Engineering stress, s, is determined as the ratio between the recorded load, P, and the initial cross-section, S_0, so that

$$s = \frac{P}{S_0} \tag{73}$$

True stress, σ, is determined through the ratio between the recorded load and the instantaneous cross-section, S, as

$$\sigma = \frac{P}{S} \tag{74}$$

where S is calculated for a rectangular section as

$$S = S_0(1 + \varepsilon_t)^2 \tag{75}$$

assuming isotropy in both transverse directions and ε_t the transverse strains computed from the DIC analysis at each instant. From the resulting stress versus strain curves, the apparent elastic modulus, E, stress at maximum, σ_m, and strain at maximum, ε_m, were obtained, following STANAG 4506 standard. Since stress and strain at rupture were close to their corresponding stress and strain at maximum, the latter were omitted.

Further analysis on the strains was made. Initial Poison's ratio, ν_0, was determined as the slope of the ε_t versus ε_l as in (76) in the linear region, which corresponds to the beginning of the test, via least squares fit.

$$\nu_0 = -\frac{\varepsilon_t}{\varepsilon_l} \tag{76}$$

Poisson's ratio, ν, was determined using (77), which is formally the same as (76), whereas in this case, strain's ratio is computed for the entire tensile test.

$$\nu = -\frac{\varepsilon_t}{\varepsilon_l} \tag{77}$$

The dewetting point is considered as the critical instant at which the effects of local dewetting, which is distributed through the specimen, starts to influence the macro mechanical response during the loading process. It is assumed to happen in the region of the stress versus strain curves in uniaxial

tensile tests where there is a transition between the elastic slope and the hardening slope, cf. **Fig. 9**. Several approaches exist to determine this critical point (Zou et al., 2023), e.g., through the ν versus ε_l curve or σ versus ε_l curve. But not only those. As known, dewetting and void growth are significant phenomena in the mechanical behaviour of composite solid propellants. They result in the variation of the volume. The dilatation curves, defined by V/V_0 versus ε_l curve, present an alternative to determine the dewetting point. The dilatation can be computed through the expression

$$\frac{V}{V_0} = (1 + \varepsilon_l)(1 + \varepsilon_t)^2 \tag{78}$$

where isotropy is assumed. The $\nu - \varepsilon_l$, $V/V_0 - \varepsilon_l$ and $\sigma - \varepsilon_l$ curves and their derivatives have been analysed to establish a unique criterion to determine the dewetting point. The employed curves are gathered in Appendix III. The longitudinal and transverse true strains, ε_l and ε_t, respectively, were obtained through DIC.

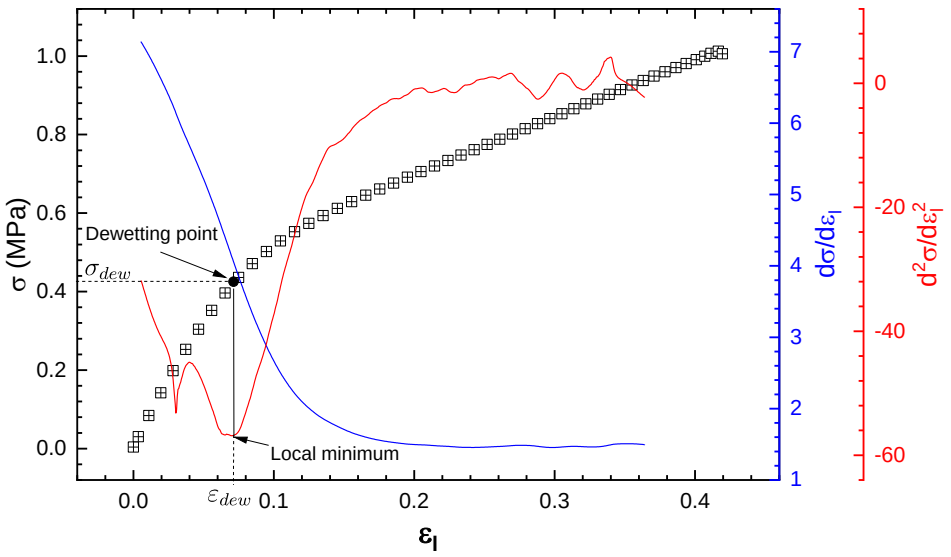

Fig. 33*. Example of a true stress, σ, versus true longitudinal strain, ε_l, curve together with its first (blue line) and second (red line) derivatives, for the determination of the dewetting point.*

After the analysis of the different approaches, the determination of the dewetting point has been carried out through the identification of a local

minimum found in the second derivative of the true stress, σ, versus longitudinal true strain, ε_l, curve in the aforementioned transition region. The strain ε_l at which the local minimum is found defines the dewetting strain, ε_{dew}, and then, the dewetting stress, σ_{dew}, is determined for $\varepsilon_l = \varepsilon_{dew}$ in the stress versus strain curve, as represented in **Fig. 33**.

Concerning the testing conditions, for the preliminary characterisation of the propellant, tests were performed at room temperature and three constant crosshead speeds of 5, 50 and 500 mm/min corresponding to strain rates of 10^{-3}, 10^{-2} and 10^{-1} s^{-1}, respectively. A load cell of ± 500 N was employed and three replica were tested for each strain rate.

For the ageing characterisation of the propellant, which is focused on the effect of ageing sources on the tensile behaviour, all the tests were performed at room temperature and at a constant crosshead displacement rate of 5 mm/min corresponding to a strain rate of 10^{-3} s^{-1}. Due to the limitations on material availability, only one replica for each ageing condition was conducted. The ageing conditions have been: mechanical prestrained up to 15% and 30%, thermal ageing during 24 and 36 days and ozone ageing during 14 and 42 days.

4.4.3. Fracture tests

Fracture tests are considered as an important source of information of the structural integrity of the composite solid propellant motor grains (James S. et al., 1973). However, no standard or guidelines are established for the fracture assessment of this kind of materials. Therefore, an extensive study on the fracture behaviour has been conducted.

The configuration of the fracture tests might affect the obtained results. As seen in **Fig. 34**, the use of different geometries or loading types affect the constraint around the crack tip. Consequently, the use of a specific specimen should be adequate for the purpose, regarding the testing capabilities. In this work, single-edge-notched-tension (SENT) configuration has been employed. One reason for this election is that they present a lower level of constraint

compared to other common and normalised specimens or loading types, such as compact tension (CT) or single-edge-notched-bending (SENB). Furthermore, SENT specimens do not present the necessity to correct the displacement due to indentation from the loading pins.

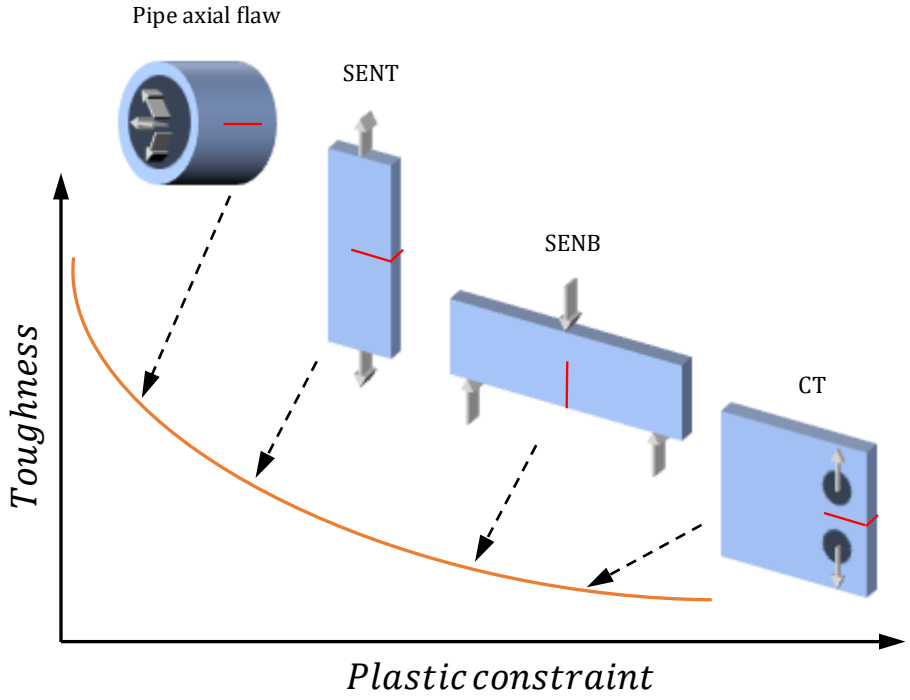

***Fig. 34**. Effect of constraining conditions on the determined toughness for several fracture testing configuration. Adapted from (Furmanski et al., 2022).*

For the SENT fracture tests, parallelepipedal samples with sizes of 12.5x25x80 mm were machined. All tests were carried out in the universal electromechanical testing machine Instron 5967, already shown in **Fig. 25**a, with a loadcell of ±500 N and the grips shown in **Fig. 25**b.

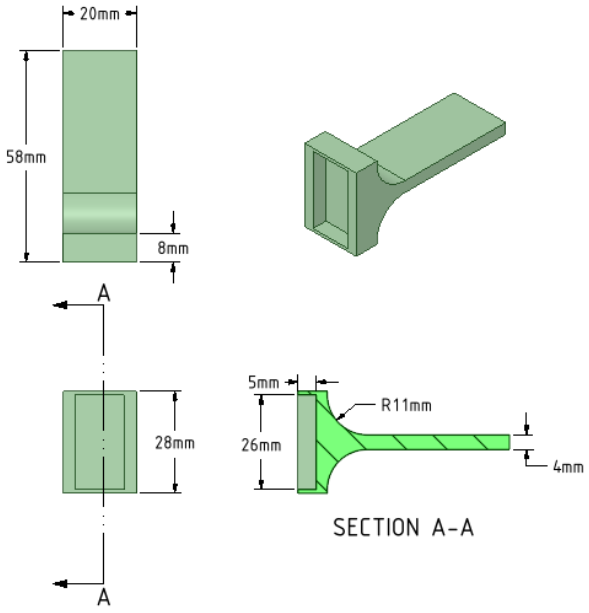

***Fig. 35**. Schematic of the designed PLA tabs for the fracture specimens.*

Since composite solid rocket propellant is too soft to be directly gripped by the generic clamps of the electromechanical machine, *ad hoc* end-tabs were designed and produced as previously described in 4.4.1 for relaxation specimens. The schematic of the designed tabs for fracture specimens is shown in Fig. 35.

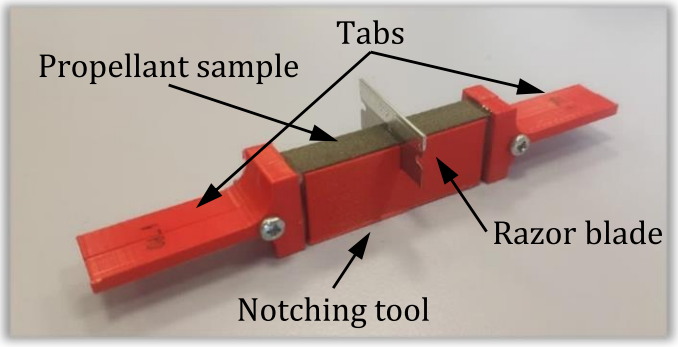

***Fig. 36**. Fracture samples' notching set-up. Fracture sample sticked to the tabs, inserted in the designed sliding tool.*

The crack in the fracture samples was introduced by sliding a sharp razor blade through one side of the sample right before the fracture test. The set-up

for the notching process is shown in **Fig. 36**. A tool was also *ad hoc* designed and produced by FDM. This tool helped to produce reproducible cracks for all samples and thus, facilitating the notching process.

For the preliminary characterisation, fracture tests were performed at four constant crosshead speeds of 0.5, 5, 50 and 500 mm/min at room temperature. The crack length, a, chosen was of 9.1 mm leading to a crack length to width ratio $a/W = 0.364$. The crack was introduced 15 min prior to the test.

According to the ageing characterisation, fracture tests were performed at the crosshead speed of 5 mm/min at room temperature. The crack length for cracked specimens was, in this case, 10 mm, giving a crack length to width ratio $a/W = 0.4$.

4.4.3.1. J resistance curves

J integral, J, was determined using (38) and its pseudo counterpart, J^R, via (43). Note that the definition of J in (38) is analogous to the work of fracture, W_F, defined by Schapery (Schapery, 1984), relating $J = W_F$ and J^R through

$$W_F = E_R D(t) \circ J^R \tag{79}$$

where $D(t)$ is the creep function.

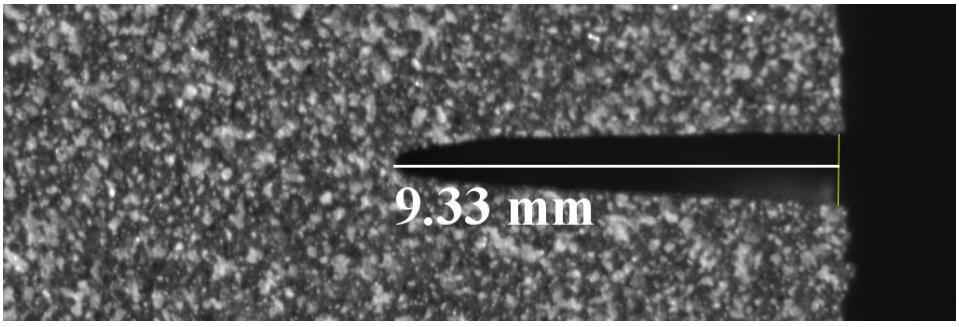

***Fig. 37**. Example of crack measurement during fracture tests*

These J integral values were used to determine the critical J integral at crack growth, J_c or J_c^R, and to construct J resistance curves. To do so, optical means were employed. Fracture tests were recorded to determine crack length

throughout the test and to determine the instant of the initiation of the crack propagation. The measurements were done on the visible surface as demonstrated in **Fig. 37**.

The equipment employed was VIC 2D composed of a camera with 5 MP with a selected sampling rate of 5 Hz (200 ms) controlled by the acquisition software VIC snap. Exceptionally, for fracture tests at crosshead displacement rates of 50 and 500 mm/min from the preliminary characterisation, it was necessary to employ a camera capable of higher acquisition frequencies. The utilised camera for these fracture tests was a Redlake MotionPro High Speed camera with selected acquisition frequencies of 50 Hz (20 ms) and 333.33 Hz (3ms) for the 50 and 500 mm/min testing conditions, respectively. Higher acquisition frequencies were not possible due to limitations on the sampling frequency of the Instron testing machine.

J resistance curves are represented in terms of $J - \Delta a$ and $J^R - \Delta a$, where Δa is the crack growth. The relationship between J and Δa usually presents a power law form as

$$J = C_1 \Delta a^{C_2} \tag{80}$$

or

$$J^R = C_1 \Delta a^{C_2} \tag{81}$$

where C_1 and C_2 are material constants and $C_2 \leq 1$.

4.4.3.2. CTOD resistance curves

In addition to the presented J and J^R fracture parameters, the crack tip opening displacement (CTOD), δ, fracture parameter has also been measured. The 90º intercept definition of the CTOD was chosen to determine the CTOD on the visible surface of the sample, from the recorded images, as shown in **Fig. 38**.

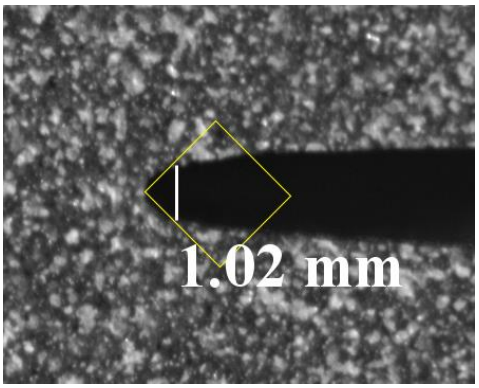

Fig. 38. *Example of a crack tip opening displacement (CTOD) measurement at the 90º interception.*

From measured CTOD, the corresponding pseudo CTOD, δ^R, values were determined using the convolution integral

$$\delta^{\mathrm{R}} = E_R^{-1} \int_0^t E(t-\tau) \frac{\partial \delta}{\partial \tau} \mathrm{d}\tau \tag{82}$$

Critical CTOD, δ_c, and pseudo critical CTOD, δ_c^R, have been identified for the initiation of the crack propagation. Analogously to the J resistance curves, CTOD resistance curves have been determined in terms of $\delta - \Delta a$ and $\delta^R - \Delta a$. Besides, experimental curves were fitted to a power law relation as

$$\delta = C_1' \Delta a^{C_2'} \tag{83}$$

or

$$\delta^R = C_1' \Delta a^{C_2'} \tag{84}$$

where C_1' and C_2' are material constants and $C_2' \leq 1$.

4.4.3.3. Determination of the η factor

To obtain the η factor, which is used in the calculation of the J integral, the procedure described in 2.4.4 has been followed. Firstly, displacement records, u, have been transformed to pseudo displacements, u^R, making use of (46) particularizing for a reference modulus as the relaxation modulus for $t = 0$, E_0, being the case of a constant displacement rate.

Once obtained the pseudo displacements, u^R, the plastic displacements are renamed as non-linear displacements. This change in the nomenclature is motivated by the fact that plastic deformation is not found after the propellant is strained up to the rupture. Here, the non-linearity shown in the load vs pseudo displacement rather occurs due to the induced dewetting and damage during the loading process, rather than plastic deformations occurring. The non-linear behaviour of the matrix is also contributing to the nonlinearity presented by the propellant. Subsequently, the non-linear pseudo displacements, u_{nl}^R, are determined through:

$$u_{nl}^R = u^R - C^R P \tag{85}$$

where C^R is the flexibility of the elastic reference sample, i.e., the inverse of the initial slope of the load versus pseudo displacement curve, obtained through a linear regression, and P is the load. Then, one of the load versus non-linear pseudo displacement curves is chosen as the reference curve, corresponding to the sample with crack length a_j. The rest of the curves for specimens with crack lengths a_i are divided by the reference curve to obtain the separation parameter S_{ij} for each specimen. The S_{ij} versus non-linear pseudo displacement curves must display a constant value. These values for each specimen are then used in (60) to obtain η_{nl} factor through a least squares fitting. Here, $\eta_{nl} = \eta$ since it is recommended to use an overall, rather than split into elastic and non-linear if the behaviour is neither fully elastic nor plastic (Turner, 1980), so that both η_{pl} and η_{el} can be assumed equal (Ernst et al., 1981).

Parallelepipedal samples with the same geometry as the fracture samples, with dimensions of 70x12.5x25 mm, were prepared. Notches with different lengths were used instead of cracks to extend the displacement range of non-linear phenomena development before crack propagation. Therefore, the regime in which S_{ij} is maintained constant is larger and η factor can be calculated more precisely. Notches were introduced by firstly drilling a hole with 2 mm in diameter using a milling machine, cf. **Fig. 39**. The crack was then inserted,

sliding a razor blade through one side of the specimen till reaching the hole. Samples with notch lengths of 9.1, 10, 12.5, 15 and 17.5 mm, giving a/W ratios of 0.364, 0.4, 0.5, 0.6 and 0.7, respectively, were manufactured.

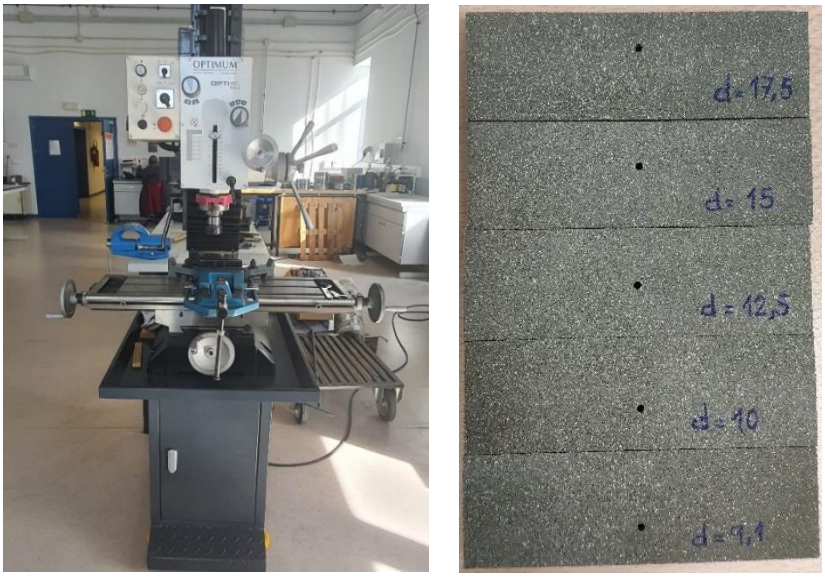

(a) (b)

Fig. 39*. Preparation of notched samples (a) milling machine used for the drilling of notched samples, and (b) notched samples with a hole.*

Preparation of the samples with tabs was also necessary, as previously described. Testing conditions were the same as the used for fracture tests, so that tests were carried out at room temperature with a crosshead displacement rate of 5 mm/min. Since the crack must remain stationary, tests were recorded to observe the instant of the initiation of the crack propagation. To do so, the VIC2D equipment was used.

The determined η factor was employed in both preliminary and ageing characterisations. It has been assumed that η is only dependent on geometry, not on material properties (Torabizadeh et al., 2019) and has been considered constant during the crack advancement in the fracture tests.

4.4.4. Fractographic characterisation

The fracture surfaces of the tensile and fracture specimens were analysed via scanning electron microscopy (SEM). The aim of this fractographic analysis was the identification of the mechanisms that lead to the crack formation and growth, as a consequence of the strain rate or ageing agent. HitachiS-3400 N microscope was used for the fractographic analysis. Fracture surfaces were prepared with a coating of gold made with a Emitech K550X Sputter Coater, cf. **Fig. 40**.

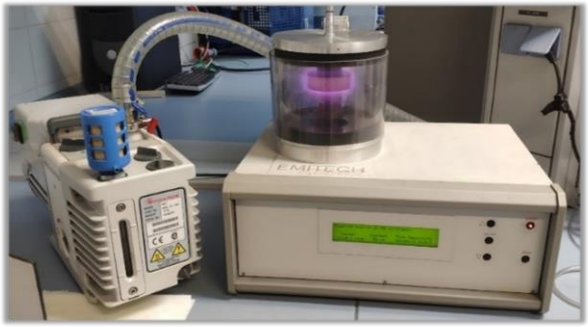

***Fig. 40**. Metallisation of the fracture surfaces set-up. Sputtering coating machine Emitech K550X.*

Chapter 5.Results

5.1. PROPELLANT PRELIMINARY CHARACTERISATION

Although the effect of the temperature and the strain rate on the mechanical behaviour of composite solid propellants is relatively well known, it was necessary to complete an initial experimental campaign to ascertain the influence of the strain rate on the mechanical and fracture performance of the carboxyl-terminated polybutadiene propellant under study. It is recalled that booster propellant from a first rocket motor was employed for this preliminary characterisation.

The results of this experimental programme will be described in the subsequent subsections. Firstly, the time dependent response is analysed, followed by the tensile and fracture behaviours.

5.1.1. Time dependent response

The experimental stress, σ, vs time, t, relaxation curves for the two specimens tested are shown in **Fig. 41**a. Since these tests were performed in a DMA Q800, data during the loading ramp was not able to be recorded, as it can be appreciated in **Fig. 41**. The computed average curve and the result of the fit according to (72) are plotted in **Fig. 41**b. A reasonable agreement is found for the fit. The resulting fitting parameters are gathered in **Table 7**.

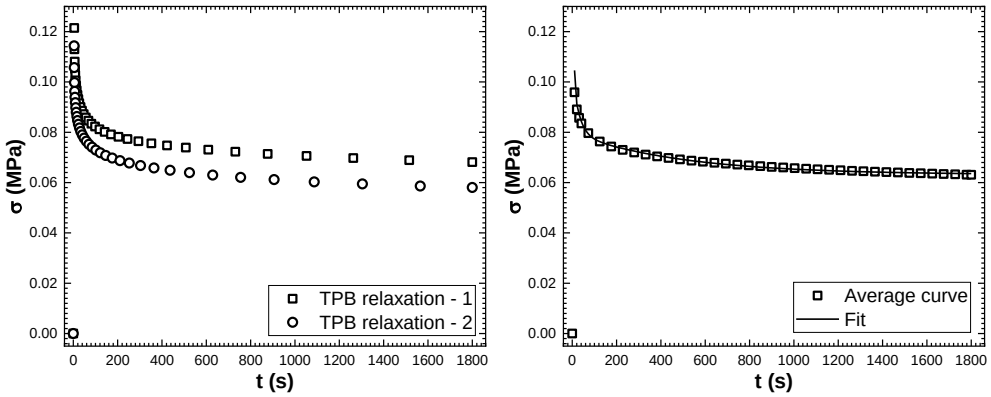

***Fig. 41**. Experimental stress relaxation curves from the preliminary characterization. (a) Experimental curves. (b) Average curve and fit to the average curve.*

As observed in **Fig. 41**, the relaxation process is emphasized in a very sudden relaxation followed by a moderate relaxation up to the end of the test. Note that the relaxation modulus drops from E_0, which is the initial modulus corresponding to the relaxation modulus at time $t = 0$, to a 50% close to the E_∞ in approximately 280 s, cf. **Table 7**.Relaxation occurs due to the mobility of the polymeric chains. It was found that fast relaxation corresponded to the lack of mobility of the segments close to cross-links and particles, intermediate relaxation times are related to the mobility of chains linked at the ends of the backbone and the long-term response to the presence of plasticiser and segments with high mobility (Azoug et al., 2015).

Table 7*. Resulting parameters of the Prony series(65) from the fitting of the average stress vs time of the preliminary relaxation characterisation.*

Modulus (MPa)		Relaxation time (s)	
E_0	9.65		
E_∞	4.21		
E_1	2.97	τ_1	1.82
E_2	1.40	τ_2	28.5
E_3	1.08	τ_3	500

5.1.2. Tensile behaviour

5.1.2.1. Stress-strain curves

The experimental true stress, σ, versus true strain, ε, curves in true magnitudes for 5, 50 and 500 mm/min crosshead speeds are shown in **Fig. 42**a and the corresponding curve for pseudo strains, ε^R, in **Fig. 42**b. If the raw curves are analysed, the strain rate effect is clearly visible, resulting in an increase of the stiffness and maximum stress and strain. When the viscous behaviour is corrected using the corresponding hereditary relation in **Table 6**, all the curves completely overlap. Therefore, the maximum stress and strain are the most severely affected characteristics by the strain rate. One of the two main differences found between the tensile response of the propellant for the different

strain rates is the deflection of the curve after the initial elastic slope happening for the highest strain rate. As it will be discussed later, this defection is linked to a change in the microstructural damage process. The other identified difference is the stress and strain at the maximum of the curve in both $\sigma - \varepsilon$ and $\sigma - \varepsilon^R$ curves, where they both increase with increasing crosshead displacement rate.

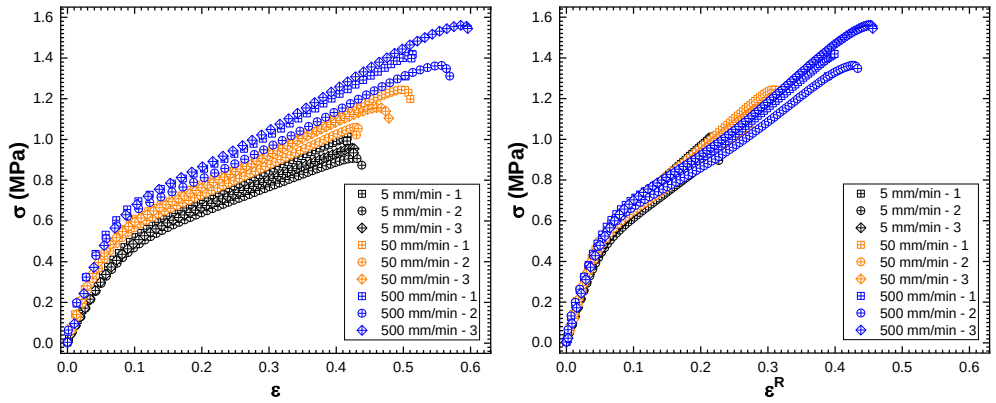

(a) (b)

Fig. 42. Experimental stress, σ, versus strain, ε, curves in true magnitudes for the preliminary characterisation in terms of (a) true strains, and (b) pseudo true strains.

The role of the election of the reference modulus is displayed in **Fig. 43**, where in addition to the actual stress versus strain curves for all displacement rates, it is included a grey envelope corresponding to the stress versus pseudo strain obtained using a reference modulus, E_R, equal to the instantaneous modulus, E_0, (**Fig. 43**a) and to the equilibrium modulus, E_∞, (**Fig. 43**b).

As seen, pseudo curves are close to the non-corrected ones for higher strain rates when $E_R = E_0$ (**Fig. 43**a), while pseudo curves are close to the curves at lower strain rates when $E_R = E_\infty$ (**Fig. 43**b). In the present work, the results related to pseudo variables will be determined using $E_R = E_0$ having the unrelaxed body behaviour as benchmark.

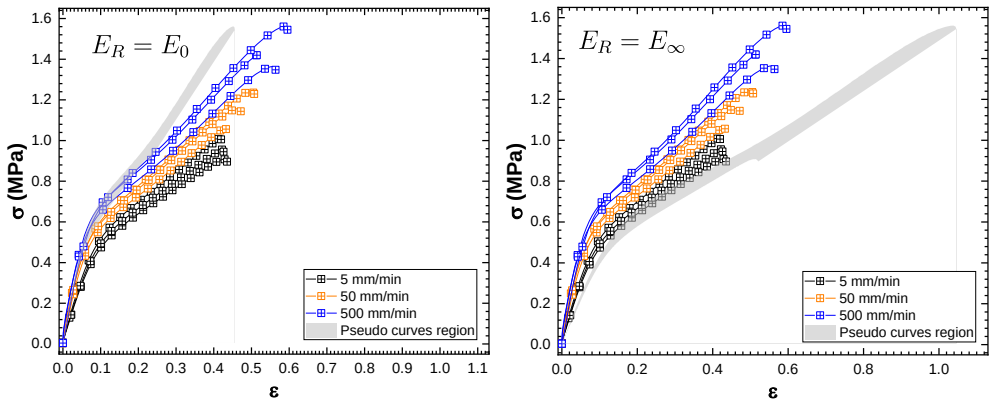

***Fig. 43**. True stress, σ, versus (pseudo) true strain, (ε^R) ε, curves from tensile samples tested at 5, 50 and 500 mm/min for the preliminary characterisation. Region occupied by the stress versus pseudo strain curves shaded in grey. (a) Pseudo strains determined with $E_R = E_0$, and (b) pseudo strains determined with $E_R = E_\infty$.*

Characteristic parameters from the uniaxial stress versus strain curves presented in **Fig. 42**, such as the apparent elastic modulus E, stress at maximum σ_{max} and strain at maximum ε_{max}, are collected in **Table 8**.

***Table 8**. Uniaxial stress versus strain characteristics for the preliminary characterisation. Apparent elastic modulus E, stress at maximum, σ_{max}, and strain at maximum, ε_{max}. Parameters obtained from stress versus pseudo strain curves are denoted with superscript R.*

Crosshead speed (mm/min)	E (MPa)	E^R (MPa)	σ_{max} (MPa)	ε_{max}	ε^R_{max}
5	6.3±0.5	10±1	0.96±0.05	0.42±0.01	0.22±0.01
50	9.3±0.6	12±1	1.15±0.09	0.46±0.03	0.29±0.02
500	10.4±0.5	12±1	1.45±0.10	0.55±0.04	0.42±0.03

The apparent elastic modulus, determined for strains lower than 3%, shows a strong dependence on the strain rate, obtaining a stiffer behaviour as the strain rate increases, with a 70.5% increase of the modulus from the lowest to the highest strain rate. As previously mentioned, σ_{max} and ε_{max} also increase when rising the strain rate, i.e., enhancing the mechanical capability of the material with 51% stress and 31% strain increments. Results are in line with the found in the literature for CTPB (Brzić et al., 2015) and similar hydroxyl-

terminated polybutadiene (HTPB) propellant (Wang et al., 2015; van Ramshorst et al., 2016; Wang et al., 2023c).

Considering the stress versus pseudo strain curves, whose corresponding characteristic parameters are also collected in **Table 8**, the pseudo strain at maximum, ε_{max}^{R}, follows the same trend as ε_{max}, while the pseudo apparent elastic modulus, E^{R}, is rate-independent. Note that E^{R} is not exactly $E_R = E_0$, but rather slightly higher.

5.1.2.2. Strains analysis

The strain and stress at the determined dewetting point, ε_{dew} and σ_{dew}, are collected in **Table 9**, together with the corresponding dewetting pseudo strain, ε_{dew}^{R}. The stress at the dewetting point, σ_{dew}, shows a similar trend as the stress at maximum, particularly with an increase of ≈20%. However, results are different considering ε_{dew} and ε_{dew}^{R}. The dewetting strain decreases from ≈6.4% at the lowest strain rate down to ≈4.6% at the highest strain rate, whereas the dewetting pseudo strain increases from ≈3.8% up to ≈4.3%.

***Table 9**. Dewetting true viscoelastic, ε, and pseudo, ε^{R}, strains and corresponding dewetting stress, σ_{dew}, at 5, 50 and 500 mm/min for the preliminary characterisation.*

Crosshead speed (mm/min)	ε_{dew}	ε_{dew}^{R}	σ_{dew} (MPa)
5	0.064 ± 0.003	0.038 ± 0.001	0.37 ± 0.03
50	0.052 ± 0.006	0.040 ± 0.004	0.42 ± 0.02
500	0.046 ± 0.003	0.043 ± 0.003	0.45 ± 0.03

Strains determined through digital image correlation allowed the determination of the initial Poisson's ratio, ν_0, and corresponding Poisson's ratio of the reference elastic bodies, ν_0^{R}, using pseudo strains in (76). The results are gathered in **Table 10**.

The obtained results show an initial value of the initial Poisson's ratio close to 0.5 for the specimens tested at the two lowest strain rates and 0.5 for the highest strain rate, a sign of incompressibility at the beginning of the test.

These results are in line with the literature (Shekhar et al., 2010). Therefore, little dependence on strain rate is considered, in line with the results obtained by Liu and Thompson (Liu et al., 2015) in cylindrical specimens. It is noted that ν_0 is independent with respect to the strains used (raw or pseudo).

Table 10*. Initial Poisson's ratio ν_0 at 5, 50 and 500 mm/min in the viscoelastic and the equivalent elastic reference bodies for the preliminary characterisation.*

Crosshead speed (mm/min)	ν_0	ν_0^R
5	0.47 ± 0.02	0.47 ± 0.02
50	0.47 ± 0.03	0.47 ± 0.04
500	0.50 ± 0.03	0.50 ± 0.03

The evolution of the Poisson's ratio, ν, and the pseudo Poisson's ratio obtained from the pseudo transverse and longitudinal strains, ν^R, with the applied longitudinal strain, ε_l, for all strain rates is shown in **Fig. 44**. Solid symbols are used to depict the determined dewetting point at the corresponding ε_{dew}. It is appreciated that the Poisson's ratio evolves in two different regions before and after the dewetting point. The first one consists in a decay of the ratio from a constant initial value in an undefined form until the dewetting strain. The second one, which comes after the dewetting strain, consists also in a reduction of the ratio with the particularity that has a form of an exponential decay.

The preceding behaviour has not been found to be reported in the literature. The way it is addressed implies some approximations, e.g., bilinear models (Landel et al., 1961; Shekhar et al., 2010, 2011), exponential decay from the very beginning of the test (James Buswell, 1975) or other type of relations (Stedry et al., 1961; Wu-jun et al., 2012).

The evolution of the Poisson's ratio with applied strain in **Fig. 44** is one way to represent the evolution of the induced damage or dewetting into the sample. This implies that, as strain is applied, the Poisson's ratio decreases and, therefore, more particles are dewetted, more interface surface is dewetted and voids grow.

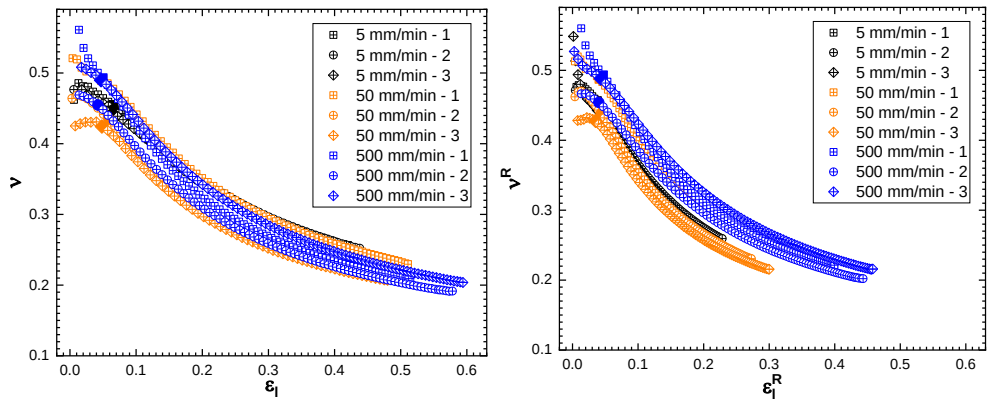

(a) (b)

Fig. 44*. (Pseudo) Poisson's ratio, (ν^R) ν, versus longitudinal strain from tensile tests at 5, 50 and 500 mm/min for the preliminary characterisation in terms of (a) true strains, ε_l, and (b) pseudo true strains, ε_l^R. Solid symbols indicate the corresponding dewetting point.*

The dilatation or volume change for the applied strain represent an alternative representation to explain the damage evolution during the loading. Dilatation, V/V_0, determined through (78) versus the applied longitudinal strain, ε_l, is shown for all the strain rates in **Fig. 45**.

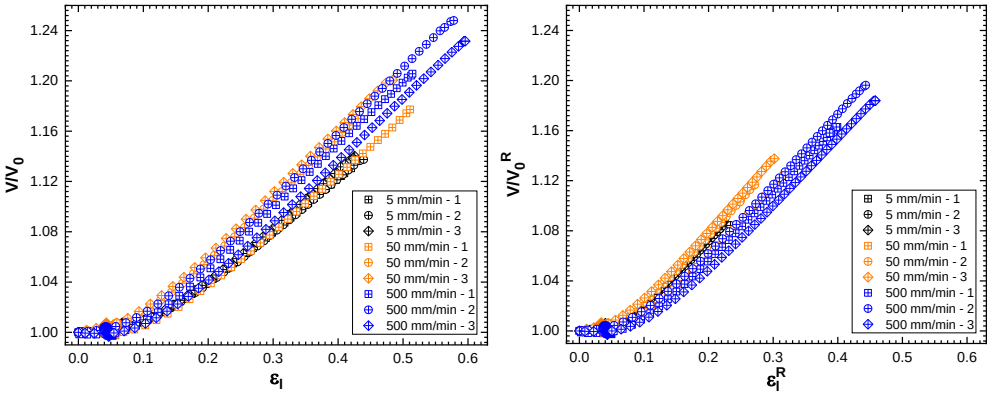

(a) (b)

Fig. 45*. Dilatation, V/V_0, versus longitudinal strain, ε_l, from tensile tests at 5, 50 and 500 mm/min for the preliminary characterisation in terms of (a) V/V_0 and ε_l, (b) $V/V_0{}^R$ and ε_l^R. Solid symbols indicate the corresponding dewetting point.*

The obtained results are in line with those determined using Farris's gas dilatometer by R. Nevière (Nevière, 2006). It is observed that the propellant's dilatation is produced in three stages. The first one where no dilatation is

produced, being the beginning of the tensile test. The following stage consisting in a growth of the dilatation linked to initiation of the dewetting (Nevière, 2006). Finally, during the last stage, the dilatation varies linearly with applied longitudinal strain up to the rupture. This last stage is associated to the growth of generated voids. Taken the strain rate into consideration, it is noted that samples tested at 50 and 500 mm/min undergoes a greater dilatation than the ones tested at 5 mm/min, although no differences are found between 50 and 500 mm/min.

5.1.3. Fracture behaviour

5.1.3.1. Determination of the η factor

The load, P, versus pseudo displacement, u^R, curves for the notched specimens are displayed in **Fig. 46** up to the observed crack initiation to ensure that notches remain stationary. Pseudo displacements are determined using (46). As expected, a longer crack results in a mechanical response with greater compliance.

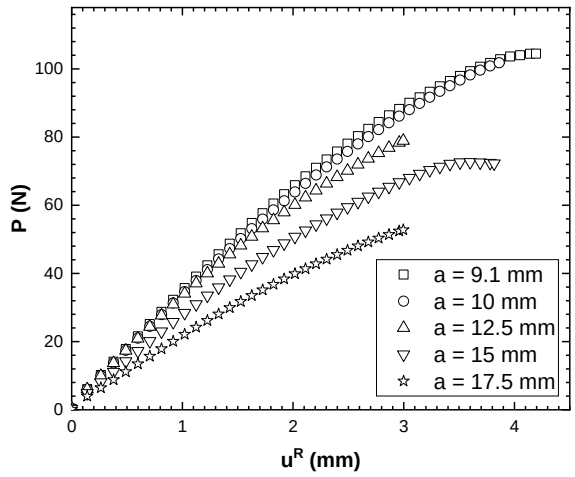

Fig. 46*. Load, P, versus pseudo displacement, u^R, curves prior to crack propagation initiation for notched specimens with notch lengths of 9.1, 10, 12.5, 15 and 17.5 mm.*

The resultant load, P, versus non-linear pseudo displacement, u_{nl}^R, curves obtained through (85) are shown in **Fig. 47**.

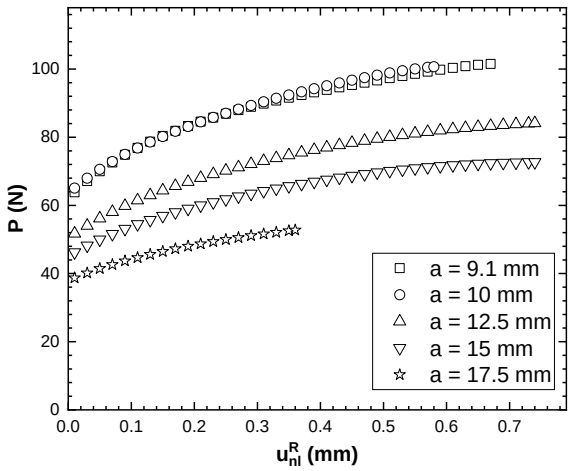

Fig. 47. Load, P, versus non-linear pseudo displacement, u^R_{nl}, for notched specimens with notch lengths of 9.1, 10, 12.5, 15 and 17.5 mm.

The subsequent S_{ij} separation parameter versus non-linear pseudo displacement, u^R_{nl}, for each pair of samples is displayed in **Fig. 48**, using as the reference sample the one with $a_j = 9.1$ mm. Constant values of S_{ij} are achieved for almost the entire range of non-linear pseudo displacement, meaning that separation principle works in the equivalent problem and, therefore, it is suitable to determine the η factor for composite solid propellants.

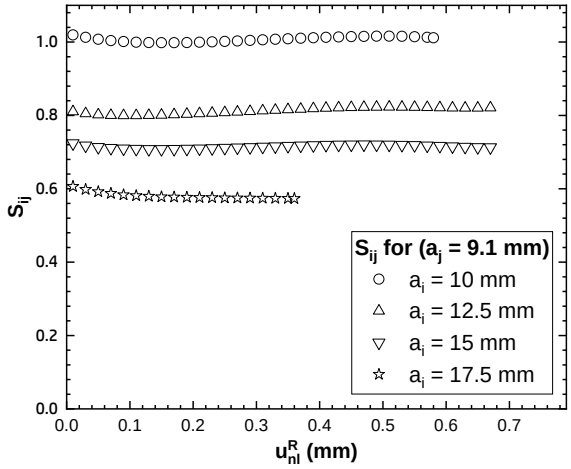

Fig. 48. S_{ij} separation parameter versus non-linear pseudo displacement, u^R_{nl}, with respect to the a_j of 9.1 mm notched sample for notched specimens with notch lengths a_i of 10, 12.5, 15 and 17.5 mm.

The values of the S_{ij} parameter are plotted against b_i/W in a double logarithmic scale in **Fig. 49**. The fitting of the data to (60) or its equivalent linear transformation shown in **Fig. 49** gives a value of $\eta_{nl} = 0.76$. As alluded to, here the difference between elastic and non-linear η factors is neglected, so $\eta = \eta_{nl} = 0.76$. Since this factor is supposed to be only dependent on geometry, it has been assumed equal for all the studied cases in this thesis and with constant value during crack growth.

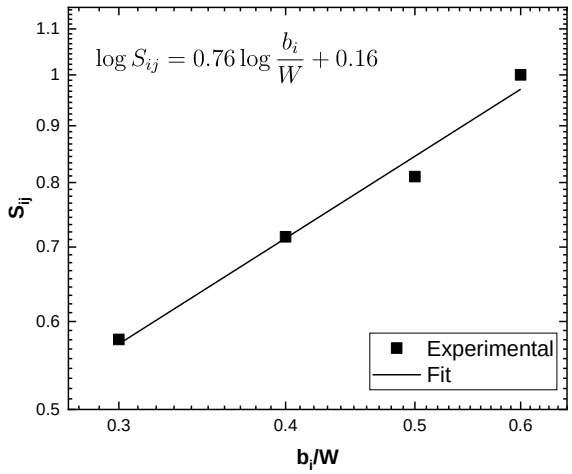

Fig. 49. S_{ij} separation parameter versus b_i/W ratio in double logarithmic scales and resulting fit to (60).

5.1.3.2. J resistance curves

The load, P, versus (pseudo) displacement, (u^R) u, curves from fracture tests at crosshead speeds of 0.5, 5, 50 and 500 mm/min are displayed in **Fig. 50**, where the solid symbols indicate crack growth initiation. The curves exhibit similar trends as those obtained from the tensile specimens. Increasing the displacement rate, the samples present a stiffer response and increase their fracture strength, ranging the load at crack growth initiation from ≈75 N to ≈140 N at the highest displacement rate.

Displacements at maximum and initiation of the crack's propagation experience both an increase as well, ranging the displacements at maximum from ≈6 mm to ≈9.5 mm and the displacements at the initiation of the crack's

propagation from ≈4 mm to ≈5.6 mm at the lowest and highest displacement rates, respectively. In other words, the maximum of the curves moves to the right and up with increasing displacement speed.

Moreover, it is remarkable that the load versus pseudo displacement curves in **Fig. 50**b overlapped for all strain rates with the only difference of the rupture, which takes place at a higher load and pseudo displacement with increasing crosshead displacement rate. This is a fact derived by the changes in the microstructural fracture process. These results, again, seem to find suitable Schapery's methodology in the characterisation of composite solid propellants based on the analogy of the reference elastic material.

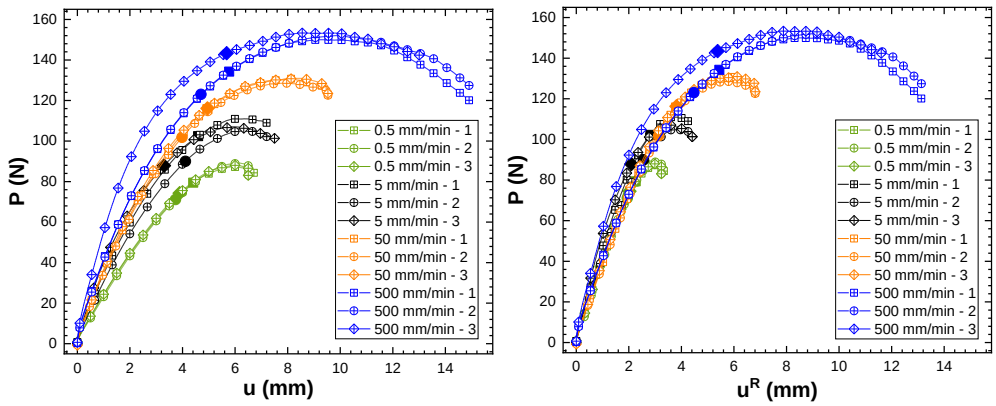

Fig. 50. Load, P, versus displacement, u, from fracture specimens tested at 0.5, 5, 50 and 500 mm/min for the preliminary characterisation in terms of (a) displacements u, and (b) pseudo displacements u^R. Solid symbols indicate crack growth initiation.

The resulting J resistance curves ($J - \Delta a$) from the fracture tests at all displacement rates are shown in **Fig. 51** for both J integral, J, and pseudo J integral, J^R. It can be clearly seen that (pseudo) J integral is affected by the strain rate, that is, given a certain crack growth, Δa, the energy required to create the new crack surface is greater when higher displacement rates are applied. Furthermore, a clear differentiation from specimens tested at different strain rates is seen for the $J^R - \Delta a$ curves.

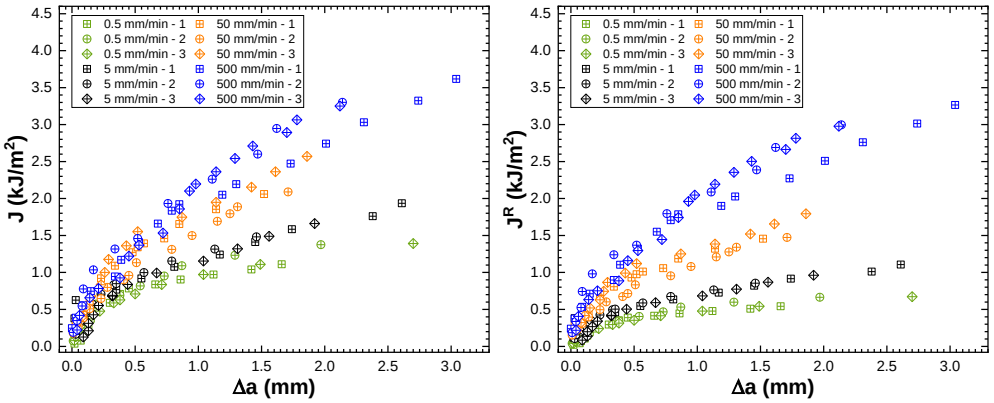

Fig. 51*. J resistance curves from fracture samples tested at 0.5, 5, 50 and 500 mm/min for the preliminary characterisation in terms of (a) J integral, J, and (b) pseudo J integral, J^R.*

The values of the J integral, J_c, and pseudo J integral, J_c^R, at the onset of the propagation of the crack are collected in **Table 11**. It is observed that both fracture parameters are influenced by the strain rate. The higher the displacement rate, the greater the energy at crack growth initiation, with around 70% and 300% increase for J_c and J_c^R, respectively. These results are in line with J_c in similar HTPB propellants (Kim et al., 2020; Wang et al., 2021, 2023b) This difference is found due to the fact that pseudo displacement at higher rates is less corrected than at lower displacements speeds. The blunting slope prior to the initiation of crack growth, also in **Table 11**, does not show a specific trend varying around 3 for $J - \Delta a$ curves and around 2 for $J^R - \Delta a$ curves for all displacement rates except for the highest of 500 mm/min, for which a notable increase is found. Indeed, the blunting slope does not vary for both, $J - \Delta a$ or $J^R - \Delta a$ curves, for the 500 mm/min displacement rate. This result implies that apparent crack growth due to the blunting of the crack front is smaller for the highest displacement rate and lesser viscous behaviour experienced.

The parameters resulting from the fitting of the curves in **Fig. 51** to the power law (80), C_1 and C_2 (from $J - \Delta a$ curves) and corresponding C_1^R and C_2^R (from $J^R - \Delta a$ curves), are also collected in **Table 11**. The C_1 and C_1^R parameters are in line with J_c and J_c^R giving a higher curve with increasing crosshead displacement rates. With respect to parameters C_2 and C_2^R, it is observed an

increase in their values with increasing crosshead speed, i.e., more stability in the fracture propagation is promoted.

Table 11. Blunting slope of the J-resistance curves, critical J integral, J_c, critical pseudo J integral, J_c^R, and parameters C_1 and C_2 and corresponding C_1^R and C_2^R obtained from the fitting of the J resistance curves to (80) with subsequent R^2 coefficient of the fracture specimens tested at 0.5, 5, 50 and 500 mm/min for the preliminary characterisation.

Crosshead speed (mm/min)	$J-\Delta a$ blunting slope	J_c (kJ/m²)	C_1	C_2	R^2
$J-\Delta a$ curves					
0.5	2.7±0.1	0.7±0.1	0.99±0.08	0.37±0.05	0.97±0.02
5	3.3±0.6	0.9±0.2	1.22±0.04	0.45±0.05	0.993±0.004
50	2.9±0.4	1.2±0.1	1.7±0.2	0.47±0.09	0.98±0.01
500	4±1	1.9±0.5	2.1±0.1	0.57±0.07	0.983±0.005
$J^R-\Delta a$ curves					
0.5	1.3±0.1	0.33±0.05	0.48±0.04	0.37±0.03	0.97±0.02
5	2.0±0.4	0.5±0.1	0.71±0.02	0.42±0.05	0.994±0.004
50	2.1±0.3	0.9±0.1	1.2±0.1	0.45±0.07	0.99±0.01
500	4±1	1.7±0.4	1.9±0.1	0.55±0.07	0.984±0.002

5.1.3.3. CTOD resistance curves

The measured CTOD, δ, resistance curves and computed pseudo CTOD, δ^R, resistance curves are shown in **Fig. 52**. As expected, CTOD resistance curves exhibit a similar trend as J resistance curves. Again, the use of the pseudo variable δ^R results in a better differentiation of the resistance curves for the different conditions.

The critical values of CTOD, δ_c, and pseudo CTOD, δ_c^R, at the onset of the propagation of the crack are collected in **Table 12**. These critical values increase with increasing displacement rate, as previously found for the critical J integral. Results are found in line to the reported in (Kim et al., 2020) for an HTPB propellant. Again, blunting slope is changes significantly for the highest displacement rate of 500 mm/min, being higher than the one for the lower

displacement rates. This means that higher local displacements at the crack tip are induced before crack growth initiates. The effect is observed for both, $\delta - \Delta a$ and $\delta^R - \Delta a$ curves.

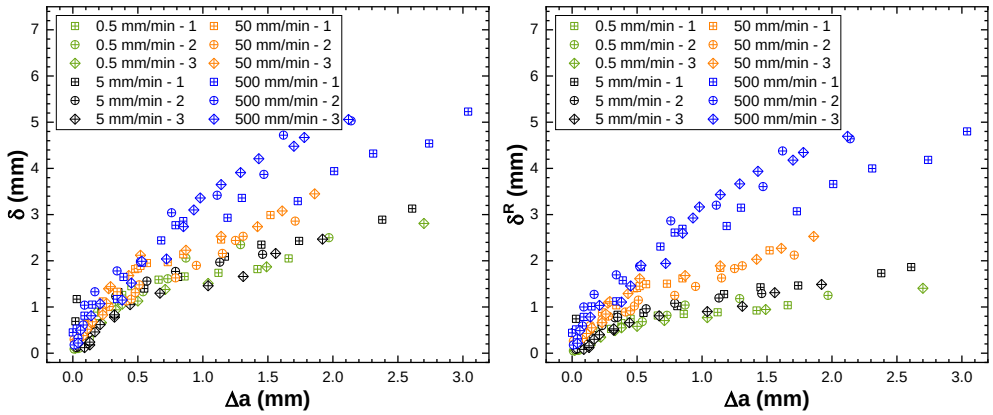

Fig. 52*. CTOD resistance curves from fracture samples tested at 0.5, 5, 50 and 500 mm/min for the preliminary characterisation in terms of (a) CTOD, δ, and (b) pseudo CTOD, δ^R.*

Table 12*. Critical CTOD, δ_c, critical pseudo CTOD, δ_c^R, and parameters C_1' and C_2' and corresponding $C_1'^R$ and $C_2'^R$ obtained from the fitting of the CTOD resistance curves to (83) with subsequent R^2 coefficient for the fracture specimens tested at 0.5, 5, 50 and 500 mm/min for the preliminary characterisation.*

Crosshead speed (mm/min)	$\delta - \Delta a$ blunting slope	δ_c (mm)	C_1'	C_2'	R^2
$\delta - \Delta a$ curves					
0.5	3.9±1.0	1.1±0.3	1.7±0.2	0.46±0.08	0.91±0.06
5	4.0±0.4	1.2±0.4	1.8±0.2	0.5±0.1	0.98±0.01
50	3.3±0.3	1.5±0.3	2.3±0.2	0.54±0.08	0.96±0.02
500	4.8±0.6	2.7±0.8	3.0±0.3	0.6±0.1	0.960±0.007
$\delta^R - \Delta a$ curves					
0.5	2.0±0.5	0.6±0.1	0.89±0.08	0.45±0.07	0.91±0.06
5	2.5±0.3	0.8±0.3	1.1±0.1	0.5±0.1	0.973±0.009
50	2.6±0.3	1.2±0.2	1.7±0.2	0.50±0.07	0.96±0.02
500	4.5±0.6	2.6±0.8	2.9±0.2	0.6±0.1	0.958±0.008

The parameters obtained from the fitting of the curves in **Fig. 52** to the power law (83), C_1' and C_2' (from $\delta - \Delta a$ curves) and corresponding $C_1'^{R}$ and $C_2'^{R}$ (from $\delta^R - \Delta a$ curves), are also collected in **Table 12**. The C_1' and $C_1'^{R}$ parameters follow the same trend shown by the critical CTOD values, increasing with the increasing displacement rate. It is also observed that C_2' and $C_2'^{R}$ slightly rise with increasing crosshead speed.

5.1.3.4. Micromechanisms of failure

The micromechanisms of failure in the fracture tests were analysed through the post-mortem observation of the fracture surfaces of the samples via SEM. The chosen images are gathered in **Fig. 53** for all the crosshead displacement rates and for three magnifications (x20, x50 and x200). Independently of the testing conditions, the primary fracture mechanism is the matrix tearing, that is, the crack propagates always though the matrix. Wang and coworkers (Wang et al., 2015) linked the temperature as the dominating factor in the changes of the fracture mechanism from matrix tearing and dewetting to the particles brittle fracture, while strain rate was only qualitatively affecting this mechanisms. Here, it is observed that by increasing the displacement rate, more cracks are induced in the matrix (pointed with arrows in **Fig. 53**) and it is also found that for higher displacement rates the promoted dewetting is greater, as can be seen in the images at x200 magnification where the surfaces of the oxidiser particles at lower rates are completely covered by the binder while those at the highest rate are completely free of matrix on their surface, also pointed with arrows in **Fig. 53**. The fracture surfaces are found rougher for higher displacement rates, which is related to the fact that at lower crosshead displacements, the crack propagation occurs through the matrix, while at higher displacement rates the cracks also propagate through the matrix-particle interface. No fracture of the particles was observed, in line with (Wang et al., 2015). Finally, the fractographic analysis is also in agreement with the values of the fracture parameters, cf. **Table 11**. The higher the displacement rate,

the rougher the fracture surface, the greater the energy at crack growth initiation and the stiffer the J resistance curves during crack propagation.

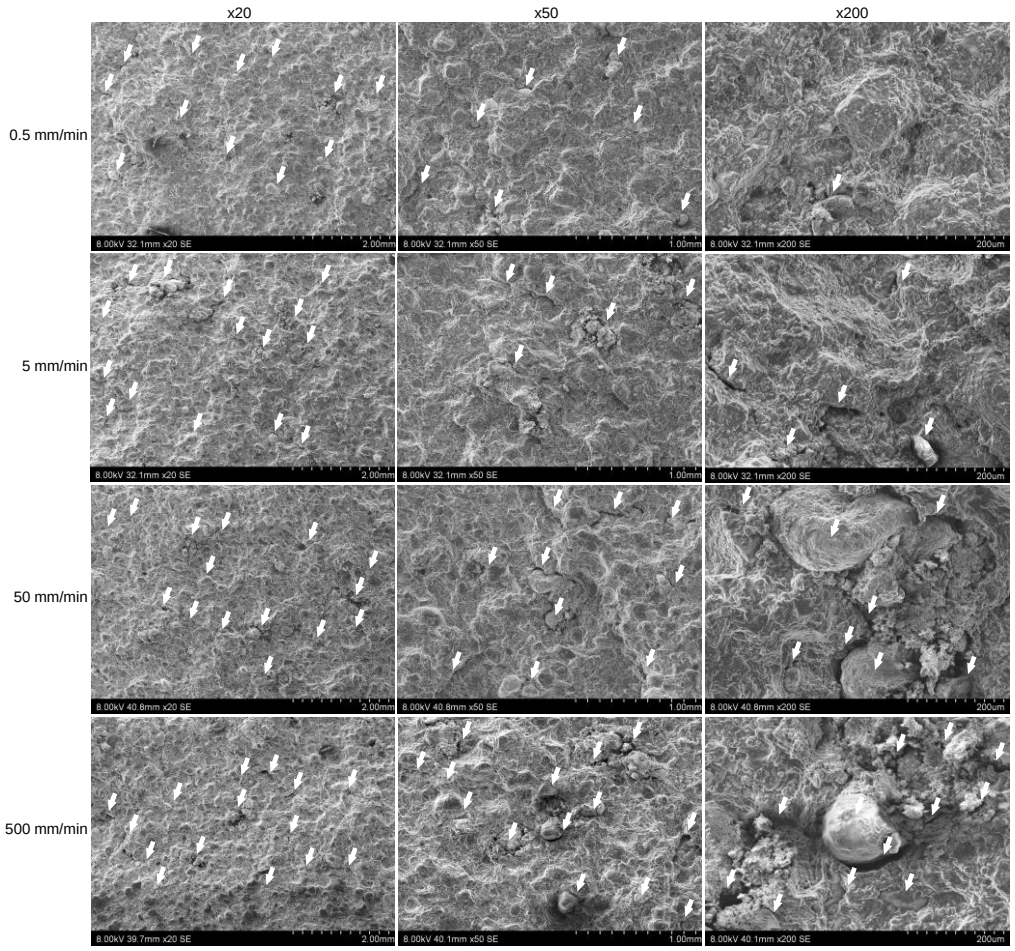

***Fig. 53**. SEM micrographs of the fracture surfaces from fracture samples tested at 0.5, 5, 50 and 500 mm/min crosshead displacement rates and x20, x50 and x200 magnifications for the preliminary characterisation. Cracks and dewetted surfaces are pointed with white arrows.*

5.2. Propellant ageing characterisation

This section is concerned to the secondary characterisation campaign which was focused on the behaviour of the CTPB composite propellant subjected to different ageing sources: mechanical strain, temperature and ozone.

In the next sections, first, the relaxation behaviour will be addressed, followed by the tensile and fracture characterisations, respectively.

5.2.1. Effects of the ageing sources on the crosslink density

The soluble fraction S was used to determine the crosslink density CLD according to (62) and (63). The results for all ageing conditions are collected in **Table 13**. To begin with, the mechanically aged samples do not experience a change in their crosslink density at any prestrain level. Consequently, the microstructural changes due to the applied strain should be linked to the strain induced dewetting, as observed in **Fig. 53** for the employed prestrain condition (500 mm/min crosshead displacement rate).

As expected, the thermal ageing process results in a rise of crosslinks in the elastomeric binder, which increases with the ageing time. This well-known change is produced due to the high temperature curing of the polymer. The effect was physically manifested in a slight shrinkage of the samples' sizes.

With respect to the ozone aged samples, the crosslink density decreases with higher ageing times. This effect was in line with the resulting shortening of the chains due to the ozonolysis reactions between polymeric binder and ozone.

***Table 13**. Soluble fraction content, S, and crosslink density, CLD, for all the ageing procedures.*

Ageing source	S	CLD
Pristine	0.066 ± 0.002	4.83 ± 0.09
Prestrain 15%	0.066 ± 0.001	4.85 ± 0.06
Prestrain 30%	0.0667 ± 0.0004	4.81 ± 0.02
Temperature 24 days	0.063 ± 0.004	5.0 ± 0.2
Temperature 36 days	0.050 ± 0.003	6.0 ± 0.2
Ozone 14 days	0.076 ± 0.001	4.35 ± 0.02
Ozone 21 days	0.079 ± 0.003	4.2 ± 0.1
Ozone 32 days	0.103 ± 0.002	3.33 ± 0.04
Ozone 42 days	0.106 ± 0.004	3.3 ± 0.1

Some changes in the microstructure were visible at a macro level as in the case of a sample of propellant subjected to ozone ageing for ca. 3 months. As observed in **Fig. 54** , when the time of exposure to the employed ozone concentration is extremely long, the material becomes powdery. This might result in a loss of mechanical capability as it will be addressed in the following sections. Moreover, the paper over which the propellant was laying during the ozone ageing process was found wet, clear evidence that this exudate would correspond to migrated constituents, such as plasticisers. However, the results of gas chromatography–mass spectrometry were not concluding about the nature of the exudate.

Fig. 54*. Propellant material subjected to ozone ageing for a 3-month period.*

The ozone ageing affects the sample from the surface, which results in the generation of a powdery layer at the surface that advances inwards. Images of the propellant sample surface were taken during the ozone ageing process up to ageing time of 21 days, shown in **Fig. 55**. During the first four days of ageing, the formation of the powdery layer is obvious, where the dark dots on the surface are material parts where the damage was not already produced. After seven days of ageing time, it was observed that the powdery layer was completely formed, getting more fragile with ageing time with the appearance of cracks on the powdery surface.

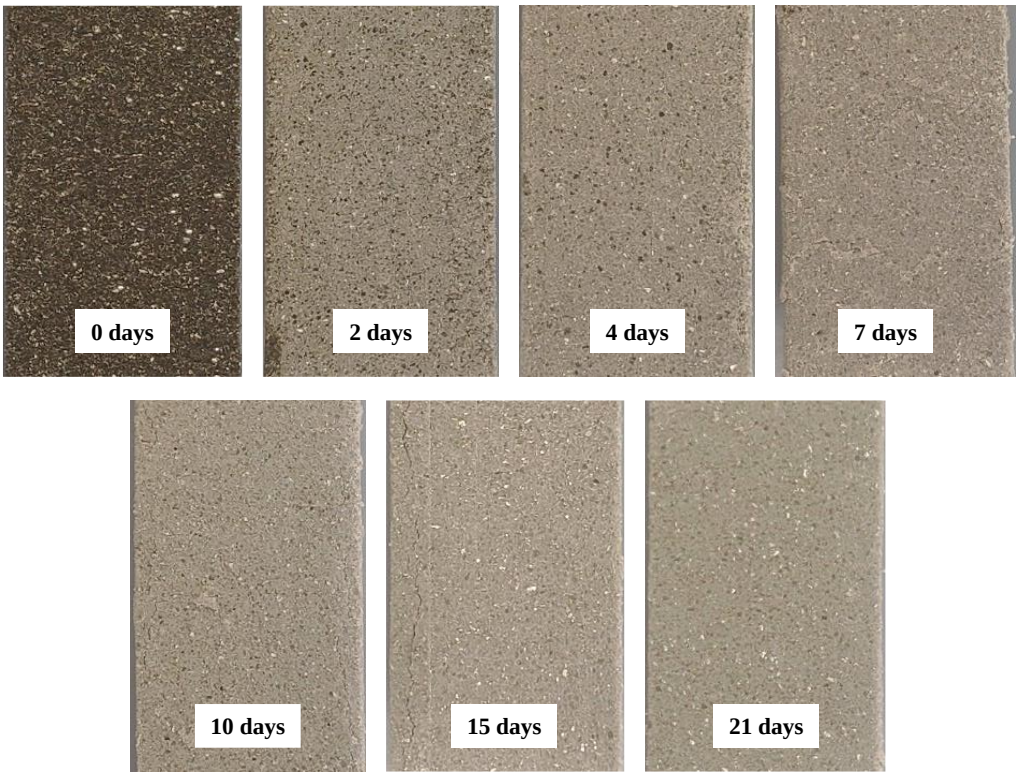

Fig. 55. Evolution of the propellant sample surface during the ozone ageing process up to 21 days of exposition to ozone.

5.2.2. Effects of the ageing sources on the time-dependent response

The experimental stress, σ, versus time, t, curves from stress relaxation tests for all ageing conditions, together with the non-aged or pristine specimens, are shown in **Fig. 56**. While 15% prestrained samples show a slight stress increase, almost overlapping the curves from the pristine samples, the 30% prestrained samples experiment a slight stress decrease, cf. **Fig. 56**a. However, these slight differences might be considered negligible.

Although tests for thermally aged samples were performed under lower applied strain, the curves are also plotted along the curves corresponding to the pristine samples in **Fig. 56**b. It can be easily seen that the stress versus time

response of thermally aged samples is clearly above the one of the pristine material.

The opposite effect is found for the ozone aged samples in **Fig. 56**c, where it is found a significant difference between the stress versus time curves of the aged samples with respect to the ones of the pristine material, being the curves of the aged samples far below the pristine ones. The difference between the different ageing times is smaller, but, assuming some scatter of the data, it can be seen that increasing ageing times lead to a greater reduction in the load bearing capacity directly correlated to lower stiffness values of the samples.

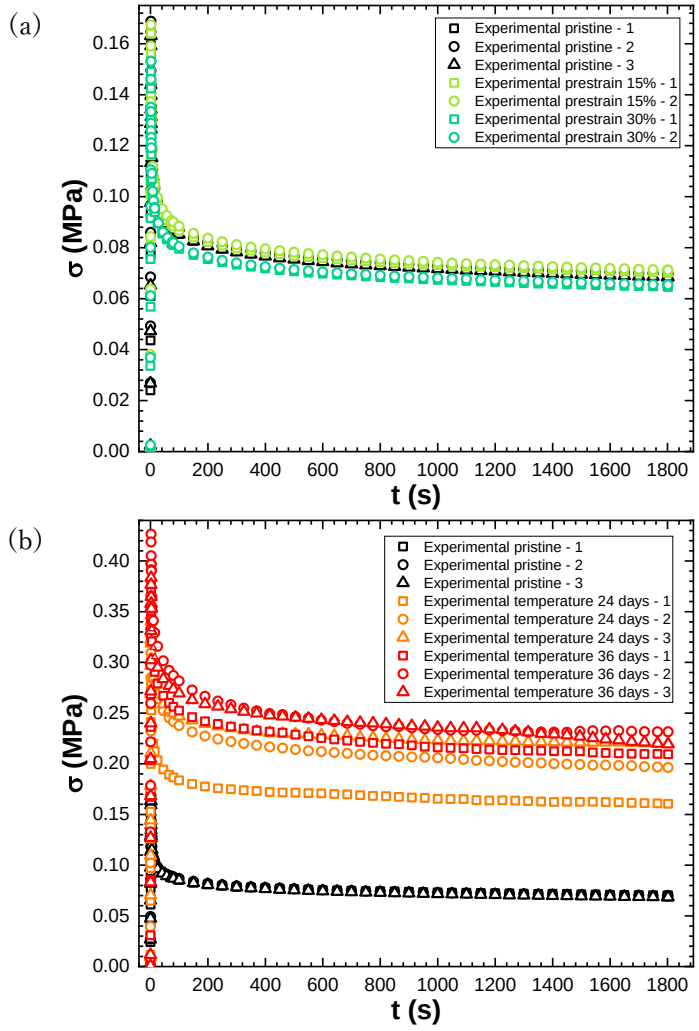

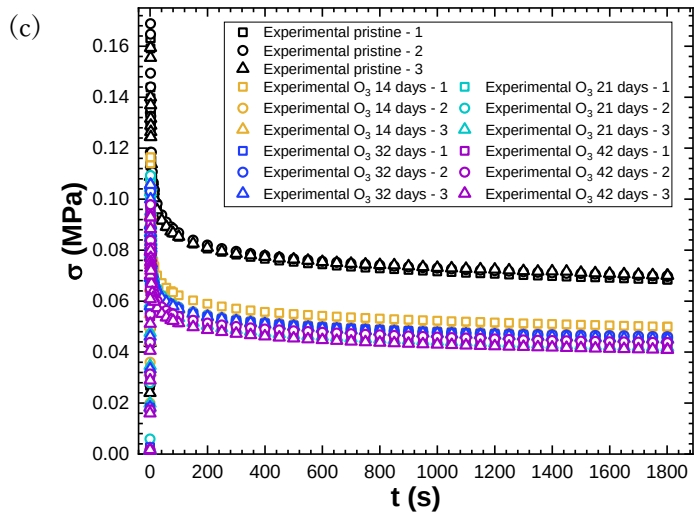

Fig. 56. Experimental stress, σ, versus time, t, curves from stress relaxation tests: (a) mechanical ageing at prestrains of 15% and 30%, (b) temperature ageing for 24 and 36 days, and (c) ozone ageing for 14, 21, 32 and 42 days. All plots include the results of the pristine propellant for comparison.

Data shown in **Fig. 56** was employed to determine the average experimental stress versus time curve for each condition. The resulting average experimental curves are displayed in **Fig. 57** together with their corresponding fit to (72). As it might be appreciated, the fit was found suitable for all the conditions.

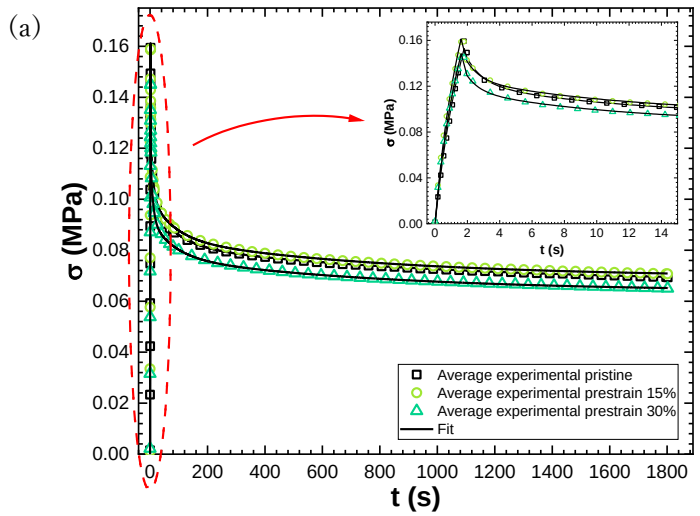

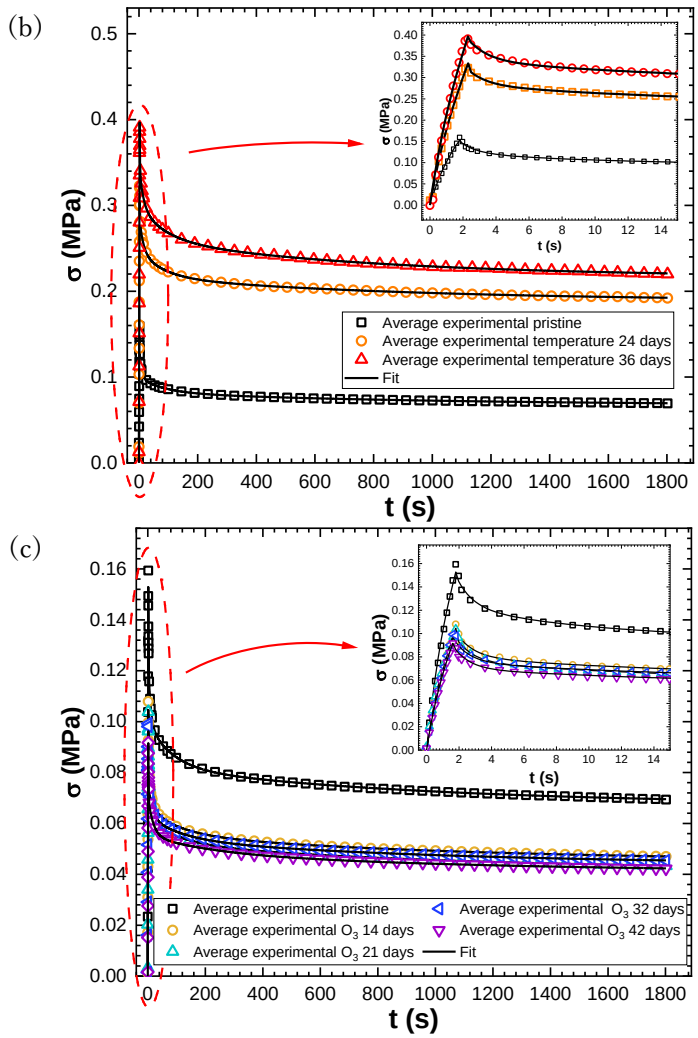

Fig. 57. *Average of the experimental stress, σ, versus time, t, curves from stress relaxation tests for each condition and its resulting fit to (72): (a) mechanical ageing at prestrains of 15% and 30%, (b) temperature ageing for 24 and 36 days. And (c) ozone ageing for 14, 21, 32 and 42 days. All plots include the results of the pristine propellant for comparison.*

The resulting fitting parameters for all ageing conditions are collected in **Table 14**. The focus will be placed on the instantaneous and equilibrium modulus, E_0 and E_∞, respectively, being E_0 the summation of all E_i.

With respect to the mechanically aged samples, the variation in the modulus is little in comparison with that of the pristine propellant. The observed trend is the same as explained for the experimental stress versus time curves,

with slight increase for 15% prestrain and slight decrease for 30% prestrain. This stiffer behaviour found for 15% prestrain was observed also for cycled samples at 10% strain with increasing number of cycles in (Aksel et al., 1996).

The thermal ageing process produces a severe increase in both modulus with higher ageing times, while a contrary effect occurred in the ozone ageing process with a reduction of the instantaneous modulus with higher ageing times. However, the equilibrium modulus seems to hold on to a threshold value, which is significantly lower than the equilibrium modulus of the pristine propellant.

Table 14*. Resulting parameters of the Prony series from the fitting of the average experimental stress vs time curves to (72) for all ageing conditions.*

	Ageing source								
	Pristine	Mech. Prestrain (%)		Temperature (days)		Ozone (days)			
		15	*30*	*24*	*36*	*14*	*21*	*32*	*42*
	Modulus (MPa)								
E_0	8.3	9.1	8.5	349	413	5.7	5.9	5.0	4.8
E_∞	2.2	2.3	2.1	126	144	1.5	1.4	1.5	1.4
E_1	6.0	6.7	6.3	0.35	265	4.2	4.4	3.5	3.4
E_2	0.13	0.11	0.11	220	3.17	0.04	0.05	0.04	0.03
E_3	0.0074	0.0064	0.0058	3	0.39	0.0033	0.0034	0.0025	0.001
E_4	0.0005	0.0006	0.0005	0.028	0.05	0.0004	0.0004	0.0003	0.0002
	Relaxation time (s)								
τ_1	0.97	0.83	0.81	80	1.19	1.02	0.98	0.96	0.96
τ_2	8.0	8.7	8.5	1.12	13.9	12.8	11.5	13.1	17.4
τ_3	83	80	80	13	89	108	100	115	211
τ_4	970	782	798	916	796	1033	1004	1027	1133

5.2.3. Effects of the ageing sources on the tensile behaviour

5.2.3.1. Stress-strain curves

The experimental true stress, σ, versus (pseudo) true strain, (ε^R) ε, curves for all ageing conditions are shown in **Fig. 58** to **Fig. 60**. In general, it is observed a marked reduction in the strains from actual strains to pseudo strains in ≈70% decrease. It has been also observed a strong dependence on the variation of the mechanical behaviour with respect of the state of the elastomeric binder.

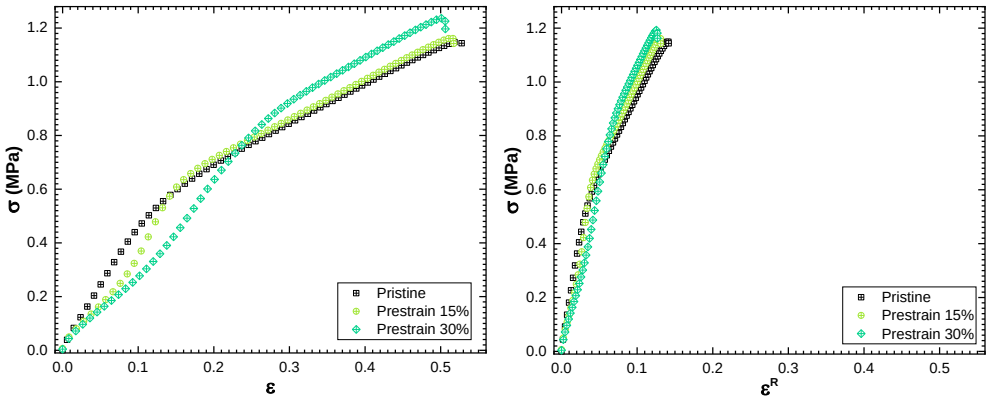

(a) (b)

***Fig. 58**. Experimental true stress, σ, versus true strain, ε, curves subjected to mechanical ageing for 15% and 30% in terms of (a) true strains, ε, and (b) pseudo true strains, ε^R.*

For the mechanically aged samples, it can be seen an ill-defined elastic region, characterised by a "stress softening" known as Mullin's effect, cf. **Fig. 58**. Gent (Gent, 2012) observed how the rubbers with high volume of particle fillers become somewhat thixotropic, that is, the elastic modulus reduces after straining, the more so the greater the previous applied strain, as in the response analysed in this study. This behaviour could be attributed to a breakdown of weak bonds between rubber molecules and filler particles, and at very small strains, between filler particles themselves or small changes in the crosslink density (Dannenberg et al., 1966), as addressed in section 5.2.1. It is also observed a slight hardening of the propellant (Diani et al., 2009). This was

already observed in previous research carried out with propellant from the first motor used in the preliminary characterisation, an extension to the research presented in (Martínez et al., 2022).

With respect to the thermally aged samples in **Fig. 59**, it is noted that the ageing process was so severe that the mechanical behaviour is completely changed. The propellant has exhibited a significant increment of its stiffness and tensile strength accompanied by a reduction in the elongation at break with increasing ageing times. This behaviour is consistent with the changes in the microstructure since the crosslinking induced by the temperature increases and so do the toughness and the brittleness.

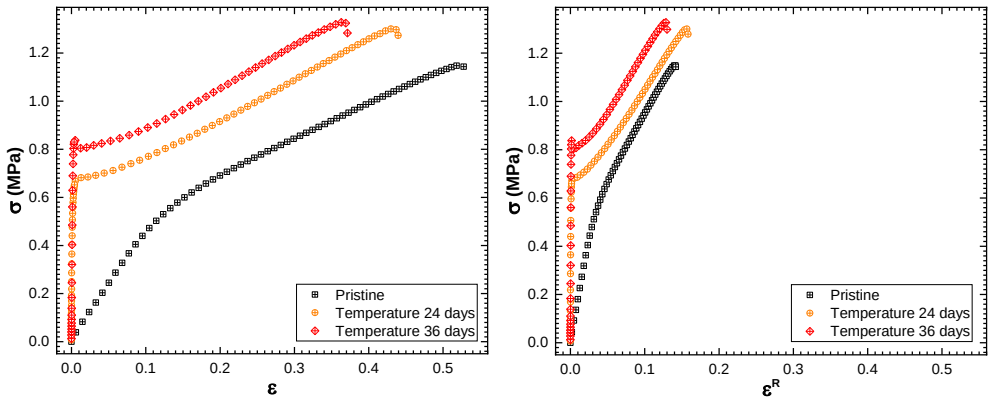

Fig. 59. Experimental true stress, σ, versus true strain, ε, curves subjected to thermal ageing for 24 and 36 days in terms of (a) true strains, ε, and (b) pseudo true strains, ε^R.

Regarding the ozone aged samples in **Fig. 60**, the sample aged for 14 days does not exhibit a different behaviour with regard to the pristine propellant. The sample aged for 42 days presents a clear lower load bearing capacity, that is, a significant reduction in the tensile strength, together with a relevant decrease in the stiffness. For both ageing times, it is identified an inflection in the elastic region. This fact evokes the behaviour presented by the prestrained samples. Therefore, it could be deduced that ozone is responsible for the damage of the matrix-particles bonds, as dewetting is produced by stretching. True strains, ε, for the specimen aged for 42 days were determined through

$$\varepsilon = \ln(1 + e) \tag{86}$$

where e is the engineering strain determined using a virtual extensometer placed in the stretching direction. This was due to the difficulties to use the DIC on the powdery layer. The true deformation values for 42 days of ozone ageing estimated by (86) are an approximation as incompressibility behaviour is far from reality for the composite under this sever ageing condition.

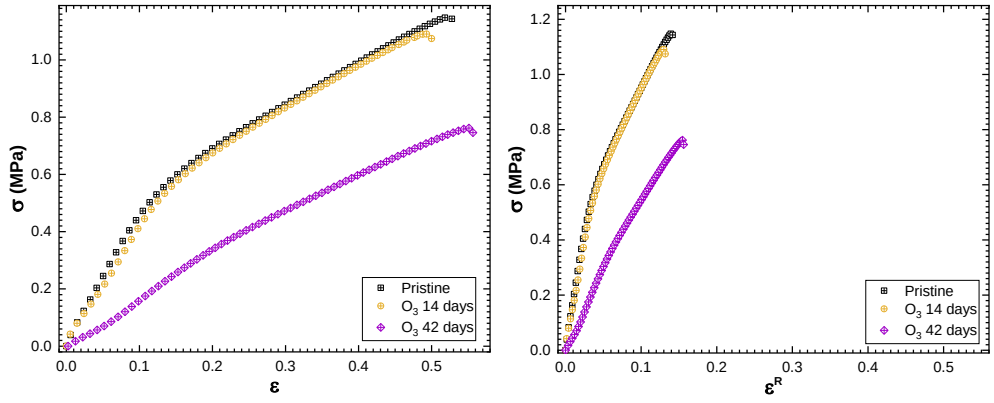

(e) (f)

Fig. 60*. Experimental true stress, σ, versus true strain, ε, curves subjected to ozone ageing for 14 and 42 days in terms of (a) true strains, ε, and (b) pseudo true strains, ε^R.*

The values of the characteristic parameters of the uniaxial stress versus strain curves in **Fig. 58** to **Fig. 60** are collected in **Table 15**. Mechanical ageing has a significant impact on the apparent elastic modulus, E, reducing it as much as ≈40% for the highest applied prestrain, related to the "stress softening" or Mullin's effect observed in the stress versus strain curves, which is in contrast with the determined relaxation functions that did not depict differences. The (pseudo) strain at maximum, (ε^R_{max}) ε_{max}, is slightly reduced while, the stress at maximum, σ_{max}, clearly increases from 1.15 MPa to 1.24 MPa for the 30% applied prestrain. The results

The thermally aged samples shown significant increases of E and σ_{max} and reduction in the ε_{max} and ε^R_{max}. The increase in the crosslinking density experienced by thermally aged samples is traduced in stiffer and less ductile material, with an increase of the stiffness of almost two orders of magnitude, a

reduction in ε_{max} of ≈30% and a rise of σ_{max} up to ≈16% for the longest ageing time of 36 days.

According to the ozone aged samples, the modulus E drops significantly to ≈70% reduction for the longest ageing time, similarly to σ_{max} experiencing a reduction of ≈30%, down to 0.76 MPa, while ε_{max} and ε_{max}^{R} do not vary significantly.

Again, the E^R determined through the $\sigma - \varepsilon^R$ curves do not match the reference modulus $E_R = E_0$, except for the case of ozone aged samples at 42 days.

***Table 15**. Uniaxial stress versus strain characteristics for all ageing conditions. Apparent elastic modulus E, stress at maximum, σ_{max}, and strain at maximum, ε_{max}. Parameters obtained from stress versus pseudo strain curves are denoted with superscript R.*

Ageing source	E (MPa)	E^R (MPa)	σ_{max} (MPa)	ε_{max}	ε_{max}^{R}
Pristine	5.9	19.4	1.15	0.52	0.14
Prestrain 15%	4.4	14.1	1.16	0.51	0.13
Prestrain 30%	4.1	13.5	1.24	0.50	0.13
Temperature 24 days	430	1043	1.3	0.43	0.15
Temperature 36 days	494	1232	1.33	0.36	0.13
Ozone 14 days	5.9	17.8	1.09	0.49	0.13
Ozone 42 days	1.7	5.2	0.76	0.55	0.16

5.2.3.2. Strains analysis

The strain and stress at the dewetting point, ε_{dew} and σ_{dew}, are collected in **Table 16**, together with the corresponding dewetting pseudo strain, ε_{dew}^{R}. Firstly, it is evident the abrupt drop of the ε_{dew}^{R} in comparison with the actual ε_{dew} independently of the ageing conditions. Secondly, as seen in the results for the pristine material, the propellant extracted from the second motor for the ageing characterisation presents a similar mechanical performance as the propellant extracted from the first motor for the preliminary characterisation, **Table 9**.

Regarding the variation of these parameters during the mechanical ageing, it is observed that both, (ε_{dew}^{R}) ε_{dew} and σ_{dew}, increase with prestrain level. It is important to highlight that the dewetting point is around the point where the stress versus strain curves reach the applied prestrain. This evidences that the "stress softening" observed in **Fig. 58** is due to the influence of the voids left by the rupture of bonds between particles and matrix during the prestrain process, while the stress-strain behaviour from the dewetting point is dominated by the new rupture of bonds.

The thermal ageing also produces an increase of the dewetting stress with increasing ageing time, increasing up to ≈84%. However, in this case the dewetting (pseudo) strain is reduced by ≈90%.

Regarding the ozone aged samples, the dewetting (pseudo) strain is slightly greater for longer ageing times in ≈15% as much, whereas the dewetting stress is notably reduced ≈60% with 42 days of ozone ageing.

***Table 16**. Dewetting strain, ε_{dew}, and pseudo strain, ε_{dew}^{R}, strains and corresponding dewetting stress, σ_{dew}, from true magnitudes for the ageing characterisation.*

Ageing source	σ_{dew} (MPa)	ε_{dew}	ε_{dew}^{R}
Pristine	0.44	0.096	0.026
Prestrain 15%	0.56	0.138	0.035
Prestrain 30%	0.85	0.267	0.067
Temperature 24 days	0.68	0.013	0.005
Temperature 36 days	0.81	0.008	0.003
Ozone 14 days	0.44	0.106	0.028
Ozone 42 days	0.18	0.112	0.031

Finally, analysing the variations among the different ageing phenomena, it is noticeable the small values of actual and pseudo strains in case of the thermal ageing and the high values for the ozone ageing condition in comparison with the pristine propellant. In turn, the dewetting stress for the thermal aged samples is higher than the virgin propellant and smaller for the material submitted to ozone ageing. This again can be explained in the light of the different

chemical modifications the matrix undergoes during the ageing process, as curing in case of the thermal ageing and decomposition during ozone ageing.

The initial Poisson's ratio, ν_0, and pseudo Poisson's ratio, ν_0^R, are shown in **Table 17**. As seen in **Table 10** from section 5.1.2.2, ν_0 and ν_0^R are equal for all ageing conditions. Mechanical ageing produces an increase of ν_0 up to ≈ 0.5. Such a result, linked to incompressibility, would mean that stress-strain response of the propellant is more reliant on the behaviour of the elastomeric matrix after the applied prestrain. This supports the idea that matrix-particle interfaces are damaged. The thermal ageing produces a significant reduction in the initial Poisson's ratio, down to 0.31 for the 36 days ageing time, while for 24 days of ageing it does not vary in comparison with pristine material. Considering the ozone ageing, for the ageing time of 42 days de DIC was not possible to be used and, therefore, no results are given. Nevertheless, for an ageing time of 14 days a reduction in ν_0 down to 0.41 was reported.

***Table 17**. Initial Poisson's ratio, ν_0, and the initial Poisson's ratio obtained as the pseudo transverse to pseudo longitudinal strains, ν_0^R, for all ageing conditions.*

Ageing source	ν_0	ν_0^R
Pristine	0.46	0.46
Prestrain 15%	0.44	0.44
Prestrain 30%	0.51	0.51
Temperature 24 days	0.45	0.45
Temperature 36 days	0.31*	0.31*
Ozone 14 days	0.41	0.42
Ozone 42 days	-	-

*Initial Poisson's ratio determined from curves in **Fig. 61**.

Poisson's ratio evolution with applied longitudinal strain is represented in **Fig. 61** for all ageing conditions and pristine propellant, in which the solid symbols indicate the dewetting point. In general, the $\nu - \varepsilon_l$ curves show two differentiated regions before and after the dewetting point, similarly to the results of the preliminary characterisation. In this case, the first region takes for a constant Poisson's ratio, except for the 30% prestrained sample. The first region

is too small for the thermally aged samples to determine whether ν is constant or not. The second takes place in the form of an exponential decay in all cases.

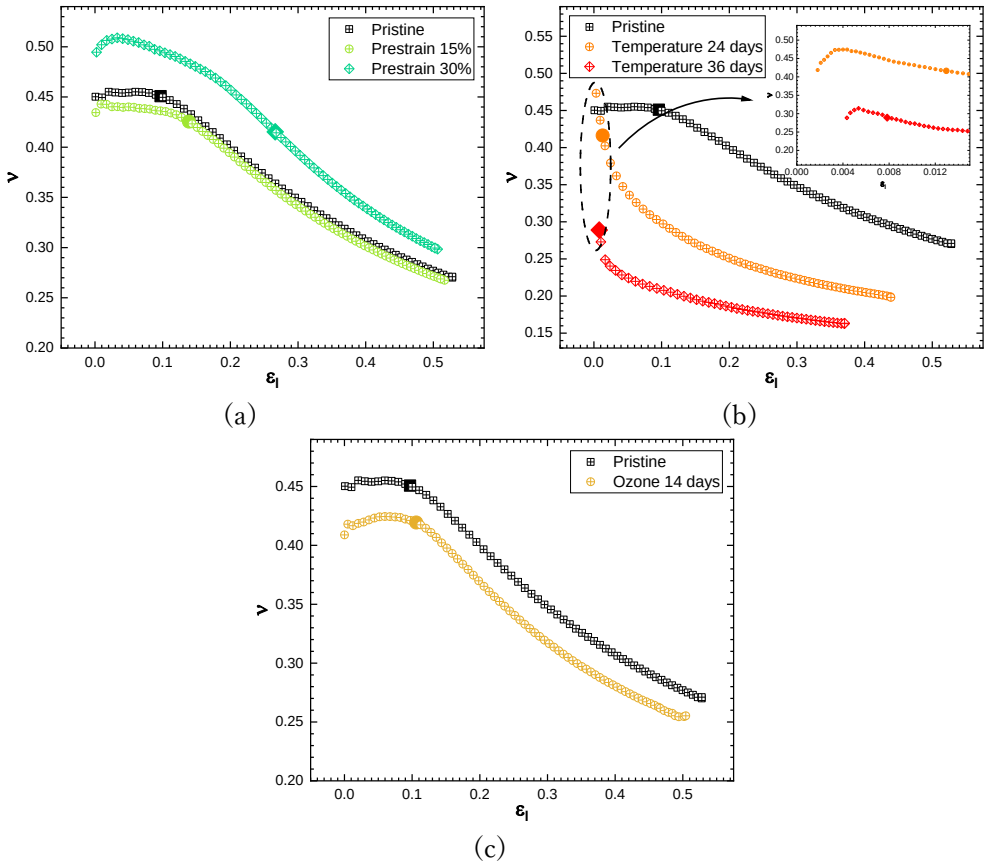

Fig. 61*. Poisson's ratio, ν, versus longitudinal true strain, ε_l, from tensile tests for (a) mechanical ageing for 15% and 30%, (b) thermal ageing for 24 and 36 days, and (c) ozone ageing for 14 days. Solid symbols indicate the corresponding dewetting point.*

Mechanical ageing above 15% applied prestrain displays a higher Poisson's ratio during the stretching compared to the one of the pristine propellant, while at 15% prestrain there is no difference, cf. **Fig. 61**a. The effect produced on the strain ratio by the thermal ageing process is noticeable. It is observed in the curves presented in **Fig. 61**b that the strain ratio decreases rapidly from the initial Poisson's ratio in an exponential decay form, ranging from a value of ≈ 0.45 down to ≈0.2 and from ≈0.31 down to ≈0.16 for the samples aged during 24 and 36 days, respectively. Regarding ozone aged samples, only the one aged

for 14 days is shown in **Fig. 61**c as previously mentioned. This sample presents lower values of Poisson's ratio during the stretching compared to the pristine propellant.

As an alternative representation of the damage induced by the stretching of the samples, the dilatation evolution during the tensile test is shown in **Fig. 62** to **Fig. 64**. The three stages (no dilatation, transition and dewetting and void growth) are again observed in all cases, except for the thermally aged samples for which dewetting and voids growth happens rapidly.

Regarding the mechanical ageing, cf. **Fig. 62**, for the lower applied prestrain of 15%, there is no effect on the volume change. On the other hand, the 30% prestrained sample displays a lower dilatation with respect to the pristine material during the test. Accounting for $V/V_0 - \varepsilon_l$ curves, cf. **Fig. 62**a, a volume decrease is observed up to an applied strain of ≈20%, which is close to the dewetting strain of ≈26%. When pseudo strains are considered, cf. **Fig. 62**b, this decrease in volume change is not observed for the 30% prestrained sample. Therefore, the observed shrinkage of the sample is not noticeable taking into account the absolute values of the dilatation, from 1 to ≈0.99.

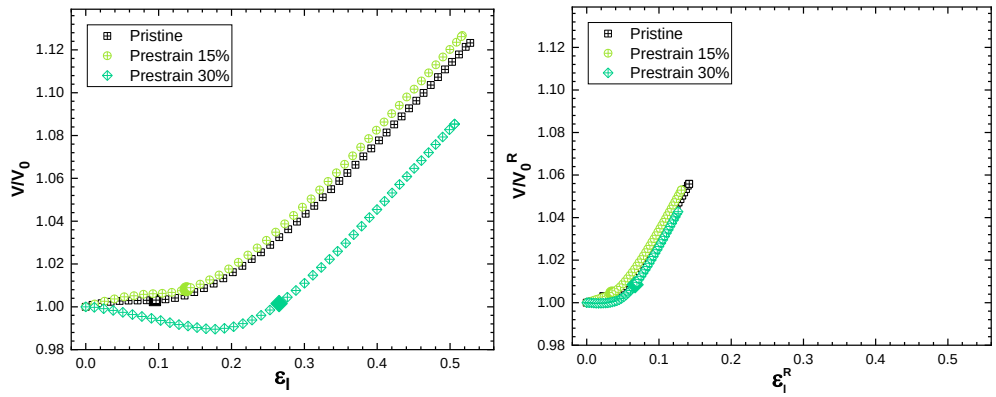

Fig. 62. *Volume change, V/V_0, versus applied longitudinal true strain, ε_l, from tensile tests of prestrained samples at 15% and 30% in terms of (a) true strains, ε_l, and (b) pseudo true strains ε_l^R. Solid symbols indicate the corresponding dewetting point.*

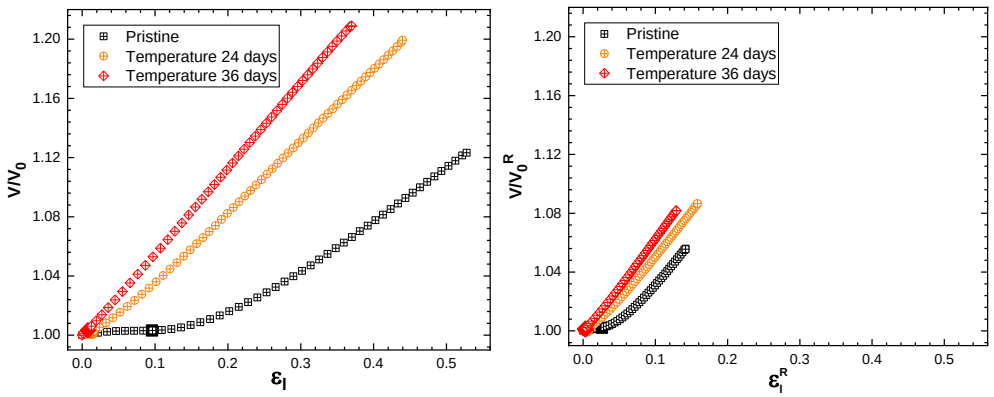

***Fig. 63**. Volume change, V/V_0, versus applied longitudinal true strain, ε_l, from tensile tests of thermally aged samples for 24 and 36 days in terms of (a) true strains, ε_l, and (b) pseudo true strains ε_l^R. Solid symbols indicate the corresponding dewetting point.*

Evolution of the dilatation for the thermally aged samples is shown in **Fig. 63**. The thermal ageing produces higher dilatation for higher ageing times, existing a strong linear relation between dilatation and applied strain. The reason lies in the loss of strain capability of the propellant, so that for an applied longitudinal strain, the propellant matrix is less able to deform. The same trends are observed for $V/V_0 - \varepsilon_l$ and $V/V_0^R - \varepsilon_l^R$ curves.

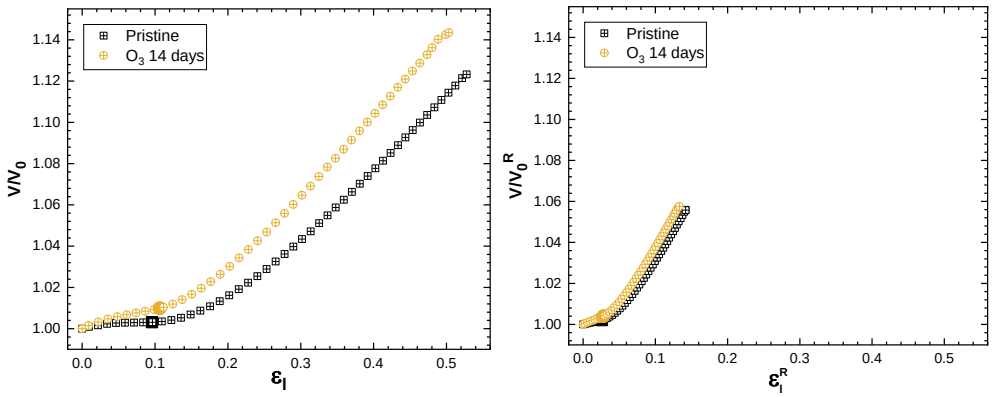

***Fig. 64**. Volume change, V/V_0, versus applied longitudinal true strain, ε_l, from tensile tests of ozone aged samples for 14 and 42 days in terms of (a) true strains, ε_l, and (b) pseudo true strains ε_l^R. Solid symbols indicate the corresponding dewetting point.*

Volume change of the ozone aged sample for 14 days during tensile test shows a higher dilatation with respect to the pristine material, as displayed in **Fig. 64**. This is explained though the higher flexibility of the sample due to the chain scissions caused by the ozonolysis reaction. Since matrix-particle interfaces are also affected, for a given strain, the amount of dewetting produced will be higher in the aged sample, leading to a greater growth of voids.

5.2.3.3. Mechanisms of failure

The fracture surface analysis, carried out on the tensile samples after testing, via Scanning Electron Microscopy (SEM) is condensed in **Fig. 65 – 67**.

In **Fig. 65** the SEM micrographs of the fracture surfaces of the mechanically aged tensile samples are gathered for several magnifications. It is observed that the applied prestrain does not affect the fracture topology in a significant manner and the appreciated roughness of the surface seems similar in all cases. Dewetting and crack formation around the bigger oxidiser particles is found to be promoted by the mechanical prestrain, which is identified with white arrows.

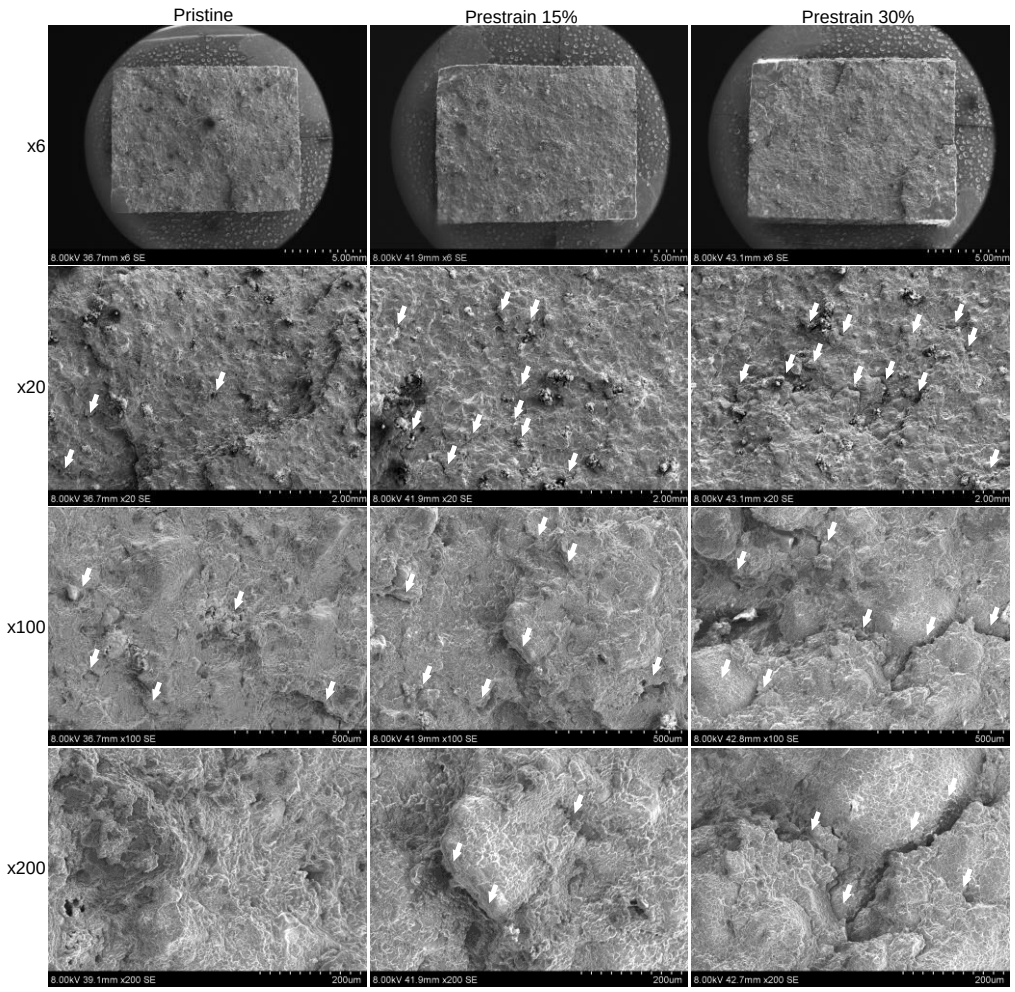

Fig. 65*. SEM micrographs of the fracture surfaces from tensile samples mechanically aged at pre-strains of 15% and 30% together with pristine propellant at x6, x20, x100 and x200 magnifications. Cracks and dewetted surfaces are pointed out with white arrows.*

Regarding the micrographs corresponding to the thermally aged samples collected in **Fig. 66**, the appreciated fracture surface appears rougher compared to the surface of the pristine material, since the rounded shape of the particles and its imprint are easier to appreciate for increasing ageing times on the surface. As a consequence of the higher crosslink density promoted by the thermal ageing process, the matrix undergoes a shrinkage and residual stresses are induced, which lead to the dewetting of the particles, being more noticeable

in the fracture surfaces of the sample aged for 36 days, indicated with white arrows.

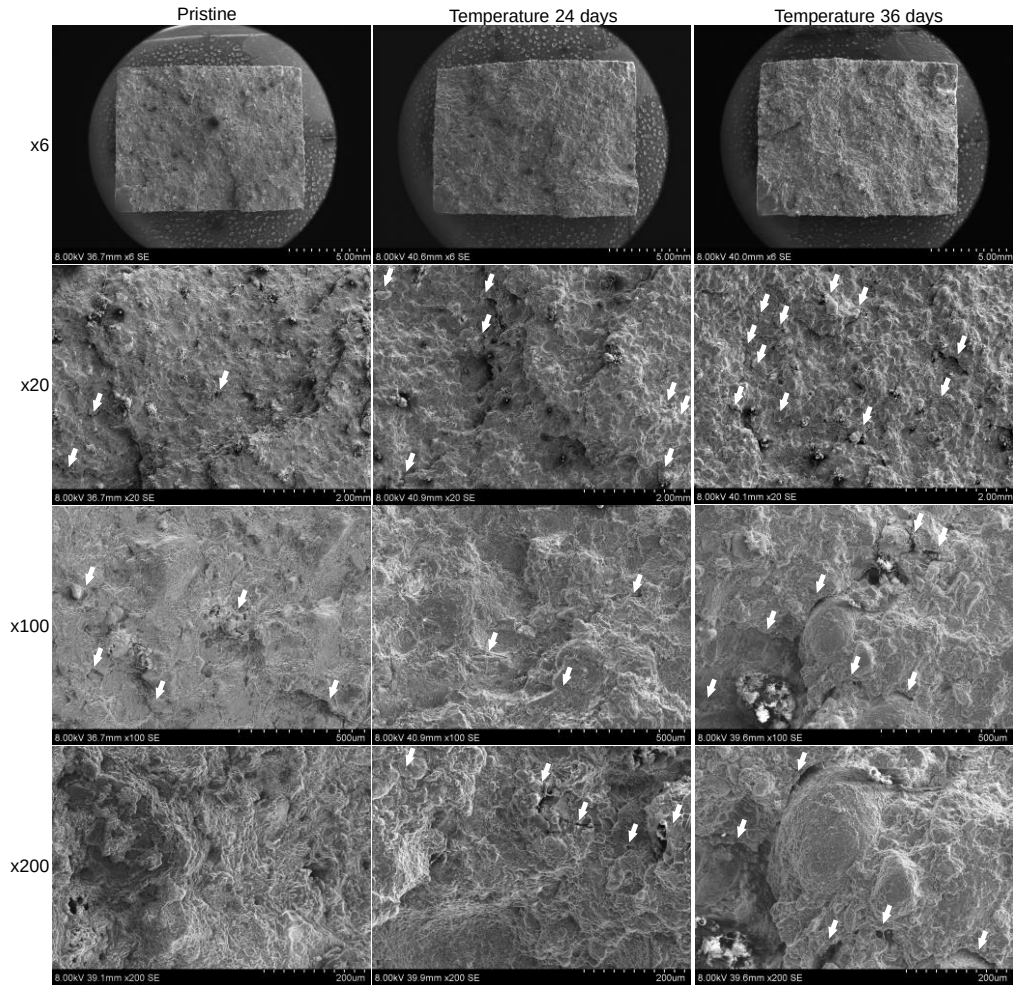

Fig. 66*. SEM micrographs of the fracture surfaces from tensile samples thermally aged at 80 ºC for 24 days and 36 days together with pristine propellant at x6, x20, x100 and x200 magnifications. Cracks and dewetted surfaces are pointed out with white arrows.*

Concerning the ozone aged tensile samples, its fracture surfaces are gathered in **Fig. 67**. At the lowest magnification, the effect of long ageing times in ozone (42 days) is severe and obvious with a marked reduction in the cross-sectional area due to the loss of the powdery layer generated during the ageing process. The rugosity of the fracture surface of this sample is the highest.

Dewetting and cracks are spread all over the fracture surfaces, identified with white arrows in **Fig. 67**, easier to observe at higher magnifications and visible for both ageing times.

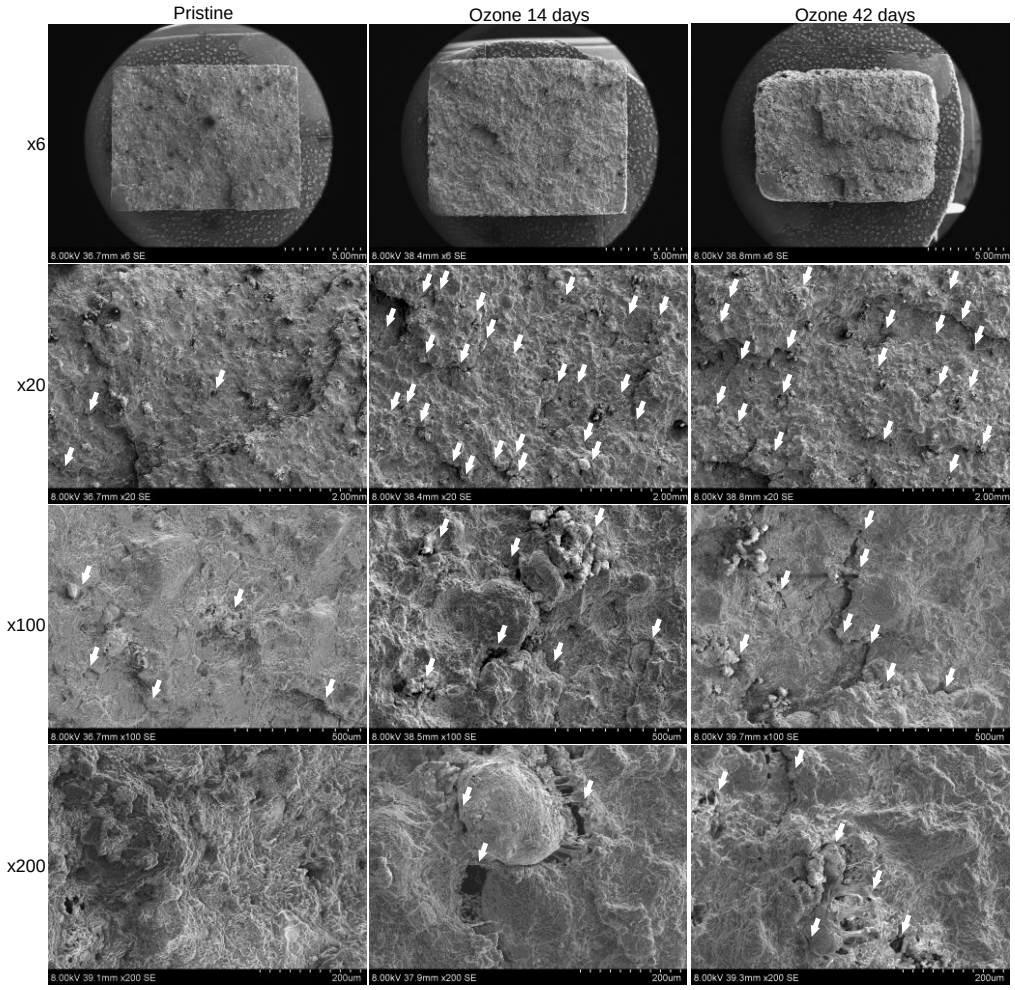

***Fig. 67**. SEM micrographs of the fracture surfaces from tensile samples aged with ozone for 14 days and 42 days together with pristine propellant at x6, x20, x100 and x200 magnifications. Cracks and dewetted surfaces are pointed out with white arrows.*

The fracture surface of a sample subjected to a 3-month ozone ageing period is shown in **Fig. 68**. The powdery layer produced due to the exposition to ozone, c.f. **Fig. 55**, is clearly identified in **Fig. 68**a, together with the inner part of the solid propellant sample. Here, the shape of the oxidiser particles is

completely visible, producing a completely rough surface, where the matrix seems to be partially removed, leaving holes throughout the whole propellant and leading to a completely loss of structural capacity. Therefore, in agreement with the crosslinking density results in **Table 13**, the ozone ageing or ozonolysis process is induced in the entire propellant body and not only on its surface. It is proved then that the ozone ageing is effective and can be severe. A closer look at the ammonium perchlorate particles is given in **Fig. 68**b and **Fig. 68**c, where it is observed the surface of the oxidiser particles free of matrix, meaning an intense weakening of the bonding between matrix and particles or, in other words, the promotion of severe dewetting.

(a)

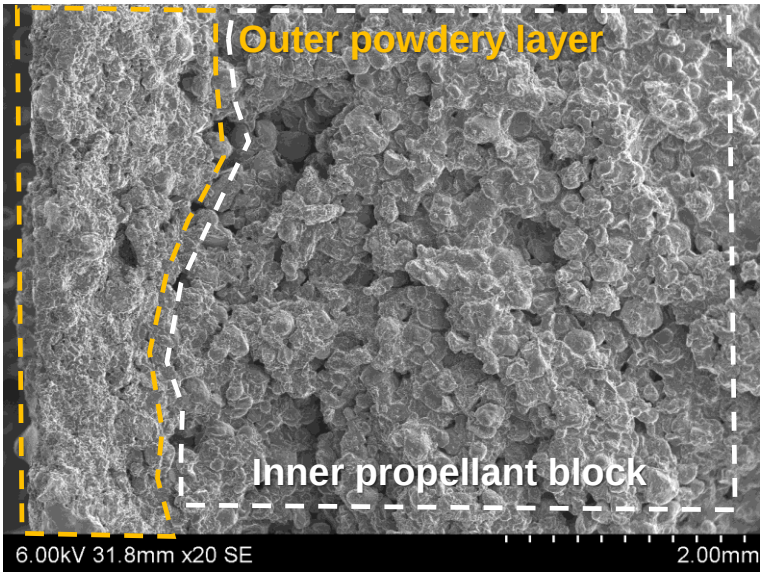

(b)

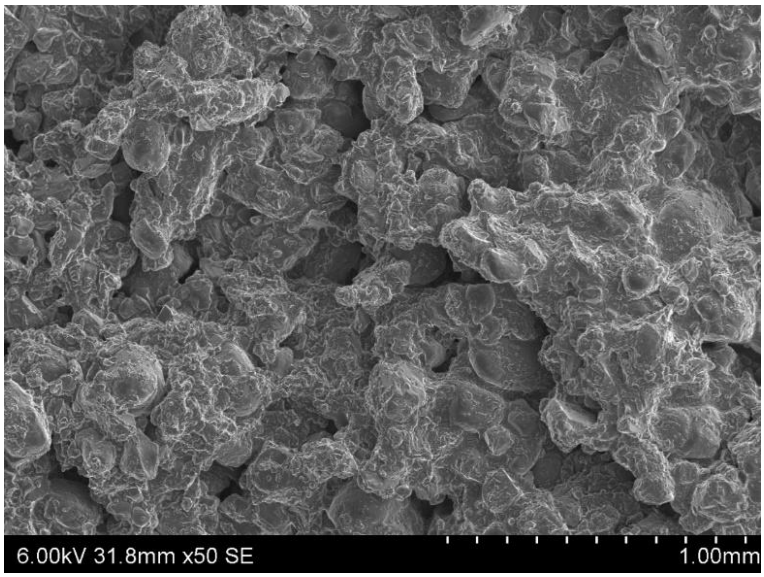

(c)

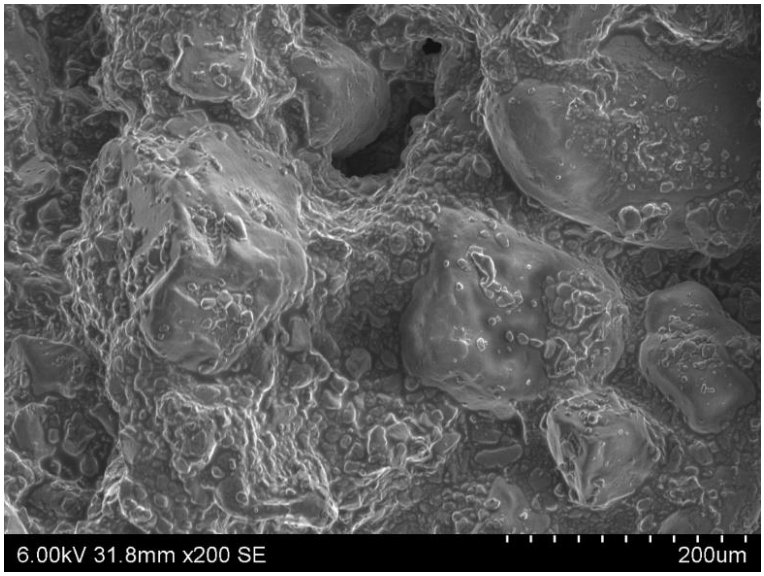

Fig. 68*. Fracture surface of a composite solid propellant sample subjected to 3-month ozone ageing period. (a) Image of the fracture surface showing the powdery layer on the sample surface and the inner part of the propellant sample at x20 magnification, (b) detail of the inner part of the sample at x50 magnification, and (c) detail of the ammonium perchlorate particles at the inner part of the sample at x200 magnification.*

The dewetting process takes place by a weakening of the bonding surface between particle and matrix, leading to the formation of strands or fibrils holding the bond, which will fail one after another to finally separate the particle

from the matrix. Examples of the dewetting process are gathered in **Fig. 69**. In the fracture surface of the ozone aged sample for 14 days, cf. **Fig. 69**a, it is seen an oxidiser particle partially connected to the matrix though several strands of matrix. In **Fig. 69**b, two adjacent ammonium perchlorate particles were almost torn off from each other, observed in the fracture surface of the ozone aged sample for 42 days. Another example is given in **Fig. 69**c, where an oxidiser particle is partially dewetted where the fibrils have already failed, taken from the fracture surface of the thermally aged sample for 36 days.

(a)

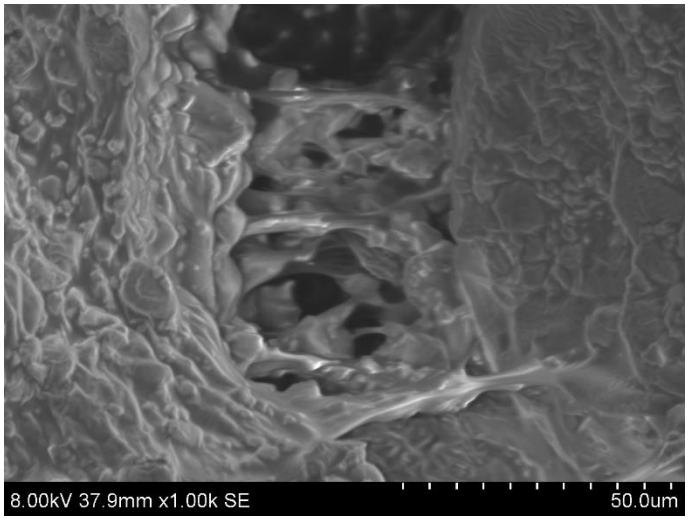

(b)

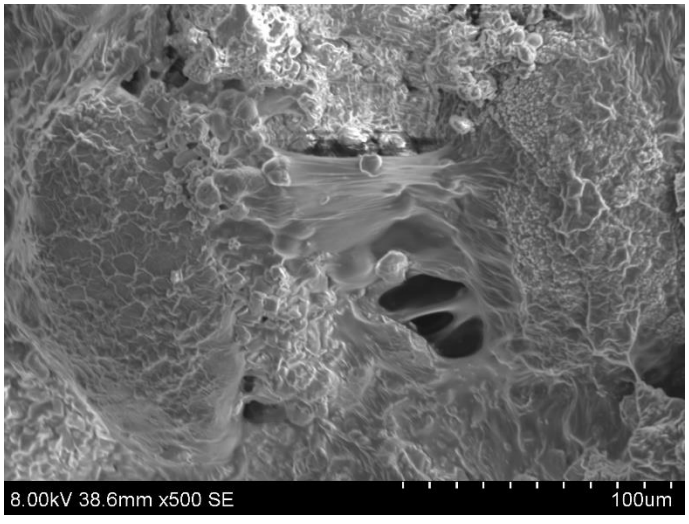

(c)

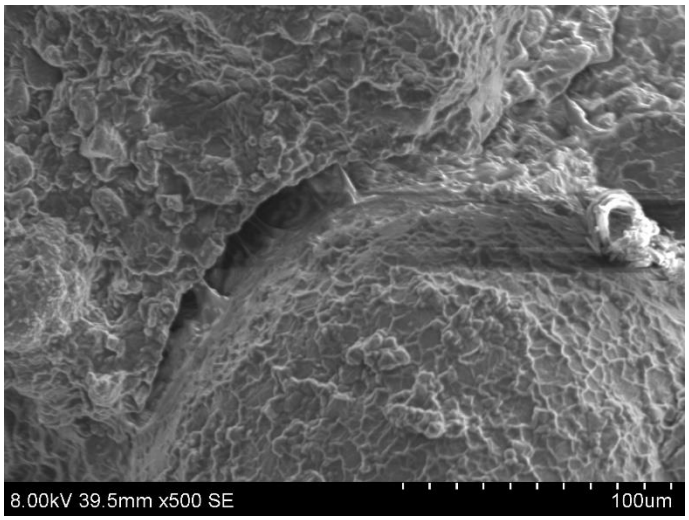

Fig. 69*. Details the dewetting or debonding process. (a) Matrix strands from an ammonium perchlorate particle debonding – from the ozone aged sample for 14 days -, (b) two adjacent ammonium perchlorate particles debonding – from the ozone aged sample for 42 days –, and (c) dewetted region around an ammonium perchlorate particle – from the thermally aged sample for 36 days –.*

A Molecular dynamics (MD) study on the interfacial interaction between ammonium perchlorate and a HTPB binder system was done by Dong et al. (Dong et al., 2022), where they demonstrate a similar failure mode, cf. **Fig. 70**, as the previously analysed and described in **Fig. 69**.

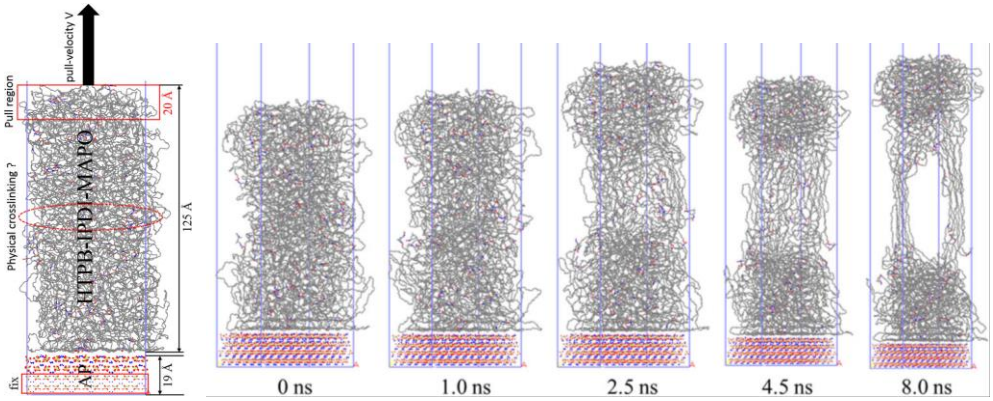

(a) (b)

Fig. 70*. Molecular dynamics (MD) simulation of hydroxyl-terminated polybutadiene (HTPB) binder system interaction with ammonium perchlorate (AP). (a) Schematic of the pulling loading case of a unit cell, (b) evolution of the microstructure of the unit cell during the pulling test. Adapted from (Dong et al., 2022).*

5.2.4. Effects of the ageing sources on the fracture behaviour

5.2.4.1. J resistance curves

The recorded load, P, versus (pseudo) displacement, (u^R) u, curves from fracture tests for all ageing conditions are shown in **Fig. 71** to **Fig. 73**. As observed, the load versus pseudo displacement curves reflect the reduction in the integrated area (energy) calculated after removing the creep strains from the viscoelastic behaviour.

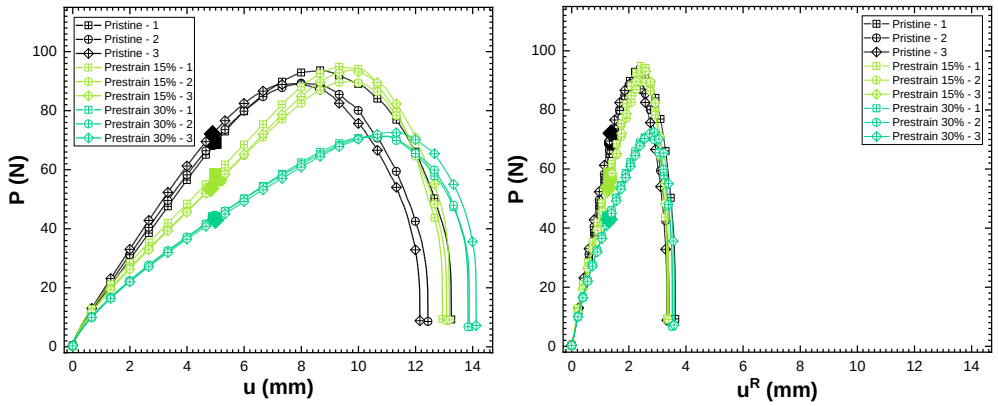

***Fig. 71**. Load, P, versus displacement, u, curves from fracture tests of the mechanically aged samples at 15% and 30% prestrains in terms of (a) displacements, u, and (b) pseudo displacements, u^R. Onset of crack growth is identified with solid symbols.*

Regarding the curves of prestrained samples shown in **Fig. 71**, all the curves show the same flexibility at the very beginning of the tests. However, right after the beginning, prestrained samples become more flexible than the pristine propellant, being more flexible for increasing applied prestrain, connected with the fact that more voids due to dewetting are present for higher applied prestrain. The loading capacity of the pristine and 15% prestrained samples is similar, while the one for the 30% prestrained sample decreases ≈ 21%, while the displacement at maximum increases up to ≈36%. This means that more time is required to reach the maximum, translating the maximum of the curves at lower loads and higher displacements for a higher applied prestrain. The onset of the crack's propagation, highlighted with solid symbols in

Fig. 71, takes place at the same displacement for all prestrained and pristine samples, that is at ≈5 mm, although at lower loading for increasing applied prestrain. The curves as a function of pseudo displacement move to smaller displacements with the onset of crack propagation in terms of pseudo displacements occurring earlier in the prestrained samples than in the pristine material.

The load versus (pseudo) displacement curves for thermally aged samples are displayed in **Fig. 72**. A considerable stiffening of the aged samples is evidenced, as well as higher values of the maximum load, P_{max}, and load at initiation of the crack's propagation, P_i. It is noted that the ageing process induces an approximation of the load at crack growth initiation to the maximum load, being the P_{max}/P_i ratio ≈1.3 for the pristine material and ≈1.05 for the longest ageing time of 36 days. The displacements at maximum and at crack growth initiation are excessively reduced for increasing ageing times. This is directly related to the reduction in the maximum strains allowed by the aged samples due to the overcuring during thermal ageing as shown in **Fig. 59**. For this case, pseudo displacements are also reduced for increasing ageing times.

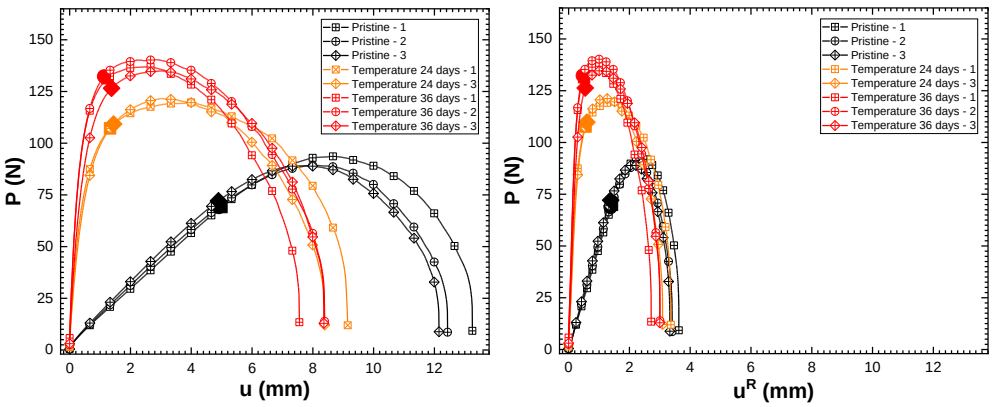

***Fig. 72**. Load, P, versus displacement, u, curves from fracture tests of thermally aged samples for 24 and 36 days in terms of (a) displacements, u, and (b) pseudo displacements, u^R. Onset of crack growth is identified with solid symbols.*

Considering the ozone ageing, the load versus (pseudo) displacement curves are shown in **Fig. 73**. Firstly, the compliance of the curves in function of the actual displacements increases with ageing time due to the larger

degradation of the matrix accompanied by larger debonding particles-matrix phenomena. This deterioration also affects the maximum load and the load at crack growth initiation, with lower values, P_{max} with respect to the pristine propellant as the ageing time is longer. Displacements at maximum do not show any variation, except for a slight reduction experimented by the samples aged for 42 days. Taking into consideration the $P - u^R$ curves, the curves of thermally aged samples tend to collapse into one leading to constant pseudo displacements at maximum for all samples and to a slight reduction of pseudo displacements at the initiation of the crack growth in comparison to that of the pristine propellant.

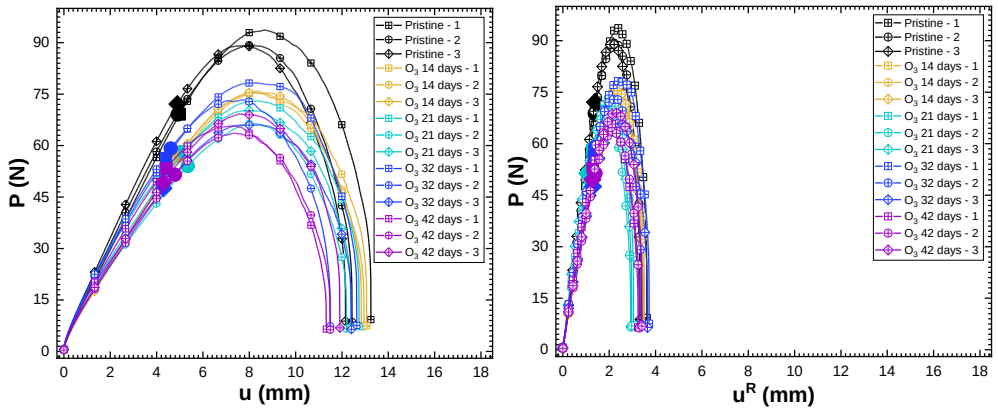

(a) (b)

Fig. 73*. Load, P, versus displacement, u, curves from fracture tests of ozone aged samples for 14, 21, 32 and 42 days in terms of (a) displacements, u, and (b) pseudo displacements, u^R. Onset of crack growth is identified with solid symbols.*

The J resistance curves in terms of J integral, J, or pseudo J integral, J^R, versus crack growth, Δa, for all ageing conditions are shown in **Fig. 74** to **Fig. 76**. Curves from mechanically aged samples are displayed in **Fig. 74**. Firstly, it is important to highlight the pronounced small values of the pseudo J-integral, cf. **Fig. 74**b, in comparison with J-integral values, cf. **Fig. 74**a, being the latter one order of magnitude lower than the former. Secondly, regarding the influence of the prestrain level on the $J - \Delta a$ curves, the differences are not marked. The resistance curves of the samples prestrained at 15% present the same crack propagation behaviour as the ones of pristine material and, when

comparing with the samples prestrained at 30%, a small decrease in the curves is seen, i.e., lower energy is required to propagate the crack when the sample is highly prestrained. Considering $J^R - \Delta a$, where the viscous effects are removed, higher differences between curves of 30% prestrained samples and those of pristine and 15% prestrained samples are observed. The results are reasonable. In case of 30% prestrained samples, more dewetting occurs than in 15% prestrained samples (as observed in the fractographic analysis of the tensile samples) and less energy is necessary for the crack advancement in a matrix full of voids and cracks due to breakage of particles-matrix debonding.

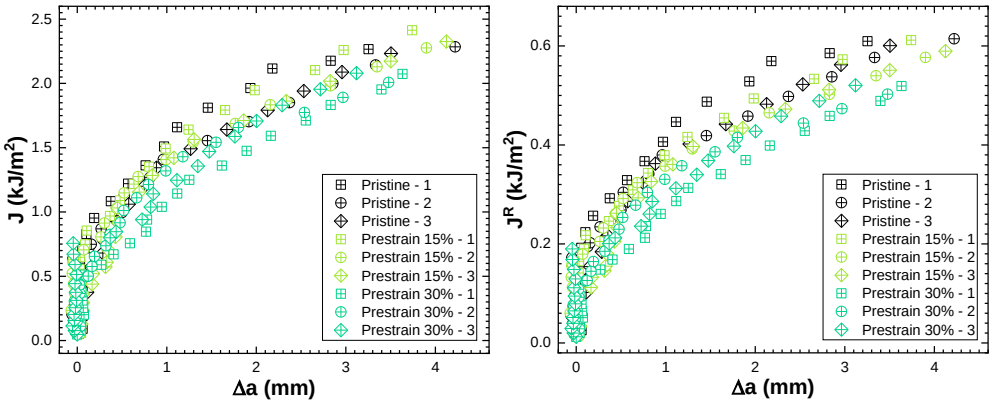

Fig. 74*. J resistance curves from fracture tests for the mechanically aged samples at 15% and 30% prestrains in terms of (a) J integral, $J - \Delta a$, and (b) pseudo J integral, $J^R - \Delta a$.*

The curves in **Fig. 75** correspond to the thermally aged samples. In this case, when comparing the $J^R - \Delta a$ and the $J - \Delta a$ curves, the values of the pseudo J integral, cf. **Fig. 75**b, are half of those of the actual J integral, cf. **Fig. 75**a, in line with the less viscous nature of an overcured binder in thermally aged propellants. Concerning the influence of the thermal ageing time in the $J - \Delta a$ curves, small variations are found with a little increase in the fracture energy to propagate the crack for the aged samples with respect to the pristine material. Attending to the $J^R - \Delta a$ curves, the increase in the propagation energy for aged samples compared to the pristine ones is noticeable and the presented curves are steeper, which is a sign of a more stable crack propagation process. It is evident that discounting greater viscoelastic dissipation energy in

the pristine material than in the thermally aged samples results in a separation of the $J^R - \Delta a$ curves. However, hardly differences were observed between the resistance curves aged for different ageing times.

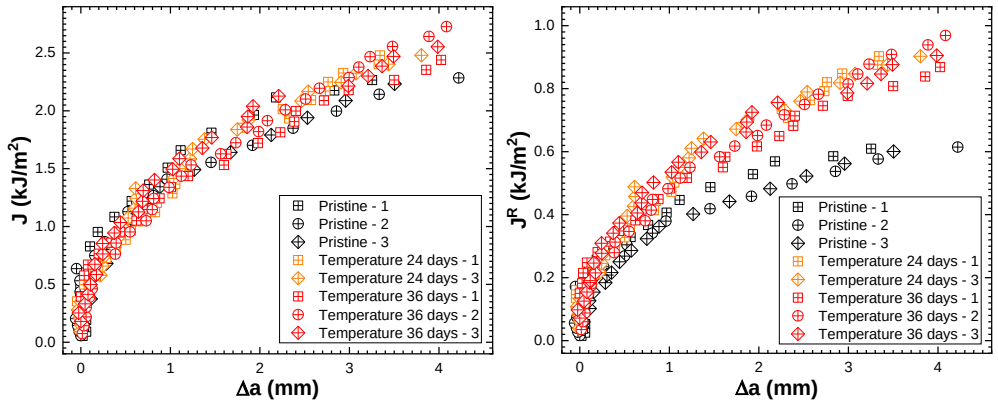

Fig. 75. J resistance curves from fracture tests for the thermally aged samples for 24 and 36 days in terms of (a) J integral, $J - \Delta a$, and (b) pseudo J integral, $J^R - \Delta a$.

Resistance curves of the ozone aged samples are shown in **Fig. 76**. Again, the pseudo J-integral values in the $J^R - \Delta a$ curves, cf. **Fig. 76**b, are one order of magnitude lower than those of the J-integral in the $J - \Delta a$ curves, cf. **Fig. 76**a. It is noticeable that the pseudo J-integral values of the ozone aged samples, cf. **Fig. 76**b, are similar to those attained in the pseudo J-integral values of the mechanically aged samples, cf. **Fig. 74**b.

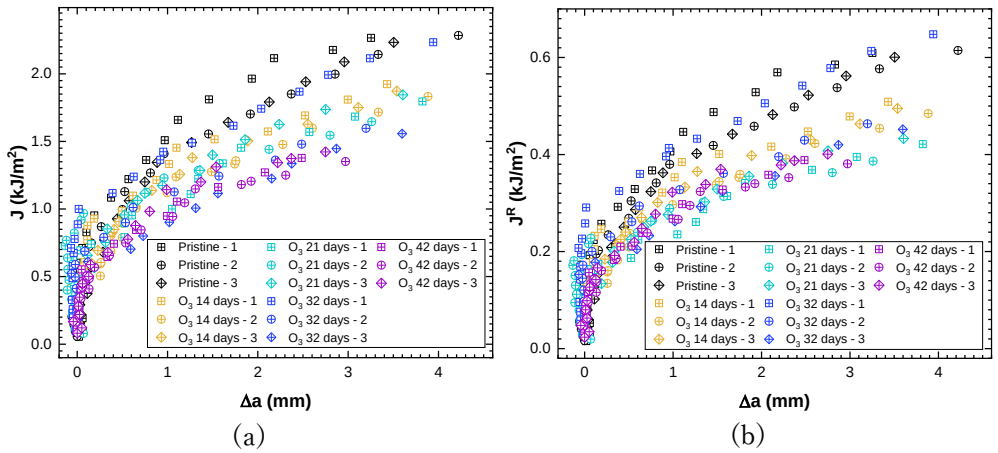

Fig. 76. J resistance curves from fracture tests for the ozone aged samples for 14, 21, 32 and 42 days in terms of (a) J integral, $J - \Delta a$, and (b) pseudo J integral, $J^R - \Delta a$.

Analysing the $J-\Delta a$ curves, it is rapidly seen that ozone has caused a reduction of the energy needed to propagate a crack, which is promoted with longer ageing times. The slopes of the curves of aged samples are less steep than the corresponding to the pristine ones, traduced to a more unstable fracture propagation. The very same trend is observed in the $J^R-\Delta a$ curves, although to a lesser extent.

***Table 18**. Energy crack propagation parameters for the ageing characterisation. Critical values of J integral, J_c and J_c^R, and fitting parameters, C_1 and C_2, of the J resistance curve to the power law (58) along with the corresponding coefficient of determination, R^2.*

Ageing	J_c, J_c^R (kJ/m²)	C_1	C_2	R^2
$J-\Delta a$ curves				
Pristine	0.73±0.03	1.4±0.1	0.38±0.04	0.989±0.006
Prestrain 15%	0.62±0.04	1.41±0.06	0.37±0.02	0.994±0.002
Prestrain 30%	0.50±0.01	1.2±0.1	0.46±0.07	0.989±0.006
Temperature 24 days*	0.44±0.03	1.36±0.08	0.48±0.06	0.988±0.008
Temperature 36 days	0.50±0.03	1.37±0.09	0.45±0.06	0.992±0.004
Ozone 14 days	0.60±0.02	1.20±0.09	0.35±0.03	0.98±0.01
Ozone 21 days	0.59±0.08	1.16±0.07	0.33±0.07	0.98±0.01
Ozone 32 days*	0.53±0.07	1.0±0.1	0.4±0.1	0.99±0.006
Ozone 42 days	0.49±0.04	1.00±0.04	0.35±0.01	0.96±0.03
$J^R-\Delta a$ curves				
Pristine	0.20±0.01	0.38±0.03	0.38±0.04	0.989±0.006
Prestrain 15%	0.16±0.01	0.36±0.02	0.38±0.02	0.992±0.007
Prestrain 30%	0.13±0.01	0.30±0.03	0.46±0.07	0.989±0.006
Temperature 24 days*	0.17±0.01	0.50±0.03	0.47±0.06	0.989±0.008
Temperature 36 days	0.19±0.01	0.49±0.03	0.44±0.06	0.992±0.004
Ozone 14 days	0.16±0.01	0.32±0.03	0.34±0.03	0.98±0.01
Ozone 21 days	0.14±0.02	0.27±0.02	0.33±0.07	0.98±0.01
Ozone 32 days*	0.15±0.03	0.29±0.04	0.4±0.1	0.990±0.006
Ozone 42 days	0.14±0.01	0.28±0.01	0.34±0.01	0.96±0.03

*Only two samples used.

The fitting parameters of the resistance curves to (58), C_1 and C_2, are collected in **Table 18**, as well as the J integral at which the crack starts to propagate, J_c or J_c^R. One important point to highlight is that the exponent of the power law, C_2, is constant for each ageing condition independently of the use of actual or pseudo variables.

For the prestrained samples, taking a look at the constants of the power law fitting, crack growth behaviour for prestrained samples at 15% was similar to that of pristine samples. However, the values of J integral at crack growth initiation decreases with increasing the degree of prestrain, attaining J_c values from ≈0.73 kJ/m^2 for the pristine material to ≈0.5 kJ/m^2 for the 30% prestrained samples. The corresponding J_c^R values follow the same trend ranging from ≈0.2 kJ/m^2 for the pristine propellant to ≈0.13 kJ/m^2 in the case of the 30% prestrained material.

Despite resistance curves of thermally aged samples are above the ones of pristine propellant, the value of J integral at the onset of crack's propagation is smaller in case of the aged samples but with no clear tendency with respect to the ageing times. In this case, the values of J_c decrease for the aged samples down to ≈0.44 kJ/m^2 for the samples aged for 24 days and increases to ≈0.50 kJ/m^2 for the 36 days aged samples. The same variability is observed in case of the pseudo J integral values. Regarding the power law constants, C_1 barely decreases with ageing for $J-\Delta a$ curves, but increases noticeably with ageing for $J^R-\Delta a$ curves, in accordance with the observed higher curves in **Fig. 75**b. C_2 values increase is found for aged samples compared to pristine propellant, which is linked to a rise of the slope of the curve, i.e., in the crack propagation stability.

Fracture energy at initiation J_c decreases for longer ozone ageing times for ≈33%, also happening for the pseudo fracture energy, J_c^R. Considering the power law fitting parameters, C_2 exponent slightly decreases for the aged samples, in terms of both $J-\Delta a$ and $J^R-\Delta a$ curves. The main difference is found

for C_1 constant, which is also reducing as much as ≈30% for both $J - \Delta a$ and $J^R - \Delta a$ curves.

5.2.4.2. CTOD resistance curves

The (pseudo) CTOD resistance curves from mechanically aged specimens are shown in **Fig. 77**. The observed trend of the (pseudo) CTOD resistance curves is similar to the displayed in the J resistance curves in **Fig. 74**. Firstly, it is obvious the drop in the pseudo CTOD values, cf. **Fig. 77**b, in compassion with the actual CTOD values, cf. **Fig. 77**a, with differences of one order of magnitude. Regarding the influence of the prestrain level, both actual and pseudo CTOD values decrease with increasing applied prestrain. This fact is related to the observed hardening in the uniaxial tensile behaviour, displayed in **Fig. 58**, after the initial inelastic response in the mechanically aged samples, so that the hardened material reduces the displacements in the vicinity of the crack tip (CTOD).

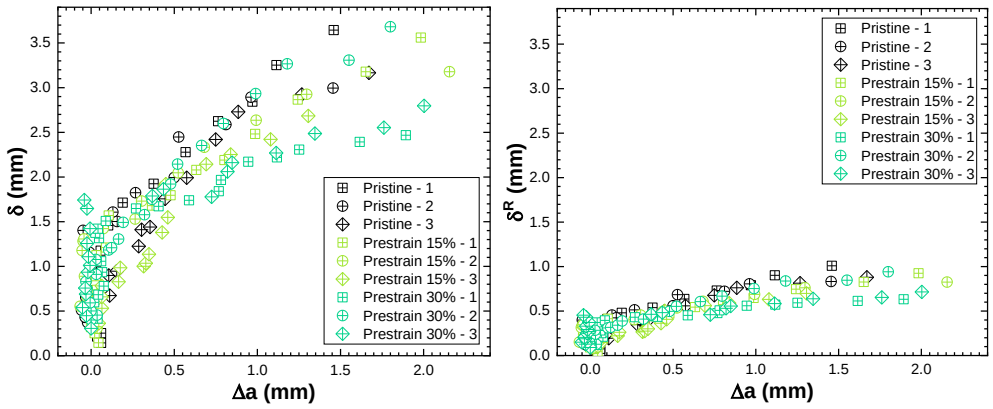

(a) (b)

Fig. 77*. CTOD resistance curves from fracture samples mechanically aged at prestrains of 15% and 30% in terms of (a) $\delta - \Delta a$ curves, and (b) $\delta^R - \Delta a$ curves.*

Corresponding (pseudo) CTOD resistance curves for thermally aged samples are shown in **Fig. 78**. Firstly, the comparison of the actual and pseudo CTOD values reveal that pseudo CTOD values, cf. **Fig. 78**a, are again one order of magnitude lower than the actual CTOD, cf. **Fig. 78**b. Secondly, CTOD for the thermally aged samples is lower than that of the pristine material. This

trend is opposite to the one observed in $J - \Delta a$ curves, cf. **Fig. 75**. However, the CTOD behaviour is associated to the higher crosslinking density, related stiffness increase and lower deformation capability. However, when $\delta^R - \Delta a$ curves are considered, curves for all ageing conditions overlap the ones of the pristine samples.

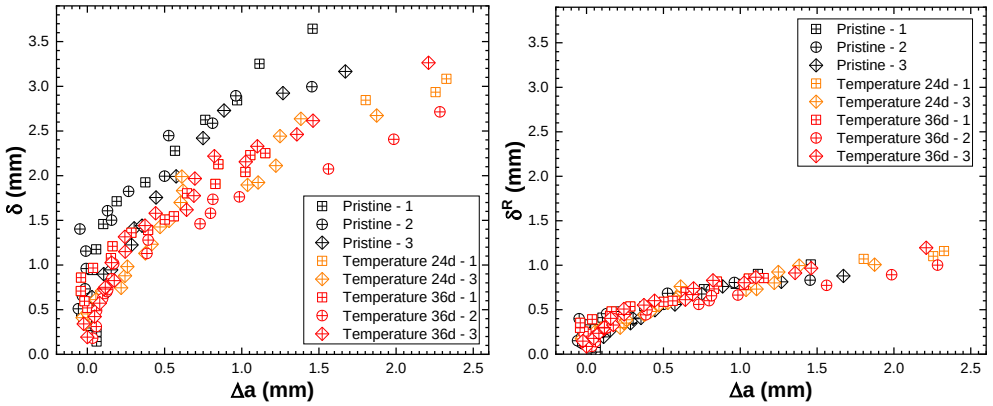

Fig. 78. CTOD resistance curves from fracture samples thermally aged for 24 and 36 days in terms of (a) $\delta - \Delta a$ curves, and (b) $\delta^R - \Delta a$ curves.

In the case of the ozone aged samples, CTOD presented strong difficulties to be measured. As represented in **Fig. 79**, the powdery layer cracks and detaches from the bulk propellant surface when the sample is loaded. This results in parts of the powdery layer covering partially or completely the crack tip, making it challenging to measure the crack growth and CTOD. As seen in **Fig. 76**, the crack growth was measured with success. Nevertheless, the CTOD encountered challenges. Instead, crack mouth opening displacement (CMOD) was found easier to measure. Since CMOD is not a fracture parameter, unlike CTOD, the latter was inferred from CMOD as motivated in the following paragraphs.

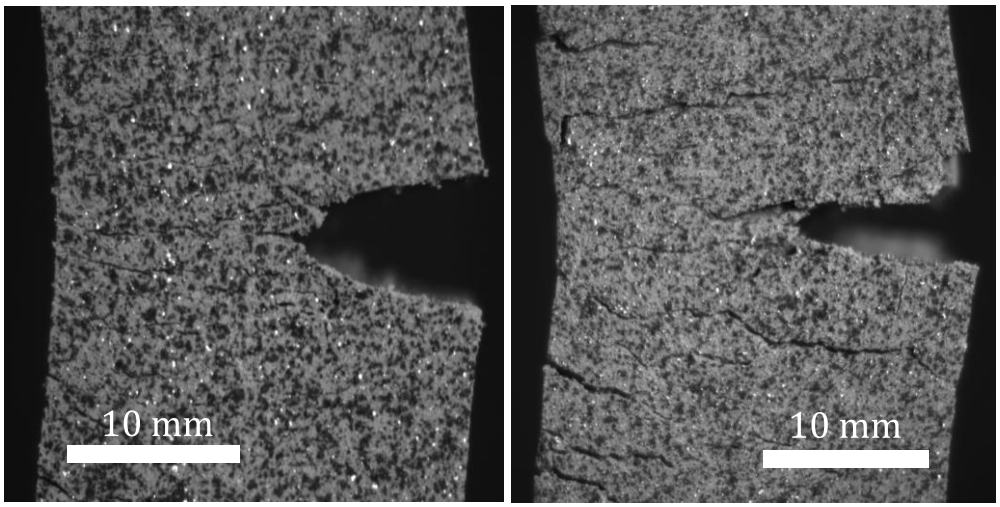

(a) (b)

Fig. 79*. Images from fracture tests for ozone aged samples showing the cracking of the powdery layer. (a) Sample aged for 21 days, (b) sample aged for 42 days.*

CTOD-CMOD relation is usually assumed to be dependent only on geometric configuration and CTOD is determined through the conversion of experimental CMOD measurements (Anderson, 2017), assumption that is not accurate when elastic displacements are dominant. In a three-point bending test, cf. **Fig. 80**, the relationship between CTOD, δ, and CMOD, V, can be considered as

$$\delta = \left[1 + \frac{a}{r(W-a)}\right]^{-1} V \tag{87}$$

where a and W are the crack length and sample's width, respectively, and r is the rotation factor, being a dimensionless constant whose value ranges between 0 and 1 (Anderson, 2017). The schematic describing these parameters is shown in **Fig. 80**.

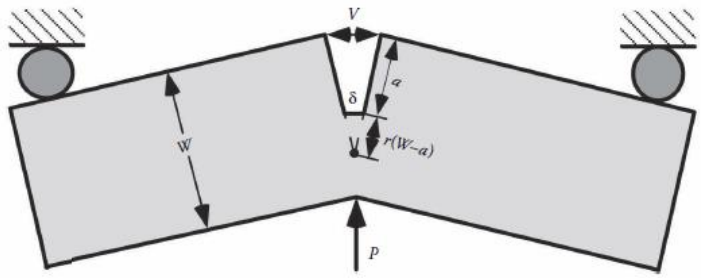

Fig. 80. Three-point bending test configuration. Schematic representing the hinge model to determine the CTOD-CMOD relationship.

Therefore, the relation between CTOD and CMOD has been determined for the pristine, mechanically and thermally aged samples, in order to infer the CTOD from the measured CMOD for the ozone aged samples. The measured CTODs are represented against measured CMODs in **Fig. 81**. It is observed that the relation between CTOD and CMOD is mostly linear for all cases in the measured ranges.

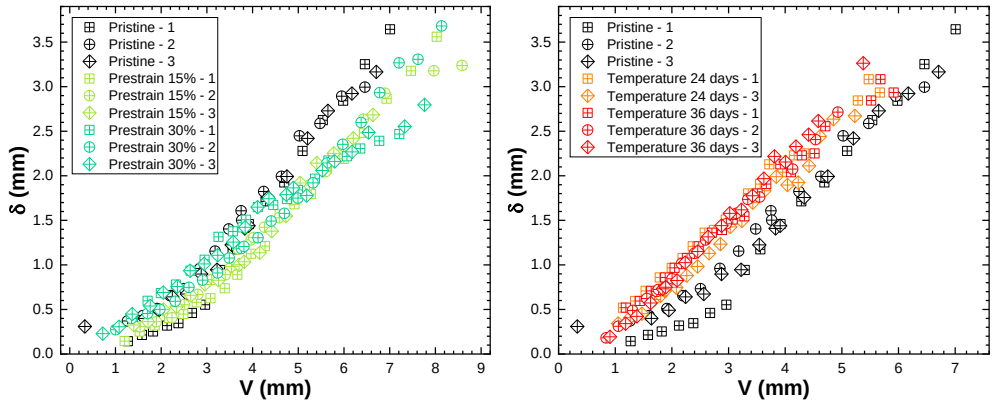

Fig. 81. CTOD, δ, vs CMOD, V, curves for (a) prestrained samples at 15% and 30%, and (b) thermally aged samples for 24 and 36 days.

The thermally aged samples show a linear trend throughout the whole fracture process, while pristine material and prestrained samples seem to present two different regions identified before crack propagation, corresponding to the blunting of the crack tip, and after crack propagation. As an approximation, a linear relation has been assumed to exist between CTOD and CMOD. The slopes of those relations for each condition are collected in **Table 19**. It is

observed that pristine propellant and thermally aged propellant present a similar slope, while prestrained samples show a decrease in the slope with increasing applied prestrain. This difference is probably found due to the Mullin's effect produced by the cyclic loading process.

***Table 19**. Slope of the linear CTOD-CMOD relation for pristine, prestrained and thermally aged samples from fracture tests.*

Ageing source	Slope
Pristine	0.65 ± 0.07
Prestrained 15%	0.58 ± 0.02
Prestrained 30%	0.42 ± 0.14
Temperature 24 days	0.59 ± 0.03
Temperature 36 days	0.61 ± 0.07

It is important to highlight that the differences mentioned above are not remarkable as the slope values are around 0.6 except for the samples prestrained at 30%. Therefore, to obtain the CTOD values for ozone aged samples, it was decided to use the corresponding 0.57 average value of the slopes collected in **Table 19**, considering all conditions, as the CTOD-CMOD slope. Corresponding CTOD resistance curves are shown in **Fig. 82**.

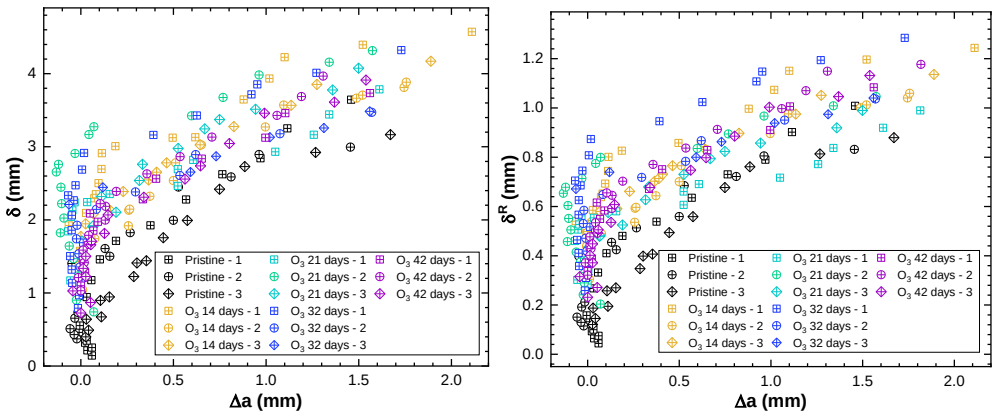

(a) (b)

***Fig. 82**. CTOD resistance curves from fracture samples aged with ozone for 14, 21, 32 and 42 days in terms of (a) $\delta - \Delta a$ curves, and (b) $\delta^R - \Delta a$ curves.*

Regarding the influence of the viscous nature, the pseudo CTOD values, cf. **Fig. 82**b, are again one order of magnitude lower than the actual CTOD values, cf. **Fig. 82**a. However, it is seen that curves corresponding to the aged samples are above the ones of the pristine material. A more flexible matrix due to the reduction of the crosslinking density allows greater CTOD values during the crack growth. Although the effect of ageing is clear, the scatter of the data prevents the observation of any trend. The $\delta^R - \Delta a$ curves display similar tendencies as the $\delta - \Delta a$ curves.

The fitting parameters of the CTOD resistance curves in **Fig. 77**, **Fig. 78** and **Fig. 82** to (83) are collected in **Table 20**, together with the critical (pseudo) CTOD. It is observed that C_2' does not change between $\delta - \Delta a$ and $\delta^R - \Delta a$ curves and it is similar to C_2 from $J - \Delta a$ and $J^R - \Delta a$ curves, with the exception of the corresponding values of the ozone aged samples. The high correlation coefficients confirm the typical power law form of the CTOD resistance curves.

Mechanically aged samples do not show a significant change in the critical (pseudo) CTOD, C_1' and $(C_2'^R)$ C_2'. Only a small decrease is for $C_1'^R$ with the increasing applied prestrain.

The thermally aged samples experience an abrupt diminution of δ_c and δ_c^R of ≈49% and ≈28%, respectively. This is related to the stiffening of the material due to crosslinking growth. The effect is translated into lower C_1', while $C_1'^R$ does not vary due to thermal ageing. The C_2' exponent slightly increases and $C_2'^R$ is maintained constant with ageing.

Samples subjected to ozone ageing experience an increment in δ_c and δ_c^R of ≈50%, noticing the higher straining capability of the matrix due to the rupture of the polymeric chains. This is accompanied by an increase of C_1' and $C_1'^R$ and a remarkable decrease of C_2' and $C_2'^R$.

Table 20. *Critical CTOD, δ_c, critical pseudo CTOD, δ_c^R, and parameters C_1' and C_2' and corresponding $C_1'^R$ and $C_2'^R$ obtained from the fitting of the CTOD resistance curves to (83) with subsequent R^2 coefficient, from fracture tests for all ageing conditions.*

Ageing	δ_c, δ_c^R (mm)	C_1'	C_2'	R^2
$\delta - \Delta a$ curves				
Pristine	1.4 ± 0.2	2.8 ± 0.2	0.4 ± 0.1	0.95 ± 0.02
Prestrain 15%	1.1 ± 0.2	2.5 ± 0.1	0.4 ± 0.1	0.92 ± 0.04
Prestrain 30%	1.3 ± 0.1	2.4 ± 0.4	0.3 ± 0.1	0.93 ± 0.05
Temperature 24 days*	0.8 ± 0.1	2.1 ± 0.1	0.46 ± 0.07	0.94 ± 0.05
Temperature 36 days	0.72 ± 0.03	2.0 ± 0.2	0.42 ± 0.05	0.96 ± 0.02
Ozone 14 days	2.2 ± 0.1	3.6 ± 0.3	0.26 ± 0.07	0.94 ± 0.07
Ozone 21 days	2.1 ± 0.2	3.5 ± 0.4	0.23 ± 0.02	0.9 ± 0.1
Ozone 32 days*	2.0 ± 0.1	3.1 ± 0.1	0.19 ± 0.06	0.9 ± 0.1
Ozone 42 days	2.0 ± 0.3	3.4 ± 0.1	0.29 ± 0.03	0.96 ± 0.01
$\delta^R - \Delta a$ curves				
Pristine	0.40 ± 0.06	0.78 ± 0.06	0.4 ± 0.1	0.95 ± 0.02
Prestrain 15%	0.31 ± 0.04	0.66 ± 0.03	0.4 ± 0.1	0.92 ± 0.04
Prestrain 30%	0.35 ± 0.03	0.6 ± 0.1	0.3 ± 0.1	0.92 ± 0.05
Temperature 24 days*	0.31 ± 0.06	0.80 ± 0.03	0.43 ± 0.07	0.94 ± 0.04
Temperature 36 days	0.29 ± 0.01	0.77 ± 0.08	0.39 ± 0.05	0.96 ± 0.03
Ozone 14 days	0.61 ± 0.04	0.97 ± 0.09	0.26 ± 0.07	0.95 ± 0.06
Ozone 21 days	0.53 ± 0.06	0.87 ± 0.08	0.24 ± 0.01	0.9 ± 0.1
Ozone 32 days*	0.61 ± 0.04	0.93 ± 0.01	0.18 ± 0.06	0.9 ± 0.1
Ozone 42 days	0.58 ± 0.08	0.97 ± 0.04	0.24 ± 0.05	0.93 ± 0.05

*Only two samples used.

5.2.4.3. Mechanisms of failure

Failure mechanisms have been studied through the analysis of the fracture surfaces of the fracture samples. SEM micrographs of the fracture surfaces of the aged samples are shown in **Fig. 83** to **Fig. 86**. As observed, independently of the ageing condition, the main mechanism of failure is matrix tearing.

Fracture surfaces of mechanically aged samples are gathered in **Fig. 83**. From the images at x20 magnification it is seen a surface containing a larger number of cracks (pointed out with white arrows) with higher applied prestrain. It is also noticeable that the fracture surface gets rougher with the increasing applied prestrain and imprints of the dewetted particles are more visible. Attending to the fracture surfaces of the thermally aged samples in **Fig. 84**, cracks are also promoted with thermal ageing, although not as severe as in the case of the mechanical ageing. Dewetting of particles is noticeable for thermally aged samples. However, the roughness of the fracture surfaces is not appreciated to be significantly rougher with respect of the ones of the pristine material. Fracture surfaces of ozone aged samples are compared in **Fig. 85**. It is observed the severity of the ozone ageing affecting the integrity of the propellant. Fracture surfaces present a large number of cracks, pointed out with white arrows, even at the lowest ageing time of 14 days and increasing the number of cracks for increasing ageing times. The longer the ageing time, the rougher fracture surface is appreciated. Details of the ozone aged fracture surfaces are shown in **Fig. 86**, where it is appreciated that particles are dewetted. Here it is confirmed that the ozone ageing affects not only to the polymer chains in the elastomeric matrix, but also to the matrix-particles bonds.

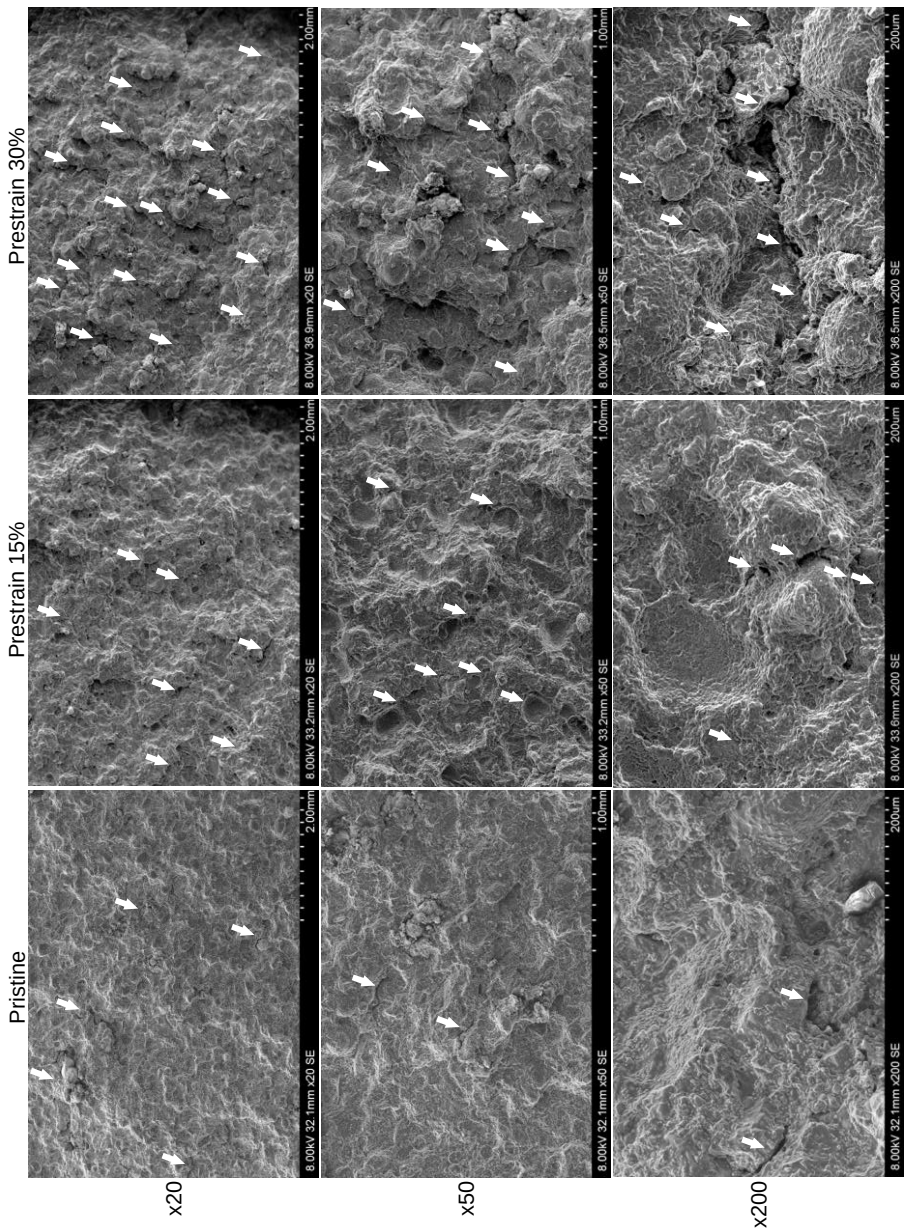

Fig. 83. SEM micrographs of the fracture surfaces from fracture samples mechanically aged at prestrains of 15% and 30% together with pristine propellant at x20, x50 and x200 magnifications. White arrows indicate visible cracks.

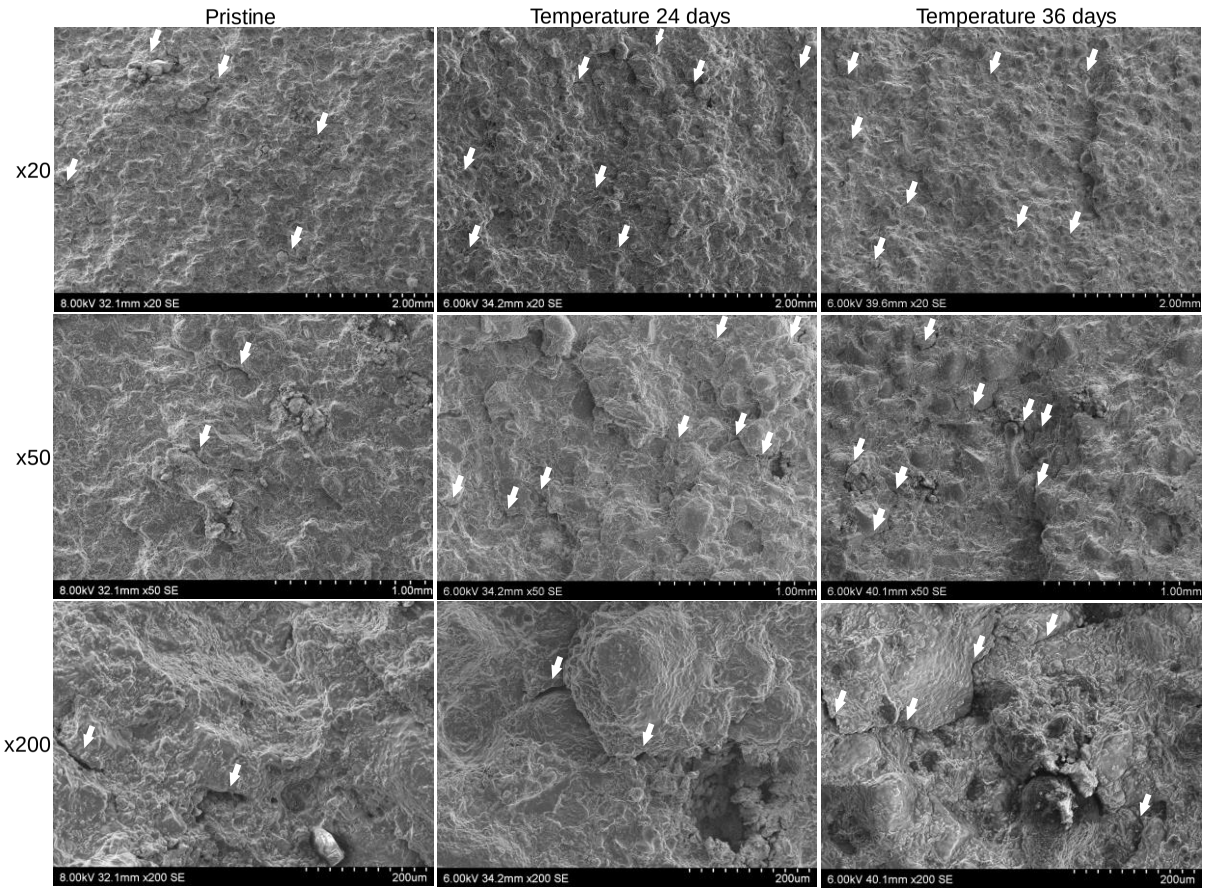

Fig. 84*. SEM micrographs of the fracture surfaces from fracture samples thermally aged for 24 and 36 days together with pristine propellant at x20, x50 and x200 magnifications. White arrows indicate visible cracks.*

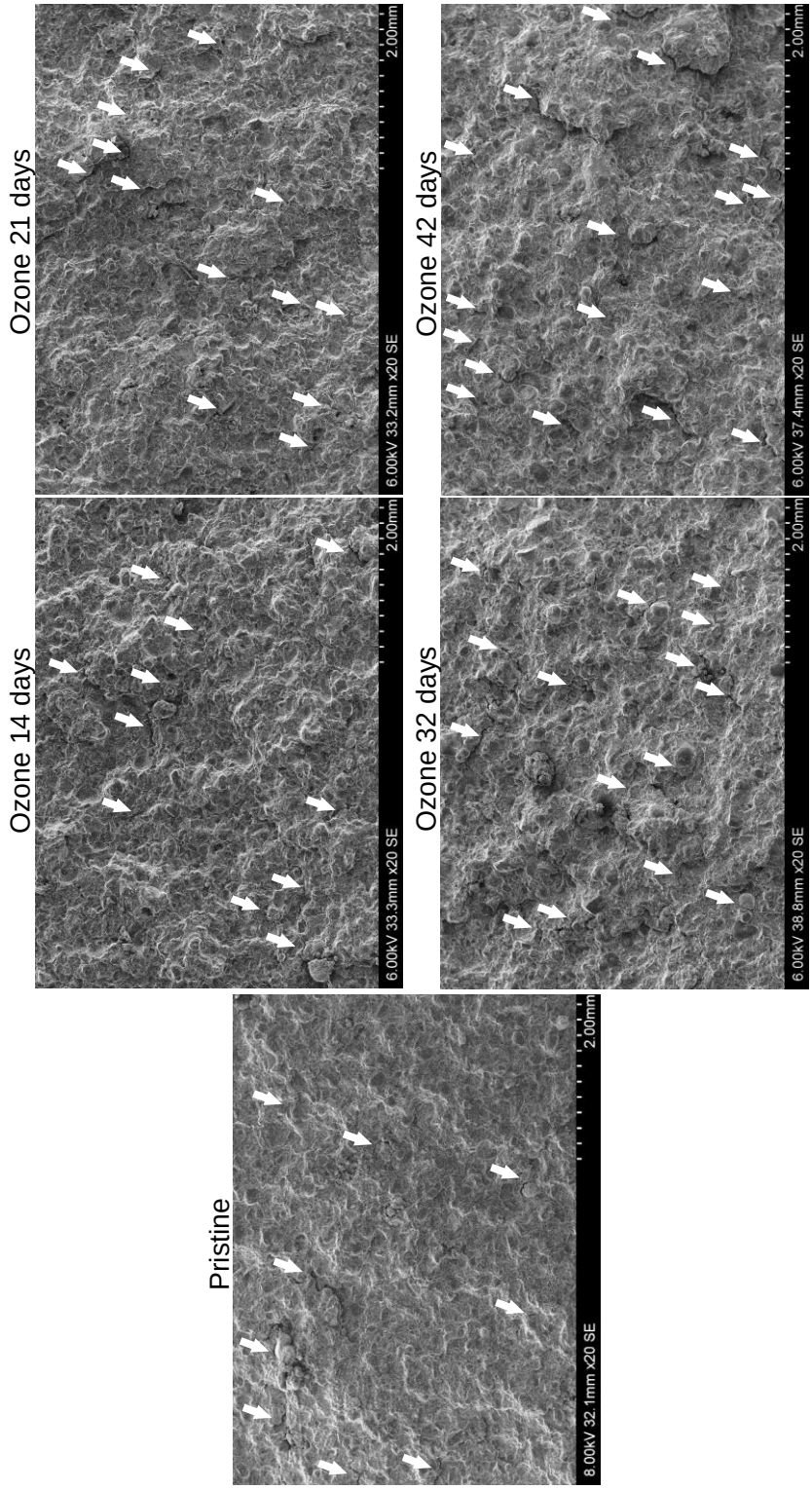

Fig. 85. SEM micrographs of the fracture surfaces from fracture samples ozone aged for 14, 21, 32 and 42 days together with pristine propellant at x20 magnifications. White arrows indicate visible cracks.

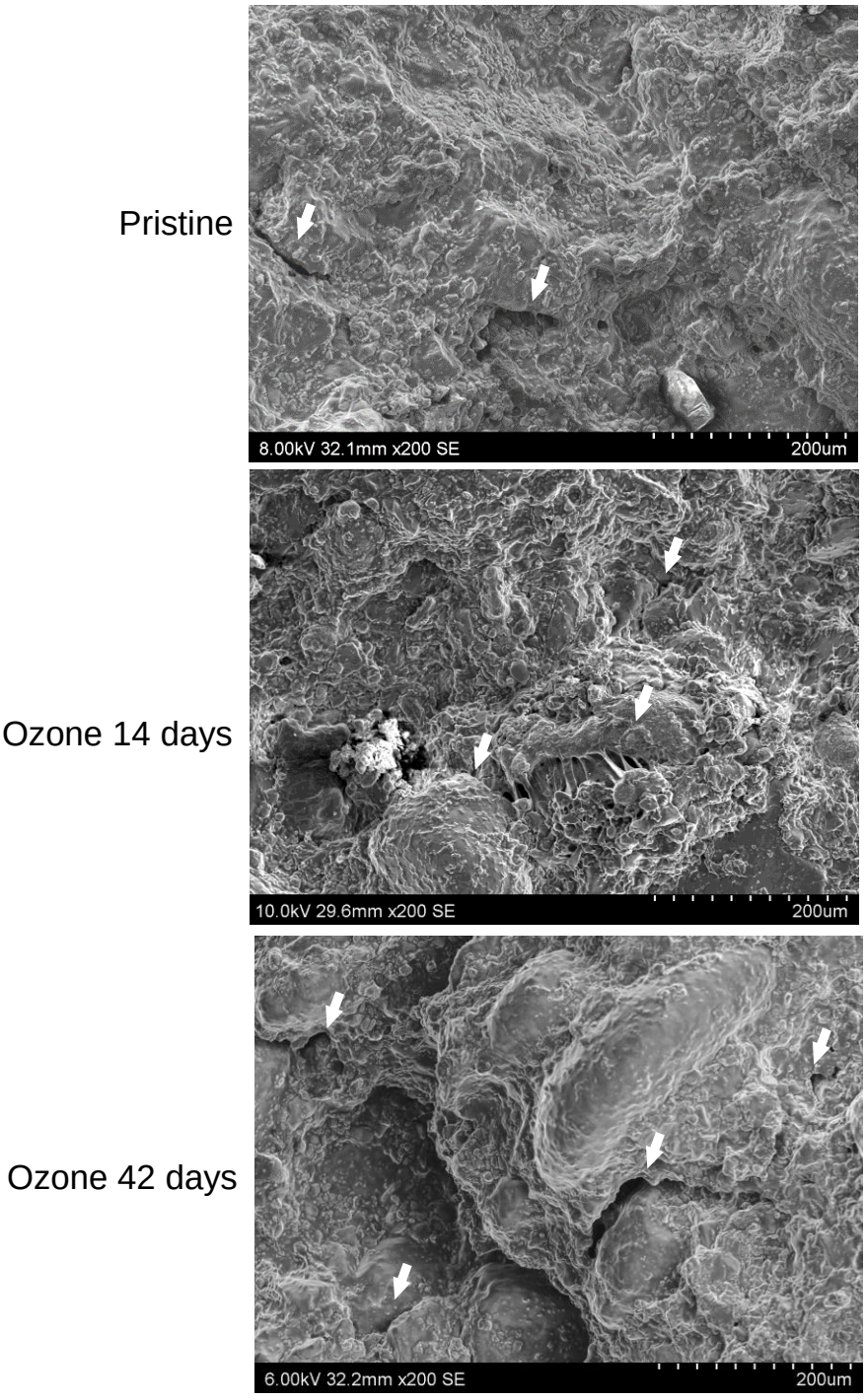

***Fig. 86**. SEM micrographs of the fracture surfaces from fracture samples ozone aged for 14, 21, 32 and 42 days together with pristine propellant at x20 magnifications. White arrows indicate visible cracks.*

Chapter 6. Discussion

6.1. Cohesive stress as a fracture characterising parameter

After studying with metals, which are considered as inelastic time-independent materials, A.A. Wells and G.R. Irwin related the displacements of the crack sides to the stress intensity factor (Irwin, 1961; Wells, 1961). The strip-yield model was rapidly derived (Dugdale, 1960; Irwin, 1961; Wells, 1961; Barenblatt, 1962) pursuing the use of the CTOD as a fracture parameter for yielding materials (Burdekin et al., 1966). This model assumes that a small plastic zone at the crack tip exists, where a closure stress hold both sides of the crack. At the end of the yield zone, the distance between crack sides is considered as the CTOD, cf. **Fig. 87**. For linear elastic fracture mechanics (LEFM) approach, the relationship between CTOD and energy release rate G is given by

$$G = m\sigma_Y\delta \tag{88}$$

where m is a dimensionless constant that depends on the crack tip triaxiality and σ_Y represents the yield stress. Expression (88) if formally equal to the derived for J integral fracture parameter in (89).

$$J = m\sigma_Y\delta \tag{89}$$

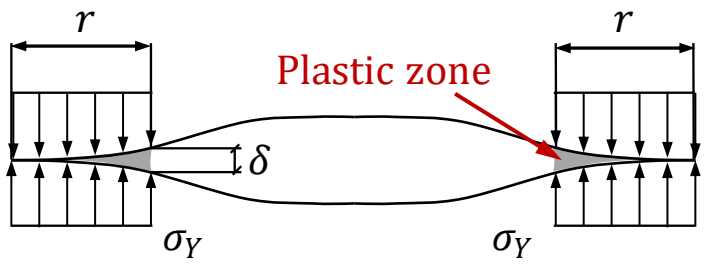

***Fig. 87**. Schematic of a strip yield model crack in a centred crack panel subjected to a tensile remote loading. Adapted from (Anderson, 2017).*

The previous expression is clearly valid for linear-elastic regime where $G = J$, (Anderson, 2017). Schapery's development of viscoelastic or pseudo J

integral is based on the previous idea of a yielding region at the crack tip as a failure zone, described in section 2.4.3.2. This was further explored with composite solid propellants (Tussiwand et al., 2009). Making use of the correspondence principle, the relation between fracture parameters J^R and δ^R might be defined as

$$J^R = \sigma_m \delta^R \tag{90}$$

where σ_m is the closure or cohesive stress at the failure zone, assumed to be constant in the failure zone.

The previously presented fracture results given in terms of the pseudo variables, pseudo J integral, J^R, and pseudo CTOD, δ^R, are dependent on the choice of the reference modulus E_R. Therefore, pseudo fracture parameters themselves cannot be interpreted as material parameters, although they might serve for comparison, as in Chapter 5. Nevertheless, the closure stress σ_m is independent on the chosen reference modulus since both fracture parameters are inversely proportional to E_R. Therefore, σ_m will be studied.

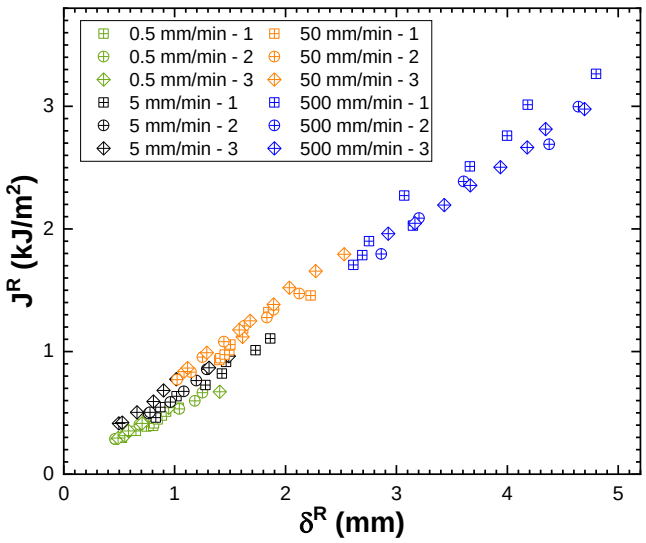

***Fig. 88**. Pseudo J integral, J^R versus pseudo CTOD, δ^R, of fracture samples tested at 0.5, 5, 50 and 500 mm/min for the preliminary characterisation.*

For the preliminary characterisation, experimental J^R and δ^R registered points are plotted against each other in **Fig. 88**. Expression in (90) assumes a linear relation between J^R and δ^R. It is appreciated in **Fig. 88** that the linear relation exists. The results of linear fitting of the experimental data of the curves to (90) are collected in **Table 21**. The closure stress σ_m as the slope of the regression and the coefficient of determination R^2 are reported. The high R^2 values confirm the linearity between J^R and δ^R. The determined σ_m shows an increase for increasing imposed crosshead displacement rate, with the exception of the 50 and 500 mm/min rates. Comparing those high rates, no difference is observed. In this case, it is observed that σ_{dew} is around 60% of σ_m.

Table 21. *Cohesive stress, σ_m, and coefficient of determination R^2 from the linear regression of the $J^R - \delta^R$ data to (90) of fracture specimens tested at 0.5, 5, 50 and 500 mm/min for the preliminary characterisation, together with the dewetting stress, σ_{dew}.*

Crosshead speed (mm/min)	σ_m (MPa)	R^2	σ_{dew} (MPa)
0.5	0.46±0.04	0.97±0.02	-
5	0.61±0.05	0.98±0.01	0.37±0.03
50	0.66±0.02	0.97±0.04	0.42±0.02
500	0.65±0.06	0.98±0.01	0.45±0.03

The corresponding $J^R - \delta^R$ curves of the aged samples are shown in **Fig. 89**. Mechanically aged samples in **Fig. 89**a experience a change in the slope compared to the pristine material, where the slope increases with the higher applied prestrain. The curves corresponding to the thermally aged samples in **Fig. 89**b move upwards with respect to the ones of the pristine samples. The opposite behaviour is shown by the ozone aged samples, cf. **Fig. 89**c, whose $J^R - \delta^R$ curves shift to lower fracture energies, J^R, and CTODs, δ^R.

The closure stress, σ_m, determined as the slope of the $J^R - \delta^R$ curves for the aged samples are gathered in **Table 22**, together with the corresponding dewetting stress, σ_{dew}. As mentioned before, mechanically aged samples at 15% and 30% shows an increase in the slope, i.e., the closure stress. The increase is believed to happen due to a hardening of the elastomeric matrix after

the initial "inelastic" region. Closure stress corresponding to the thermally aged samples also shows an increase with the increasing ageing times due to the reduction of the pseudo CTOD and growth of the fracture energy J^R, cf. **Fig. 89**b, derived from the growth in the crosslinking density. Ozone aged samples present a reduction of σ_m with respect to the pristine material, as a consequence of the rupture of the polymeric chains.

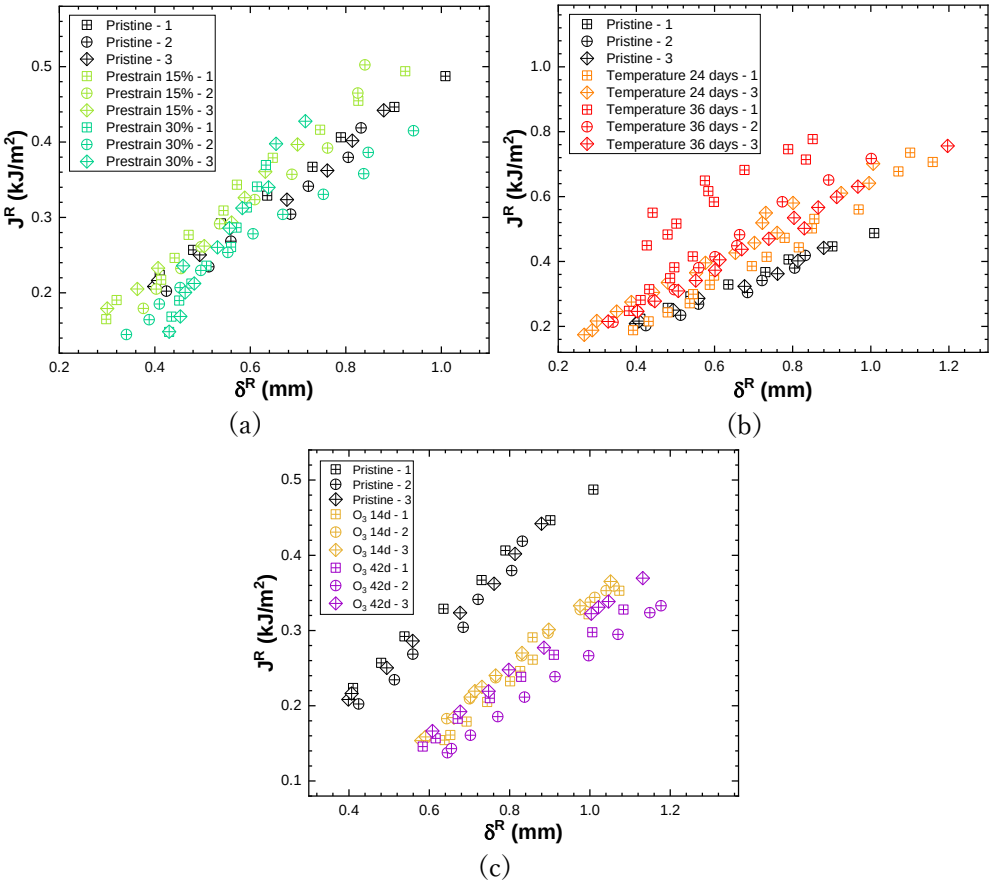

***Fig. 89**. Pseudo J integral, J^R, versus pseudo CTOD, δ^R, curves of the fracture samples for: (a) mechanical ageing for 15% and 30%, (b) thermal ageing for 24 and 36 days, and (c) ozone ageing for 14 and 42 days.*

Finally, all the determined σ_m have been correlated to the corresponding dewetting stress, with the exception of the data of the samples aged with ozone for 42 days. The differences found in the preliminary characterisation, cf.

Table 21, might be explained due to a less accurate determination of the relaxation function, which was improved for the ageing characterisation.

This demonstrates the approximation of the failure zone model to the strip yield model where σ_m in (90) would be the equivalent to σ_Y in (89). This would also mean that one of the most important fracture parameters could be determined just analysing the uniaxial tensile curves, allowing to have an expanded characterisation of the propellant grain without the necessity to carry out more tests, saving material, equipment, testing, time and, definitively, costs.

Table 22. Cohesive stress, σ_m, and coefficient of determination R^2 from the linear regression of the $J^R - \delta^R$ data to (90) together with the dewetting stress, σ_{dew}. Fracture specimens for the ageing characterisation.

Ageing source	σ_m (MPa)	R^2	σ_{dew} (MPa)
Pristine	0.47 ± 0.03	0.99 ± 0.01	0.44
Prestrain 15%	0.57 ± 0.05	0.98 ± 0.01	0.56
Prestrain 30%	0.8 ± 0.3	0.98 ± 0.02	0.85
Temperature 24 days	0.69 ± 0.03	0.98 ± 0.01	0.68
Temperature 36 days	0.8 ± 0.2	0.91 ± 0.2	0.81
Ozone 14 days	0.43 ± 0.02	0.99 ± 0.01	0.44
Ozone 42 days	0.35 ± 0.02	0.99 ± 0.01	0.18

6.2. On the use of the reference modulus

Cohesive models are somehow similar to the strip yield type models, in the sense that a failure zone ahead of the crack tip is considered. One of the simplest models for a cohesive model is a linear model, as represented in Fig. 90a, where σ is the stress in a material point, f_t is the stress at which the crack at the material point initiates its opening, u is the relative displacement between the crack's sides at the material point, u_c is the relative displacement at which the material point is no longer capable of bearing stresses (i.e., complete rupture) and W_F is the fracture energy.

The failure process zone is a similar conception. The closure stress, σ_m, varies along the failure zone, cf. **Fig. 90**b, although it is usually assumed constant, as in section 0. The definition of δ is u at the material point at the end of the failure zone.

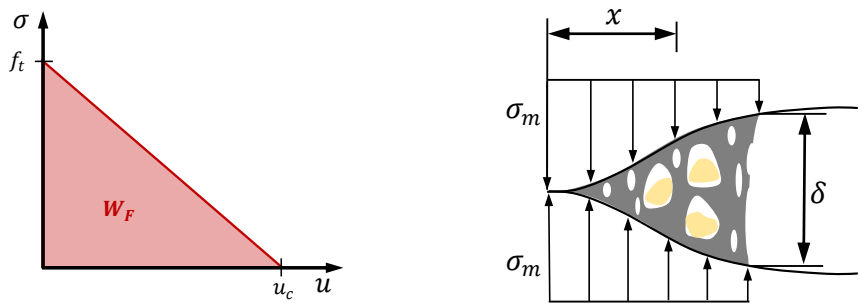

***Fig. 90**. Cohesive analogy to the failure process zone in composite solid propellants. (a) Linear cohesive model, (b) Schematic of a failure process zone at a crack tip for a composite solid propellant.*

Therefore, from a simplistic point of view, a linear cohesive model can be inferred for composite solid propellants using the closure stress σ_m as f_t and δ_c^R as u_c or J_c^R as W_F. All these fracture parameters are obtained through the viscoelastic fracture mechanics approach. Nevertheless, σ_m is the only parameter that is independent of the reference modulus E_R. The reference modulus is used as a normalising constant and its value is arbitrary, so that at least one more parameter needs to be defined removing the arbitrariness of the choice of E_R.

The reference modulus can be determined as a material parameter that best fits the load versus pseudo displacement curve to the load versus actual displacement. In that case, pseudo displacement would be equal to the actual displacements. This can also be done for strains.

An example of a fitting of a load versus displacement curve from a fracture test is shown in **Fig. 91**. The achieved result is fairly good. The difference between experimental and fitted curves is explained through the $u(t)$ and $u^R(t)$ being the displacements and pseudo displacement functions. Since the

displacement is imposed at a constant rate, $u(t)$ is a linear function of time. On its side, the $u^R(t)$ implies the relaxation in the loading process. Thus, $u^R(t)$ is a non-linear function. The relation between both function is given by (20), where the relaxation function is known. It is then, the reference modulus E_R the only fitting parameter involved in the fit. Since E_R is a constant, it is hard to believe that a perfect fitting can be reached.

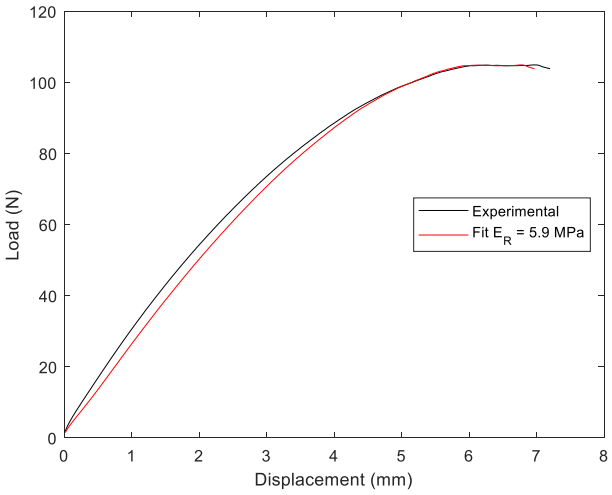

Fig. 91*. Fitting of load versus actual displacement curve with reference modulus E_R as a fitting parameter.*

The explained fit was done for fracture (load versus displacement curves) and tensile (stress versus strain curves) tests. The resulting E_R values are collected in **Table 23** and **Table 24**. Data from the preliminary characterisation in **Table 23** reveals that, following this methodology, E_R is dependent on the strain rate as it is the apparent elastic modulus E. It is also observed that E_R is lower than E for all tested strain rates, being E_R similar to an averaged modulus during the tests. The E_R values are coherent with the instantaneous and equilibrium modulus, E_0 and E_∞, respectively, since E_R for lower strain rates tends to E_∞ and E_R for higher strain rates tends to E_0.

***Table 23**. Comparison of the reference modulus, E_R, obtained through the fitting of the pseudo variables to the actual variables from fracture and tensile tests with the instantaneous modulus, E_0, equilibrium modulus, E_∞, and the apparent elastic modulus, E, for the preliminary characterisation.*

Crosshead displacement rate (mm/min)	Modulus (MPa)				
	E_0	E_∞	E	E_R as best fit (fracture)	E_R as best fit (tensile)
0.5	9.65	4.21	-	4.94±0.01	-
5	"	"	6.3±0.5	5.88±0.01	5.14±0.02
50	"	"	9.3±0.6	7.17±0.01	6.22±0.06
500	"	"	10.4±0.5	8.77±0.05	7.73±0.03

The E_R results for the ageing characterisation in **Table 24** reveal that E_R is more sensitive to strain rate that E. E_R is always lower than E and matches E_∞ for all conditions. This is reasonable since all the tests were performed at the crosshead displacement rate of 5 mm/min.

***Table 24**. Comparison of the reference modulus, E_R, obtained through the fitting of the pseudo variables to the actual variables from fracture and tensile tests with the instantaneous modulus, E_0, equilibrium modulus, E_∞, and the apparent elastic modulus, E, for the ageing characterisation.*

Crosshead displacement rate (mm/min)	Modulus (MPa)				
	E_0	E_∞	E	E_R as best fit (fracture)	E_R as best fit (tensile)
Pristine	8.3	2.2	6.2	2.33±0.01	2.25
Prestrain 15%	9.1	2.3	5.1	2.39±0.01	2.32
Prestrain 30%	8.5	2.1	4.5	2.19±0.01	2.14
Temperature 24 days	349	126	455	132.5±0.7	126
Temperature 36 days	413	144	494	153.3±0.6	144
Ozone 14 days	5.7	1.5	7.6	1.57±0.01	1.51
Ozone 42 days	4.8	1.4	1.4	1.41±0.01	1.36

Once the reference modulus is determined, the resulting critical pseudo J integral J_c^R or critical pseudo CTOD δ_c^R could define the cohesive law, i.e., characterise the fracture in the composite solid propellant.

6.3. Principal component analysis as a decision-making tool

Characterisation of composite solid propellant grains is vital to determine the usability of the solid rocket motors. An extensive number of tests are carried out in the surveillance programs of composite solid motors worldwide. Different approaches are followed to assess the prediction of remaining life of the motors. One of the most common is the Layton's law (2) based on the monitoring of chemical properties such as soluble fraction, crosslinking density (Dubois et al., 2002), or oxygen consumption (Tayefi et al., 2023), or mechanical properties such as elastic modulus (Adel et al., 2019), strain or stress at maximum of stress-strain curves (Shekhar, 2011), amongst others, but also through failure criteria under different loading (Wang et al., 2018a, 2023c, 2022f). As mentioned, different characteristics are tested during surveillance programs and generic guidelines are given to assess the in-service life of the motors (NATO-AOP-46, 2022). Nevertheless, no standardisation is found to determine precise criteria to order the disposal of the composite solid propellant motors. Indeed, most of the work available in the literature is focused on accelerated ageing based on isothermal accelerated ageing methods, so that developed criteria do not discriminate the source of the ageing that is inducing most damage in the propellant grain. To do this accurately, it would require intensive monitoring of the storage conditions over the life cycle of the motors (Chelner et al., 2005).

In this thesis, the principal component analysis (PCA) has been explored to analyse the determined chemical, mechanical and fracture properties. PCA has already been used by some authors for, e.g., in-service time prediction using FTIR testing (Chelouche et al., 2022) and vacuum stability tests

(Chelouche et al., 2021) of homogeneous solid propellants – or both (Chelouche et al., 2020) –, discrimination of thermal ageing conditions via laser-induced breakdown spectroscopy (Farhadian et al., 2016), Raman spectroscopy (Farhadian et al., 2017) or acousto-optic tuneable filtering technology to monitor the ageing of M1MP propellant (Feigley et al., 2004).

Principal component analysis is an algorithm to extract factors for a factor analysis (FA), a multivariate data analysis method. The FA methods allow the reduction of variables, while preserving most of the information of the original data and help to structure the information so that it is possible to devise causes that determine the correlation between variables. PCA stands as a useful tool for the handling of all properties analysed in the surveillance programs and, particularly, in this thesis. A number of properties showing different trends presents a challenge. A reduced number of variables can be worked to facilitate the identification of samples affected by different ageing sources.

Firstly, since available data is scarce, Monte Carlo method was used to generate an arbitrary large amount of 500 data points for each ageing condition and measured variable. Data points were created randomly using the average value of each property and within its standard deviation, assuming a normal distribution. The standard deviation of properties where there is no standard deviation, has been considered as a 5% of the mean value. Since measured properties have different natures and employed quantifying magnitudes may differ significantly, standardisation of data is necessary before applying the PCA algorithm. Standardisation was performed as

$$z_{ij} = \frac{x_{ij} - \bar{x}_j}{s_j} \tag{91}$$

where i denotes the observation (sample) and j the variable (property). Then, z_{ij} is the standardised value of the j^{th} variable corresponding to the i^{th} observation, x_{ij} is the value of the j^{th} variable corresponding to the i^{th} observation, $\bar{x}_j$ the mean value of the j^{th} variable and s_j the standard deviation of the j^{th}

variable. Standardisation assures that z_j has a mean value of 0 and its variance and standard deviation are 1. If a variable presents a variance of 0, it means that the variable does not carry information for the analysis.

To determine if a factor analysis is suitable, the correlation matrix R must be analysed. If Z is the matrix containing the standardised values, the correlation matrix is R can be determined through

$$R = \frac{1}{n-1} Z^T Z \tag{92}$$

where n is the total number of observations (samples). In this case, $n = 3500$ since there are 500 data point for each ageing condition plus pristine condition. The resulting correlation matrix for instantaneous modulus, E_0, apparent elastic modulus, E, true strain at maximum, ε_{max}, true stress at maximum, σ_{max}, true strain at dewetting, ε_{dew}, critical pseudo J integral, J_c^R, J resistance parameters C_1 and C_2 and cohesive or closure stress, σ_m, variables is shown in **Table 25**. Correlation coefficients are, in general, high enough (above 0.3) to find factor analysis (PCA) suitable.

***Table 25**. Correlation matrix, R, for instantaneous modulus, E_0, apparent elastic modulus, E, true strain at maximum, ε_{max}, true stress at maximum, σ_{max}, true strain at dewetting, ε_{dew}, critical pseudo J integral, J_c^R, J resistance parameters C_1 and C_2 and cohesive stress, σ_m.*

	E_0	E	ε_{max}	σ_{max}	ε_{dew}	J_c^R	C_1	C_2	σ_m
E_0	1.000	0.996	-0.860	0.573	-0.740	0.417	0.868	0.472	0.515
E	0.996	1.000	-0.857	0.571	-0.744	0.414	0.869	0.473	0.509
ε_{max}	-0.860	-0.857	1.000	-0.654	0.568	-0.412	-0.753	-0.426	-0.589
σ_{max}	0.573	0.571	-0.654	1.000	-0.180	0.371	0.655	0.545	0.660
ε_{dew}	-0.740	-0.744	0.568	-0.180	1.000	-0.641	-0.734	-0.035	-0.035
J_c^R	0.417	0.414	-0.412	0.371	-0.641	1.000	0.595	0.033	0.070
C_1	0.868	0.869	-0.753	0.655	-0.734	0.595	1.000	0.431	0.436
C_2	0.472	0.473	-0.426	0.545	-0.035	0.033	0.431	1.000	0.487
σ_m	0.515	0.509	-0.589	0.660	-0.035	0.070	0.436	0.487	1.000

The idea behind factor analysis is to express the observations as a linear combination of uncorrelated latent factors (principal components) that maximises the variance of data. Then, Z can be expressed as

$$Z = PK^T \tag{93}$$

where P is the factor scores matrix and K is the factor loading matrix. If standardised data is used, the correlation matrix R is equivalent to the covariance matrix and, therefore, singular value decomposition (SVD) can be used to determine the latent factors (principal components) in K. Following SVD, a matrix can be factorised as

$$R = USV^T \tag{94}$$

where U is a rotation matrix whose columns are the eigenvectors of RR^T, S is a scaling diagonal matrix whose values correspond to the square root of RR^T and V^T is a rotation matrix who rows are the eigenvectors of R^TR. In the case of the correlation matrix R, both U and V^T are equal and their columns are the principal components, i.e., the eigenvectors of RR^T define the principal components. Since the analysis is made through the correlation matrix (standardised values), the loading factor matrix K presents the correlation between original variables and latent variables.

The loading factor matrix for the case under study is shown in **Table 26**. For the first principal component (PC1), cross-loading is found since all variables seem to correlate similarly to PC1. Attending to PC2, it is ε_{dew}, C_2 and σ_m the most important variables, closely followed by σ_{max} and J_c^R, whereas for PC3 the variables that are more correlated are σ_{max} and J_c^R. Analogous analysis can be made for all principal components. Nevertheless, the interest lies in the reduction of variables. Hence, it is necessary to decide which of the new variables (principal components) contain enough information. Eigenvalues in S explain the variance of each principal component. Consequently, the higher the eigenvalue, the higher the share of variance explained by the PC. Data

corresponding to the eigenvalues associated to each of the principal components and the percentage of the variance explained by each PC as the ratio of the eigenvalue to the sum of all eigenvalues ($S_{ii} = \mathrm{tr}\,(S)$) is collected in **Table 27**.

***Table 26**. Loading factor matrix values for all possible (nine) principal components. Each principal component is defined by an eigenvector with loading factor in each variable of the original subspace.*

	PC1	PC2	PC3	PC4	PC5	PC6	PC7	PC8	PC9
E_0	0.40646	-0.05587	-0.3098	-0.03996	-0.02542	0.03734	0.2361	0.42942	-0.70137
E	0.40607	-0.05837	-0.31529	-0.032	-0.03436	0.05003	0.24723	0.39877	0.71235
ε_{max}	-0.38389	-0.04676	0.09592	0.26707	0.17579	0.76666	0.33061	0.20472	-0.00526
σ_{max}	0.31548	0.31921	0.49887	-0.0276	-0.59534	0.14277	0.38041	-0.17127	-0.00901
ε_{dew}	-0.29859	0.51473	0.19536	-0.03075	-0.14263	-0.1544	-0.29768	0.68819	0.01951
J_c^R	0.2377	-0.41746	0.6937	0.15434	0.37247	-0.22355	0.04374	0.271	0.01104
C_1	0.39597	-0.12185	0.0558	0.11908	-0.1678	0.49431	-0.73379	0.01115	-0.00004
C_2	0.23077	0.45579	-0.10635	0.78678	0.25743	-0.14184	0.01175	-0.1487	-0.00439
σ_m	0.25941	0.47704	0.11285	-0.51702	0.59945	0.22287	-0.00343	-0.12673	0.00333

***Table 27**. Eigenvalues of S scaling matrix for all principal components, together with their correspondent percentage of variance and cumulative variance.*

Principal component	Eigenvalue	Percentage of variance (%)	Cumulative percentage of variance (%)
1	5.48	60.92	60.92
2	1.63	18.13	79.05
3	0.71	7.88	86.93
4	0.55	6.07	93.00
5	0.26	2.88	95.88
6	0.21	2.31	98.19
7	0.09	0.99	99.18
8	0.07	0.78	99.96
9	0.004	0.04	100

It is common to represent this data graphically as in **Fig. 92**, called scree plot. The convention is that there are as many necessary PC as PC components are before reaching the "elbow". It is seen that using PC1 and PC2 would maintain ≈80% of the original information and using the first three components would keep ≈87% of the information.

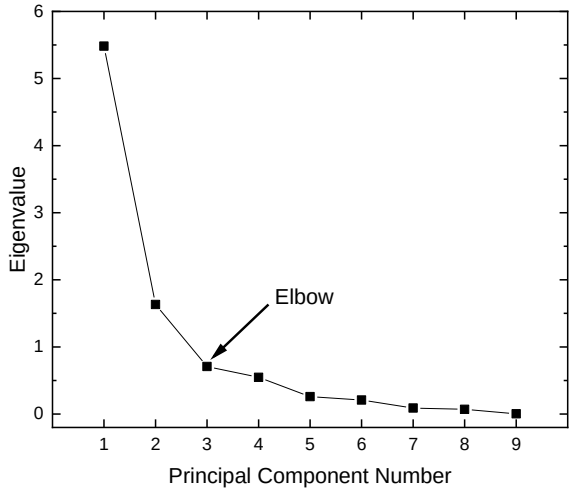

***Fig. 92**. Scree plot of the principal component analysis for all the possible principal components.*

Finally, data from each sample must be represented in the new subspace. Once K is known, scores in P matrix can be determined through (95).

$$P = ZK \tag{95}$$

The representation of the data for PC1, PC2 and PC3, i.e., score plot for principal components 1, 2 and 3 is displayed in **Fig. 93**. Data points associated with each type of ageing has been identified. It is seen in **Fig. 93**a that the components carrying the most information, PC1 and PC2 explain ≈80% of the variance, help to discriminate the propellant affected by the different ageing sources at a glance. The observed general trends are that mechanical ageing shifts data to higher values of PC2 with respect to pristine propellant, while thermal ageing moves to higher PC1 values and ozone aged samples to lower PC1 values than pristine material. Smaller shifts are contemplated in the other principal component. If PC1 and PC3 are contemplated, cf. **Fig. 93**b, the

reported information is not enough to discriminate mechanical ageing from ozone ageing, although it is to differentiate the thermal ageing. Looking at **Fig. 93**c, PC2 again seems to carry the information corresponding to the mechanical ageing, while PC3 does not contain the information to differentiate ozone ageing from thermal ageing. In all cases, pristine material is distinguished from the aged samples.

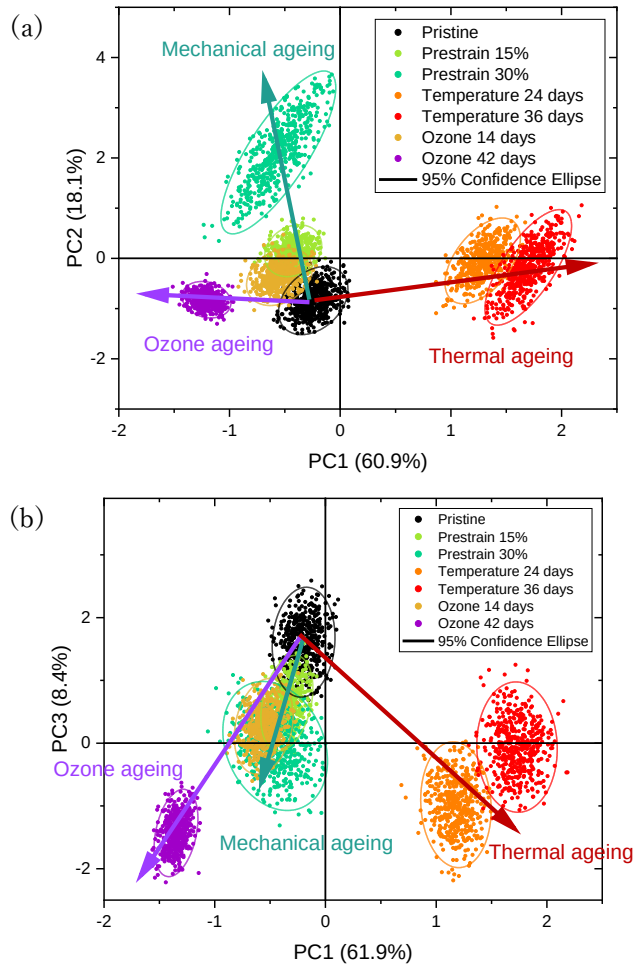

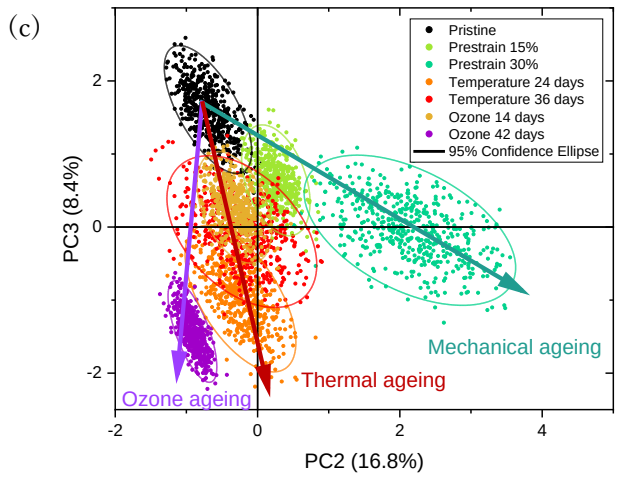

Fig. 93*. Score plot for (a) PC1 and PC2, (b) PC1 and PC3, (c) PC2 and PC3. Data points belonging to each ageing type have been identified together with the corresponding 95% confidence ellipse.*

The loading factors in K are plotted together with the scores in P as shown in **Fig. 94** for PC1 and PC2. This is a graphical representation of results in **Table 26** known as biplot. The conclusions are the same as stated above. PC1 is affected by all variables in a similar manner. PC2 is rather affected by ε_{dew}, σ_{max}, σ_m, J_c^R and C_2.

Here, correlation between original variables and principal components is translated to the ageing groups. Mechanical aged samples are correlated positively to ε_{dew} and σ_m and inversely to J_c^R. Thermal aged samples undergo greatest variations of E, E_0 and C_1 with strong inverse correlation to ε_{max} and ε_{dew}. σ_{max}, σ_m. Ozone ageing is correlated positively to greater ε_{max} while inversely to the E, E_0 and C_1. Conclusions are in line with the mentioned in section 5.2. This is a proof of the suitability of PCA to maintain the information given by the original variables.

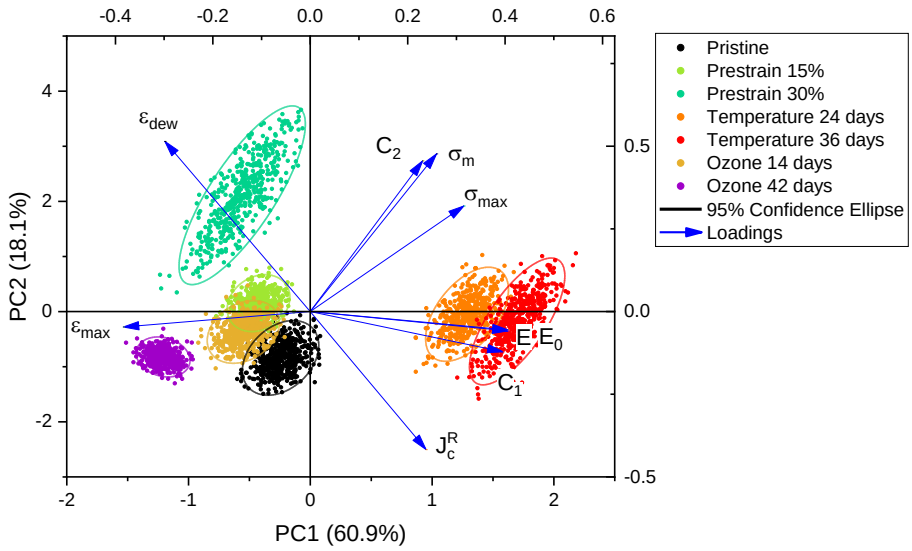

Fig. 94*. Biplot for principal components 1 and 2. Influence of original variables on the ageing of the propellant.*

Thus, it is demonstrated that PCA represents a useful tool to determine the ageing of composite solid propellants. Further work is needed to stablish criteria to make PCA a decision-making tool when it comes to service life prediction or safety address. As seen, discrimination of the different ageing has been achieved without accounting for the chemical characterisation of the propellant. There is, therefore, possibility to redefine surveillance programs in order to optimise the required testing and data analysis, leading to more economic surveillance systems.

Chapter 7. Conclusions

The main conclusion of this work is that fracture characterisation of composite solid propellants still represents a challenge, although practical information can be derived from the fracture behaviour of these materials. Further conclusions have arisen throughout the thesis. They are described as follows.

- Schapery's approach effectively accounts for the viscous behaviour of the elastomeric matrix.
- Load separation property is confirmed for composite solid propellants when Schapery's viscoelastic theory is applied. Therefore, constraint parameter η can be determined experimentally making use of this property.
- Primary rupture process in the propellant is the matrix tearing. However, dewetting damage is induced when the loading rate is sufficiently high. Otherwise, fracture occurs only due to matrix tearing.
- After the application of Schapery's viscoelastic fracture mechanics approach, determined fracture parameters are still strain rate dependent.
- Mechanical ageing at high strain rates is linked to dewetting and slight hardening of the elastomeric matrix, without resulting in changes in the crosslinking density. Relaxation behaviour did not vary with this ageing and mechanical behaviour showed Mullin's effect affectation. Fracture behaviour was hardly modified, requiring little less energy to propagate the crack in aged propellant. While propagation initiates easier in mechanically aged material, crack propagation takes place in a similar manner as in non-aged propellant. The variation of the fracture energy was associated to the energy already used in the ageing to produce the dewetting, since the elastomeric matrix does not experience significant changes. Regarding the CTOD, similar trend was observed as for J integral.
- Thermal ageing has been associated with the increase in crosslinking density and, therefore, in propellant stiffness and strength. Comparing

J integral and CTOD response, once the viscoelastic part is discarded, the resistance curves in terms of J integral are above the ones of the pristine material but those in terms of CTOD of aged samples tend to collapse to one curve independently of the ageing time. This is directly correlated to the changes in the mechanical capabilities of the elastomeric matrix and the fact that the fracture process is produced primarily through the matrix tearing, with a more stable crack propagation with ageing time.

- Ozone ageing has been successfully employed to simulate the ageing produced due to the exposition to ambient conditions. The ozonolysis reactions affected the elastomeric matrix reducing its crosslinking density. This resulted in lowered stiffness, mechanical and fracture performances. Cracks in ozone aged propellant begin to grow at lower fracture energies and its propagation is less resistant and stable as compared to the non-aged material, which directly related to the weakening of the polymeric chains, since fracture progress happens fundamentally through the tearing of the matrix. Due to the lack of cohesion in the aged material, the CTOD resistance curves of aged samples were above those of the pristine material.
- The concept of pseudo fracture parameters as defined through Schapery's viscoelastic fracture mechanics approach presents as a main drawback the dependence of the parameters on the arbitrarily chosen reference modulus.
- The unique fracture parameter that is free of the chosen reference modulus is the closure or cohesive stress, which has been found suitable to describe partially the fracture behaviour of the composite solid propellant.
- The cohesive or closure stress has been correlated to the identified dewetting stress.

- Principal component analysis represents a suitable tool to assess the in-service life prediction of composite solid propellant. Moreover, with this method, it is possible to account for the ageing source affecting the propellant grain.

Chapter 8. Future work

The results and conclusions of this thesis have put some issues to the table and greater efforts are needed to solve them. It has opened the door to new possible pathways to walk as well. Some of the most interesting issues or future work to address could be the following:

- Fracture tests have been analysed removing the creep effects of the material. Nevertheless, in this analysis, the effect of the induced damage in the bulk of the sample during the loading has not been accounted for. Further analysis to account for the damage or even ageing would improve the characterisation.
- To correlate microstructural variables that depend on ingredients of the binder system to the fracture parameters.
- The constraint factor η has been assumed independent on the ageing of the propellant, i.e., material properties, and crack length. A study of the constraint factor evolution with the different ageing procedures would provide more knowledge about, constraint factor in elastomeric materials.
- Mentioned issues with reference modulus in the application of Schapery's viscoelastic fracture mechanics approach requires further analysis and derivations of the methodology, making it an exciting field to explore in order to have trustful and handy testing and analysis procedures to implement in the surveillance programs.
- The work summarised in this thesis is based on experimental approach. Then, there is a large set of data that could be exploited to develop constitutive or fracture numerical models that accounts for the different types of ageing. Multiscale approach seems a good start point.
- Mechanical ageing in this thesis was chosen as an extreme case. To simulate different mechanical ageing conditions, it is suggested to explore the application of the loading based on small dynamic loadings (vibrations).

- The ozone ageing is a novel approach to simulate the exposition of the propellant grain to ambient air. There are lots of remaining issues to address here such as the determination of how the ageing is taking place or settle appropriate ozone concentration and ageing times to reproduce actual ageing of the composite solid propellants.
- Surveillance systems for composite solid propellants in Spain are not fully optimised. As seen, there are tools to redefine the programs based on the relevance of the measured characteristics. Therefore, a research opportunity arises to determine the pertinent variables and the corresponding tests to perform.
- Following the latter, PCA might be a useful and widespread known statistical tool, but it has limitations. To optimise the surveillance programs and help in the service life predictions of composite solid propellant motors, neural networks and artificial intelligence are alternative approaches to PCA as they are more versatile and powerful.

References

Adel, W. M., and Liang, G. (2019). Service life prediction of AP/Al/HTPB solid rocket propellant with consideration of softening aging behavior. *Chinese Journal of Aeronautics*, *32*(2), 361–368. doi: 10.1016/j.cja.2018.08.003

Aksel, N., and Hübner, Ch. (1996). The influence of dewetting in filled elastomers on the changes of their mechanical properties. *Archive of Applied Mechanics*, *66*(4), 231–241. doi: 10.1007/BF00787351

Alfrey, T. (1944). Non-homogeneous stresses in visco-elastic media. *Quarterly of Applied Mathematics*, *2*(2), 113–119. doi: 10.1090/qam/10499

Anachkov, M. P., Rakovsky, S. K., Shopov, D. M., Razumovskii, S. D., Kefely, A. A., and Zaikov, G. E. (1985). Study of the ozone degradation of polybutadiene, polyisoprene and polychloroprene in solution. *Polymer Degradation and Stability*, *10*(1), 25–42. doi: 10.1016/0141-3910(85)90018-7

Anderson, T. L. (2017). *Fracture Mechanics*. CRC Press. doi: 10.1201/9781315370293

Antich, P., Vázquez, A., Mondragon, I., and Bernal, C. (2006). Mechanical behavior of high impact polystyrene reinforced with short sisal fibers. *Composites Part A: Applied Science and Manufacturing*, *37*(1), 139–150. doi: 10.1016/j.compositesa.2004.12.002

AOP-48. (2008). *Explosives, nitrocelulose-based propellants, stability test procedures and requirements using stabilizer depletion*. North Atlantic Treaty Organization (NATO).

ASTM D1149. (2018). *Standard Test Methods for Rubber Deterioration—Cracking in an Ozone Controlled Environment* (p. 14). ASTM International.

ASTM D6068. (2018). *Standard Test Method for Determining J-R Curves of Plastic Materials* (p. 8). ASTM International.

ASTM E1830. (2018). *Standard Test Method for Measurement of Fracture Toughness* (p. 55). ASTM International.

Azoug, A., Constantinescu, A., Nevière, R., and Jacob, G. (2015). Microstructure and deformation mechanisms of a solid propellant using 1H NMR spectroscopy. *Fuel*, *148*, 39–47. doi: 10.1016/j.fuel.2015.01.074

Azoug, A., Constantinescu, A., Pradeilles-Duval, R. M., Vallat, M. F., Nevière, R., and Haidar, B. (2013a). Effect of the sol fraction and hydrostatic deformation on the viscoelastic behavior of prestrained highly filled elastomers. *Journal of Applied Polymer Science*, *127*(3), 1772–1780. doi: 10.1002/APP.37800

Azoug, A., Thorin, A., Nevière, R., Pradeilles-Duval, R. M., and Constantinescu, A. (2013b). Influence of orthogonal prestrain on the

viscoelastic behaviour of highly-filled elastomers. *Polymer Testing*, *32*(2), 375–384. doi: 10.1016/J.POLYMERTESTING.2012.12.005

Bader, H. (1982). Determination of Ozone In Water By The Indigo Method: A Submitted Standard Method. *Ozone: Science & Engineering*, *4*(4), 169–176. doi: 10.1080/01919518208550955

Bader, H., and Hoigné, J. (1981). Determination of ozone in water by the indigo method. *Water Research*, *15*(4), 449–456. doi: 10.1016/0043-1354(81)90054-3

Badgujar, D. M., Talawar, M. B., Zarko, V. E., and Mahulikar, P. P. (2017). New directions in the area of modern energetic polymers: An overview. *Combustion, Explosion, and Shock Waves*, *53*(4), 371–387. doi: 10.1134/S0010508217040013

Barenblatt, G. I. (1962). The Mathematical Theory of Equilibrium Cracks in Brittle Fracture. In *Advances in Applied Mechanics* (Vol. 7, pp. 55–129). Elsevier. doi: 10.1016/S0065-2156(08)70121-2

Begley, J. A., and Landes, J. D. (1972). The J Integral as a Fracture Criterion. In H. Corten (Ed.), *Fracture Toughness, Proceedings of the 1971 National Symposium on Fracture Mechanics, Part II, ASTM STP 514* (pp. 1–23). American Society for Testing and Materials. doi: 10.1520/STP38816S

Belitsky, J., Ore, E., and Weller, T. (2023, January 23). Solid Propellant Macro-scale Behavior in Presence of Micro-scale Failure Mechanisms under Tension and Cyclic Loads. *AIAA SCITECH 2023 Forum*. AIAA SCITECH 2023 Forum, National Harbor, MD & Online. doi: 10.2514/6.2023-2234

Bencher, C. D., Dauskard, R. H., and Ritchie, R. O. (1995). Microstructural damage and fracture processes in a composite solid rocket propellant.

Journal of Spacecraft and Rockets, *32*(2), 328–334. doi: 10.2514/3.26614

Bennet, J. (1997). Technical evaluation report for the 87th symposium of the propulsion and energetics panel on service life of solid propellant systems. *AGARD Conference Proceedings 586*, T1–T17.

Blanchard, A. F., and Parkinson, D. (1952). Breakage of Carbon-Rubber Networks by Applied Stress. *Industrial & Engineering Chemistry*, *44*(4), 799–812. doi: 10.1021/ie50508a034

Bohn, M. A. (2017, November 10). Principles of ageing of double base propellants. *Advances in Munition Health Management Technologies and Implementation*. STO-MP-AVT-268. doi: 10.14339/STO-MP-AVT-268

Boltzmann, L. E. (1874). Zur Theorie der elastischen Nachwirkung. *Sitzungsberichte der Mathematisch-Naturwissenschaftlichen Classe der Kaiserlichen Akademie der Wissenschaften*, *70*(2), 275–300.

Bondarchuk, S. S., Matveev, A. E., Promakhov, V. V., Vorozhtsov, A. B., Zhukov, A. S., Zhukov, I. A., and Ziatdinov, M. H. (2018). Synthesis and Properties of Energetics Metal Borides for Hybrid Solid-Propellant Rocket Engines. *Proceedings of the Scientific-Practical Conference 'Research and Development - 2016'*, 511–519. doi: 10.1007/978-3-319-62870-7_54

Bozic, V., and Jankovski, B. (2017). Some Civilian Applications of Solid Propellants. In *Chemical Rocket Propulsion* (pp. 935–962). Springer International Publishing. doi: 10.1007/978-3-319-27748-6_39

Brzić, S., Dimić, M., Jelisavac, L., Djonlagić, J., Uščumlić, G., and Bogdanov, J. (2015). Influence of Polyglycidyl-type Bonding Agents on the

Viscoelastic Properties of a Carboxyl-terminated Poly(butadiene-co-acrylonitril e)-based Composite Rocket Propellant. *Central European Journal of Energetic Materials*, *12*(2), 307–321.

Bucci, R. J., Paris, P. C., Landes, J. D., and Rice, J. R. (1972). J integral estimation procedures. *Fracture Toughness, Proceedings of the 1971 National Symposium on Fracture Mechanics, Part II, ASTM STP 514*, 40–69. doi: 10.1520/STP38818S

Bueche, F. (1960). Molecular basis for the mullins effect. *Journal of Applied Polymer Science*, *4*(10), 107–114. doi: 10.1002/app.1960.070041017

Bunyan, P., Cunliffe, A. V., Davis, A., and Kirby, F. A. (1993). The degradation and stabilisation of solid rocket propellants. *Polymer Degradation and Stability*, *40*(2), 239–250. doi: 10.1016/0141-3910(93)90211-Z

Burdekin, F. M., and Stone, D. E. W. (1966). The crack opening displacement approach to fracture mechanics in yielding materials. *Journal of Strain Analysis*, *1*(2), 145–153. doi: 10.1243/03093247V012145

Carvalho, H. S. S., and Ruggieri, C. (2010). Significance of the Plastic Eta Factor in J Estimation Procedures for Tensile SE(T) Fracture Specimens. *ASME 2010 Pressure Vessels and Piping Conference: Volume 6, Parts A and B*, 991–1000. doi: 10.1115/PVP2010-25031

Cataldo, F. (2019). Protection Mechanism of Rubbers from Ozone Attack. *Ozone: Science & Engineering*, *41*(4), 358–368. doi: 10.1080/01919512.2018.1542518

Celina, M., Gillen, K. T., and Assink, R. A. (2005). Accelerated aging and lifetime prediction: Review of non-Arrhenius behaviour due to two competing processes. *Polymer Degradation and Stability*, *90*(3), 395–404. doi: 10.1016/j.polymdegradstab.2005.05.004

Celina, M., Minier, L., and Assink, R. (2002). Development and application of tools to characterize the oxidative degradation of AP/HTPB/Al propellants in a propellant reliability study. *Thermochimica Acta*, *384*(1), 343–349. doi: 10.1016/S0040-6031(01)00793-6

Cerri, S., Bohn, M. A., Menke, K., and Galfetti, L. (2009). Ageing Behaviour of HTPB Based Rocket Propellant Formulations. *Central European Journal of Energetic Materials*, *6*(2), 149–165.

Cerri, S., Bohn, M. A., Menke, K., and Galfetti, L. (2013). Aging of HTPB/Al/AP Rocket Propellant Formulations Investigated by DMA Measurements. *Propellants, Explosives, Pyrotechnics*, *38*(2), 190–198. doi: 10.1002/prep.201200186

Chang, S., Han, S., and Malone, B. (2000, July 24). *Numerical analysis of moisture propagation and chemical reaction in a solid propellant*. 36th AIAA/ASME/SAE/ASEE Joint Propulsion Conference and Exhibit, Las Vegas, NV, U.S.A. doi: 10.2514/6.2000-3180

Chaturvedi, S., and Dave, P. N. (2019). Solid propellants: AP/HTPB composite propellants. *Arabian Journal of Chemistry*, *12*(8), 2061–2068. doi: 10.1016/J.ARABJC.2014.12.033

Chelner, H., Buswell, J., and Evans, D. (2005, July 10). *Embedded Sensors for Monitoring Solid Propellant Grains*. 41st AIAA/ASME/SAE/ASEE Joint Propulsion Conference & Exhibit, Tucson, AZ, U.S.A. doi: 10.2514/6.2005-4362

Chelouche, S., Trache, D., Benayachi, Z. I., Tarchoun, A. F., Khimeche, K., and Mezroua, A. (2020). A New Procedure for Stability Control of Homogeneous Solid Propellants by Combination of Vacuum Stability Test, FTIR and PCA. *Propellants, Explosives, Pyrotechnics*, *45*(7), 1088–1102. doi: 10.1002/prep.201900424

Chelouche, S., Trache, D., Benlemir, R., and Soudani, A. (2022). Principal Component Analysis of FTIR Data to Accurately Assess the Real/Equivalent In-Service-Times of Homogenous Solid Propellant. *Propellants, Explosives, Pyrotechnics*, *47*(6). doi: 10.1002/prep.202100352

Chelouche, S., Trache, D., Maamache, I., Tarchoun, A. F., Khimeche, K., and Mezroua, A. (2021). A new experimental way for the monitoring of the real/equivalent in-service-time of double base rocket propellant by coupling VST and PCA. *Defence Technology*, *17*(2), 440–449. doi: 10.1016/J.DT.2020.04.008

Cheng, T. (2019). Review of novel energetic polymers and binders – high energy propellant ingredients for the new space race. *Designed Monomers and Polymers*, *22*(1), 54–65. doi: 10.1080/15685551.2019.1575652

Chevalier, S., Liebens, E., and Neviere, R. (2003). Effects of the Diffusion Processes in the Modelling of Composite Propellant Ageing. *RTO-MP-091 AVT-089 Meeting Proceedings 91, Advances in Rocket Performance Life and Disposal*, 27-1/27-14.

Christiansen, A. G., Layton, L. H., and Carpenter, R. L. (1981). HTPB Propellant Aging. *Journal of Spacecraft and Rockets*, *18*(3), 211–215. doi: 10.2514/3.57807

Coquillat, M., Verdu, J., Colin, X., Audouin, L., and Nevière, R. (2007). Thermal oxidation of polybutadiene. Part 3: Molar mass changes of additive-free non-crosslinked polybutadiene. *Polymer Degradation and Stability*, *92*(7), 1343–1349. doi: 10.1016/j.polymdegradstab.2007.03.018

Criegee, R. (1975). Mechanism of Ozonolysis. *Angewandte Chemie International Edition in English*, *14*(11), 745–752. doi: 10.1002/anie.197507451

Cui, H., Shen, Z., and Li, H. (2018). A new constitutive equation for solid propellant with the effects of aging and viscoelastic Poisson's ratio. *Meccanica*, *53*(9), 2393–2410. doi: 10.1007/s11012-018-0829-z

Dannenberg, E. M. (1986). Bound Rubber and Carbon Black Reinforcement. *Rubber Chemistry and Technology*, *59*(3), 512–524. doi: 10.5254/1.3538213

Dannenberg, E. M., and Brennan, J. J. (1966). Strain Energy as a Criterion for Stress Softening in Carbon-Black-Filled Vulcanizates. *Rubber Chemistry and Technology*, *39*(3), 597–608. doi: 10.5254/1.3544867

Darwell, H. M., Parker, A., and Leeming, H. (1966). Mechanical behavior of cast-double-base propellants in rocket motors. *Journal of Spacecraft and Rockets*, *3*(3), 399–407. doi: 10.2514/3.28459

Davenas, A. (2003). Development of Modern Solid Propellants. *Journal of Propulsion and Power*, *19*(6), 1108–1128. doi: 10.2514/2.6947

Davis, A. (1963). Solid propellants: The combustion of particles of metal ingredients. *Combustion and Flame*, *7*, 359–367. doi: 10.1016/0010-2180(63)90212-8

Davis, D. (2001, July 8). *Use of dilatation in understanding composite propellant aging*. 37th Joint Propulsion Conference and Exhibit, Salt Lake City, UT ,U.S.A. doi: 10.2514/6.2001-3283

de Francqueville, F., Diani, J., Gilormini, P., and Vandenbroucke, A. (2021). Use of a micromechanical approach to understand the mechanical

behavior of solid propellants. *Mechanics of Materials*, *153*, 103656. doi: 10.1016/J.MECHMAT.2020.103656

de la Fuente, J. L. (2009). An analysis of the thermal aging behaviour in high-performance energetic composites through the glass transition temperature. *Polymer Degradation and Stability*, *94*(4), 664–669. doi: 10.1016/j.polymdegradstab.2008.12.021

DeLuca, L. T. (2016). Innovative Solid Formulations for Rocket Propulsion. *Eurasian Chemico-Technological Journal*, *18*(3), 181. doi: 10.18321/ectj424

DeLuca, L. T., Galfetti, L., Maggi, F., Colombo, G., Merotto, L., Boiocchi, M., Paravan, C., Reina, A., Tadini, P., and Fanton, L. (2013). Characterization of HTPB-based solid fuel formulations: Performance, mechanical properties, and pollution. *Acta Astronautica*, *92*(2), 150–162. doi: 10.1016/j.actaastro.2012.05.002

DeLuca, L. T., Shimada, T., Sinditskii, V. P., and Calabro, M. (Eds.). (2017a). *Chemical Rocket Propulsion: A Comprehensive Survey of Energetic Materials*. Springer International Publishing. doi: 10.1007/978-3-319-27748-6

DeLuca, L. T., Shimada, T., Sinditskii, V. P., and Calabro, M. (2017b). Highlights of Solid Rocket Propulsion History. In *Chemical Rocket Propulsion* (pp. 1015–1032). Springer International Publishing. doi: 10.1007/978-3-319-27748-6_42

DeLuca, L. T., Shimada, T., Sinditskii, V. P., Calabro, M., and Manzara, A. P. (2017c). An Introduction to Energetic Materials for Propulsion. In *Chemical Rocket Propulsion: A Comprehensive Survey of Energetic Materials* (pp. 3–59). Springer International Publishing. doi: 10.1007/978-3-319-27748-6_1

Diani, J., Fayolle, B., and Gilormini, P. (2009). A review on the Mullins effect. *European Polymer Journal*, *45*(3), 601–612. doi: 10.1016/J.EURPOLYMJ.2008.11.017

Doll, D. W., and Lund, G. K. (1992). Magnesium-neutralized propellant. *Journal of Propulsion and Power*, *8*(6), 1185–1191. doi: 10.2514/3.11460

Dong, G., Liu, H., Deng, L., Yu, H., Zhou, X., Tang, X., and Li, W. (2022). Study on the interfacial interaction between ammonium perchlorate and hydroxyl-terminated polybutadiene in solid propellants by molecular dynamics simulation. *E-Polymers*, *22*(1), 264–275. doi: 10.1515/epoly-2022-0016

Dubois, C., and Perreault, F. (2002). Shelf Life Prediction of Propellants Using a Reaction Severity Index. *Propellants, Explosives, Pyrotechnics*, *27*(5), 253–261. doi: 10.1002/1521-4087(200211)27:5<253::AIDPREP253>3.0.CO;2-8

Dugdale, D. S. (1960). Yielding of steel sheets containing slits. *Journal of the Mechanics and Physics of Solids*, *8*(2), 100–104. doi: 10.1016/0022-5096(60)90013-2

El-Sayed, A. F. (2016). *Fundamentals of Aircraft and Rocket Propulsion*. Springer London. doi: 10.1007/978-1-4471-6796-9

Ernst, H. A., Paris, P. C., and Landes, J. D. (1981). Estimations on J-Integral and Tearing Modulus. *Fracture Mechanics, Proceedings of the Thirteenth National Symposium on Fracture Mechanics, ASTM STP 743*, 476–502. doi: 10.1520/STP28814S

Ernst, H., Paris, P. C., Rossow, M., and Hutchinson, J. W. (1979). Analysis of Load-Displacement Relationship to Determine J-R Curve and Tearing Instability Material Properties. *Fracture Mechanics, Proceedings of the*

Eleventh National Symposium on Fracture Mechanics, Part I, ASTM STP 677, 581–599. doi: 10.1520/STP34937S

Farhadian, A. H., Tehrani, M. K., Keshavarz, M. H., and Darbani, S. M. R. (2017). Raman spectroscopy combined with principle component analysis to investigate the aging of high energy materials. *Laser Physics*, *27*(7), 075701. doi: 10.1088/1555-6611/aa7485

Farhadian, A. H., Tehrani, M. K., Keshavarz, M. H., Karimi, M., and Reza Darbani, S. M. (2016). Relationship between the results of laser-induced breakdown spectroscopy and dynamical mechanical analysis in composite solid propellants during their aging. *Applied Optics*, *55*(16), 4362. doi: 10.1364/AO.55.004362

Feigley, R., Jin, F., Lorenzo, J., Soos, J., and Trivedi, S. (2004). *Monitoring of chemical degradation in propellants using AOTF spectrometer*. 96. doi: 10.1117/12.518569

Frontini, P. M., Fasce, L. A., and Rueda, F. (2012). Non linear fracture mechanics of polymers: Load Separation and Normalization methods. *Engineering Fracture Mechanics*, *79*, 389–414. doi: 10.1016/j.engfracmech.2011.11.020

Fuente, J. L. de la, and Rodríguez, O. (2003). Dynamic mechanical study on the thermal aging of a hydroxyl-terminated polybutadiene-based energetic composite. *Journal of Applied Polymer Science*, *87*(14), 2397–2405. doi: 10.1002/app.12125

Furmanski, J., and Neeraj, T. (2022). Pin-loaded SENT specimen for constraint-matched fracture testing of radially propagating longitudinal cracks in thin-walled pipelines. *Engineering Fracture Mechanics*, *268*, 108498. doi: 10.1016/j.engfracmech.2022.108498

Geisler, R. (2002, July 7). *A Global View of the Use of Aluminum Fuel in Solid Rocket Motors*. 38th AIAA/ASME/SAE/ASEE Joint Propulsion Conference & Exhibit, Indianapolis, IN, U.S.A. doi: 10.2514/6.2002-3748

Geisler, R. L., and Frederick, R. A. (2010). Historical Overview and Solid Rocket Motor Fundamentals. In R. Blockley and W. Shyy (Eds.), *Encyclopedia of Aerospace Engineering* (p. eae101). John Wiley & Sons, Ltd. doi: 10.1002/9780470686652.eae101

Gent, A. N. (2012). *Engineering with Rubber: How to Design Rubber Components* (3rd ed.). Carl Hanser Verlag GmbH & Co. KG. doi: 10.3139/9783446428713

Gligorijević, N., Živković, S., Subotić, S., Rodić, V., and Gligorijević, I. (2015). Effect of Cumulative Damage on Rocket Motor Service Life. *Journal of Energetic Materials*, *33*(4), 229–259. doi: 10.1080/07370652.2014.970245

Gohardani, A. S., Stanojev, J., Demairé, A., Anflo, K., Persson, M., Wingborg, N., and Nilsson, C. (2014). Green space propulsion: Opportunities and prospects. *Progress in Aerospace Sciences*, *71*, 128–149. doi: 10.1016/j.paerosci.2014.08.001

Gorman, F., and White, H. (1970, January 19). A review of atmospheric contamination associated with exhaust products from beryllium solid propellant. *8th Aerospace Sciences Meeting*. 8th Aerospace Sciences Meeting, West Germany. doi: 10.2514/6.1970-117

Gottlieb, L., and Bar, S. (2003). Migration of Plasticizer between Bonded Propellant Interfaces. *Propellants, Explosives, Pyrotechnics*, *28*(1), 12–17. doi: 10.1002/prep.200390000

Griffith, A. A. (1921). VI. The phenomena of rupture and flow in solids. *Philosophical Transactions of the Royal Society of London*, *221*(582–593), 163–198. doi: 10.1098/rsta.1921.0006

Gurtin, M. E., and Sternberg, E. (1962). On the linear theory of viscoelasticity. *Archive for Rational Mechanics and Analysis*, *11*(1), 291–356. doi: 10.1007/BF00253942

Hanson, D. E., Hawley, M., Houlton, R., Chitanvis, K., Rae, P., Orler, E. B., and Wrobleski, D. A. (2005). Stress softening experiments in silica-filled polydimethylsiloxane provide insight into a mechanism for the Mullins effect. *Polymer*, *46*(24), 10989–10995. doi: 10.1016/j.polymer.2005.09.039

Harris, D. J., Assink, R. A., and Celina, M. (2001). NMR Analysis of Oxidatively Aged HTPB/IPDI Polyurethane Rubber: Degradation Products, Dynamics, and Heterogeneity. *Macromolecules*, *34*(19), 6695–6700. doi: 10.1021/ma0108766

Hashim, S. A., Karmakar, S., and Roy, A. (2019). Effects of Ti and Mg particles on combustion characteristics of boron–HTPB-based solid fuels for hybrid gas generator in ducted rocket applications. *Acta Astronautica*, *160*, 125–137. doi: 10.1016/j.actaastro.2019.04.002

Houwink, R. (1956). Slipping of Molecules during the Deformation of Reinforced Rubber. *Rubber Chemistry and Technology*, *29*(3), 888–893. doi: 10.5254/1.3542602

Humble, R. W. (Ed.). (1995). *Space propulsion analysis and design* (1. ed., rev). McGraw-Hill.

Hunley, J. (1999, June 20). *The history of solid-propellant rocketry - What we do and do not know*. 35th Joint Propulsion Conference and Exhibit, Los Angeles, CA, U.S.A. doi: 10.2514/6.1999-2925

Hur, J., Park, J. B., Jung, G. D., and Youn, S. K. (2016). Enhancements on a micromechanical constitutive model of solid propellant. *International Journal of Solids and Structures*, *87*, 110–119. doi: 10.1016/J.IJSOLSTR.2016.02.025

Husband, D. M. (1992). Use of Dynamic Mechanical Measurements to determine the aging behavior of solid propellant. *Propellants, Explosives, Pyrotechnics*, *17*(4), 196–201. doi: 10.1002/prep.19920170410

IARC monographs on the evaluation of carcinogenic risks to humans. (1993). *Beryllium, Cadmium, Mercury, and Exposures in the Glass Manufacturing Industry* (Vol. 58). International Agency for Research on Cancer.

Iqbal, M. M., and Liang, W. (2006). Modeling the moisture effects of solid ingredients on composite propellant properties. *Aerospace Science and Technology*, *10*(8), 695–699. doi: 10.1016/j.ast.2006.07.003

Irwin, G. R. (1956). *Onset of fast crack propagation in high strength steel and aluminum alloys* (Technical Report No. AD0099305; p. 23). Naval Research Laboratory Washington DC.

Irwin, G. R. (1961). Plastic zone near a crack and fracture toughness. *Proceedings of the Eighth Sagamore Ordnance Materials Research Conference*, *4*, 63–78.

ISO 1431-1. (2022). *Rubber, vulcanized or thermoplastic - Resistance to ozone cracking - Part 1: Static and dynamic strain testing*. International Organization for Standarization.

ISO 13586. (2018). *Plastics - Determination of fracture toughness (GIC and KIC) - Linear elastic fracture mechanics (LEFM) approach*. International Organization for Standarization.

J. Mills, G., L. Dowler, W., and A. Gordon, D. (1965). *Propellant fuel containing magnesium aluminium alloy* (Secretary of the Army Patent No. 3,180,770).

Jain, S. R. (2002). Solid Propellant Binders. *Journal of Scientific & Indutrial Research*, *61*(11), 899–911.

Jalocha, D., Constantinescu, A., and Nevière, R. (2015a). Prestrained biaxial DMA investigation of viscoelastic nonlinearities in highly filled elastomers. *Polymer Testing*, *42*, 37–44. doi: 10.1016/j.polymertesting.2015.01.005

Jalocha, D., Constantinescu, A., and Neviere, R. (2015b). Prestrain-dependent viscosity of a highly filled elastomer: experiments and modeling. *Mechanics of Time-Dependent Materials*, *19*(3), 243–262. doi: 10.1007/S11043-015-9262-Z

James Buswell, H. (1975). *An investigation into mechanical failure of composite propellants*. University of Surrey.

James S., N., B. Russell, K., and L. D., W. (1973). *Solid Propellant Grain Structural Integrity Analysis* (Special Publication (SP) NASA-SP-8073). NASA.

Ji, Y., Cao, L., Li, Z., Chen, G., Cao, P., and Liu, T. (2022). Numerical Conversion Method for the Dynamic Storage Modulus and Relaxation Modulus of Hydroxy-Terminated Polybutadiene (HTPB) Propellants. *Polymers*, *15*(1), 3. doi: 10.3390/polym15010003

Jia, P., Jiang, W., Zhan, S., and Zhao, X. (2020). Estimation of plastic eta factors for clamp-end SE(T) specimens with undermatched weld metal based on 3D finite element analyses. *Theoretical and Applied Fracture Mechanics*, *106*, 102496. doi: 10.1016/j.tafmec.2020.102496

Kim, S. D., Yoon, D. H., Lee, S. Y., and Kim, J. H. (2020). Crack resistance behavior of particulate reinforced composites at various test speeds and temperatures. *Materialwissenschaft Und Werkstofftechnik*, *51*(5), 603–612. doi: 10.1002/mawe.201900241

Klager, K. (1984). Polyurethanes, the most versatile binder for solid composite propellants. *20th Joint Propulsion Conference*. 20th Joint Propulsion Conference, Cincinnati, OH, U.S.A. doi: 10.2514/6.1984-1239

Klager, K., and Wrightson, J. M. (1967). RECENT ADVANCES IN SOLID PROPELLANT BINDER CHEMISTRY. In *Mechanics and Chemistry of Solid Propellants* (pp. 47–74). Elsevier. doi: 10.1016/B978-1-4831-9837-8.50010-7

Knauss, W. G. (2015). A review of fracture in viscoelastic materials. *International Journal of Fracture*, *196*(1–2), 99–146. doi: 10.1007/s10704-015-0058-6

Kraus, G., Childers, C. W., and Rollmann, K. W. (1966). Stress softening in carbon black-reinforced vulcanizates. Strain rate and temperature effects. *Journal of Applied Polymer Science*, *10*(2), 229–244. doi: 10.1002/app.1966.070100205

Krishnamurthy, V. N., and Varghese, T. L. (2017). *The chemistry and technology of solid rocket propellants: a treatise on solid propellants*. Allied Publishers Pvt. Ltd.

Landel, R. F., and Smith, T. L. (1961). Viscoelastic Properties of Rubberlike Composite Propellants and Filled Elastomers. *ARS Journal*, *31*(5), 599–608. doi: 10.2514/8.5572

Landes, J. D., and Begley, J. A. (1974). Test Results from J-Integral Studies: An Attempt to Establish a Testing Procedure. *Fracture Analysis,*

Proceedings of the 1973 National Symposium on Fracture Mechanics, Part II, ASTM STP 560, 170–186. doi: 10.1520/STP33140S

Landes, J. D., and Begley, J. A. (1972). The effect of Specimen Geometry on JIc. *Fracture Toughness, Proceedings of the 1971 National Symposium on Fracture Mechanics, Part II, ASTM STP 514*, 24–39. doi: 10.1520/STP38817S

Layton, L. H. (1974). *Chemical Aging Studies on ANB-3066 and TP-H1011 Propellants* (Technical Report AFRPL-TR-74-16; p. 115). Morton Thiokol Inc.

Layton, L. H. (1975). *Chemical Structural Aging Studies on an HTPB Propellant* (Technical Report AFRPL-TR-75-13; p. 90). Morton Thiokol Inc.

Lei, M., Wang, J., Cheng, J., Xiao, J., Wen, L., Lu, H., and Hou, X. (2020). A constitutive model of the solid propellants considering the interface strength and dewetting. *Composites Science and Technology*, *185*, 107893. doi: 10.1016/j.compscitech.2019.107893

Lempert, D. B., Nechiporenko, G. N., and Manelis, G. B. (2011). Energetic capabilities of high-density composite solid propellants containing zirconium or its hydride. *Combustion, Explosion, and Shock Waves*, *47*(1), 45–54. doi: 10.1134/S0010508211010060

Lewis, P. M. (1986). Effect of ozone on rubbers: Countermeasures and unsolved problems. *Polymer Degradation and Stability*, *15*(1), 33–66. doi: 10.1016/0141-3910(86)90004-2

Li, H., Xu, J., Chen, X., Zhang, J., and Li, J. (2023). A nonlinear viscoelastic constitutive model with damage and experimental validation for composite solid propellant. *Scientific Reports*, *13*(1), 2049. doi: 10.1038/s41598-023-29214-7

Liu, C. T. (1995). Effect of predamage on crack growth behavior in a particulate composite material. *Journal of Spacecraft and Rockets*, *32*(3), 533–537. doi: 10.2514/3.26647

Liu, C. T., and Ravichandran, G. (2006). Influence of Confining Pressure on the Crack Growth Behavior in a Highly Filled Elastomer. *Journal of Applied Mechanics*, *73*(5), 778–782. doi: 10.1115/1.2189874

Liu, C., and Thompson, D. G. (2015). Mechanical response and failure of High Performance Propellant (HPP) subject to uniaxial tension. *Mechanics of Time-Dependent Materials*, *19*(2), 95–115. doi: 10.1007/s11043-015-9254-z

López, R., Ortega de la Rosa, A., Salazar, A., and Rodríguez, J. (2018). Structural Integrity of Aged Hydroxyl-Terminated Polybutadiene Solid Rocket Propellant. *Journal of Propulsion and Power*, *34*(1), 75–84. doi: 10.2514/1.B36496

López Sánchez, R. (2018). *Fatiga de Propulsantes Sólidos de Material Compuesto*. Universidad Rey Juan Carlos.

Lysien, K., Stolarczyk, A., and Jarosz, T. (2021). Solid Propellant Formulations: A Review of Recent Progress and Utilized Components. *Materials*, *14*(21), 6657. doi: 10.3390/ma14216657

Martínez, M., López, R., Rodríguez, J., and Salazar, A. (2022). Efecto del daño mecánico en el comportamiento a fractura de propulsantes sólidos de material compuesto. *Revista Española de Mecánica de la Fractura*, *4*, 115–120.

Matous, K., Inglis, H., Gu, X., Rypl, D., Jackson, T., and Geubelle, P. (2007). Multiscale modeling of solid propellants: From particle packing to

failure. *Composites Science and Technology*, *67*(7–8), 1694–1708. doi: 10.1016/j.compscitech.2006.06.017

Merrit, J. (1981). *Method of age testing rubber based propellants* (Patent No. US4262541A).

Miller, M., Fortner, J., Buswell, J., Chelner, H., and Lossner, M. (2007, July 8). *Health Monitoring of Munitions for Mission Readiness*. 43rd AIAA/ASME/SAE/ASEE Joint Propulsion Conference & Exhibit, Cincinnati, OH. doi: 10.2514/6.2007-5789

Moore, D. R., Pavan, A., and Williams, J. G. (2001). *Fracture mechanics testing methods for polymers, adhesives, and composites*. Elsevier.

Mullins, L. (1949). Permanent Set in Vulcanized Rubber. *Rubber Chemistry and Technology*, *22*(4), 1036–1044. doi: 10.5254/1.3543010

Mullins, L. (1969). Softening of Rubber by Deformation. *Rubber Chemistry and Technology*, *42*(1), 339–362. doi: 10.5254/1.3539210

Naseem, H., Murthy, H., and Ramakrishna, P. A. (2020). Accelerated ageing of composite solid propellants under cyclic temperature variations. *Journal of Energetic Materials*, *39*(4), 452–478. doi: 10.1080/07370652.2020.1815899

Naseem, H., Yerra, J., Murthy, H., and Ramakrishna, P. A. (2021). Ageing studies on AP/HTPB based composites solid propellants. *Energetic Materials Frontiers*, *2*(2), 111–124. doi: 10.1016/j.enmf.2021.02.001

NATO-AOP-46. (2022). *The scientific basis for the whole life assessment of munitions*. NATO.

Nevière, R. (2006). An extension of the time–temperature superposition principle to non-linear viscoelastic solids. *International Journal of Solids and Structures*, *43*(17), 5295–5306. doi: 10.1016/j.ijsolstr.2005.09.009

Ozone Gas Sensor. Model: MQ131 High Concentration. (2021). [Datasheet]. Zhengzhou Winsen Electronics Technology Co., Ltd.

Özüpek, Ş., and Becker, E. B. (1992). Constitutive Modeling of High-Elongation Solid Propellants. *Journal of Engineering Materials and Technology*, *114*(1), 111–115. doi: 10.1115/1.2904130

Özüpek, Ş., and Becker, E. B. (1997). Constitutive Equations for Solid Propellants. *Journal of Engineering Materials and Technology*, *119*(2), 125–132. doi: 10.1115/1.2805983

Pang, W., De Luca, L. T., Fan, X., Glotov, O. G., and Zhao, F. (2019). *Boron-Based Fuel-Rich Propellant: Properties, Combustion, and Technology Aspects* (W. Pang, Ed.; 2nd ed.). CRC Press. doi: 10.1201/9780429030680

Pang, W., and DeLuca, L. T. (2023). *Nano and Micro - Scale Energetic Materials: Propellants and Explosives* (1st ed.). Wiley. doi: 10.1002/9783527835348

Pang, W., Fan, X., Zhang, W., Xu, H., Li, J., Li, Y., Shi, X., and Li, Y. (2011). Application of Amorphous Boron Granulated With Hydroxyl- Terminated Polybutadiene in Fuel-Rich Solid Propellant. *Propellants, Explosives, Pyrotechnics*, *36*(4), 360–366. doi: 10.1002/prep.200900112

Pang, W., Li, Y., DeLuca, L. T., Liang, D., Qin, Z., Liu, X., Xu, H., and Fan, X. (2021). Effect of Metal Nanopowders on the Performance of Solid Rocket Propellants: A Review. *Nanomaterials*, *11*(10), 2749. doi: 10.3390/nano11102749

Paris, P. C., Ernst, H. A., and Turner, C. E. (1980). A J-integral Approach to Development of η -Factors. *Fracture Mechanics, Proceedings of the Twelfth National Symposium on Fracture Mechanics, ASTM STP 700*, 338–351. doi: 10.1520/STP36979S

Payne, A. R. (1962). The dynamic properties of carbon black-loaded natural rubber vulcanizates. Part I. *Journal of Applied Polymer Science*, *6*(19), 57–63. doi: 10.1002/app.1962.070061906

Quagliano Amado, J. C., Ross, P. G., Mattos Silva Murakami, L., and Narciso Dutra, J. C. (2022). Properties of Hydroxyl‐Terminal Polybutadiene (HTPB) and Its Use as a Liner and Binder for Composite Propellants: A Review of Recent Advances. *Propellants, Explosives, Pyrotechnics*, *47*(5). doi: 10.1002/prep.202100283

Rao, B. N. (1992). Fracture of solid rocket propellant grains. *Engineering Fracture Mechanics*, *43*(3), 455–459. doi: 10.1016/0013-7944(92)90113-S

Read, D. T. (1982). *Applied J-integral in HY130 tensile panels and implications for fitness for service assessment* (NBS IR 82-1670; 0 ed., p. NBS IR 82-1670). National Bureau of Standards. doi: 10.6028/NBS.IR.82-1670

Reeling Brouwer, G., Weterings, F.-P., and Keizers, H. (2005). *Evaluation of Ageing in Composite Propellant Grains Part 2*. 41st AIAA/ASME/SAE/ASEE Joint Propulsion Conference & Exhibit, Tucson, Arizona. doi: 10.2514/6.2005-3803

Reid, D. L., Draper, R., Richardson, D., Demko, A., Allen, T., Petersen, E. L., and Seal, S. (2014). In situ synthesis of polyurethane–TiO2 nanocomposite and performance in solid propellants. *Journal of Materials Chemistry A*, *2*(7), 2313. doi: 10.1039/c3ta14027j

Rice, J. R. (1968). A Path Independent Integral and the Approximate Analysis of Strain Concentration by Notches and Cracks. *Journal of Applied Mechanics*, *35*(2), 379–386. doi: 10.1115/1.3601206

Rice, J. R., Paris, P. C., and Merkle, J. G. (1973). Some further results of J-integral analysis and estimates. *Progress in Flaw Growth and Fracture Toughness Testing, ASTM STP 536*, 231–245.

Rodríguez, C., Maspoch, M. Ll., and Belzunce, F. J. (2009). Fracture characterization of ductile polymers through methods based on load separation. *Polymer Testing*, *28*(2), 204–208. doi: 10.1016/j.polymertesting.2008.12.004

Salazar, A., and Rodríguez, J. (2008). The use of the load separation parameter Spb method to determine the J–R curves of polypropylenes. *Polymer Testing*, *27*(8), 977–984. doi: 10.1016/j.polymertesting.2008.08.013

Schapery, R. A. (1969). On the characterization of nonlinear viscoelastic materials. *Polymer Engineering & Science*, *9*(4), 295–310. doi: 10.1002/pen.760090410

Schapery, R. A. (1984). Correspondence principles and a generalized J integral for large deformation and fracture analysis of viscoelastic media. *International Journal of Fracture*, *25*(3), 195–223. doi: 10.1007/BF01140837

Schapery, R. A. (2022a). A theory of viscoelastic crack growth: revisited. *International Journal of Fracture*, *233*(1), 1–16. doi: 10.1007/s10704-021-00605-z

Schapery, R. A. (2022b). Stable and unstable viscoelastic crack growth: experimental validation of nonlinear theory for rubber. *International Journal of Fracture*. doi: 10.1007/s10704-022-00639-x

Schapery, R. A. (2023). Crack growth in viscoelastic media with large strains: further results and validation of nonlinear theory for rubber. *International Journal of Fracture*. doi: 10.1007/s10704-023-00696-w

Schapery, R. A. (1982). Models for damage growth and fracture in nonlinear viscoelastic particulate composites. *Proceedings of the Ninth U.S. National Congress of Applied Mechanics*, 237–245.

Schapery, R. A. (1981). *On Viscoelastic Deformation and Failure Behavior of Composite Materials with Distributed Flaws: Vol. AD-01* (S. S. Wang and W. J. Renton, Eds.; pp. 5–20). ASME.

Seyidoglu, T., and Bohn, M. A. (2017). Characterization of Aging Behavior of Butacene® Based Composite Propellants by Loss Factor Curves. *Propellants, Explosives, Pyrotechnics*, *42*(7), 712–723. doi: 10.1002/prep.201700060

Sforza, P. M. (2016). *Theory of aerospace propulsion* (Second edition). Butterworth-Heinemann.

Sharobeam, M. H., and Landes, J. D. (1991). The load separation criterion and methodology in ductile fracture mechanics. *International Journal of Fracture*, *47*(2), 81–104. doi: 10.1007/BF00032571

Sharobeam, M. H., and Landes, J. D. (1993). The load separation and η pl development in precracked specimen test records. *International Journal of Fracture*, *59*(1), 213–226. doi: 10.1007/BF00012362

Shekhar, H. (2011). Prediction and Comparison of Shelf Life of Solid Rocket Propellants Using Arrhenius and Berthelot Equations. *Propellants, Explosives, Pyrotechnics*, *36*(4), 356–359. doi: 10.1002/prep.200900104

Shekhar, H., and Sahasrabudhe, A. (2010). Assessment of Poisson's Ratio for Hydroxy-terminated Polybutadine-based Solid Rocket Propellants. *Defence Science Journal*, *60*(5), 497–501. doi: 10.14429/dsj.60.572

Shekhar, H., and Sahasrabudhe, A. D. (2011). Longitudinal Strain Dependent Variation of Poisson's Ratio for HTPB Based Solid Rocket Propellants in Uniaxial Tensile Testing. *Propellants, Explosives, Pyrotechnics*, *36*(6), 558–563. doi: 10.1002/prep.200900079

Shetye, S. S., Troyer, K. L., Streijger, F., Lee, J. H. T., Kwon, B. K., Cripton, P. A., and Puttlitz, C. M. (2014). Nonlinear viscoelastic characterization of the porcine spinal cord. *Acta Biomaterialia*, *10*(2), 792–797. doi: 10.1016/j.actbio.2013.10.038

Singh, H. (2017). Survey of New Energetic and Eco-friendly Materials for Propulsion of Space Vehicles. In *Chemical Rocket Propulsion* (pp. 127–138). Springer International Publishing. doi: 10.1007/978-3-319-27748-6_4

STANAG 4506. (2000). *Explosive Materials, Physical/Mechanical Properties Uniaxial Tensile Test*. North Atlantic Treaty Organization (NATO).

STANAG 4540. (2002). *Explosives, Procedures for Dynamic Mechanical Analysis (DMA) and Determination of Glass Transition Temperature*. North Atlantic Treaty Organization (NATO).

STANAG 4581. (2022). *Energetic materials; assessment of ageing characteristics of composite propellants containing an inert binder*. North Atlantic Treaty Organization (NATO).

Stedry, P. J., Landel, R. F., and Shelton, H. T. (1961). *Volume Changes and Poisson's Ratio of Polyurethane Propellants under Tensile*

Deformations (Technical Report No. 32–168; p. 23). Jet Propulsion Laboratory California Institute of Technology.

Sutton, G. P., and Biblarz, O. (2017). *Rocket Propulsion Elements* (9th ed). John Wiley & Sons.

Tayefi, M., Eesaee, M., Hassanipour, M., Elkoun, S., David, E., and Nguyen-Tri, P. (2023). Recent progress in the accelerated aging and lifetime prediction of elastomers : A review. *Polymer Degradation and Stability*, *214*, 110379. doi: 10.1016/j.polymdegradstab.2023.110379

Thorin, A., Azoug, A., and Constantinescu, A. (2012). Influence of prestrain on mechanical properties of highly-filled elastomers: Measurements and modeling. *Polymer Testing*, *31*(8), 978–986. doi: 10.1016/j.polymertesting.2012.07.014

Torabizadeh, M., Putnam, Z. A., Sankarasubramanian, M., Moosbrugger, J. C., and Krishnan, S. (2019). The effects of initial crack length on fracture characterization of rubbers using the J-Integral approach. *Polymer Testing*, *73*, 327–337. doi: 10.1016/j.polymertesting.2018.11.026

Tormey, J. F., and Britton, S. C. (1963). Effect of cyclic loading on solid propellant grain structures. *AIAA Journal*, *1*(8), 1763–1770. doi: 10.2514/3.1922

Torry, S., and Cunliffe, A. (2001). Humid Ageing of Polybutadiene Based Propellants. *Energetic Materials: Analysis, Diagnosis and Testing. 31st International Annual Conference of ICT*, *25*, 1–11.

Trache, D., Klapötke, T. M., Maiz, L., Abd-Elghany, M., and DeLuca, L. T. (2017). Recent advances in new oxidizers for solid rocket propulsion. *Green Chemistry*, *19*(20), 4711–4736. doi: 10.1039/C7GC01928A

Tschoegl, N. W. (1989). *The Phenomenological Theory of Linear Viscoelastic Behavior*. Springer Berlin Heidelberg. doi: 10.1007/978-3-642-73602-5

Tunç, B., and Özüpek, Ş. (2017). Constitutive modeling of solid propellants for three dimensional nonlinear finite element analysis. *Aerospace Science and Technology*, *69*, 290–297. doi: 10.1016/J.AST.2017.06.025

Turner, C. E. (1980). The Ubiquitous η Factor. *Fracture Mechanics, Proceedings of the Twelfth National Symposium on Fracture Mechanics, ASTM STP 700*, 314–337. doi: 10.1520/STP36978S

Tussiwand, G. S., Saouma, V. E., Terzenbach, R., and De Luca, L. T. (2009). Fracture Mechanics of Composite Solid Rocket Propellant Grains: Material Testing. *Journal of Propulsion and Power*, *25*(1), 60–73. doi: 10.2514/1.34227

Valiente Cancho, A. (2018). *Curso de comportamiento mecánico de materiales: elasticidad y viscoelasticidad*. García-Maroto Editores.

van Ramshorst, M. C. J., Di Benedetto, G. L., Duvalois, W., Hooijmeijer, P. A., and van der Heijden, A. E. D. M. (2016). Investigation of the Failure Mechanism of HTPB/AP/Al Propellant by In-situ Uniaxial Tensile Experimentation in SEM. *Propellants, Explosives, Pyrotechnics*, *41*(4), 700–708. doi: 10.1002/prep.201500264

Venkatesan, D., Srinivasan, M., Reddy, K. A., and Pendse, V. V. (1993). The migration of plasticizer in solid propellant grains. *Polymer International*, *32*(4), 395–399. doi: 10.1002/pi.4990320410

Volterra, V. (1909). Sulle equazioni integro-differenziali della teoria dell'elasticità. *Atti Della Reale Accademia Dei Lincei*, *18*(2), 295–301.

Wainstein, J., Frontini, P. M., and Cassanelli, A. N. (2004). J-R curve determination using the load separation parameter S method for ductile polymers. *Polymer Testing*, *23*(5), 591–598. doi: 10.1016/j.polymertesting.2003.10.010

Wang, J., Bao, F., and Cui, H. (2022a). Structural analysis of solid rocket motor with effects of viscoelastic Poisson's ratio. *Journal of Physics: Conference Series*, *2285*(1), 012020. doi: 10.1088/1742-6596/2285/1/012020

Wang, J., Cheng, J., Lei, M., Hu, X., and Wen, L. (2020). Mechanical properties and constitutive model of a composite solid propellant under the synergistic effects of accelerated aging time, pre-strain, and damage growth. *Mechanics of Materials*, *148*, 103453. doi: 10.1016/j.mechmat.2020.103453

Wang, J., Cui, H., and Ma, W. (2022b). Investigation on Aging Model of Solid Propellant Using the Degree of Crosslinking. *International Journal of Aerospace Engineering*, *2022*, 1–8. doi: 10.1155/2022/2700740

Wang, J., Xiong, Y., and He, X. (2023a). Simulation of Solid Propellant Regression with Cracks Based on Level-Set Method. *Journal of Physics: Conference Series*, *2478*(3), 032029. doi: 10.1088/1742-6596/2478/3/032029

Wang, Q., Wang, G., Wang, Z., Qiang, H., Wang, X., Li, S., and Zhu, Z. (2022c). Biaxial tensile test and meso damage numerical simulation of HTPB propellant. *Scientific Reports*, *12*(1), 17635. doi: 10.1038/s41598-022-22726-8

Wang, T., Xu, J., Li, H., Chen, X., and Zhang, J. (2023b). Crack propagation velocity and fracture toughness of hydroxyl-terminated polybutadiene propellants with consideration of a thermo-viscoelastic constitutive

model: Experimental and numerical study. *Theoretical and Applied Fracture Mechanics*, *124*, 103732. doi: 10.1016/j.tafmec.2022.103732

Wang, T., Xu, J., Li, H., Ding, W., Liu, J., and Chen, X. (2021). Crack propagation velocity and fracture toughness of hydroxyl-terminated polybutadiene propellants: Experiments and simulations. *Engineering Fracture Mechanics*, *257*(September), 108034. doi: 10.1016/j.engfracmech.2021.108034

Wang, X., Huang, Q., Yang, Q., Zhang, Y., and Geng, T. (2023c). Study on strength criterion of composite solid propellants under complex loading. *AIP Advances*, *13*(5), 055321. doi: 10.1063/5.0141443

Wang, J. xiang, Qiang, H. fu, and Wang, Z. jun. (2022d). Strength Criterion of HTPB Composite Solid Propellant under Tension-Shear Loading at Low Temperature. *Propellants, Explosives, Pyrotechnics*, *47*(5), e202100267. doi: 10.1002/PREP.202100267

Wang, Y., Li, G., Li, J., Xiao, Y., Liu, Z., and Qu, K. (2022e). Experimental research on accelerated aging of solid propellant under alternating temperature. *FirePhysChem*, *2*(4), 374–381. doi: 10.1016/j.fpc.2022.08.005

Wang, Z., and Qiang, H. (2022f). Mechanical properties of thermal aged HTPB composite solid propellant under confining pressure. *Defence Technology*, *18*(4), 618–625. doi: 10.1016/j.dt.2021.06.014

Wang, Z., Qiang, H., Wang, G., and Geng, B. (2018a). Strength criterion of composite solid propellants under dynamic loading. *Defence Technology*, *14*(5), 457–462. doi: 10.1016/j.dt.2018.06.016

Wang, Z., Qiang, H., Wang, G., and Huang, Q. (2015). Tensile mechanical properties and constitutive model for HTPB propellant at low

temperature and high strain rate. *Journal of Applied Polymer Science*, *132*(24), 42104(1)-42104(9). doi: 10.1002/app.42104

Wang, Z., Qiang, H., Wang, T., Wang, G., and Hou, X. (2018b). A thermovisco-hyperelastic constitutive model of HTPB propellant with damage at intermediate strain rates. *Mechanics of Time-Dependent Materials*, *22*(3), 291–314. doi: 10.1007/S11043-017-9357-9/TABLES/3

Warby, M. K., Walton, J. R., and Whiteman, J. R. (1992). A finite element model of crack growth in a finite body in the context of mode I linear viscoelastic fracture. *Computer Methods in Applied Mechanics and Engineering*, *97*(3), 375–397. doi: 10.1016/0045-7825(92)90052-L

Wells, A. A. (1961). Unstable crack propagation in metals: cleavage and fast fracture. *Proceedings of the Crack Propagation Symposium*, *1*, 210–230.

Whitehouse, A., Couturier, R., Donguy, P., Besser, H., and Meyer, L. (1997). *Structural Assessment of Solid Propellant Grains* (Technical Report RDP AGARD-AR-350). NATO.

Whittaker, M. L., Cutler, R. A., and Anderson, P. E. (2012). Boride-Based Materials for Energetic Applications. *MRS Proceedings*, *1405*. doi: 10.1557/opl.2012.64

Williams, M. L. (1965). Initiation and Growth of Viscoelastic Fracture. *International Journal of Fracture Mechanics*, *1*(4), 292–310. doi: 10.1007/BF03545561

Wubuliaisan, M., Wu, Y., Hou, X., Duan, H., and Huang, F. (2022). Viscoelastic debonding criterion-based interface for modeling the mechanical behavior of solid propellants subjected to large deformation. *European*

Journal of Mechanics - A/Solids, 104873. doi: 10.1016/j.euromechsol.2022.104873

Wubuliaisan, M., Wu, Y., Hou, X., and Huang, F. (2023a). A viscoelastic constitutive model considering deformation and environmental-induced damages for solid propellants. *Aerospace Science and Technology*, *132*, 108055. doi: 10.1016/j.ast.2022.108055

Wubuliaisan, M., Wu, Y., Hou, X., Liu, X., and Wu, Y. (2023b). Multiscale viscoelastic constitutive modeling of solid propellants subjected to large deformation. *International Journal of Solids and Structures*, *262–263*, 112084. doi: 10.1016/j.ijsolstr.2022.112084

Wu-jun, C., Yu-tao, J., and Peng-bo, W. (2012). Research on Correlation Between Dewetting and Mechanical Property of HTPB Propellant. *Acta Armamentarii*, *33*(3), 261–266.

Xiao, Y., Gong, T., Zhang, X., and Sun, Y. (2023). Multiscale modeling for dynamic compressive behavior of polymer bonded explosives. *International Journal of Mechanical Sciences*, *242*, 108007. doi: 10.1016/j.ijmecsci.2022.108007

Xu, F., Aravas, N., and Sofronis, P. (2008). Constitutive modeling of solid propellant materials with evolving microstructural damage. *Journal of the Mechanics and Physics of Solids*, *56*(5), 2050–2073. doi: 10.1016/j.jmps.2007.10.013

Xu, J., Chen, X., Wang, H., Zheng, J., and Zhou, C. (2014). Thermo-damage-viscoelastic constitutive model of HTPB composite propellant. *International Journal of Solids and Structures*, *51*(18), 3209–3217. doi: 10.1016/j.ijsolstr.2014.05.024

Xu, J., Ju, Y., Han, B., Zhou, C., and Zheng, J. (2013). Research on relaxation modulus of viscoelastic materials under unsteady temperature states based on TTSP. *Mechanics of Time-Dependent Materials*, *17*(4), 543–556. doi: 10.1007/s11043-012-9203-z

Zaikov, G., Rakovsky, S., and Anachkov, M. (2012). Ozone and its Reactions with Diene Rubbers. *Chemistry & Chemical Technology*, *6*(3), 307–319. doi: 10.23939/chcht06.03.307

Zhang, G., Wang, J., Liu, X., Li, M., Chen, C., Wang, N., and Hou, X. (2023a). Correlation between the micro-structure and macroscopic mechanical properties of GAP-based propellant during aging. *Polymer Degradation and Stability*, 110411. doi: 10.1016/j.polymdegradstab.2023.110411

Zhang, J., Shi, L., Luo, P., and Zhou, J. (2023b). Mechanical properties and deformation behaviors of the hydroxyl-terminated polybutadiene and ammonium perchlorate interface by molecular dynamics simulation. *Computational Materials Science*, *221*, 112077. doi: 10.1016/j.commatsci.2023.112077

Zhou, D., Liu, X., Sui, X., Wei, Z., and Wang, N. (2016). Effect of pre-strain during ageing on the maximum elongation of composite solid propellants and its modelling. *Polymer Testing*, *50*, 200–207. doi: 10.1016/J.POLYMERTESTING.2015.12.012

Zhu, X.-K. (2017). Progress in development of fracture toughness test methods for SENT specimens. *International Journal of Pressure Vessels and Piping*, *156*, 40–58. doi: 10.1016/j.ijpvp.2017.07.004

Zou, Z.-J., Qiang, H.-F., Li, Y.-Y., and Wang, X.-R. (2023). Review on the Dewetting of the Particle-Matrix Interface in Composite Solid

Propellants. *Propellants, Explosives, Pyrotechnics*, *48*(3), e202200270. doi: 10.1002/prep.202200270

Scientific contributions

The Ph.D. candidate has contributed to the diffusion of the research activities in which he has been involved during the doctoral period. Diffusion has been made through the publication of journal articles and contributions to conferences such as oral presentations and their corresponding conference proceedings or poster presentations. All contributions directly related to the research of this thesis will be marked with *.

Journal publications

1)* Title: Evaluation of the structural integrity of solid rocket propellant by means of the viscoelastic fracture mechanics approach at low and medium strain rates

Authors: M. Martínez, R. López, A. Salazar, J. Rodríguez

Journal, Year: Theoretical and Applied Fracture Mechanics, 2022

JIF, quartile: 5.3, Q1 (JCR)

Doi: 10.1016/j.tafmec.2021.103237

2) Title: On the Failure Assessment Diagram Methodology in polyamide 12
Authors: M. Martínez, A.J. Cano, A. Salazar, J. Rodríguez
Journal, Year: Engineering Fracture Mechanics, 2022
JIF, quartile: 5.4, Q1 (JCR)
Doi: 10.1016/j.engfracmech.2022.108558

3) Title: Fracture of notched samples of chocolate
Authors: F.J. González, A. Salazar, M. Martínez, S. Rana; J. Rodríguez
Journal, Year: Theoretical and Applied Fracture Mechanics, 2022
JIF, quartile: 5.3, Q1 (JCR)
Doi: 10.1016/j.tafmec.2022.103477

Conferences (oral presentations)

1) Authors: A. Salazar, C. Reinhards, M. Martínez, A. Rico, **J. Rodríguez**
Title: Fracture of polyacrylamide-alginate hydrogels: analysis of the available methodologies
Conference: 9th International Conference on Fracture of Polymers, composites and adhesives
Place and date: Les Diablerets, Switzerland. 24-27 March 2024
Contribution: oral presentation
Publication: -

2)* Authors: **M. Martínez**, R. López, A. Salazar, J. Rodríguez
Title: Efecto del envejecimiento mecánico, por temperatura y por ozono en el comportamiento a fractura de propulsantes sólidos de material compuesto de base CTPB
Conference: 40 Congreso del Grupo Español de Fractura GEF 2024
Place and date: Palma de Mallorca, Spain. 6-8 March 2024
Contribution: oral presentation
Publication: to be published in Revista de Mecánica de la Fractura (ISSN 2792-4246)

3) Authors: A. Salazar, M. Martínez, C. Reinhards, **J. Rodríguez**
Title: Análisis viscoelástico de la fractura de hidrogeles poliacrilamida-alginato.
Conference: 40 Congreso del Grupo Español de Fractura GEF 2024
Place and date: Palma de Mallorca, Spain. 6-8 March 2024
Contribution: oral presentation
Publication: to be published in Revista de Mecánica de la Fractura (ISSN 2792-4246)

4)* Authors: **M. Martínez**, R. López, A. Salazar, J. Rodríguez
Title: Evaluación de la degradación mecánica, térmica y por ozono en las propiedades mecánicas de propulsantes sólidos de material compuesto
Conference: X Congreso Nacional de I+D en Defensa y Seguridad (DESEi+d 2023)
Place and date: Cartagena, Spain. 14-16 November 2023
Contribution: oral presentation
Publication: Actas del X Congreso Nacional de I+D en Defensa y Seguridad (DESEi+d 2023)

5)* Authors: **M. Martínez**, R. López, A. Salazar, J. Rodríguez
Title: Influencia del envejecimiento por ozono en la integridad estructural de propulsantes sólidos de material compuesto
Conference: 39 Congreso del Grupo Español de Fractura GEF 2023
Place and date: Gijón, Spain. 22-24 March 2023
Contribution: oral presentation
Publication: Revista de Mecánica de la Fractura, vol.6 (ISSN 2792-4246)

6)* Authors: **M. Martínez**, R. López, A. Salazar, J. Rodríguez
Title: Identificación del efecto del envejecimiento en propulsantes de material compuesto mediante análisis de componentes principales sobre ensayos físicos y mecánicos
Conference: IX Congreso Nacional de I+D en Defensa y Seguridad (DESEi+d 2022)
Place and date: Pontevedra, Spain. 15-17 November 2022
Contribution: oral presentation
Publication: Actas del IX Congreso Nacional de I+D en Defensa y Seguridad (DESEi+d 2022)

7)* Authors: **M. Martínez**, R. López, A. Salazar, J. Rodríguez
Title: Efecto del daño mecánico en el comportamiento a fractura de propulsantes sólidos de material compuesto
Conference: 5th Iberian Conference on Structural Integrity
Place and date: Coimbra, Portugal. 30 March – 1 April 2022
Contribution: oral presentation
Publication: Revista de Mecánica de la Fractura, vol.4 (ISSN 2792-4246)

8) Authors: **A. Salazar,** A.J. Cano, M. Martínez, J. Rodríguez
Title: Fatigue behaviour of polyamide 12 processed via additive manufacturing and injection moulding
Conference: 1st Virtual ESIS TC4 Conference on Fracture of Polymers, Composites and Adhesives
Place and date: Les Diablerets, Switzerland. 28-29 September 2021
Contribution: oral presentation
Publication: -

9)* Authors: **M. Martínez**, R. López, A. Salazar
Title: Fractura viscoelástica en propulsantes sólidos
Conference: 37 Congreso del Grupo Español de Fractura GEF 2021
Place and date: Online meeting. 7-8 June 2021
Contribution: oral presentation
Publication: Revista de Mecánica de la Fractura, vol.2 (ISSN 2792-4246)

10)* Authors: **M. Martínez**, R. López, A. Salazar
Title: Determinación de las funciones de relajación de propulsantes sólidos de matriz CTPB
Conference: VIII Congreso Nacional de I+D en Defensa y Seguridad (DESEi+d 2020)
Place and date: León, Spain. 24-26 November 2020
Contribution: oral presentation
Publication: Actas del VIII Congreso Nacional de I+D en Defensa y Seguridad (DESEi+d 2020)

11) Authors: **A. Salazar,** A.J. Cano, M. Martínez, J. Rodríguez
Title: Propagación de grietas por fatiga de la poliamida 12: fabricación aditiva frente a moldeo por inyección
Conference: 1st Virtual Iberian Conference on Structural Integrity
Place and date: Online meeting. 25-27 March 2020
Contribution: oral presentation
Publication: -

12) Authors: **M. Martínez**, A. Salazar, F.J. Gómez, J. Rodríguez
Title: Diagramas de rotura en poliamida 12
Conference: 1st Virtual Iberian Conference on Structural Integrity
Place and date: Online meeting. 25-27 March 2020
Contribution: oral presentation
Publication: Anales de Mecánica de la Fractura, vol. 37 (ISSN 0213-3725)

Conferences (posters)

1)* Authors: M. Martínez, R. López, J. Rodríguez, A. Salazar
Title: Influence of the mechanical, thermal and ozone degradation on the fracture behaviour of solid composite propellants
Conference: 9th International Conference on Fracture of Polymers, Composites and Adhesives
Place and date: Les Diablerets, Switzerland. 24-27 March 2024
Contribution: poster
Publication: -

2) Authors: J. Rodríguez; A. Salazar; M. Martínez; A.J. Cano; F.J. Gómez
Title: Failure assessment diagrams of Polyamide 12: Additive manufacturing technique versus injection moulding
Conference: 1st Virtual ESIS TC4 Conference on Fracture of Polymers, Composites and Adhesives
Place and date: Les Diablerets, Switzerland. 28-29 September 2021
Contribution: poster
Publication: -

List of figures

List of tables

Appendix I. Ozone ageing chamber

The ozone ageing chamber in **Fig. 95** was manufactured for the specific purpose of the ageing of composite solid rocket propellant samples. The chamber consists simply in a box, which is instrumented with an ozoniser and an e-nose sensor to measure the ozone concentration. The ease of implementation and handiness, as well as low cost, were considered for the adequation of the chamber.

***Fig. 95**. Ozone ageing chamber with ozoniser and ozone monitoring system.*

An IONCARE GH-2128 Mini Ionic Freshener & Deodorizer was used to produce the ozone in the chamber. It was manipulated to adapt it to the chamber and remove the automatic control, so that the production of ions is fully controlled by the operator, cf. **Fig. 96**.

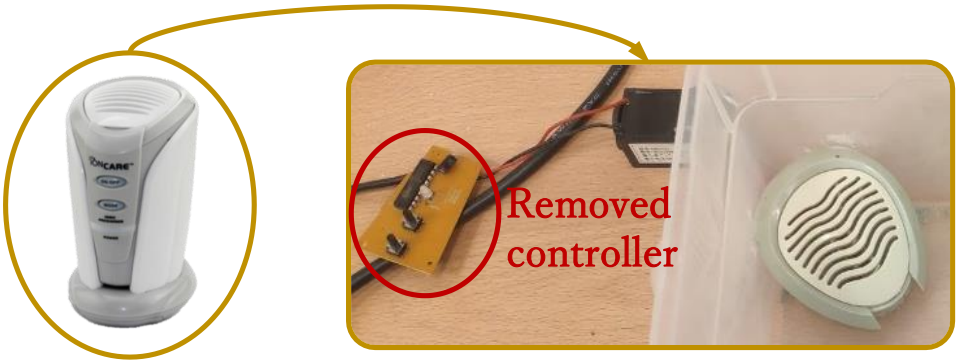

***Fig. 96**. IONCARE™ GH-2128 Mini Ionic Freshener & Deodorizer.*

To measure the ozone concentration during the ageing process, a MQ131 gas sensor from Winsen®, cf. **Fig. 97**a, was employed on an electronic nose (e-

nose) platform developed at the National Institute of Aerospace Technology (INTA) facilities, with the capability to use up to three different sensors. The e-nose is based in an Arduino Nano board microcontroller. This principal board with the installed sensor was connected to a second board by wireless means to register and visualise measured data, cf. **Fig. 97**b.

(a)

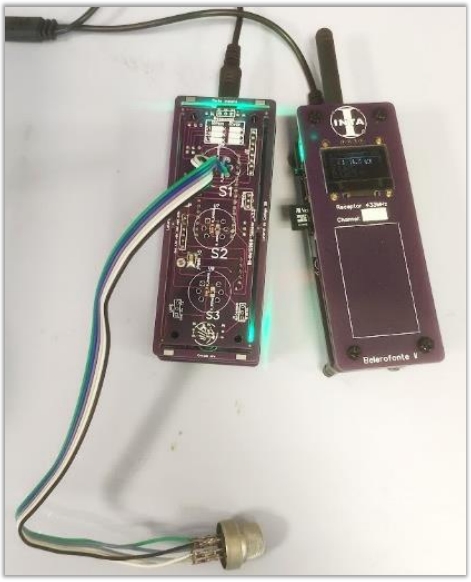

(b)

Fig. 97*. Ozone concentration measurement setup. (a) MQ131 gas sensor, (b) MQ131 gas sensor installed on the e-nose platform.*

The schematic of the basic test circuit configuration of the MQ131 gas sensor is shown in **Fig. 98**, where the sensor is identified with pins 1 to 6. The connection of the sensor to the e-nose platform was done following that configuration, with same voltages for sensor and heating circuits, V_s and V_c, respectively, of DC 8.35 V and using a resistance $R_L = 2.95$ kΩ. Further modifications of the circuit were implemented in the e-nose platform to assure stable and durable connection between the sensor and e-nose.

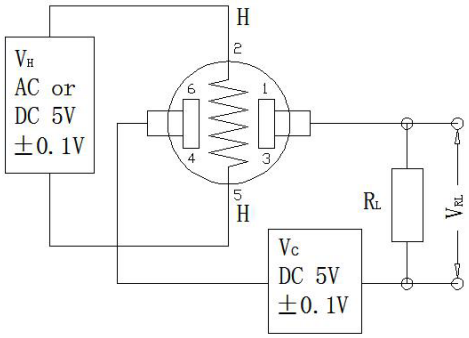

***Fig. 98**. Schematic of the basic test circuit configuration for the MQ131 gas sensor.*

The determination of the concentration using the MQ131 gas sensor was calculated through the resistance of the sensor R_s, which varies under the exposition to certain gases, such as ozone. The variation of R_s with ozone concentration is given in **Fig. 99**, where R_0 is the resistance R_s in clean air.

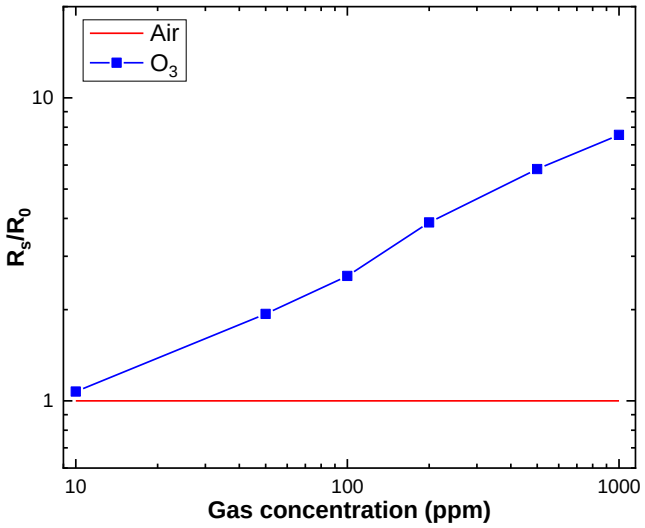

***Fig. 99**. Resistance ratio vs ozone concentration in ppm. Sensitivity characteristics of the MQ131 gas sensor. Adapted from (*Ozone Gas Sensor. Model: MQ131 High Concentration*, 2021).*

Calculation of resistance R_s is done through

$$R_s = R_L \frac{V_c - V_{R_L}}{V_{R_L}} \tag{96}$$

where V_c the feed voltage of the circuit, V_{R_L} is the measured voltage at the resistance R_L and R_L is the resistance in series with the gas sensor. The previously

mentioned setup conditions are not as specified in the datasheet of the component (*Ozone Gas Sensor. Model: MQ131 High Concentration*, 2021). Therefore, a calibration of this sensor was done. Several measures of ozone were taken, along with the corresponding measuring voltage V_{R_L}.

The ozone concentration was measured by the indigo colorimetric method proposed by Bader and Hoigné for the detection of ozone in water (Bader et al., 1981; Bader, 1982), based in the indigo trisulfonate reaction with ozone, shown in **Fig. 100**.

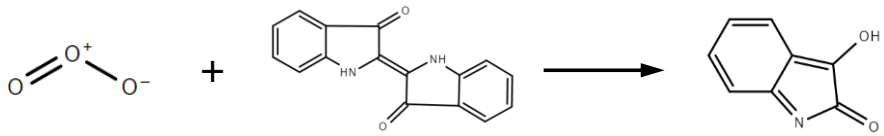

***Fig. 100**. Indigo trisulfonate reaction with ozone producing sulfonated isatine.*

For that, Dräger tubes for ozone detection were employed, cf. **Fig. 101**. Dräger tubes are colorimetric gas detectors used to detect leaks or measure air quality through a chemical reaction between a reagent and the objective gas. Particularly, these ozone detection tubes work under the reaction of ozone with indigo trisulfonate leading to isatine, previously mentioned. This reaction results in the decolouration of the reactive indigo material in the tube, which turns from a turquoise colour to yellow/white, as it can be seen in **Fig. 101**.

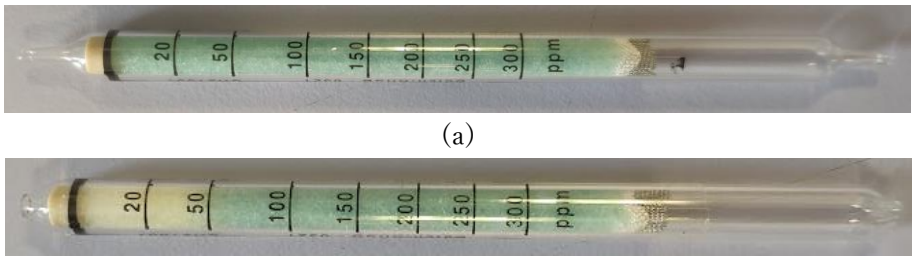

(a)

(b)

***Fig. 101**. Dräger tubes used for ozone detection. (a) Before use, (b) after exposure to ozone.*

The measured voltage V_{R_L} is represented against the measured ozone concentration via Dräger tubes in **Fig. 102**. Measurements were taken until

concentration levels reached a maximum at around 160 ppm. All measurements were carried out at room temperature.

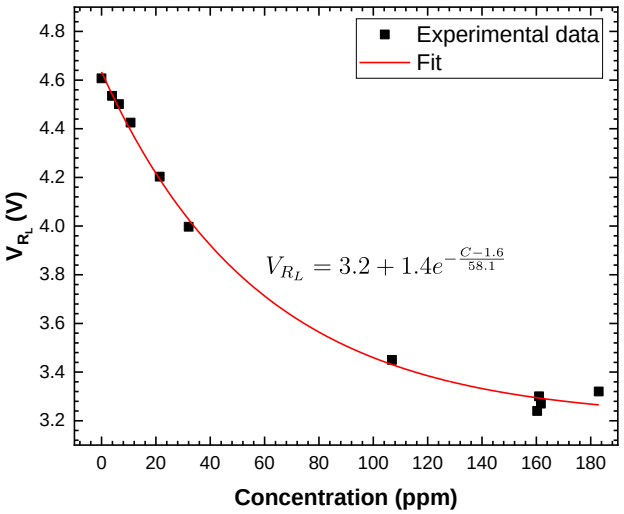

***Fig. 102**. Sensing voltage, V_{R_L}, versus ozone concentration. Experimental calibration of the MQ131 gas sensor.*

To interpolate ozone concentration values using the measured V_{R_L}, least squares fit of the data in **Fig. 102** was done using an exponential decay function as in (97).

$$V_{R_L} = V_{R_L,0} + Ae^{-\frac{C-C_0}{C_1}} \tag{97}$$

where $V_{R_L,0}$ is the measured voltage at R_L at the asymptotic concentration, C is the concentration and A, C_0 and C_1 are constants.

Appendix II. Stress relaxation fitting MATLAB code

```
% This script is used to fit stress relaxation test data to a Prony series
function.
clear all;
close all;

% Data file reading
ID_file = 'pristine'; % pristine, pr_15%, pr_30%, oz_14d, oz_21d, oz_32d,
oz_42d, te_24d, te_36d
T = readtable(['average_',ID_file,'.txt']);

% Saving data in variables
t_data = table2array(T(:,1)); % Time data
s_data = table2array(T(:,2)); % Stress data
t_1 = t_data(s_data==max(s_data)); % Time at maximum stress (end of load-
ing ramp)

% Experimental procedure data
if strcmp(ID_file,'te_24d') || strcmp(ID_file,'te_36d')
    e_0 = 0.0015; % Applied strain for temperature conditions!

else
    e_0 = 0.03; % Applied strain for all conditions

end

% Set model equation of Prony series of order n
n = 4; % Order of the Prony series
[eqn_left, eqn_right] = stress_prony_eqn(n, e_0, t_1);

% Convert string into function handles
eqn_left = str2func(eqn_left);
eqn_right = str2func(eqn_right);

% Set optimization conditions
if strcmp(ID_file,'pr_15%') || strcmp(ID_file,'pr_30%') ||
strcmp(ID_file,'te_24d') || strcmp(ID_file,'te_36d')
    P0 = [2, 2, 0.01, 0.5, 1, 0.5, 10, 0.2, 1000]; % Initial guess parame-
ters

elseif strcmp(ID_file,'oz_14d') || strcmp(ID_file,'oz_21d') ||
strcmp(ID_file,'oz_42d')
    P0 = [2 2 0.1 0.5 1 0.5 100 0.1 1000]; % Initial guess parameters

elseif strcmp(ID_file,'pristine') || strcmp(ID_file,'oz_32d')
    P0 = [1 1 0.1 0.5 1 0.2 100 0.1 1000]; % Initial guess parameters

end
```

```
A = []; % Matrix, left-hand side linear inequalities
b = []; % Vector, right-hand side linear inequalities
Aeq = []; % Matrix, left-hand side linear equalities
beq = [];% Vector, right-hand side linear equalities
lb = [0 0 0 0 1 0 10 0 100]; % Vector, lower bounds of the parameters
ub = []; % Vector, upper bounds of the parameters
nonlcon = []; % Function, non-linear constraints

% Perform minimization
P = fmincon(@(P)obj_func2(s_data, t_data, t_1, P,eqn_left,eqn_right), P0,
A,b,Aeq,beq, lb,ub,nonlcon);

% Computing stresses from fit
s_fit = stress_prony2(P,t_data, t_1, eqn_left, eqn_right);

% Saving data .mat file
save(['RelaxationFitData_',ID_file, '.mat'])

% Saving fitting parameters
fileID = fopen(['FittingParameters_',ID_file,'.txt'],'w');
fprintf(fileID, 'Einf\t%f\n',P(1));
fprintf(fileID, 'E1\t%f\n',P(2));
fprintf(fileID, 't1\t%f\n',P(3));
fprintf(fileID, 'E2\t%f\n',P(4));
fprintf(fileID, 't2\t%f\n',P(5));
fprintf(fileID, 'E3\t%f\n',P(6));
fprintf(fileID, 't3\t%f\n',P(7));
fprintf(fileID, 'E4\t%f\n',P(8));
fprintf(fileID, 't4\t%f\n',P(9));
fclose('all');

% Saving fitting stress results
fileID = fopen(['FittedCurve_',ID_file,'.txt'],'w');
fprintf(fileID, 'Time\tStress\n');
fprintf(fileID, 's\tMPa\n');
fprintf(fileID, '%f\t%f\n',[t_data,s_fit]');
fclose('all');

% Function to optimize in the least squares sense using a given Prony se-
ries (J. Xu, 2013 - doi:10.1007/s11043-012-9203-z).
% Inputs:
%    - s_data = vector, experimental stress values.
%    - t_data: vector, experimental time values.
%    - t_1: scalar, time employed for the loading ramp.
%    - mp: vector, material parameters. Should be written as [Einf, E1,
t1,
%    E2, t2, ..., En, tn].
```

```
%    - eqn_left: equation handle, equation during loading ramp.
%    - eqn_right: equation handle, equation during strain holding.
% Outputs:
%    - F: scalar, sum of the squared residuals.
%    - s_fit: vector, stresses at times t_data.
function [F, s_fit] = obj_func2(s_data, t_data, t_1,
mp,eqn_left,eqn_right)

% Compute stresses
s_left = eqn_left(mp,t_data(t_data<=t_1));
s_right = eqn_right(mp,t_data(t_data>=t_1));
s_fit = [s_left;s_right(2:end)];
% Compute the squared residuals
F = sum((s_fit - s_data).^2);

end
% Function to compute stresses for a linear viscoelastic solid in a stress
% relaxation test using a given Prony series (J. Xu, 2013 -
doi:10.1007/s11043-012-9203-z).
% Inputs:
%    - mp: vector, material parameters. Should be written as [Einf, E1,
t1,
%    E2, t2, ..., En, tn].
%    - t: vector, times at which stresses are computed.
%    - t_1: scalar, time employed for the loading ramp.
% Outputs:
%    - s: vector, stresses at times t.
function [s] = stress_prony2(mp,t, t_1, eqn_left, eqn_right)

s_left = eqn_left(mp,t(t<=t_1));
s_right = eqn_right(mp,t(t>=t_1));
s = [s_left;s_right(2:end)];

end
% Function to create a string with the function of a Pony series of order
% n for a stress relaxation curve.
% Outputs:
%    - eqn_left: equation for stresses below ramp time.
%    - eqn_right_ equation for stresses above ramp time.
% Inputs:
%    - n: order of the Prony series
function [eqn_left, eqn_right] = stress_prony_eqn(n,e_0,t_1)

    eqn_left = ['@(mp,t)(',num2str(e_0./t_1),').*(mp(1).*t +
mp(2).*mp(3).*(1-exp(-t./mp(3)))'];
    eqn_right = ['@(mp,t)(',num2str(e_0./t_1),').*(mp(1).*',num2str(t_1),'
+ mp(2).*mp(3).*(exp(-(t-mp(3))./mp(3))-exp(-t./mp(3)))'];
```

```
    if n<2
        eqn_left = [eqn_left,')'];
        eqn_right = [eqn_right,')'];

    else

        for i = 2:n

            eqn_left = [eqn_left, ' +
mp(',num2str(2*i),').*mp(',num2str(2*i+1),').*(1-exp(-
t./mp(',num2str(2*i+1),')))'];
            eqn_right = [eqn_right, '
+mp(',num2str(2*i),').*mp(',num2str(2*i+1),').*(exp(-(t-
mp(',num2str(2*i+1),'))./mp(',num2str(2*i+1),'))-exp(-
t./mp(',num2str(2*i+1),')))'];
        end

        eqn_left = [eqn_left,')'];
        eqn_right = [eqn_right,')'];

    end

end
```

Appendix III. Strain analysis. Dewetting point determination

The determination of the dewetting point is not defined by a specific method. It is usually inferred from the analysis of the stress-strain curve, Poisson's ratio or dilatation. Here, the $\nu - \varepsilon_l$, $\sigma - \varepsilon_l$ and $V/V_0 - \varepsilon_l$ curves are examined to identify the most feasible solution to determine the dewetting point. This significant point in the mechanical behaviour of the composite solid propellant is assumed to exist in the vicinity of the region where the elastic slope of the uniaxial stress versus strain curve shifts to the hardening slope.

The analysis includes the determination of the two first derivatives of the mentioned curves in this transition region. The dewetting point is identified for the ε_l at which a local maximum or minimum of the derivatives is found. Since the curves present two different slopes in the analysed region, the dewetting point has also been determined at the corresponding ε_l at which both slopes intersect.

All analysed $\nu - \varepsilon_l$, $\sigma - \varepsilon_l$ and $V/V_0 - \varepsilon_l$ curves are shown in **Fig. 103** to **Fig. 105** for the preliminary characterisation samples and in **Fig. 106** to **Fig. 109** for the samples used in the ageing characterisation.

The resulting dewetting strains for each method, ε_{dew}, are listed in **Table 28** and **Table 29** for the preliminary and ageing characterisations, respectively.

The identified dewetting strain through the second derivative of the stress versus strain curves has been chosen as the best method to determine the dewetting point. The main reasons are:

- Only stress versus strain curve is needed. Uniaxial tensile tests are usually a part of the surveillance programs for composite solid propellant. Therefore, it is information easily available.
- No calculation or additional equipment is required, unlike it is necessary to measure strains in the transverse direction.
- The identified dewetting point corresponds to a change in the trend of the curves before the dewetting point in the corresponding $\nu - \varepsilon_l$ and $V/V_0 - \varepsilon_l$ analysed curves, specifically, the results

are similar to the ones obtained through the $\nu - \varepsilon_l$ curves for most of the cases.

- It has been proved to be more consistent when applied to all different conditions.

Table 28. *Dewetting strain, ε_{dew}, determined from the analysis of the dilatation, V/V_0, uniaxial stress, σ, and Poisson' s ratio, ν, versus applied longitudinal strain ε_l curves for the preliminary characterisation.*

Crosshead speed (mm/min)	ε_{dew}								
	$V/V_0 - \varepsilon_l$			$\sigma - \varepsilon_l$			$\nu - \varepsilon_l$		
	Slopes Intersection	1st Derivative	2nd Derivative	Slopes Intersection	1st Derivative	2nd Derivative	Slopes Intersection	1st Derivative	2nd Derivative
5	0.14±0.01	0.03±0.03	0.06±0.05	0.093±0.004	0.019±0.004	0.064±0.003	0.07±0.01	0.09±0.04	0.08±0.01
50	0.12±0.01	-	0.07±0.01	0.070±0.003	-	0.052±0.006	0.04±0.01	0.09±0.01	0.07±0.02
500	0.13±0.01	-	0.08±0.01	0.064±0.007	-	0.046±0.003	0.04±0.01	0.10±0.01	0.13±0.01

Table 29. *Dewetting strain, ε_{dew}, determined from the analysis of the dilatation, V/V_0, uniaxial stress, σ, and Poisson's ratio, ν, versus applied longitudinal strain ε_l curves for the ageing characterisation.*

Ageing source	ε_{dew}								
	$V/V_0 - \varepsilon_l$			$\sigma - \varepsilon_l$			$\nu - \varepsilon_l$		
	Slopes Intersection	1st Derivative	2nd Derivative	Slopes Intersection	1st Derivative	2nd Derivative	Slopes Intersection	1st Derivative	2nd Derivative
Pristine	0.182	0.072	0.127	0.124	0.051	0.096	0.105	0.179	0.096
Prestrain 15%	0.198	0.097	0.129	0.156	0.118	0.138	0.126	0.201	0.119
Prestrain 30%	0.228	0.106	0.189	0.263	0.175	0.267	0.174	0.257	0.178
Temperature 24	0.021	0.002	0.004	0.006*	0.012	0.013	0.004*	0.008	0.009
Temperature 36	0.017	0.004	0.005	0.005*	0.007	0.008	0.005*	0.007	0.008
Ozone 12 days	0.17	0.069	0.142	0.151	0.078	0.106	0.108	0.176	0.113
Ozone 42 days				0.225	0.095	0.112			

*Chosen as the end of the elastic slope

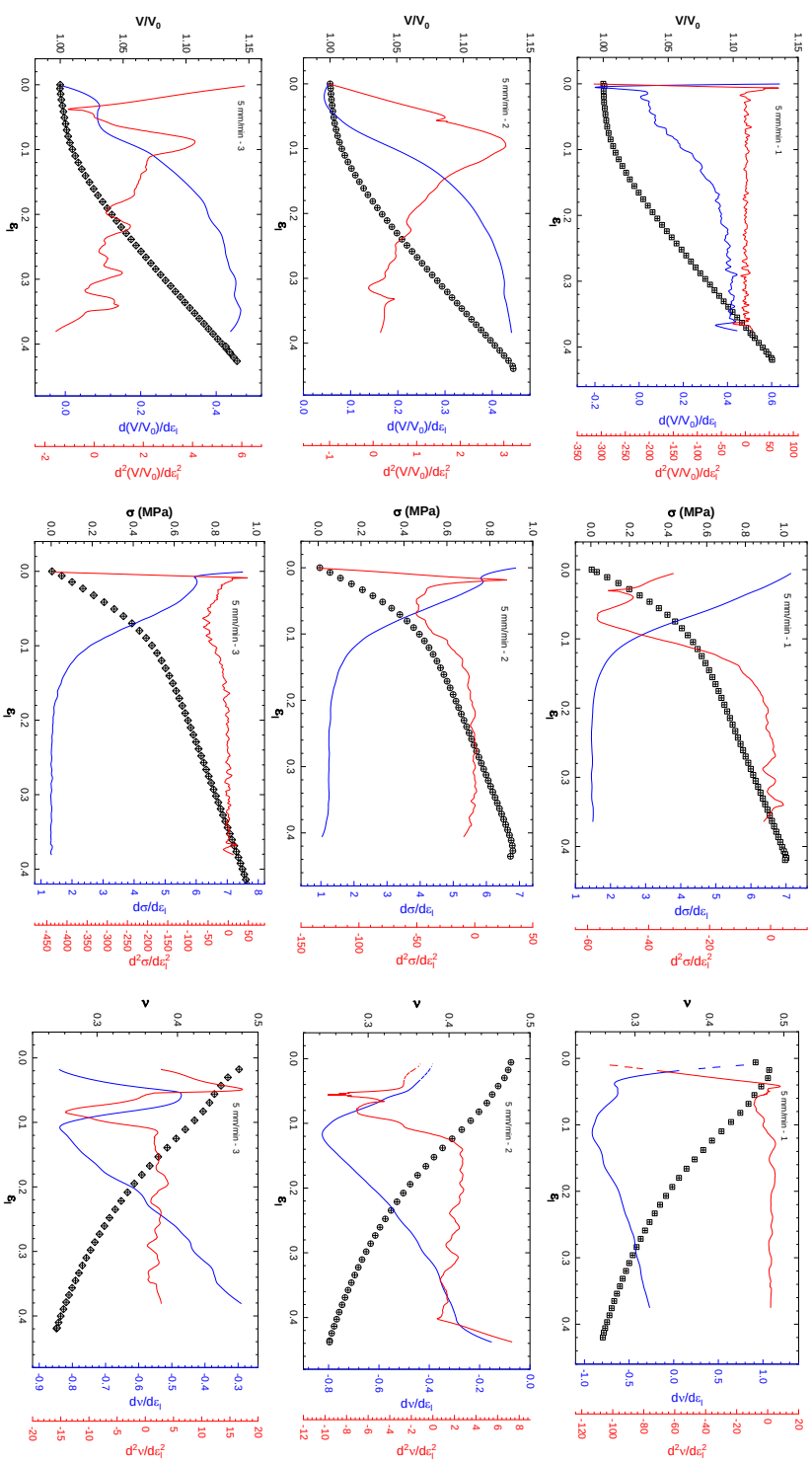

Fig. 103. Dilatation $V/V_0 - \varepsilon_l$, uniaxial stress $\sigma - \varepsilon_l$ and Poisson' s ratio $\nu - \varepsilon_l$ curves for the samples tested at 5 mm/min for the preliminary characterisation.

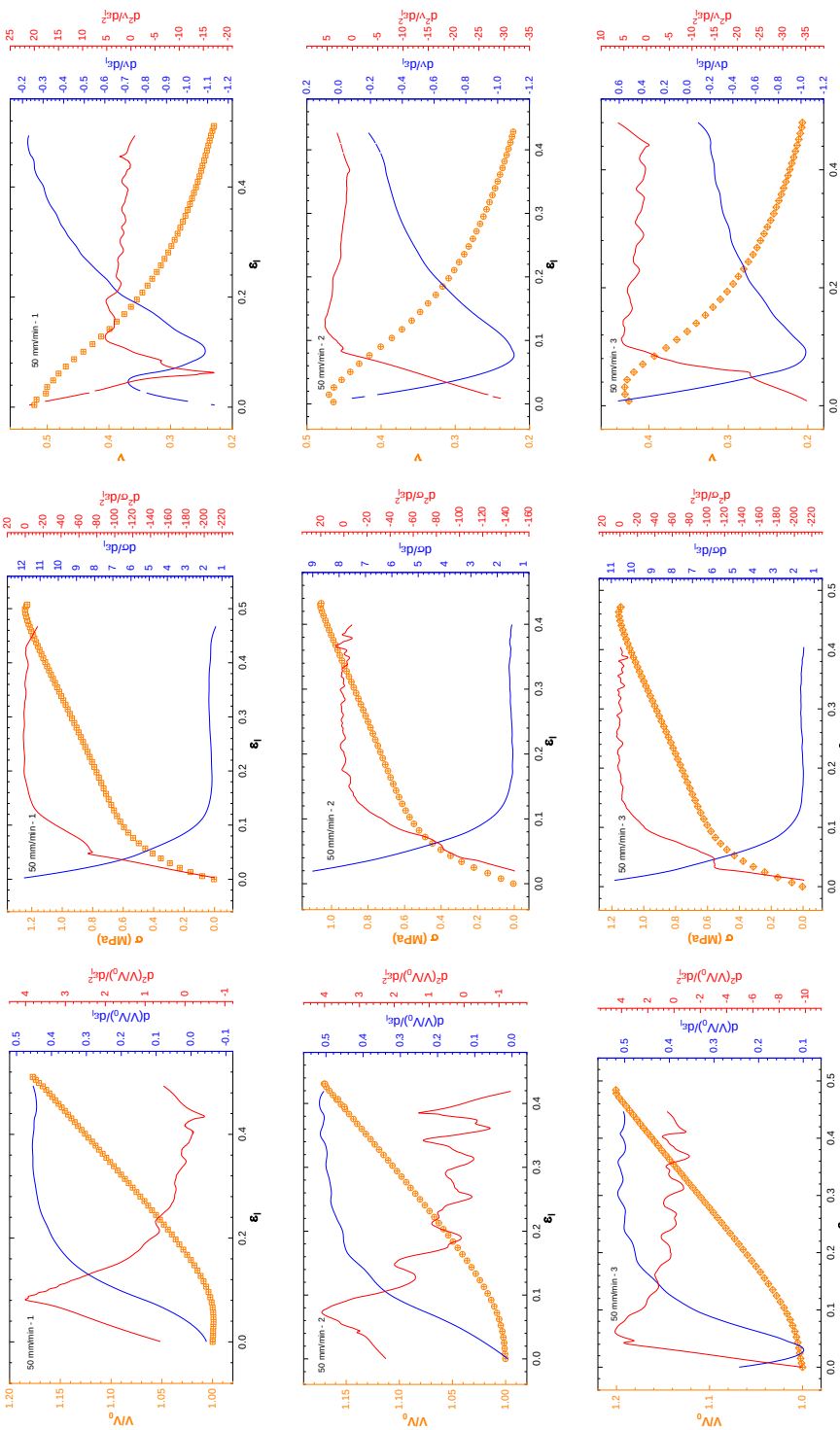

Fig. 104. *Dilatation $V/V_0 - \varepsilon_l$, uniaxial stress $\sigma - \varepsilon_l$ and Poisson´s ratio $\nu - \varepsilon_l$ curves for the samples tested at 50 mm/min for the preliminary characterisation.*

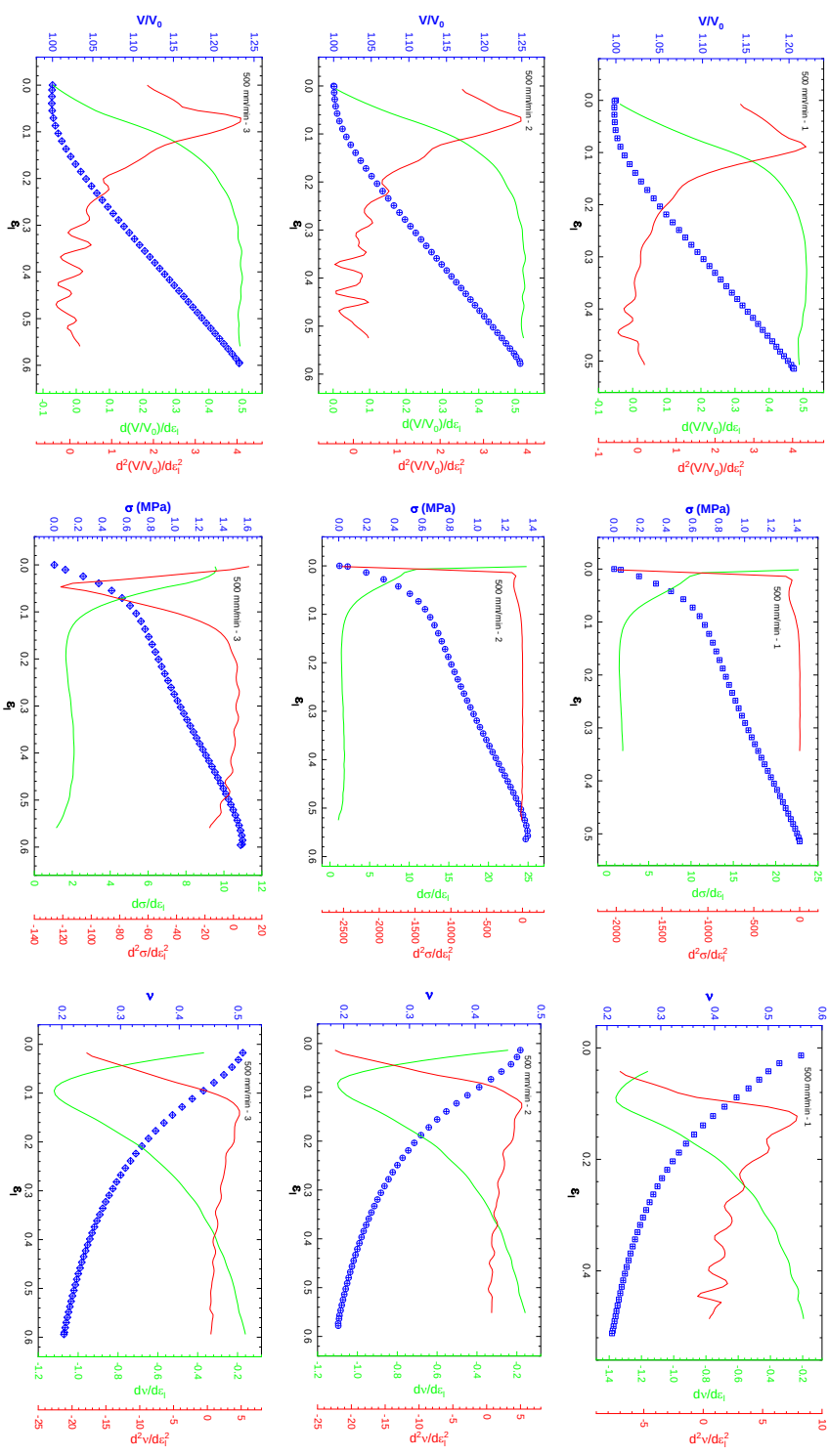

Fig. 105. Dilatation $V/V_0 - \varepsilon_l$, uniaxial stress $\sigma - \varepsilon_l$ and Poisson's ratio $\nu - \varepsilon_l$ curves for the samples tested at 500 mm/min for the preliminary characterisation.

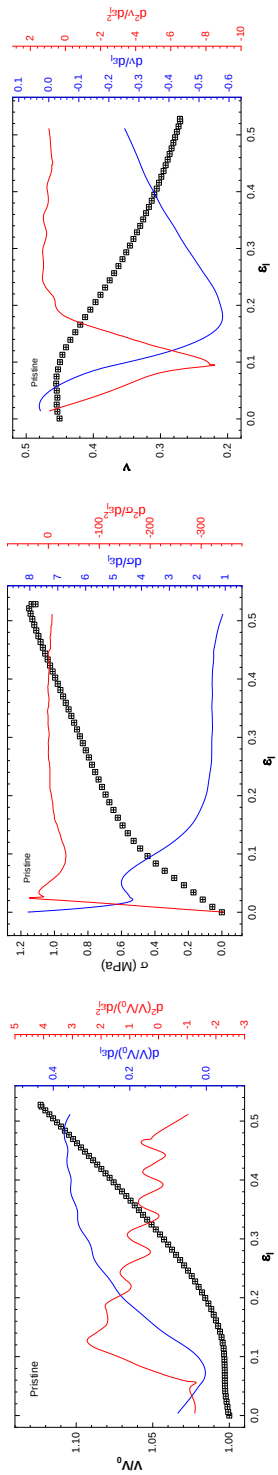

Fig. 106. *Dilatation $V/V_0 - \varepsilon_1$, uniaxial stress $\sigma - \varepsilon_1$ and Poisson's ratio $\nu - \varepsilon_1$ curves for the pristine sample for the ageing characterisation.*

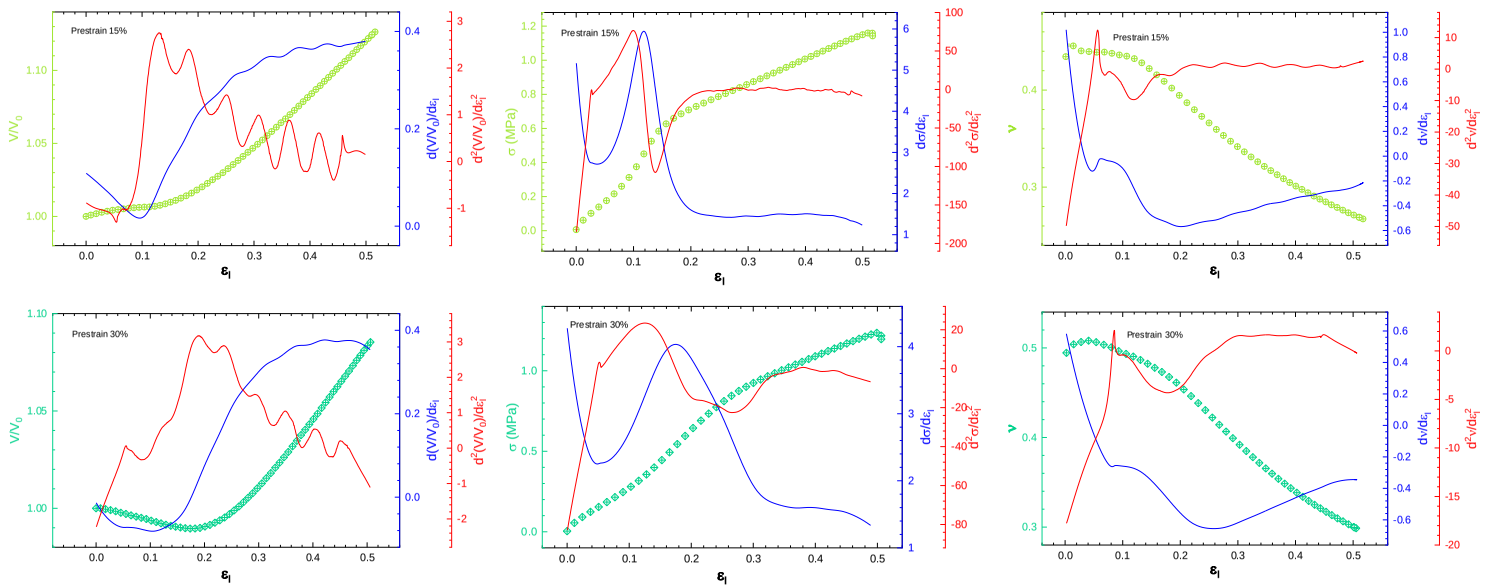

Fig. 107. *Dilatation $V/V_0 - \varepsilon_l$, uniaxial stress $\sigma - \varepsilon_l$ and Poisson's ratio $\nu - \varepsilon_l$ curves for the mechanically aged samples for the ageing characterisation.*

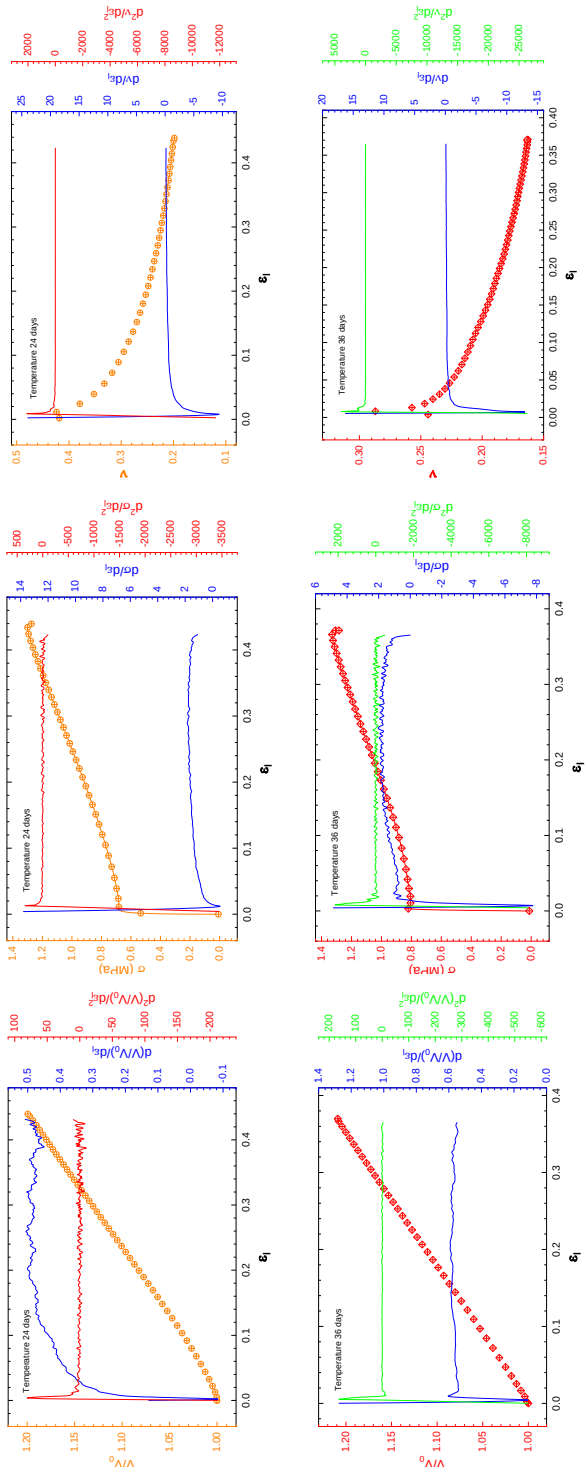

Fig. 108. *Dilatation $V/V_0 - \varepsilon_l$, uniaxial stress $\sigma - \varepsilon_l$ and Poisson's ratio $\nu - \varepsilon_l$ curves for the thermally aged samples for the ageing characterisation.*

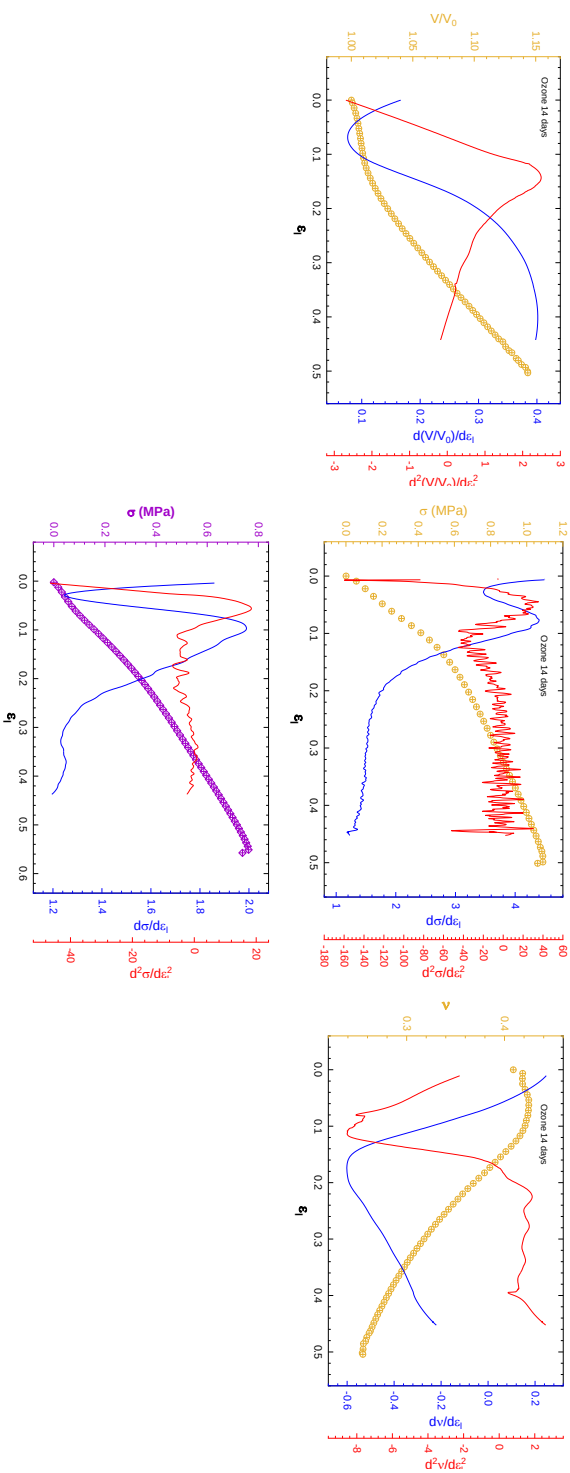

Fig. 109. *Dilatation $V/V_0 - \varepsilon_l$, uniaxial stress $\sigma - \varepsilon_l$ and Poisson' s ratio $\nu - \varepsilon_l$ curves for the ozone aged samples for the ageing characterisation.*